Polarisation and angular momentum of light in guided modes theory and implementations of dipolar sources coupling

Picardi, Michela

Awarding institution:
King's College London

Polarisation and angular momentum of light in guided modes: theory and implementations of dipolar sources coupling

Candidate: Michela Florinda Picardi

Supervisor: Francisco Rodríguez-Fortuño

King's College London

Faculty of Natural and Mathematical Sciences

Department of Physics

Thesis submitted for the degree of Doctor of Philosophy

A mio fratello Manfredi

Acknowledgements

The book you are holding in your hands is the result of a work which has been made possible by many incredible people, each of whom deserves my deepest thankfulness. I have been extremely lucky to meet all these people and to learn something from each of them.

To start, of course, the biggest thanks go to my supervisor, Dr Francisco Rodríguez-Fortuño, universally known as Paco. With a single data point and entirely denying the scientific method I should be familiar with by now, I am going to say with confidence he's the best supervisor one could hope for. Paco's scientific knowledge, together with his passion for mentoring, have turned my research into a fun ride, in which I was encouraged to pick my own route, knowing there would be someone holding a map if I got lost. Of course, my gratitude is also reserved for Prof Anatoly Zayats who has always been kindly available for guidance and advice. I also wish to thank Drs Konstantin Bliokh and Franco Nori for welcoming me in their group in Tokyo, allowing me to both widen my research extents and discover a beautiful country.

London has become home quite immediately after my arrival, and this is definitely thanks to the fantastic friends and colleagues I've met here. My gratitude goes first and foremost to Francesco, with whom I've shared uncountable movie nights, game nights, Sunday lunches and trips to the comic book store. He's been my emergency contact in every form I've had to fill and the emergency chocolate and friendship dispenser in every stressful situation. His books and games suggestions costed me a fortune but it was a pleasure to share my PhD days with him. I am thankful to Diane for being the perfect buddy in every situation, be it at the pub, crossing the bridge, while in the lab or at a pride parade. She has offered me a safe-space friendship and allowed me to fill it with cat videos. A large chunk of my thankfulness is reserved to the very British duo, Luke and Will, who have introduced me to *Twiggles*, pork scratchings and *Jaffa Cakes*, rarely agreed on grammar in their native language and tried their best to teach me cricket. I do remember that the leg must not go before the wicket, but I'm not really sure whether the wicket is the bat or the top stick, so, guys, I suspect I failed you on this. I also wish to thank Wayne for enthusiastically listening to and appreciating my ideas, sharing his

thoughts with me on our breaks (whether it's science or politics) and, most of all, for crushing my insecurities with a few words, giving me reasons not to worry and volunteering to step in countless times, when he thought I might have needed support.

All my research has been made possible by the wonderful working environment I found at King's. My scientific knowledge has greatly benefited from sharing my research with Paco's group of incredibly talented scientists. My deepest gratitude goes to Lei and Jack, who have been the first people I would go to with my bag of doubts, ranging from science all the way to color palettes for plots. By the way, yes, *Avocadocolors* is the very best color palette for a density plot. Let me also mention the two visiting scientists who, even if for a short period of time, were a fantastic addition to our group: Kike and Boris. I really hope that our paths shall meet again. Also, I wish to thank all the admin staff, without whom I'd probably still be trying to figure out how to access the building, particularly Megan and Rowena for relentlessly supporting me and never doing so without a big smile. My experience in science would have felt incomplete without the possibility of sharing my enthusiasm with a vaster audience than a selected group of peers and, for this, I shall thank Eva, who has let me share with her the fun of numerous outreach activities. Finally, the possibility of staying in the department for the whole evening has a very sweet taste when it means spending the night with a bunch of adventurers on a quest to save the world from evil. Therefore, the most sincere thanks go to my fabulous D&D party, Claudio, Jack, Francesco and Boris and, of course, to the mind behind every dragon, minotaur, banshee, lycanthrope and assassin we've faced, Furqaan.

I would not have been able to focus on this work without the safety net of peacefulness provided by my family, the people I love the most, who have been there in every step of this journey. I wish to express my deepest gratitude to my best friends, Roberta and Fabiana, who have never been farther than a phone call away and managed to feel as close as the day I met them, nineteen and sixteen years ago, respectively. I relied on them so heavily that this thesis should probably list them as co-authors. To these two marvellous humans I owe much more than a thank you sentence and I am sure they know that. A gigantic thank you goes to my parents, their partners, my grandma and my beloved little brother, to whom this thesis is dedicated. My hope is that this dedication acts as a reminder that he can achieve whatever he sets his mind to, no matter what anyone tells him he should be doing. I know I have made you all proud, I'm honoured to have done so and I will do my best to continue doing it. Finally, my most sincere gratitude goes to Antigone, for believing in me, trusting me, motivating me and, substantially, making me happier day by day. She has been the most amazing partner in every travel, discovery, experience and emotion and I could not have been more lucky than to find someone like her to share this trip with. You know, after all I've only done this so that we can both book our plane tickets as doctors.

Abstract

Light possesses many degrees of freedom, the most distinctive of which are polarisation, angular momenta, Poynting vector and helicity, which, in confined geometries, behave very differently than in free space. In said confined geometries, such as those required for the existence of guided modes, these degrees of freedom can interact with one-another giving rise to phenomena such as Spin-to-Orbital angular momentum transfer or Spin-momentum locking. In this thesis, we focus our attention on the exchange between the degrees of freedom of dipolar sources, superpositions of electric and magnetic dipoles in the most general case, and those of guided modes. This allows to achieve interesting excitations of guided modes, such as polarisation-dependent coupling (or absence thereof), or unidirectional excitation. The dipoles needed to achieve these phenomena are found analytically, with a very simple notation. Via numerical analysis both realistic sources, usually being nanoparticles under plane wave illumination, and waveguiding structures are designed and optimised. We extend the unidirectional excitation of guided modes, previously obtained with circularly polarised electric dipoles, to circularly polarised magnetic dipoles and superpositions of electric and magnetic dipoles, such as the Huygens dipole. This is done using the angular spectrum approach, and we prove it provides the same results that would be obtained using Fermi's golden rule. We also reveal the existence of a source, the Janus dipole, whose coupling to guided modes is not directional but can be arbitrarily switched on-and-off simply inverting its polarisation, of which we show an experimental realisation. Moreover, we demonstrate that a superposition of electric and magnetic dipoles is sufficient to control amplitude, phase and direction of individually up to five different guided modes in the same waveguide. Finally, we present accurate calculations, both numerical and analytical of spin, angular momenta and helicity for the eigenmodes of nanofibers and nanowires, showing, among other properties, the quantization of the total angular momenta of cylindrical guided modes without the need for paraxial approximation.

Contents

Introduction and objectives

This thesis collects and summarises the work performed under the doctoral program of *King's College London* for the degree of Doctor of Philosophy in Physics. All the work presented here has been carried out under the supervision of Dr. Francisco Rodriguéz- Fortuño as part of the *Photonics and Nanotechnology* group of King's College London headed by professor Anatoly Zayats, second supervisor of this project. Part of the work presented in this thesis, moreover, has been performed over two short-term stays at RIKEN Centre, Tokyo, under the guidance of Dr. Konstantin Bliokh as part of the *Theoretical Quantum Physics* laboratory. Finally, the experimental results presented in this thesis have been obtained by our collaborators at Max Planck Institute in Erlangen belonging to the *Interference Microscopy, Polarization and Nano-Optics* group, led by Dr. Peter Banzer.
Most of the work presented in this thesis has been published in peer reviewed journals and is, therefore, presented in the form of published papers, collected in chapters according to their topic. Supporting theoretical and background materials, together with unpublished works, make up the rest of this doctoral dissertation.
This thesis constitutes the final work of the grant awarded by the EPSRC Doctoral Training Program.

Nanophotonics

The main character of the following story is undoubtedly *light* and most of the plot is set in the realm of *nanophotonics*. Nanophotonics dwells on light in nanoscale environments, substantially dealing with the physics that happens when the wavelength of light and the structures said light interacts with are of the same size, which usually spans a range between tens to hundreds of nanometers [1–3]. This nanometric range, usually dangerously close to or even below the diffraction limit,

is becoming an accessible experimental reality due to the tremendous technological advances which are constantly redefining the boundary between what is feasible and what is not. At this scale elusive phenomena, which don't take place or are not detectable when light propagates in free-space, are boosted, such as spin-to-orbit conversions [4], nonlinear effects [5] and subwavelength localisation and enhancement of the electromagnetic fields [6]. Initial access to this very small scale was granted by metallic nanostructures, giving birth to the field of *plasmonics* [7, 8]. Today, however, the field is no longer dominated by metals only, as the use of dielectric nanostructures is growing, in an attempt to overcome the ohmic losses which are unavoidable in metals [9]. Metallic, dielectric and hybrid nanostructures can nowadays be tailored to satisfy the requirements of very different applications, depending on the desired level of, for example, field confinement, localised heating, dispersion, organic compatibility and speed, to name a few.

Objectives

Our contribution to such a fast-evolving field has been focused on the study, the description and the optimisation of light, its degrees of freedom and their interaction at the nanoscale. This has been done using multiple strategies and seeking, whenever possible, experimental realisations, together with analytical calculations and numerical simulations, performed using both commercial softwares and home-made codes. We are confident that our research has resulted in a collection of tools, in the form of analytical expressions or developed softwares, which might serve as a basis for future research in the field.

Structure of the thesis

This thesis is developed as follows:

- The current *Introduction and objectives*, followed by a series of thematic numbered chapters.
- Chapter 1: *Theory foundations*, in which the fundamental theoretical background necessary for a comprehensive understanding of our work is laid out. It starts from Maxwell's equations and Poynting theorem, to continue with a description of time-harmonic fields, the angular spectrum approach, and Green's function formalism. In this chapter we also provide an introduction to evanescent waves, guided modes and surface plasmons. These concepts will serve as a useful theoretical toolbox for the more advanced applications described in the subsequent chapters.
- Chapter 2: *Unidirectionality of dipolar near fields*, where light's angular momenta are described, together with one mechanism for spin-orbit interaction of light. An overview of the state of the art in the literature on the topic is presented and an application of the angular spectrum approach is also presented in order to calculate of the fields of dipolar sources. The main result of this approach leads to unidirectionality in the fields of circular electric and magnetic dipoles and is presented in our work [Paper A], included in the chapter. This approach is also compared with Fermi's golden rule technique.
- Chapter 3: *Near-field directionality beyond spin-momentum locking*, deals with the scattering from nanostructures and the dipolar sources which may be obtained by it, with a special focus on the three elemental sources which achieve some expression of directional coupling. Particularly, the dipolar source named Janus dipole is presented in this chapter within our works [Paper B] and [Paper C], in which it is described theoretically and [Paper D], in which it is observed experimentally.
- Chapter 4: *Multimode control*, extends the results of chapter 3 to the control of amplitude, phase and direction of more than one mode with a single dipolar source. The results therein are still unpublished and are therefore not presented as a paper.

- Chapter 5: *Nanofibers and nanowires*, gives an overview of the degrees of freedom of light in a medium and frames them into the picture of the Abraham-Minkowski controversy. This chapter includes our work [Paper E] on angular momenta in nanofibers and nanowires.

- Finally, we conclude our dissertation summarising our results in a comprehensive *Discussion of results and conclusions*, where we also suggest potential extensions and applications of this work.

- After the conclusions, a list of *Author's merits* is provided, including our main contributions in internationally published papers, additional contributions as a co-author, a yet unpublished preprint and the list of conferences at which our work has been presented.

Chapter 1

Theory foundations

In this chapter, the fundamental theory concepts which will be employed throughout the whole thesis are introduced. All of what is derived here can be found in multiple textbooks, so we will only summarize what is relevant to the thesis and introduce the notation which will be adopted in subsequent chapters. We will start our discussion from the fundamental concepts for the description of electromagnetic radiation: Maxwell's equations and Poynting theorem, and build on that to describe the angular spectrum approach, time harmonic fields and Green's function formalism. We will also briefly introduce evanescent waves, surface plasmons and guided modes, as these have often been the subjects to which our studies were applied.

1.1 Maxwell's equation

While professor of Natural Philosophy in this very same building at King's College London, James Clerk Maxwell formulated the most notable equations of electromagnetism, in a series of four papers between 1861 and 1862 [10–13], later collected together in 1865 [14]. These equations relate the electric and magnetic vector fields $\mathbf{E}(\mathbf{r}, t)$ and $\mathbf{H}(\mathbf{r}, t)$ and their spatial and temporal evolution. Maxwell's equations

read [15, 16]:

$$\begin{aligned}\nabla \times \mathbf{H} &= \frac{\partial \mathbf{D}}{\partial t} + \mathbf{J} \\ \nabla \times \mathbf{E} &= -\frac{\partial \mathbf{B}}{\partial t} \\ \nabla \cdot \mathbf{D} &= \rho \\ \nabla \cdot \mathbf{B} &= 0\end{aligned} \tag{1.1}$$

where $\mathbf{D}$ is the electric displacement field, $\mathbf{J}$ is the external current density, $\mathbf{B}$ is the magnetic induction field, and ρ is the external charge density. The electric and magnetic responses of the medium are included in the $\mathbf{D}$ and $\mathbf{B}$ vectors via the polarization $\mathbf{P}$ and magnetization $\mathbf{M}$, respectively, according to:

$$\begin{aligned}\mathbf{D} &= \varepsilon_0 \mathbf{E} + \mathbf{P} \\ \mathbf{B} &= \mu_0 \mathbf{H} + \mu_0 \mathbf{M}\end{aligned} \tag{1.2}$$

with ε_0 being the electric permittivity and μ_0 the magnetic permeability of free space. Due to these terms, Maxwell's equations provide a good description not only of the currents and charges responsible for free-space radiation, but also of those which are formed in matter under illumination. If we replace equations (1.2) into Maxwell's equations (1.1) and take the curl of the two *curl* equations we obtain the wave equations for $\mathbf{E}$ and $\mathbf{H}$ fields:

$$\begin{aligned}\nabla \times \nabla \times \mathbf{E} + \frac{1}{c^2}\frac{\partial^2}{\partial t^2}\mathbf{E} &= -\mu_0 \frac{\partial}{\partial t}\left(\frac{\partial}{\partial t}\mathbf{P} + \mathbf{J} + \nabla \times \mathbf{M}\right) \\ \nabla \times \nabla \times \mathbf{H} + \frac{1}{c^2}\frac{\partial^2}{\partial t^2}\mathbf{H} &= -\frac{1}{c^2}\frac{\partial}{\partial t}\left(\frac{\partial}{\partial t}\mathbf{M} + c^2 \nabla \times \mathbf{P}\right) + \nabla \times \mathbf{J}\end{aligned} \tag{1.3}$$

Presented for the first time in Maxwell's 1865 paper [14], the wave equations unveil the relation between the electric and magnetic fields with the speed of light c, proposing a description of light as an electromagnetic wave. Solving these equations we can know the value of the electric and magnetic fields at every point in space and time.

1.2 Poynting's theorem

Of paramount importance for the description of electromagnetic fields was, in 1884, Poynting's derivation of a fundamental theorem which relates to the conservation of energy and has ever since gone under the name of Poynting's theorem [17]. Via this theorem we will be able to define the time-dependent Poynting vector, the fundamental quantity from which the time averaged energy flow and reactive power (i.e., its real and imaginary parts) will be derived and used in our subsequent calculations in chapter 3. Following Jackson's derivation [15], the rate of work done by an external field on a single charge q is given by $q\mathbf{v}\cdot\mathbf{E}$, where $\mathbf{v}$ is the charge's velocity. The work is done by the electric field only since the magnetic field's force $\mathbf{F}_{\mathrm{B}} = q\mathbf{v}\times\mathbf{B}$ is orthogonal to $\mathbf{v}$. Extending our considerations from a single point charge to a continuous distribution of charge and current and integrating in a finite volume V, the total rate of work done by the fields is given by:

$$\int_V \mathbf{J}\cdot\mathbf{E}\,dV, \tag{1.4}$$

where $\mathbf{J}$ is the current density. We can substitute $\mathbf{J}$ in equation (1.4) using Maxwell's first equation (1.1):

$$\int_V \mathbf{J}\cdot\mathbf{E}\,dV = \int_V \left[\mathbf{E}\cdot(\nabla\times\mathbf{H}) - \mathbf{E}\cdot\frac{\partial\mathbf{D}}{\partial t}\right] dV\,. \tag{1.5}$$

Employing the properties of the triple product, the term $\mathbf{E}\cdot(\nabla\times\mathbf{H})$ can be written as:

$$\mathbf{E}\cdot(\nabla\times\mathbf{H}) = \mathbf{H}\cdot(\nabla\times\mathbf{E}) - \nabla\cdot(\mathbf{E}\times\mathbf{H}),$$

and the term $\mathbf{H}\cdot(\nabla\times\mathbf{E})$ can be substituted by means of Maxwell's second equation (1.1). This leaves us with equation (1.5) reduced to:

$$\int_V \mathbf{J}\cdot\mathbf{E}\,dV = -\int_V \left[\nabla\cdot(\mathbf{E}\times\mathbf{H}) + \mathbf{E}\cdot\frac{\partial\mathbf{D}}{\partial t} + \mathbf{H}\cdot\frac{\partial\mathbf{B}}{\partial t}\right] dV\,. \tag{1.6}$$

In a linear, lossless medium, we can write the total electromagnetic energy density as:

$$u = \frac{1}{2}(\mathbf{E}\cdot\mathbf{D} + \mathbf{B}\cdot\mathbf{H}),$$

where we are using the fact that $\frac{1}{2}\int_V(\mathbf{E}\cdot\mathbf{D})\,dV$ is the total electrostatic energy and $\frac{1}{2}\int_V(\mathbf{B}\cdot\mathbf{H})\,dV$ is the magnetostatic one and assuming that they do not change in time-varying fields. We can then rewrite equation (1.6) as:

$$-\int_v \mathbf{J}\cdot\mathbf{E}\,dV = \int_V \left[\frac{\partial u}{\partial t} + \nabla\cdot(\mathbf{E}\times\mathbf{H})\right] dV\,. \tag{1.7}$$

Due to the arbitrarity of the integration volume we chose, we can safely rewrite equation (1.7) as a differential continuity equation, i.e., a conservation law:

$$\frac{\partial u}{\partial t} + \nabla\cdot\mathbf{P} = -\mathbf{J}\cdot\mathbf{E}, \tag{1.8}$$

where $\mathbf{P} = \mathbf{E}\times\mathbf{H}$ is the long awaited Poynting vector, which physically represents the energy flow of electromagnetic fields. Physically, equation (1.8) describes the exchange of energy in the system: the time variation of the electromagnetic energy u, plus the flow of energy through a given volume, is equal to the negative work done by the fields on the charge distribution in the volume.
Maxwell's equations and Poynting theorem are the very fundamental blocks of electromagnetic theory. Starting from these concepts, we can build the mathematical description that best suits the physics we are studying and we will start doing so by introducing time-harmonic fields.

1.3 Time harmonic fields

In a linear medium, a time-dependent electromagnetic field can be written as a superposition of monochromatic fields employing the so-called spectral representation [16]. This is made possible by the properties of Fourier transforms. We apply a Fourier transform to a time dependent field:

$$\tilde{\mathbf{E}}(\mathbf{r},\omega) = \frac{1}{2\pi}\int_{-\infty}^{\infty}\mathbf{E}(\mathbf{r},t)e^{i\omega t}dt, \tag{1.9}$$

and simultaneously to Maxwell's equations (1.1). This leads to:

$$\begin{aligned}
\nabla \times \tilde{\mathbf{E}}(\mathbf{r},\omega) &= i\omega\tilde{\mathbf{B}}(\mathbf{r},\omega) \\
\nabla \times \tilde{\mathbf{H}}(\mathbf{r},\omega) &= -i\omega\tilde{\mathbf{D}}(\mathbf{r},\omega) + \tilde{\mathbf{J}}(\mathbf{r},\omega) \\
\nabla \cdot \tilde{\mathbf{D}}(\mathbf{r},\omega) &= \tilde{\rho}(\mathbf{r},\omega) \\
\nabla \cdot \tilde{\mathbf{B}}(\mathbf{r},\omega) &= 0
\end{aligned} \tag{1.10}$$

We can then solve Maxwell's equations for $\tilde{\mathbf{E}}(\mathbf{r},\omega)$ and obtain the time-dependent field via inverse Fourier transform of equation (1.9):

$$\mathbf{E}(\mathbf{r},t) = \int_{-\infty}^{\infty} \tilde{\mathbf{E}}(\mathbf{r},\omega)e^{-i\omega t}d\omega. \tag{1.11}$$

This is a very common and convenient procedure to simplify time-dependent calculations, the time dependence can be overcome by Fourier transform and every spectral component can be treated separately as a single monochromatic field. We can then safely factor out the time dependence in the wave equation and only deal with superpositions of time-harmonic monochromatic fields, each of which can be written as:

$$\begin{aligned}
\mathbf{E}(\mathbf{r},t) &= \mathrm{Re}\{\tilde{\mathbf{E}}(\mathbf{r})e^{-i\omega t}\} \\
\mathbf{H}(\mathbf{r},t) &= \mathrm{Re}\{\tilde{\mathbf{H}}(\mathbf{r})e^{-i\omega t}\},
\end{aligned} \tag{1.12}$$

where we have dropped the ω dependence from the fields as each of them is monochromatic, i.e: $\tilde{\mathbf{E}}(\mathbf{r},\omega) = \tilde{\mathbf{E}}(\mathbf{r})$.
Writing Maxwell's equations for time harmonic fields leads to:

$$\begin{aligned}
\nabla \times \tilde{\mathbf{E}}(\mathbf{r}) &= i\omega\tilde{\mathbf{B}}(\mathbf{r}) \\
\nabla \times \tilde{\mathbf{H}}(\mathbf{r}) &= -i\omega\tilde{\mathbf{D}}(\mathbf{r}) + \tilde{\mathbf{J}}(\mathbf{r}) \\
\nabla \cdot \tilde{\mathbf{D}}(\mathbf{r}) &= \tilde{\rho}(\mathbf{r}) \\
\nabla \cdot \tilde{\mathbf{B}}(\mathbf{r}) &= 0
\end{aligned} \tag{1.13}$$

Equations (1.13) correspond to the Fourier transform of time-dependent Maxwell's equations (1.10) but for a fixed value of ω, which is to be expected since we are considering monochromatic fields.
Maxwell's equations, and consequently the wave equation, are greatly simplified when they are applied to linear, isotropic and source-free media. In this kind of

medium, in fact, $\tilde{\mathbf{P}}$ and $\tilde{\mathbf{M}}$ acquire a simple form:

$$\begin{aligned}\tilde{\mathbf{P}} &= \varepsilon_0 \chi_e \tilde{\mathbf{E}} \\ \tilde{\mathbf{M}} &= \chi_m \tilde{\mathbf{H}},\end{aligned} \tag{1.14}$$

where χ_e and χ_m are the electric and magnetic susceptibilities. This allows us to rewrite equations (1.2) as:

$$\begin{aligned}\tilde{\mathbf{D}} &= \varepsilon \tilde{\mathbf{E}} \\ \tilde{\mathbf{B}} &= \mu \tilde{\mathbf{H}}\end{aligned} \tag{1.15}$$

where $\varepsilon = \varepsilon_0 \varepsilon_r$ and $\mu = \mu_0 \mu_r$, with ε_r and μ_r being the relative electric permittivity and magnetic permeability characteristic of the medium. The parameters ε and μ are in general functions of both frequency and wavevector, i.e.: $\varepsilon = \varepsilon(\omega, \mathbf{k})$ and $\mu = \mu(\omega, \mathbf{k})$. This functional dependence accounts for temporal and spatial dispersion.
In this case, we can use equations (1.15) and the terms $\mathbf{J} = \rho = 0$. The wave equations simply become:

$$\begin{aligned}\nabla^2 \tilde{\mathbf{E}} - \frac{\varepsilon\mu}{c^2} \frac{\partial^2}{\partial t^2} \tilde{\mathbf{E}} = 0 \\ \nabla^2 \tilde{\mathbf{H}} - \frac{\varepsilon\mu}{c^2} \frac{\partial^2}{\partial t^2} \tilde{\mathbf{H}} = 0\end{aligned} \tag{1.16}$$

These equations can be further simplified taking into account that the fields $\tilde{\mathbf{E}}$ and $\tilde{\mathbf{H}}$ are time-harmonic, according to equation (1.12), which means that the time derivative results in a multiplicative factor $-i\omega$, i.e., $(\frac{\partial}{\partial t} \to -i\omega)$.

$$\begin{aligned}\nabla^2 \tilde{\mathbf{E}} + \frac{\varepsilon\mu\omega^2}{c^2} \tilde{\mathbf{E}} = 0 \\ \nabla^2 \tilde{\mathbf{H}} + \frac{\varepsilon\mu\omega^2}{c^2} \tilde{\mathbf{H}} = 0\end{aligned} \tag{1.17}$$

Equations (1.17) are known as Helmholtz equations. Despite the number of assumptions we had to make to derive them (time harmonic fields in a linear, homogeneous, isotropic and source-free medium) Helmholtz equations are actually the most commonly applied in classical nanophotonics, as the majority of experiments vastly satisfies these requirements. The factor $\sqrt{\frac{\varepsilon\mu\omega^2}{c^2}} = k$ is the wavenumber in the medium, related to the free space wavenumber k_0 by $k = k_0\sqrt{\varepsilon\mu} = k_0 n$, with n

being the refractive index of the medium. Solutions of the Helmholtz equation are characterised by an amplitude which is independent of k and a phase dependence which, in rectangular coordinates, is complex exponential such as $e^{i\mathbf{k}\cdot\mathbf{r}}$. The condition $\mathbf{J} = \rho = 0$ implies that $\nabla \cdot \mathbf{D} = \nabla \cdot \mathbf{B} = 0$ which results in the so-called transversality condition:

$$\mathbf{k} \cdot \tilde{\mathbf{E}} = \mathbf{k} \cdot \tilde{\mathbf{H}} = 0. \tag{1.18}$$

Each wave which is a solution of the Helmholtz equation can then be described by a triad of vectors, $\tilde{\mathbf{E}}$, $\tilde{\mathbf{H}}$ and $\mathbf{k}$ which are orthogonal to one another, with $\mathbf{k}$ being along its propagation direction. It is important to notice that, since the spatial dependence is given by the exponential $e^{i\mathbf{k}\cdot\mathbf{r}}$, the operator ∇ corresponds to a simple factor, i.e., $(\nabla \rightarrow i\mathbf{k})$. This means that the two Maxwell's curl equations can be rewritten as:

$$\begin{aligned} \tilde{\mathbf{E}} &= -\frac{1}{\omega\varepsilon}(\mathbf{k} \times \tilde{\mathbf{H}}) \\ \tilde{\mathbf{H}} &= \frac{1}{\omega\mu}(\mathbf{k} \times \tilde{\mathbf{E}}). \end{aligned} \tag{1.19}$$

These equations highlight very clearly how, for waves which solve the Helmholtz equation, it is straightforward to calculate the magnetic field once the electric one is known or viceversa, determine the values of the electric field orthogonal to a known magnetic field and a given propagation direction. The time-harmonicity considerations we derived for the fields clearly also influence our derivation of the Poynting vector. In fact, being the Poynting vector the product of two time-harmonic fields each oscillating at the same frequency ω, it can be written as the sum of a DC component with $\omega' = \omega - \omega = 0$, the time-averaged Poynting vector, and an oscillating component with $\omega' = \omega + \omega = 2\omega$. The time-averaged Poynting vector can be written as the real part of the complex quantity $\mathbf{P}_0 = \frac{1}{2}(\tilde{\mathbf{E}}^* \times \tilde{\mathbf{H}})$, which is therefore termed complex Poynting vector. The relations between $\tilde{\mathbf{E}}$ and $\tilde{\mathbf{H}}$, particularly their relative phase, will be fundamental when discussing Janus and Huygens dipoles in chapter 3, when we will examine the real and imaginary parts of the complex Poynting vector.

To prevent the notation from becoming too heavy, from now on we will avoid the wiggling superscript on the temporally Fourier-transformed complex phasors $\tilde{\mathbf{E}}$ and $\tilde{\mathbf{H}}$, just referring to them as $\mathbf{E}(\mathbf{r})$ and $\mathbf{H}(\mathbf{r})$, while we will use the hat superscript for the spatially Fourier-transformed fields.

1.4 The angular spectrum

The angular spectrum representation of optical fields is, as we said, a powerful tool as it allows us to rewrite every field as superpositions of monochromatic plane waves and evanescent waves, which will be described in detail in section 1.6 [16]. Let us now expand explicitly the electric field using the angular spectrum approach. We start from an electric field in 3D free-space $\mathbf{E}(x, y, z)$ and choose one of the three spatial direction as an arbitrary axis, for example z. We can then fix a plane at constant z and calculate the 2D Fourier transform of the field on that plane:

$$\hat{\mathbf{E}}(k_x, k_y, z) = \frac{1}{4\pi^2} \iint_{-\infty}^{\infty} \mathbf{E}(x, y, z) e^{-i[k_x x + k_y y]} \, dx \, dy \tag{1.20}$$

where k_x and k_y are the spatial frequencies in Fourier space associated with x and y. The inverse Fourier transform, conversely, is given by:

$$\mathbf{E}(x, y, z) = \iint_{-\infty}^{\infty} \hat{\mathbf{E}}(k_x, k_y, z) e^{i[k_x x + k_y y]} \, dk_x \, dk_y \, . \tag{1.21}$$

Assuming that in the transverse plane the medium, with refractive index n, is homogeneous, isotropic, linear and source-free, the time-harmonic field $\mathbf{E}(\mathbf{r}) = \mathbf{E}(x, y, z)$, oscillating at a frequency ω has to satisfy the Helmholtz equation:

$$(\nabla^2 + k^2)\mathbf{E}(\mathbf{r}) = 0, \tag{1.22}$$

where $k = \omega n/c$. Solving the Helmholtz equation with the angular representation of the field $\mathbf{E}(\mathbf{r})$ given in equation (1.21) we find the behaviour of the Fourier transform $\hat{\mathbf{E}}$ along the z-axis:

$$\hat{\mathbf{E}}(k_x, k_y, z) = \hat{\mathbf{E}}(k_x, k_y, 0) e^{\pm i k_z z}, \tag{1.23}$$

with k_z defined as $k_z \equiv \sqrt{k^2 - k_t^2}$ and $k_t = \sqrt{k_x^2 + k_y^2}$. The angular spectrum in an arbitrary plane $z =$ constant can then be written in 3D space as its value in the transverse plane $z = 0$ multiplied by a transfer function which accounts for the phase advance of each plane wave across a distance z. The sign of the exponential determines if the plane in which we are calculating the two-dimensional Fourier transform is placed above or below $z = 0$ and the term $e^{\pm i k_z z}$ is sometimes referred to as the propagator of the field. With this result we can finally write a convenient

expression of the angular spectrum as:

$$\mathbf{E}(x,y,z) = \iint_{-\infty}^{\infty} \hat{\mathbf{E}}(k_x,k_y,0)e^{i[k_x x+k_y y\pm k_z z]}\,dk_x\,dk_y\,. \tag{1.24}$$

Absolutely analogous considerations can be done for the magnetic field $\mathbf{H}$, whose angular spectrum can be written as:

$$\mathbf{H}(x,y,z) = \iint_{-\infty}^{\infty} \hat{\mathbf{H}}(k_x,k_y,0)e^{i[k_x x+k_y y\pm k_z z]}\,dk_x\,dk_y\,. \tag{1.25}$$

1.5 Green's function formalism

A very common concept often used in electromagnetism is that of the Green's function, which is a way of describing a field generated by a point source [16]. Knowing the field generated by a single point source allows us to retrieve the more complex fields generated by arbitrarily shaped sources, simply assembling them out of multiple point sources. We will now formally introduce dyadic Green's functions (i.e., Green's functions for vector fields) and then derive that for the Helmholtz operator. We will use this to write the angular spectrum of electromagnetic fields in [Paper A].
Let's consider the simple scenario of an operator $\mathcal{O}$ acting on a vector field $\mathbf{A}(\mathbf{r})$, returning a vector field $\mathbf{B}(\mathbf{r})$.

$$\mathcal{O}\mathbf{A}(\mathbf{r}) = \mathbf{B}(\mathbf{r}) \tag{1.26}$$

We assume the vector field $\mathbf{B}(\mathbf{r})$ to be known, as well as $\mathbf{A}_0$, the trivial solution of $\mathcal{O}\mathbf{A}(\mathbf{r}) = 0$. The Green's function for the field $\mathbf{A}(\mathbf{r})$ is the function $\mathbf{G}(\mathbf{r})$ defined such that when the operator $\mathcal{O}$ is applied to $\mathbf{G}(\mathbf{r})$ the result is a delta function $\delta(\mathbf{r})$. If such function exists and is unique, then:

$$\mathbf{A}(\mathbf{r}) = \int \mathbf{B}(\mathbf{r}')\mathbf{G}(\mathbf{r}-\mathbf{r}')\mathrm{d}^3\mathbf{r}' \tag{1.27}$$

We omit the derivation since it is outside the scope of this thesis and can be found in full details in [15, 16]. For the electric field, the scalar Green's function can be calculated in free space as:

$$G_0(\mathbf{r},\mathbf{r}') = \frac{e^{\pm ik|\mathbf{r}-\mathbf{r}'|}}{4\pi|\mathbf{r}-\mathbf{r}'|} \tag{1.28}$$

which corresponds to spherical waves propagating either outwards or inwards depending on the sign of the exponential. The dyadic Green's function can then be calculated from the scalar one as:

$$\mathbf{G}(\mathbf{r},\mathbf{r}') = \left[\hat{\mathbf{I}} + \frac{1}{k^2}\nabla\nabla\right] G_0(\mathbf{r},\mathbf{r}') \tag{1.29}$$

where $\hat{\mathbf{I}}$ is the identity matrix. This is the Green's function that in chapter 2, and particularly in [Paper A], we will use to calculate the angular spectrum of a dipolar source over a substrate.

1.6 Evanescent waves

Evanescent waves are a class of solutions of Maxwell's equations (1.1) in which the amplitude of the field is exponentially decaying in at least one spatial direction [18, 19]. These waves are a result of light interacting with a spatial inhomogeneity, such as the interface between two media or a point source, hence, in free-space, they do not propagate but rapidly decay. In this class of fields, the wavevector component along the direction of evanescent decay is imaginary. Such waves are always present whenever light is confined in a medium. The boundary conditions dictated by Maxwell's equations, in fact, would be violated if the field was to be nonzero in a medium and drop to exactly zero in an adjacent medium. Therefore, a field that is said to be *confined* in a medium is actually exponentially decaying in any adjacent media. The higher the confinement the quicker the decay will be, which is usually described by a material-dependent quantity referred to as the penetration length. An easy derivation of evanescent waves properties can be obtained studying total internal reflection [20]. Let's consider the interface between two linear and homogeneous media, characterised by refractive indexes n_1 and n_2 with $n_1 > n_2$, light being incident from the denser medium, see figure 1.1. We can reduce our considerations to the xz plane since the reflected and refracted rays will lie in the same plane as the incident ray, so we are dealing with a two-dimensional problem. The laws that are commonly mentioned when dealing with reflection and refraction at an interface are named after the Dutch astronomer Snell, who derived them in 1621, although they were not published during his lifetime. However, these laws had been known since hundreds of years before Snell, and their first appearance can be traced back to chapters 5 and 7 of *The Book of Optics* by the Arab mathematician

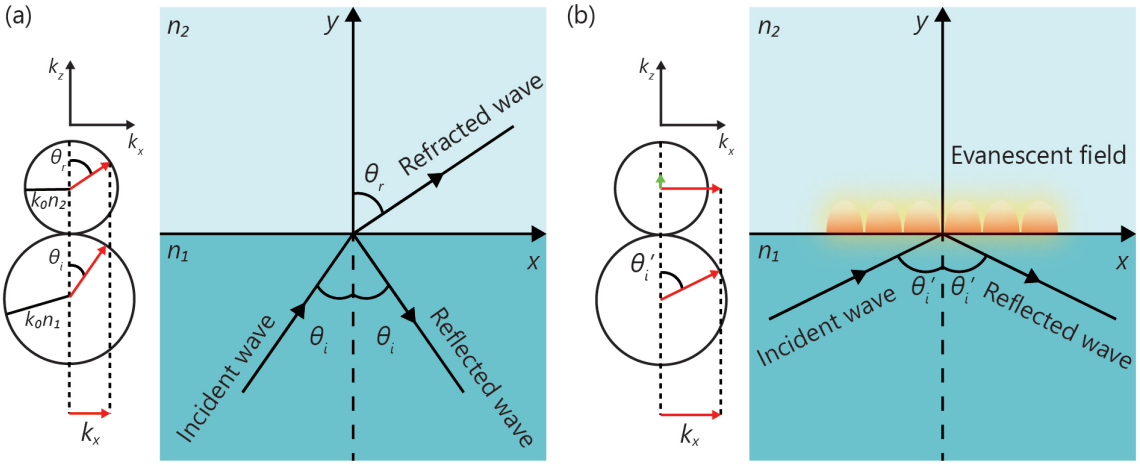

Figure 1.1: Schematics representation of evanescent waves formation in total internal reflection. In (a) the angle of incidence θ_i is smaller than the critical angle, therefore light coming from the medium n_1 is partially reflected and partially transmitted in the medium n_2. In momentum space this means that the x component of the wavevector in n_1 does not exceed the total $k_2 = k_0 n_2$ in the medium n_2. In (b) the angle of incidence in the medium n_1 is larger than the critical angle hence the light cannot be refracted and is fully reflected back, except for the evanescent field in n_2. In momentum space, it can be seen that the x component of the wavevector in the medium n_1 exceeds the total momentum in the second medium. The conservation of momentum then imposes the emergence of an imaginary k_z component so that $k^2 = k_x^2 + k_y^2$ is still satisfied with $k_x > k$ and $k_z^2 < 0$.

Ibn al-Haytham, written between 1011 and 1021 and survived in its Latin translation [21]. Figure 1.2 shows two selected pages of the Latin translation, in which the

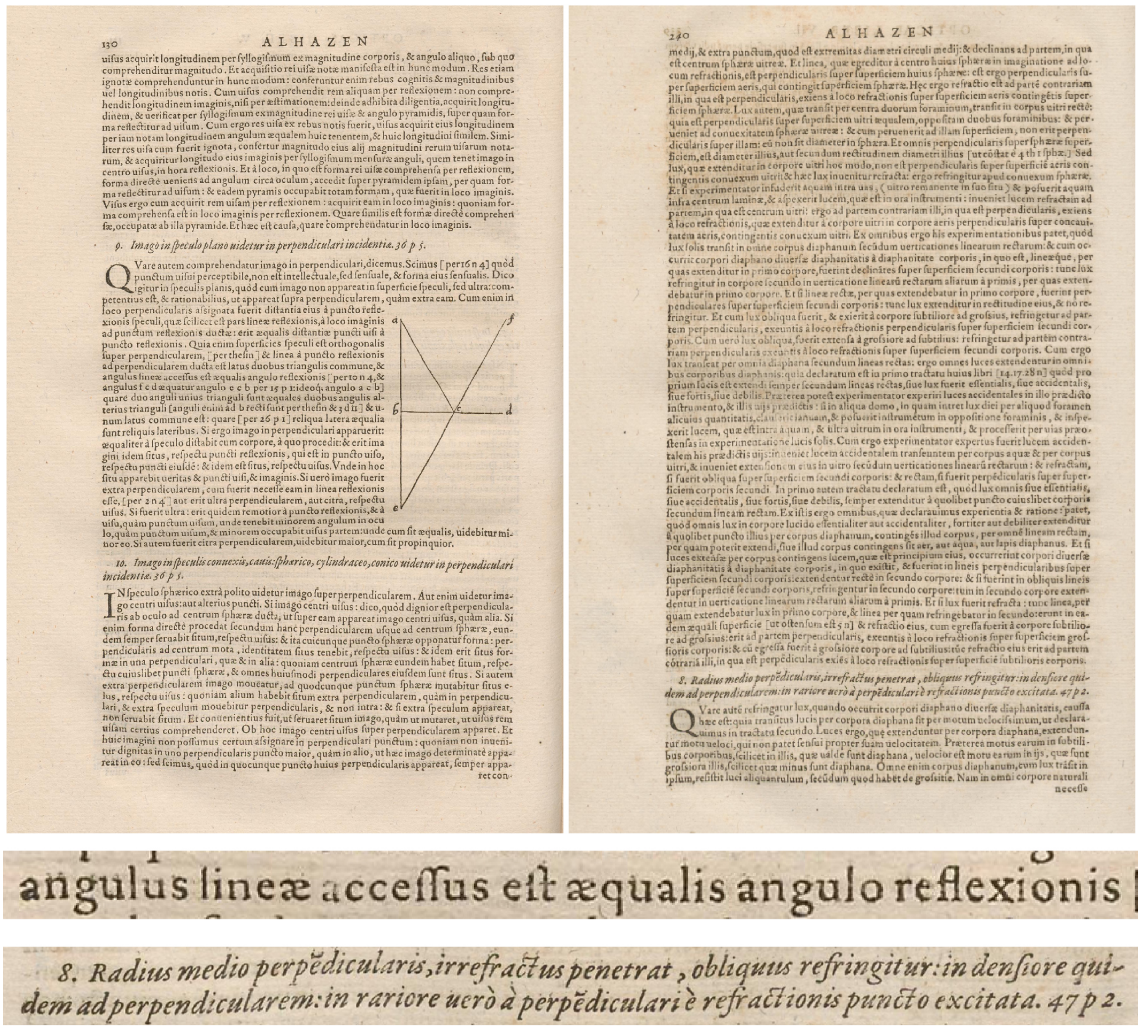

Figure 1.2: Selected pages from the Latin translation of the fifth and seventh volumes of Ibn al-Haytham's Book of Optics, devoted to the study of reflection and refraction, respectively. The selected quotes read: *"angulus lineae accessus est aequalis angulo reflexionis"* which literally translates as: *"the angle of incidence is equal to the angle of reflection"* and *"radius medio perpendicularis, irrefractus penetrat, obliquus refringitur: in densiore quidem ad perpendicularem; in rariore vero a perpendiculari e refractionis puncto excitata"* which can be translated as: *"At normal incidence the refracted ray is not deflected, when incident at an angle it is refracted: closer to the normal in a denser medium; further from it in a rarer one"* predating the laws of reflection and refraction by hundreds of years.

phenomena of reflection and refraction are described with a striking clarity. With this in mind, we will still refer to the law of refraction as Snell's law for the sake of

agreement and consistency with all the literature on the topic, and for the immediacy of its mathematical formulation, which is missing in any previous work. Snell's law provides the angle θ_r at which, depending on the incidence angle θ_i, the light will be transmitted in the second medium (see figure 1.1):

$$n_1 \sin\theta_i = n_2 \sin\theta_r \tag{1.30}$$

We can immediately see from Snell's law (1.30) that for $\theta_i = \theta_c = \arcsin(\frac{n_2}{n_1})$, $\sin\theta_r = 1$, hence the angle at which the beam is transmitted in the second medium is equal to $\pi/2$. The angle θ_c for which this happens is called the critical angle and for every incidence angle greater then θ_c the light impinging on the interface will not be transmitted into the medium n_2 but will be completely reflected. This very well-known phenomenon is called total internal reflection and is the working principle of waveguiding structures such as optical fibers [19]. While the light is not refracted in the second medium, an evanescent field will arise on the interface. Let's examine this phenomenon mathematically looking at the wavevector space. The boundary conditions imposed by Maxwell's equations require the conservation of the momentum component parallel to the interface, so, in our reference system, $k_{x_1} = k_{x_2}$. The total momentum in the two media is given by $\mathbf{k_1} = \mathbf{k_0} n_1$ and $\mathbf{k_2} = \mathbf{k_0} n_2$ so, since $n_1 > n_2$, for large enough angles the x-component of the wavevector in the first medium can exceed the total momentum in the second medium. The condition on the total momentum, then $n_2 k_0^2 = k_x^2 + k_z^2$ with $k_x^2 > n_2 k_0^2$ can be satisfied only if $k_z \in \mathbb{I}$, so we can define $k_z = i\alpha_z$. When we write the field propagator $e^{i\mathbf{k}\cdot\mathbf{r}}$, then, we see the exponential decay along the z-axis:

$$e^{i\mathbf{k}\cdot\mathbf{r}} = e^{i(k_x x + k_z z)} = e^{i(k_x x + i\alpha_z z)} = e^{ik_x x} \cdot e^{-\alpha_z z} \tag{1.31}$$

This family of waves, although fastly decaying in space, has an impressive importance in nanophotonics. For example, evanescent fields have been used to increase the resolution and overcome the diffraction limit in microscopy [22–24], thin film characterisation [25, 26], optical trapping and cooling [27–30] and gas sensing [31–33], to cite a few. Recently, our group has proposed the use of evanescent waves to design directional far-field of antennas [34], a method for ultrasensitive displacement and phase measurements [35], and has also predicted the existence of evanescent gravitational waves [36], which are expected to be found in the near fields of black holes. We will make use of evanescent field coupling in chapters 2, 3 and 4 when

discussing the excitation of guided modes using point sources.
It is interesting to take into account the polarisation of evanescent waves. Using the transversality conditions $\mathbf{k}\cdot\mathbf{E} = \mathbf{k}\cdot\mathbf{H} = 0$ (1.18) for evanescent fields, we can get an expression for the $\mathbf{E}$ field of purely TM (p-) and TE (s-) polarised evanescent waves:

$$\mathbf{E}^p = A_{\mathrm{TM}} \begin{pmatrix} k_z \\ 0 \\ -k_x \end{pmatrix}; \qquad \mathbf{E}^s = A_{\mathrm{TE}} \begin{pmatrix} 0 \\ 1 \\ 0 \end{pmatrix}, \tag{1.32}$$

where A_{TM} and A_{TE} are the amplitudes for the p- and s-polarised electric fields, respectively. Since $k_z \in \mathbb{I}$ and $k_x \in \mathbb{R}$, there is an i phase difference between the x and z components of the $\mathbf{E}^p$ evanescent wave, which is therefore elliptically polarised. This polarisation tends to circular in the limit for which $|k_x| = |k_z|$. In a totally analogous way, or simply by applying equation (1.19) to equation (1.32), we can derive the $\mathbf{H}$ field for s- and p-polarised evanescent waves, obtaining:

$$\mathbf{H}^p = A'_{\mathrm{TM}} \begin{pmatrix} 0 \\ 1 \\ 0 \end{pmatrix}; \qquad \mathbf{H}^s = A'_{\mathrm{TE}} \begin{pmatrix} k_z \\ 0 \\ -k_x \end{pmatrix}, \tag{1.33}$$

with again, A'_{TM} and A'_{TE} amplitudes for the p- and s-polarised magnetic fields, respectively. Figure 1.3 shows the electric (magnetic) field for a p- (s-) polarised evanescent wave, with the blue arrows representing the polarisation ellipse and the red arrows depicting the instantaneous field, its amplitude decaying along z.

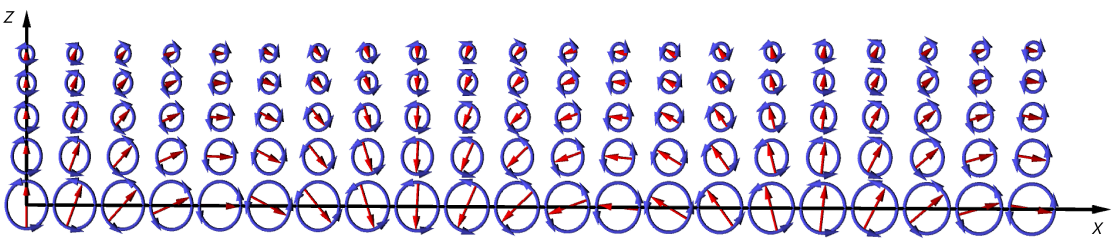

Figure 1.3: $\mathbf{E}$ ($\mathbf{H}$) field of a p- (s-) polarised evanescent wave

The transversality conditions require $\mathbf{H}$ and $\mathbf{E}$ to be orthogonal hence the behaviour of the $\mathbf{H}$ fields is exactly the same as that of the $\mathbf{E}$ fields but for the orthogonal polarisations (i.e., the $\mathbf{H}^s$ component is the circularly polarised one). This stunning

specularity between electric and magnetic fields is not prerogative to evanescent waves, since it is dictated by Maxwell's equations and is therefore present in all the fields that solve them, as is clear from equations (1.19). Apart from being beautiful, as often happens with symmetries in physics, this relationship is very convenient to employ when performing analytical calculations as one's considerations can be restricted to the electric field, for example, without any need of extra insight to determine the behaviour of the magnetic one.

1.7 Surface plasmons

We have seen that at the interface between two media with different refractive indices there is a condition on the angle of incidence which determines the presence of an evanescent field. Things can get even more interesting when the interface is between materials with opposite signs of the dielectric constant, such as a metal and a dielectric. To understand the negative sign in the real part of the dielectric

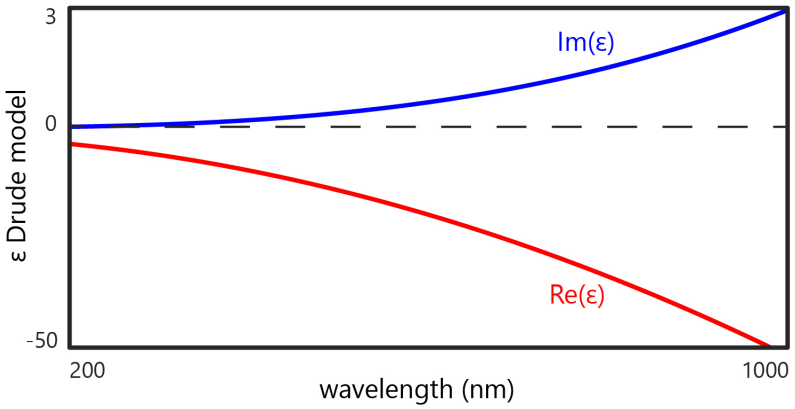

Figure 1.4: Real (red) and imaginary (blue) parts of the dielectric function of gold at optical frequencies calculated using the Drude model with $\omega_p = 1.38 \times 10^{16}$ Hz and $\Gamma = 1.075 \times 10^{14}$ Hz. Please note that a different vertical scale has been chosen below and above $\varepsilon = 0$.

constant of metals, we can make use of the Drude model [37, 38]. This model considers the response of the metal under illumination as that of a free-electron gas with n carriers per unitary volume, each with mass m_e and charge $-e$. The motion of each electron is that of a damped harmonic oscillator driven at the frequency of the incident electric field. We can write Newton's law associated to this motion.
If we consider the magnetic response to be negligible ($\mu = 1$), like in most natural

materials, the force that the electric field exerts on the free electrons is proportional to their charge: $\mathbf{F_E} = -e\mathbf{E}$. The electrons' motion is damped by the collisions with other electrons, hence the damping factor Γ is inversely proportional to the electrons' mean free path between two collisions. The law of motion for a free electron illuminated at a frequency ω is then given by:

$$m_e \frac{d^2\mathbf{r}}{dt^2} = -m_e\Gamma\frac{d\mathbf{r}}{dt} - e\mathbf{E}. \tag{1.34}$$

Since we are assuming harmonic motion for the electrons under the harmonic field $\mathbf{E}e^{-i\omega t}$, we can solve the differential equation for $\mathbf{r}(t) = \mathbf{r}e^{-i\omega t}$, with time derivatives becoming simple multiplicative factors. The displacement $\mathbf{r}$ is all we need to know to determine the dielectric constant of the metal at each frequency. In fact, each of the electrons produces a dipole moment proportional to its charge and displacement, $\mathbf{p} = -e\mathbf{r}$, and the sum of all the n dipole moments results in a macroscopic polarisation $\mathbf{P} = n\mathbf{p} = \varepsilon_0\chi_e\mathbf{E}$, as we derived in equation (1.14). Finally, using equation (1.2), we can write:

$$\varepsilon(\omega) = 1 - \frac{\omega_p^2}{\omega^2 + i\Gamma\omega}, \tag{1.35}$$

where $\omega_p = \sqrt{\frac{ne^2}{\varepsilon_0 m_e}}$ is called the plasma frequency and is characteristic of every metal, as is Γ. For gold, as an example, $\omega_p = 1.38 \times 10^{16}\,\text{rad/s}$ and $\Gamma = 1.075 \times 10^{14}\,\text{rad/s}$. In figure (1.4), the real and imaginary parts of ε for gold at optical frequencies are plotted. The Drude model for gold, then, predicts a negative real part of ε througout the whole visible range, which results in very small penetrations of light into the metal, which in turn determines the excellent behaviour of metal as mirrors and the high losses associated with electrons' motion inside the metal. Let us now derive why a change in sign of the dielectric constant between two materials could lead to the existence of evanescent modes, at the interface, called surface plasmon polaritons (SPPs) [39–41]. We consider a planar interface ($z = 0$) between two media with dielectric constants $\varepsilon_1(\omega) \in \mathbb{C}$ and $\varepsilon_2(\omega) \in \mathbb{R}$, respectively. To find solutions that are localised at the interface we have to find the homogeneous solution to the wave equation, namely:

$$\nabla \times \nabla \times \mathbf{E}(\mathbf{r},\omega) - \frac{\omega^2}{c^2}\varepsilon(\mathbf{r},\omega)\mathbf{E}(\mathbf{r},\omega) = 0, \tag{1.36}$$

with

$$\varepsilon(\mathbf{r},\omega) = \begin{cases} \varepsilon_1(\omega) & \text{for} \quad z < 0 \\ \varepsilon_2(\omega) & \text{for} \quad z > 0. \end{cases} \tag{1.37}$$

Since we are dealing with a bidimensional problem we can reduce our analysis to p- and s- polarised modes and then limit our considerations to p-polarised modes only (see figure 1.5) as there is no guided-mode solution to equation (1.36) for s-polarised modes. The electric field of p- polarised plane waves lies in the xz-plane and can be

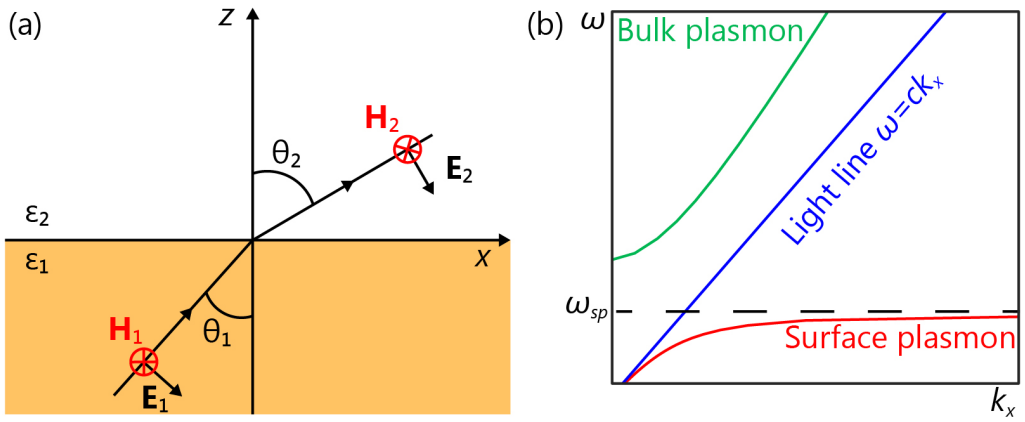

Figure 1.5: (a) Schematic of the interface between two media with dielectric constants ε_1 and ε_2, respectively, with p-polarised light in both half-spaces. p-polarised waves have the electric field in the xz-plane and the magnetic field along the y-axis. (b) Dispersion relation for a surface plasmon at the interface between gold and air.

written in the two media as:

$$\mathbf{E}_1 = \begin{pmatrix} E_{x_1} \\ 0 \\ E_{z_1} \end{pmatrix} e^{ik_x x - i\omega t} e^{k_{z_1} z}; \quad \mathbf{E}_2 = \begin{pmatrix} E_{x_2} \\ 0 \\ E_{z_2} \end{pmatrix} e^{ik_x x - i\omega t} e^{k_{z_2} z}, \tag{1.38}$$

where we have simplified $k_{x_1} = k_{x_2} = k_x$ because of the conservation of the momentum component parallel to the interface. The total wavevectors in each medium must satisfy:

$$\begin{aligned} k_x^2 + k_{z_1}^2 &= \varepsilon_1 k^2 \\ k_x^2 + k_{z_2}^2 &= \varepsilon_2 k^2. \end{aligned} \tag{1.39}$$

Moreover, the transversality condition $\mathbf{k} \cdot \mathbf{E} = 0$ gives us

$$\begin{aligned} k_x E_{x_1} + k_{z_1} E_{z_1} &= 0 \\ k_x E_{x_2} + k_{z_2} E_{z_2} &= 0. \end{aligned} \tag{1.40}$$

These are the conditions in the two half-spaces, to which we need to add the boundary conditions at the interface which require the parallel component of $\mathbf{E}$ and the perpendicular component of $\mathbf{D}$ to be continuous:

$$\begin{aligned} E_{x_1} &= E_{x_2}, \\ \varepsilon_1 E_{z_1} &= \varepsilon_2 E_{z_2}. \end{aligned} \tag{1.41}$$

Equations (1.40) and (1.41) form a linear system with the variables being the four electric field components. The system admits a solution if the associate determinant vanishes, which is obtained when:

$$\varepsilon_1 k_{z_2} = \varepsilon_2 k_{z_1}. \tag{1.42}$$

Combining the condition (1.42) and equations (1.39) we obtain the dispersion relations for the two components of the wavevector:

$$k_x^2 = \frac{\varepsilon_1 \varepsilon_2}{\varepsilon_1 + \varepsilon_2} k^2 = \frac{\varepsilon_1 \varepsilon_2}{\varepsilon_1 + \varepsilon_2} \frac{\omega^2}{c^2}, \tag{1.43}$$

$$k_{z_1}^2 = \frac{\varepsilon_1^2}{\varepsilon_1 + \varepsilon_2} \frac{\omega^2}{c^2}; \qquad k_{z_2}^2 = \frac{\varepsilon_2^2}{\varepsilon_1 + \varepsilon_2} \frac{\omega^2}{c^2}. \tag{1.44}$$

The dispersion relation for a surface plasmon at the air-gold interface is plotted in figure 1.5 (b). The dispersion relations (1.43, 1.44) derived for k_x and k_z clearly show why surface plasmons appear at the interface between two media with opposite sign in dielectric constants. We assume that the materials are lossless, which means $\varepsilon_1, \varepsilon_2 \in \mathbb{R}$, and that the second medium is a dielectric, which means $\varepsilon_2 > 0$. First of all, for the mode to be propagating along k_x we need k_x to be real. This means that the numerator and the denominator in equation (1.43) must be either both positive or both negative. The sign of the sum $\varepsilon_1 + \varepsilon_2$ is determined imposing that the mode is evanescent along z in both media, meaning that k_{z_1} and k_{z_2} must be purely imaginary, hence $\varepsilon_1 + \varepsilon_2 < 0$ and therefore $\varepsilon_1 \cdot \varepsilon_2 < 0$, with $|\varepsilon_2| > |\varepsilon_1|$.

The realm of applications of surface plasmons, or plasmonics, is enormous and there is a vast amount of resources dedicated to their study. To name some, plasmonics has been used to enhance the sensitivity for Raman measurements [42–50], design waveguiding structures [51–59], achieve extraordinary optical transmission [60–65], data storage [66–68], medical applications such as cancer therapy [69–73], refractive index sensing [74–77] and subwavelength imaging [78–80]. To give a hint at how unlikely it is to be comprehensive when citing the possible applications of plasmonics, it is useful to report that a quick search in Google Scholar of the keyword "plasmonics" returns more than ten thousand research papers published in 2018 only. Neither surface plasmons, nor plasmonics, are the main topic of this thesis. Nonetheless, they are an example of guided mode which is easy to treat analytically, to simulate and simple to realise experimentally. Many of the results presented in this thesis are *applied* to surface plasmons, a convenient platform to test our theories. In figure (1.6), the electric field of a surface plasmon at the gold-air interface is plotted, which is exactly a p-polarised evanescent field. It is worth noticing how the exponential decay along the z-axis, although present in both half-spaces, is much more dramatic in the metal than it is in the dielectric.

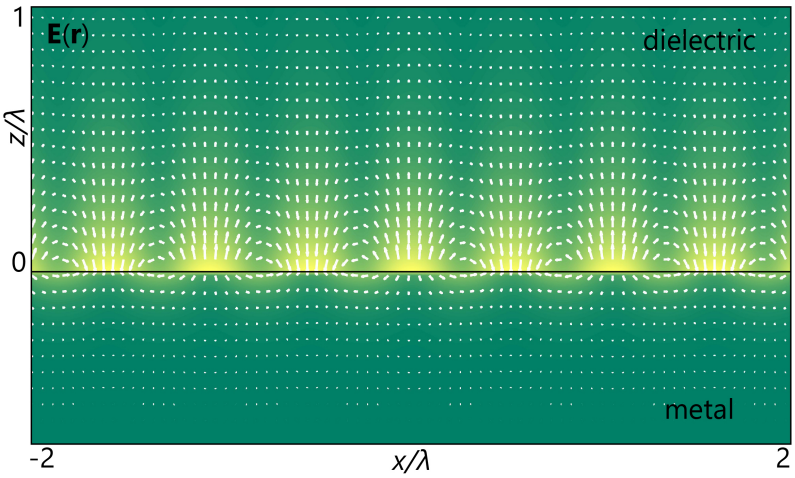

Figure 1.6: Electric field of a surface plasmon at the interface between metal ($\varepsilon < 0$) and dielectric ($\varepsilon > 0$). The white arrows depict the instantaneous orientation of the field.

1.8 Guided modes

Guided modes are a family of solutions of Maxwell's equations which are confined in at least one spatial direction and propagate along another direction. We have already seen an example of them in the previous section: surface plasmons. While surface plasmons are characteristic of the interface between a metal and a dielectric, guided modes can appear in a variety of materials and geometry, and the objects that support guided modes are generally called *waveguides*. Guided modes are of fundamental importance both in photonics research and in everyday life, with optical fibers having applications ranging from information routing [81–83], to sensing [84–86] and endoscopy [87, 88]. This thesis is devoted mostly to the design of sources aimed at their excitation (chapters 2, 3 and 4), but a consistent part of our studies has also been aimed at the characterisation of their fundamental properties, such as angular momenta and helicity (chapter 5). Henceforth, we will now describe the basic physics of guided modes and highlight all the aspects which will become significant in the next chapters.

The simplest example of a guided mode is that which can be obtained shining light at an angle between two parallel mirrors facing each other. Let's assume the mirrors are in the xy-plane and that they are separated by a distance d along the z-axis. We can always orient our system so that the light entering the waveguide lies in the xz-plane so that we can reduce our considerations to a two-dimensional problem in the xz-plane. Light entering this waveguide bounces off the surface of the first mirror and hits the second mirror at a distance along the x-axis equal to $2d\cos\theta$, where θ is the angle between the wave and the x-axis. So the light is effectively confined in the z-direction and propagating along x. This trivial example is not far from how dielectric waveguides actually work. Let's assume we have a dielectric planar slab, whose refractive index n_2 is higher than that of the surrounding material, n_1, which we can assume to be, for simplicity, air. We have seen in section 1.6 that light hitting the interface between two dielectrics at an angle larger than the critical angle will undergo total internal reflection. This means that, for each dielectric slab, there is a series of acceptance angles at which light can be guided along the x-direction by means of total internal reflections at the two interfaces on the z-direction, as schematically represented in figure 1.7. Together with the guided mode *inside* the waveguide, there is an evanescent field that surrounds the slab. The wave is travelling in the xz-plane with $k_2 = n_2 k_0$, $k_x = k_2\cos\theta$ and $k_z = k_2\sin\theta$. To determine the modes that are guided by this structure we can impose a self-consistency condition

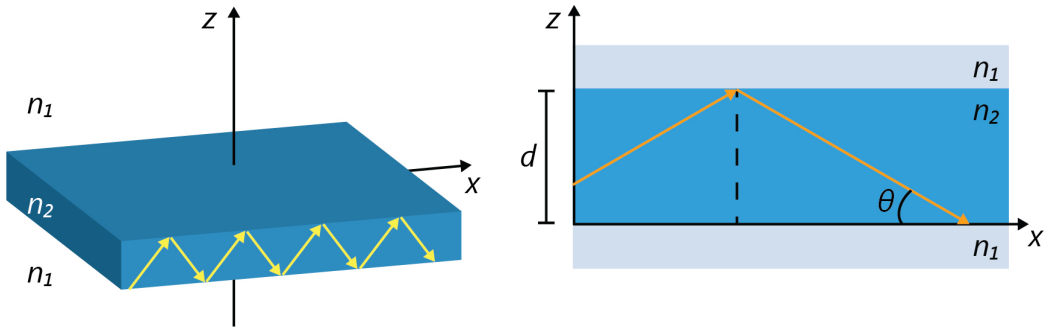

Figure 1.7: Schematics of a planar dielectric slab of thickness d with refractive index $n_2 = 3.45$ surrounded by air ($n_1 = 1$).

that a wave reproduces itself after a round trip, so, after two reflections [19, 89], with an overall phase change which is an integer multiple of 2π. This results in:

$$2k_z d - 2\phi_r = 2\pi m, \tag{1.45}$$

where d is the thickness of the slab, ϕ_r is the phase that the wave acquires at every total internal reflection and m is an integer number. The phase shift ϕ_r depends on the polarisation of the incident wave. We can distinguish two orthogonal cases and solve for them separately: TE (s-polarised) modes, in which the electric field lies along y, and TM (p-polarised) modes, in which the magnetic field is along y. This allows us to rewrite ϕ_r as a function of the wavevector components and ω only. This problem has very well known solutions which are available in multiple textbooks [19, 89], although they are somewhat cumbersome to retrieve, as they are obtained from a transcendental equation. Transcendental equations are those in which the variables that one is solving for are functions which do not satisfy a polynomial equation, known as transcendental functions. In this case said functions are Bessel functions and their first derivatives, which are also Bessel functions of different orders. Often, these equations do not have closed-form solutions, hence a simple way of calculating the fields of these modes is to solve the transcendental equation graphically. It is, in fact, convenient to plot the determinant associated to the system of equations for the fields, made out of Helmholtz equations (1.17) and the necessary boundary conditions. Plotting this determinant as a function of wavevector and frequency, as we did in figure 1.8, we can graphically see the points for which it is zero, corresponding to values of ω and k_x for which the system possesses a solution. The curves on which the zero points lie are the dispersion relations for the guided modes, each of which corresponds to a mode with a different

value of m. The dispersion relations for the various modes lie between the red and green lines (Figure 1.8) $\omega = n_2 c_0 k_x$ and $\omega = n_1 c_0 k_x$, which represent free propagation in homogeneous media with the refractive index of the slab and of air, respectively.

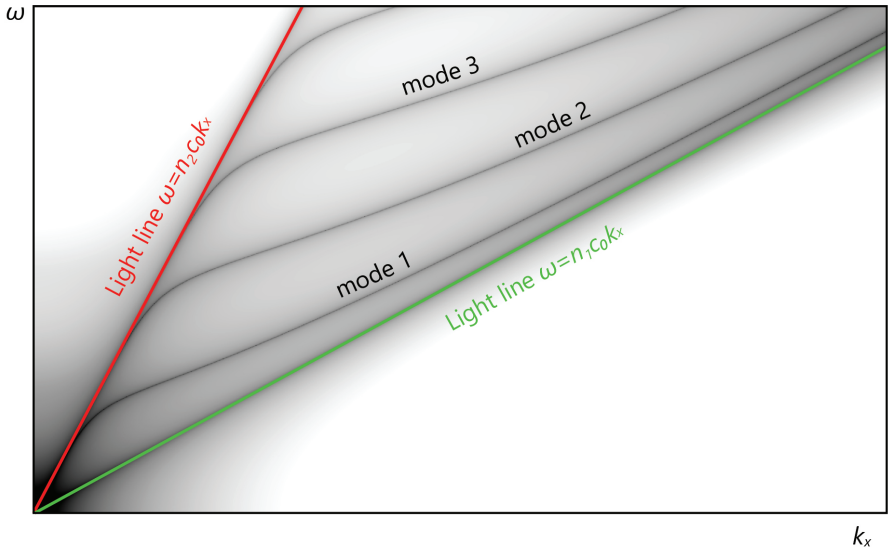

Figure 1.8: Dispersion relation of p-polarised modes of a dielectric slab waveguide of thickness d with refractive index $n_2 = 3.45$ surrounded by air ($n_1 = 1$). The red and green lines encompass the wavevector-frequency range in which the modes are guided in the slab. Each line corresponds to a guided mode, with increasing values of m from mode 1 upwards. Outside of the range delimited by the light lines, light freely propagates in the two media.

We see from figure 1.8 that increasing m the modes start to exist at higher frequencies (i.e., the higher the order of the mode, the higher its cutoff frequency). One can choose the frequency range in which to work so that the number of modes that a waveguide supports is fixed. Every waveguide can, in this way, be used as a single mode waveguide, for a specific frequency.

Chapter 2

Unidirectionality of dipolar near fields

This chapter is devoted to the study of the fields generated by dipolar sources, with a particular attention to their near-field directionality. We will start with a description of light's angular momenta, followed by an example of spin-orbit interaction of light, namely spin-momentum locking in evanescent fields, which is one of the possible mechanisms to achieve unidirectional excitation of guided modes by means of evanescent coupling. We will then move on to deriving the angular spectra for electric and magnetic dipoles using the techniques detailed in the previous chapter (sections 1.4 and 1.5). Furthermore, we will briefly discuss Fermi's golden rule as an alternative method to the angular spectrum to predict, quantify and engineer the coupling between a source and a waveguide. We will then briefly review the current state of art in the field of unidirectional excitation of guided modes by means of dipolar sources and present our contribution in the form of paper [Paper A], in which we show the unidirectionality of the near field of circular electric and magnetic dipoles adopting the angular spectrum approach.

2.1 Light's angular momentum

That light possesses a linear momentum was predicted by Kepler in 1607 when observing that the tails of comets always point away from the Sun [90]. This was further rigorously confirmed first by Maxwell in 1862 [12, 13] and then experimentally by Nichols and Hull [91] in 1903. Soon afterwards, in 1909, Poynting hypothesised

the existence of an *angular* momentum associated with circularly polarised light [92], verified experimentally in 1936 by Beth [93] with the first measurement of light-induced torque on birefringent materials. Beth's measurement unveiled the existence of the angular momentum associated with the polarisation of light, the spin angular momentum (SAM). However, this is not the only angular momentum that light can possess, as a beam can also carry the so-called orbital angular momentum (OAM). OAM can be further decomposed in two separate contributions: the intrinsic orbital angular momentum (IOAM) and the extrinsic orbital angular momentum (EOAM) [94, 95]. In 1992, Allen and colleagues [96] described the IOAM, which is associated with the spatial distribution of the wavefront. Beams with helical wavefronts carry an IOAM which is determined by the number of intertwined helices making up the wavefront, such number corresponds to the beam's topological charge ℓ. Finally, in analogy to the mechanical OAM, any beam can carry EOAM, which is given by the cross product between the position of the centre of the beam, measured from the origin of an arbitrary coordinate system, $\mathbf{R}$ and the linear momentum $\mathbf{P}$. Whenever the origin of the coordinate system used does not lie along the axis of the beam, $\mathbf{R} \neq 0$, the EOAM has a nonzero value. The EOAM value depends on our arbitrary choice of origin, hence why it is called extrinsic. However, once an origin has been defined, the conservation of angular momentum applies to the net sum of the three types of angular momentum. In calculations dealing with transfer from one type of angular momentum to another, we must not forget to account for changes in the centroid of the beams and their momentum, in order to properly include the EOAM. These three angular momenta are schematically depicted in figure 2.1.

The SAM $\mathbf{S}$, IOAM $\mathbf{L}^{\text{int}}$ and EOAM $\mathbf{L}^{\text{ext}}$ per photon, i.e. in units of $\hbar = 1$, can be written as [95]:

$$\mathbf{S} = \sigma \frac{\mathbf{P}}{P}, \qquad \mathbf{L}^{\text{int}} = \ell \frac{\mathbf{P}}{P}, \qquad \mathbf{L}^{\text{ext}} = \mathbf{R} \times \mathbf{P};$$

where σ is the degree of circular polarisation, i.e. $\sigma \in (-1, 1)$ with $\sigma = \pm 1$ corresponding to left- and right-handed circular polarisations.
While the SAM, depending on the polarisation state of light, induces rotations in birefringent materials, the IOAM is bound to the azimuthal structure of the wavefront and hence gives rise to rotations in spatially inhomogeneous media. SAM eigenstates belong to a bidimensional space, i.e. the state of polarisation is fully described by two components, horizontal and vertical, or left- and right-circular, while the IOAM

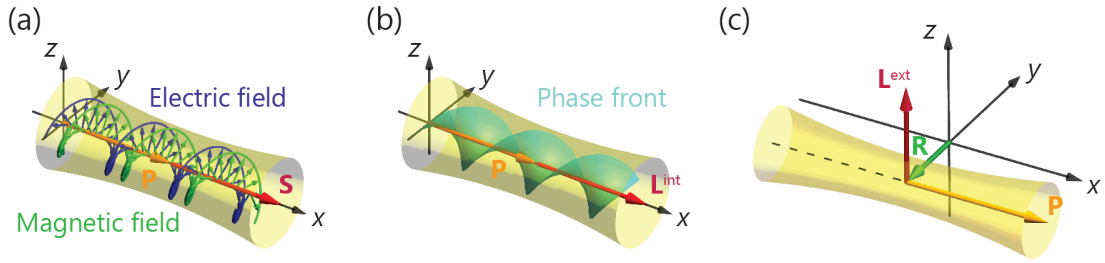

Figure 2.1: The angular momenta of paraxial beams of light. In (a), circularly polarised light carries spin angular momentum (**S**), aligned to the direction of the linear momentum (**P**). The blue and green arrows depict the instantaneous orientation of the electric and magnetic fields, respectively. In (b), the phase front of a vortex beam is shown. Such a beam carries IOAM $\mathbf{L}^{\text{int}}$, proportional to the topological charge of the vortex ℓ, in the figure being $\ell = 2$. Panel (c) depicts a beam whose centre is translated from the origin of the coordinate system by a distance **R**. This shift determines the presence of EOAM $\mathbf{L}^{\text{ext}}$. Figure reprinted from [95].

possesses an infinite space of eigenvectors. This is one of the main reasons why it is considered an excellent candidate for light-based information transfer, as many bits of information can be encoded in a single photon with a high-order IOAM [97–104]. SAM and OAM are independent degrees of freedom, as it is possible to have a light beam that possesses one of the two without necessarily having the other. However, from their interaction a huge amount of interesting physics has been produced and one of the most common methods of generation of beams with OAM is based on SAM-to-OAM conversion [105–113]. The conversion of one of these quantities into the other is called spin-orbit interaction (SOI) of light and we will see an example of conversion of SAM into EOAM in this chapter, namely spin-momentum locking, which we will explain in the next paragraph, with our main contribution to the topic being our work [Paper A]. The sum of SAM and OAM is the total angular momentum of light (TAM), which is a conserved quantity in electromagnetism. Therefore, in the conversion from one angular momentum to the other, the total must remain unchanged.

2.2 Spin-momentum locking

Recently, an interesting property of evanescent waves, such as surface modes or the tails of guided modes, has been unveiled [114, 115] and it relates the propagation direction of the mode with its intrinsic transverse spin. Consider the field of an

evanescent wave propagating along x with $|k_x| > k$ and decaying along z with $k_z = i\alpha_z$. The transverse spin, oriented along the y-axis, and therefore transverse to the propagation direction and the direction of evanescent decay, is defined as [115, 116]:

$$\mathbf{S}_\perp = \frac{\mathrm{Re}(\mathbf{k}) \times \mathrm{Im}(\mathbf{k})}{[\mathrm{Re}(\mathbf{k})]^2}. \tag{2.1}$$

The sign of the transverse spin in equation (2.1), hence, the handedness of the polarisation of the evanescent field, depends on the relative sign between k_x and k_z. Therefore, if we fix the direction of the evanescent decay, for example towards the positive z-direction, oppositely propagating surface waves, corresponding to $\pm k_x$, will have opposite transverse spin. This result is of fundamental importance. Saying that surface waves propagating in a given direction are *locked* to a specific transverse spin means that exciting a surface wave with a designed transverse spin will determine its unidirectional propagation [95, 117, 118]. It is easy to verify this phenomenon by means of Maxwell's equations (1.1). Particularly for a source-free, homogeneous, isotropic medium, as we saw before in 1.3, time harmonic fields satisfy the transversality condition (1.18). For the evanescent wave propagating along x and decaying along z with wavevector $\mathbf{k} = (k_x, 0, i\alpha_z)$ this means:

$$\begin{aligned} \mathbf{k} \cdot \mathbf{E} = 0 \Rightarrow \\ k_x E_x + i\alpha_z E_z = 0 \Rightarrow \\ E_x = -i\frac{\alpha_z}{k_x} E_z. \end{aligned}$$

Maxwell's equations require the polarisation of the evanescent wave to be elliptical and locked to the direction of propagation (k_x being a positive or negative determining the direction). The wave equation imposes the condition $k_x^2 - \alpha_z^2 = k^2$. In the limit of very high $kx \gg k$, which is associated with more confined evanescent waves, we have $\alpha_z \approx \pm k_x$, and hence the polarisation becomes circular. In that case, the transverse spin (2.1) is maximum and its sign determines the propagation direction of the wave. The discovery of spin-momentum locking in evanescent waves provided a completely new mechanism to achieve topologically protected routing of light into waveguiding structures. The evanescent wave can be excited directionally by a source which matches its spin, and since the spin is locked to the propagation direction, the spin of the source will be translated into a precise linear momentum. This effect is one of the phenomena we referred to as spin-orbit interactions of light, as the spin of the

source is converted into EOAM, i.e. a specific linear momentum, in the evanescent wave. In the following two paragraphs we will see two different ways in which we can describe and predict spin-momentum locking between the fields emitted by a dipolar source and the modes excited in a waveguide. The first method, which is also the one that we will rely on in our paper [Paper A], consists of calculating the angular spectrum of the dipolar source and is sometimes referred to as Green's function approach. The second requires calculating the degree of similarity between the field of the source and that of the guided mode and is known as the Fermi's golden rule. In both these descriptions, the modes of the waveguide will be excited via evanescent coupling to the source. This means that the source must be placed very close (or inside) the waveguide as the coupling amplitude between the source and the mode decays exponentially together with the evanescent decay of the mode.

2.3 The angular spectrum of dipolar sources

Dipoles are the simplest electromagnetic sources, first term approximation of the multipolar expansion of any electromagnetic field. Later, in chapter 3, we will see that dipolar sources are particularly common in nanophotonics due to the ease of inducing them into very small nanostructures such as metallic or dielectric nanoparticles [119–127]. These point sources are fundamental building blocks for electromagnetic radiation and their free-space fields have a simple analytical description [15, 128]. In chapter 1, we have anticipated that the angular spectrum is a powerful tool to describe the fields of electromagnetic sources, as it separates the fields in their propagating and evanescent components. Here, we will derive the angular spectra for electric and magnetic dipoles. For our calculations we will make use of the Green's function we described earlier in section 1.5. The full derivation of the fields is detailed in our paper [Paper A], particularly in the appendices B and C, so here we will only summarise the main points.

In the time-harmonic case, an electric dipole can be described in terms of a dipole moment $\mathbf{p}$, associated to an electric current density $\mathbf{J} = -i\omega\delta^3(\mathbf{r}-\mathbf{r_0})\mathbf{p}$. Analogously, a magnetic dipole has a dipole moment $\mathbf{m}$, associated to a magnetic current density $\mathbf{J_m} = -i\omega\mu\delta^3(\mathbf{r}-\mathbf{r_0})\mathbf{m}$. The time-harmonic approximation means that the time dependence corresponds to an $e^{-i\omega t}$ factor.

The electric and magnetic fields generated by these dipoles in a homogeneous medium

can be written as [129]:

$$\begin{aligned}\mathbf{E}^{\mathrm{ED}} &= k^2\boldsymbol{\pi} + \boldsymbol{\nabla}(\boldsymbol{\nabla}\cdot\boldsymbol{\pi}),\\ \mathbf{H}^{\mathrm{ED}} &= -i\omega\varepsilon\boldsymbol{\nabla}\times\boldsymbol{\pi},\\ \mathbf{H}^{\mathrm{MD}} &= k^2\boldsymbol{\pi}_m + \boldsymbol{\nabla}(\boldsymbol{\nabla}\cdot\boldsymbol{\pi}_m),\\ \mathbf{E}^{\mathrm{MD}} &= i\omega\mu\boldsymbol{\nabla}\times\boldsymbol{\pi}_m,\end{aligned} \tag{2.2}$$

where $\boldsymbol{\pi}$ and $\boldsymbol{\pi}_m$ are electric and magnetic vector potentials, often referred to as the Hertz potentials [129]. We will now derive the angular spectrum of the Hertz potential and from them the spectrum of the fields, which can then be projected onto the two orthogonal s- and p-polarisations. All these calculations are carried out in further detail in the appendices at the end of our paper [Paper A]. First of all, however, we must spend a few words on the polarisation basis.

Conventionally, s- and p- polarisations are defined with respect to a surface through and off of which light is, respectively, refracted and reflected. The normal to this surface, together with the wavevector, define the plane of incidence [130]. Then, a beam whose electric field oscillates parallel to the plane of incidence is called p-polarised while, if the electric field lies orthogonal to the plane of incidence, the beam is s-polarised. Even though we are not necessarily dealing with a physical surface, in our calculations of the angular spectrum we always define a plane at a constant $z = z_0$. The normal to this plane, together with the wavevector, defines the plane of incidence, allowing us to separate our fields into their s and p components. It might seem like an odd choice to pick a polarisation basis which is conventionally defined by means of a surface, when our description of the fields is not bound to the presence of any surface, particularly considering that *mathematically* any orthogonal basis would be adequate to describe them. However, our choice is motivated by at least two *physical* reasons. The first one is that TE (s-polarised) and TM (p-polarised) fields are eigenmodes of planar waveguides which, in turn, are one of the few waveguides possessing analytical eigenmodes. Since our goal is to observe the excitation of guided modes it is convenient to describe the fields of the source in the basis of the modes of the simplest waveguide. The same can be said for surface plasmon polaritons, which are p-polarised. The second reason is that, as we will see in [Paper A], for circularly polarised dipoles, the unidirectionality is manifest only in one angular spectrum, the p-polarised one for the electric dipole and the s-polarised one for the magnetic dipole. In summary, it makes sense to describe our fields, even in free space, in a basis which is descriptive of the modes which said

fields are designed to excite. This simplifies the process of comparison between the fields of the sources and those of the modes and allows us to look at the source only in order to *predict* the excitation of specific guided modes. With all these caveats,

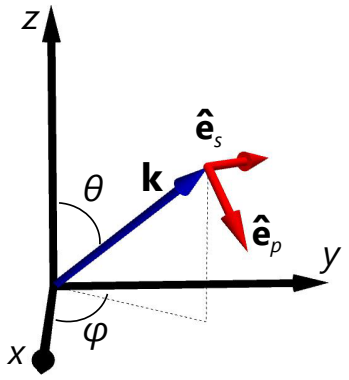

Figure 2.2: Reference system and orientations of the electric field of s- and p-polarised fields.

we can now describe some properties of the polarisation basis, where the vectors $\hat{\mathbf{e}}_s$ and $\hat{\mathbf{e}}_p^{\pm}$ are depicted in figure 2.2. We can immediately see that they correspond to the azimuthal and polar unit vectors, $\hat{\mathbf{e}}_\phi$ and $\hat{\mathbf{e}}_\theta$ respectively, in spherical coordinates. They are defined as:

$$\begin{aligned}
\hat{\mathbf{e}}_s(k_x,k_y) &= \frac{\hat{\mathbf{z}}\times\mathbf{k}^{\pm}}{|\hat{\mathbf{z}}\times\mathbf{k}^{\pm}|} \qquad (2.3)\\
&= (-\sin\phi,\cos\phi,0)\\
&= \frac{1}{\sqrt{k_x^2+k_y^2}}\left(-k_y\hat{\mathbf{x}}+k_x\hat{\mathbf{y}}\right)=\hat{\mathbf{e}}_\phi,\\
\hat{\mathbf{e}}_p^{\pm}(k_x,k_y) &= \frac{\hat{\mathbf{z}}\times\mathbf{k}^{\pm}}{|\hat{\mathbf{z}}\times\mathbf{k}^{\pm}|}\times\frac{\mathbf{k}^{\pm}}{k} \qquad (2.4)\\
&= (\pm\cos\theta\cos\phi,\pm\cos\theta\sin\phi,-\sin\theta)\\
&= \frac{1}{k\sqrt{k_x^2+k_y^2}}\left[\pm k_xk_z\hat{\mathbf{x}}\pm k_yk_z\hat{\mathbf{y}}-(k_x^2+k_y^2)\hat{\mathbf{z}}\right]=\hat{\mathbf{e}}_\theta.
\end{aligned}$$

where k is the wavenumber of the medium and $\hat{\mathbf{z}}$ is the unit vector normal to the plane in which we choose to expand the angular spectrum, for a dipole located along the z-axis in $z=z_0$. The subscript $\pm$ distinguishes between the orientation of the z-component of the wavevector $\mathbf{k}$, hence between the half-spaces above and below the dipole. The unit vector $\hat{\mathbf{e}}_s$ does not depend on k_z, it is orthogonal to the z-axis as can be seen in figure 2.2, and therefore does not change above or below the dipole. The three orthogonal unit vectors that we will then use as a basis are $\hat{\mathbf{e}}_s$, $\hat{\mathbf{e}}_p^{\pm}$ and

$\hat{\mathbf{e}}_k^{\pm} = \frac{\hat{\mathbf{k}}^{\pm}}{k}$, and, between the three, the relation $\hat{\mathbf{e}}_i \cdot \hat{\mathbf{e}}_j = \delta_{ij}$ holds, where δ_{ij} is the Kronecker delta function. This allows us to find the i-th component of a vector $\mathbf{v}$ as $v_i = \mathbf{v} \cdot \hat{\mathbf{e}}_i$. Notice that $\hat{\mathbf{e}}_i \cdot \hat{\mathbf{e}}_j = \delta_{ij}$ is an unusual definition for a complex orthonormal basis, as usually one of the two unit vectors would have to be complex conjugated for this relationship to hold. This is because of the peculiar nature of $\hat{\mathbf{k}}^{\pm}$ in the evanescent case. In the propagating and lossless case, so for the plane wave part of the spectrum, $\hat{\mathbf{k}}^{\pm}$ is always real, hence its magnitude is $|\hat{\mathbf{k}}^{\pm}|^2 = \hat{\mathbf{k}}^{\pm} \cdot \hat{\mathbf{k}}^{\pm *} = k^2$, so $\hat{\mathbf{e}}_s$ and $\hat{\mathbf{e}}_p^{\pm}$ are both real and unitary. However, when the fields are evanescent along z, $|\hat{\mathbf{k}}^{\pm}|^2 > k^2$, which means that the vector $\hat{\mathbf{e}}_p^{\pm}$ is no longer real and unitary. Nonetheless, the relation $\hat{\mathbf{k}}^{\pm} \cdot \hat{\mathbf{k}}^{\pm} = k^2$ still holds, which is why defining the inner product without the complex conjugation allows us to use $\hat{\mathbf{e}}_s$, $\hat{\mathbf{e}}_p^{\pm}$ and $\hat{\mathbf{e}}_k^{\pm}$ as unit vectors of an orthonormal basis. Finally, it is useful to have the following identities at hand:

$$\begin{aligned} \hat{\mathbf{e}}_k^{\pm} \times \hat{\mathbf{e}}_p^{\pm} &= \hat{\mathbf{e}}_s, \\ \hat{\mathbf{e}}_k^{\pm} \times \hat{\mathbf{e}}_s &= -\hat{\mathbf{e}}_p^{\pm}, \\ \hat{\mathbf{e}}_p^{\pm} \times \hat{\mathbf{e}}_s &= \hat{\mathbf{e}}_k^{\pm}. \end{aligned} \tag{2.5}$$

In real space, the Hertz potentials are proportional to the dipole moments times the scalar Green's function for the Helmholtz operator, i.e. $\boldsymbol{\pi} \propto \mathbf{p}\frac{e^{i\mathbf{k}\cdot\mathbf{r}}}{r}$ and $\boldsymbol{\pi}_m \propto \mathbf{m}\frac{e^{i\mathbf{k}\cdot\mathbf{r}}}{r}$. From the potentials in the spatial domain we can finally obtain the angular spectrum by rewriting them as Fourier transforms, taking advantage of Weyl's identity [16, 129–132], so that $\boldsymbol{\pi}$ and $\boldsymbol{\pi}_m$ result in:

$$\begin{aligned} \boldsymbol{\pi} &= \frac{i}{8\pi^2\varepsilon} \iint \frac{\mathbf{p}}{k_z} e^{i(k_x x + k_y y)} e^{ik_z|z-z_0|}\, dk_x\, dk_y, \\ \boldsymbol{\pi}_m &= \frac{i}{8\pi^2} \iint \frac{\mathbf{m}}{k_z} e^{i(k_x x + k_y y)} e^{ik_z|z-z_0|}\, dk_x\, dk_y, \end{aligned} \tag{2.6}$$

and use these expressions to find the angular spectrum of the fields, by applying equations (2.2). Notice that, when dealing with angular spectra, we can simplify

$\nabla \to i\hat{\mathbf{k}}^{\pm}$. Starting with the first of equations (2.2):

$$\begin{aligned}\mathbf{E}^{\mathrm{ED}}(k_x,k_y) =& k^2\boldsymbol{\pi} + \boldsymbol{\nabla}(\boldsymbol{\nabla}\cdot\boldsymbol{\pi}) = \\ =& k^2\boldsymbol{\pi} + i\hat{\mathbf{k}}^{\pm}(i\hat{\mathbf{k}}^{\pm}\cdot\boldsymbol{\pi}) = \\ =& k^2\boldsymbol{\pi} - k^2\hat{\mathbf{e}}_k^{\pm}(\hat{\mathbf{e}}_k^{\pm}\cdot\boldsymbol{\pi}) = \\ =& k^2(\boldsymbol{\pi} - \pi_k\hat{\mathbf{e}}_k^{\pm}) = \\ =& k^2(\pi_p\hat{\mathbf{e}}_p^{\pm} + \pi_s\hat{\mathbf{e}}_s),\end{aligned} \tag{2.7}$$

where we have used $\boldsymbol{\pi} = \pi_k\hat{\mathbf{e}}_k^{\pm} + \pi_p\hat{\mathbf{e}}_p^{\pm} + \pi_s\hat{\mathbf{e}}_s$. Analogously for the magnetic field we have:

$$\begin{aligned}\mathbf{H}^{\mathrm{ED}}(k_x,k_y) =& -i\omega\varepsilon\boldsymbol{\nabla}\times\boldsymbol{\pi} = \\ =& -i\omega\varepsilon(i\hat{\mathbf{k}}^{\pm}\times\boldsymbol{\pi}) = \\ =& \omega\varepsilon k(\hat{\mathbf{e}}_k^{\pm}\times\boldsymbol{\pi}) \\ =& \omega\varepsilon k(\pi_p\cdot\hat{\mathbf{e}}_s - \pi_s\cdot\hat{\mathbf{e}}_p^{\pm}).\end{aligned} \tag{2.8}$$

And similarly for the fields generated by a magnetic dipole:

$$\mathbf{E}^{\mathrm{MD}}(k_x,k_y) = \omega\mu k(\boldsymbol{\pi}_{ms}\cdot\hat{\mathbf{e}}_p^{\pm} - \boldsymbol{\pi}_{mp}\cdot\hat{\mathbf{e}}_s), \tag{2.9}$$

$$\mathbf{H}^{\mathrm{MD}}(k_x,k_y) = k^2(\boldsymbol{\pi}_{mp}\cdot\hat{\mathbf{e}}_p^{\pm} + \boldsymbol{\pi}_{ms}\cdot\hat{\mathbf{e}}_s). \tag{2.10}$$

With all of the above we have all the ingredients required to compose the electric and magnetic angular spectra of the dipoles' fields, defined as [16]:

$$\begin{aligned}\mathbf{E}^{\mathrm{ED+MD}}(x,y,z) &= \iint \left[\mathbf{E}^{\mathrm{ED}}(k_x,k_y)|_{z=z_0} + \mathbf{E}^{\mathrm{MD}}(k_x,k_y)|_{z=z_0}\right] e^{i(k_x x + k_y y + k_z|z-z_0|)}\,dk_x\,dk_y, \\ \mathbf{H}^{\mathrm{ED+MD}}(x,y,z) &= \iint \left[\mathbf{H}^{\mathrm{ED}}(k_x,k_y)|_{z=z_0} + \mathbf{H}^{\mathrm{MD}}(k_x,k_y)|_{z=z_0}\right] e^{i(k_x x + k_y y + k_z|z-z_0|)}\,dk_x\,dk_y,\end{aligned} \tag{2.11}$$

which acquire a particularly laconic form when we substitute $\boldsymbol{\pi}$ and $\boldsymbol{\pi}_m$ from equations (2.6):

$$\begin{aligned}\mathbf{E}^{\mathrm{ED+MD}}(k_x,k_y)|_{z=z_0} &= \frac{i}{8\pi^2\varepsilon}\frac{k^2}{k_z}\left[(\hat{\mathbf{e}}_s\cdot\mathbf{p} - \hat{\mathbf{e}}_p^{\pm}\cdot\frac{\mathbf{m}}{c})\hat{\mathbf{e}}_s + (\hat{\mathbf{e}}_p^{\pm}\cdot\mathbf{p} + \hat{\mathbf{e}}_s\cdot\frac{\mathbf{m}}{c})\hat{\mathbf{e}}_p^{\pm}\right], \\ \mathbf{H}^{\mathrm{ED+MD}}(k_x,k_y)|_{z=z_0} &= \frac{i\omega}{8\pi^2}\frac{k}{k_z}\left[(\hat{\mathbf{e}}_p^{\pm}\cdot\mathbf{p} + \hat{\mathbf{e}}_s\cdot\frac{\mathbf{m}}{c})\hat{\mathbf{e}}_s - (\hat{\mathbf{e}}_s\cdot\mathbf{p} - \hat{\mathbf{e}}_p^{\pm}\cdot\frac{\mathbf{m}}{c})\hat{\mathbf{e}}_p^{\pm}\right].\end{aligned} \tag{2.12}$$

Equations (2.12) are of fundamental importance to our work. They are the angular spectra of the fields radiated by dipolar sources, intuitively described in terms of the dipole moments $\mathbf{p}$ and $\mathbf{m}$. This, in chapter 4, will be at the basis of our source-engineering procedure, in which the dipole moments are *tailored* so that the fields achieve specific values at given points in k-space.

2.4 Fermi's golden rule

The angular spectrum description of dipolar sources allows us to describe the fields of dipoles in free space and quantify their amplitude and phase for each spectral component. Once the source's behaviour in free space is known, it is straightforward to predict the coupling between said source and a waveguide, by comparing the angular spectrum of the dipole to the dispersion relation of the waveguide, both of which lie in k-space. There is, however, another way to determine the excitation of a guided mode by means of a point source *in real space* which consists of comparing the degree of similarity between the polarisation of the source and the fields of the modes supported by the waveguide, point by point. This method is described by Fermi's golden rule [118, 133–135]. For a superposition of an electric $\mathbf{p}$ and a magnetic $\mathbf{m}$ dipole, placed in $z = z_0$, in close proximity of a waveguiding structure, or inside it, the coupling amplitude between the dipole moments and the guided fields of the waveguide is proportional to:

$$A \propto |\mathbf{p}^* \cdot \mathbf{E}(z_0) + \mathbf{m}^* \cdot \mu\mathbf{H}(z_0)|, \tag{2.13}$$

where $\mathbf{E}(z_0)$ and $\mathbf{H}(z_0)$ are the electric and magnetic fields calculated at the position of the dipole, respectively.

Although it requires the exact knowledge of the fields supported by the waveguide, this method is very intuitive, since the coupling amplitude is directly proportional to how similar the source and the waveguide modes are. Explicitly, for example, if the waveguide was to support fields whose electric field was polarised in the xz-plane, an electric dipole oriented along y would not excite them at all, as the dot product between the dipole moment and the field would be null. Together with the angular spectrum approach, this technique provides us with another method to design dipole moments so that they achieve custom excitation of guided modes. As an example, we can realise the excitation of a guided mode that only propagates in one direction

inside a waveguide, which we will examine in detail in chapter 4.
The angular spectrum approach and Fermi's golden rule approach are both widely used in literature. In our works, we also make use of both of them, adopting any of the two according to the system under study. The angular spectrum approach has the advantage of being source-dependent only. To adopt Fermi's golden rule, in fact one needs to be able to write the fields of the modes to excite, in order to estimate the coupling amplitude between them and the dipolar source. On the other hand, the angular spectrum is an analytical description of the fields of the source only, in free space, on a two dimensional plane. The possible unidirectionality is hence described as an intrinsic property of the source itself and the maths is very easy to deal with (guided modes, on the other hand, can often have strikingly complex and non analytical expressions). The difference between these two approaches boils down, at the very end, on the subject of our study and the parameter we are willing to keep free. If we are willing to study the behaviour of a specific source, we might as well look at the fields it radiates in free space by means of an analytical description, adapting later the requirements on the waveguide to find one that is suitable to preserve its directional features. This can be a planar waveguide, which would preserve the angular spectrum exactly, apart from a multiplicative factor given by Fresnel coefficients, or any other single-mode waveguide. Although different from the modes of planar slabs, in fact, a directional source will still preferentially couple to one side of a single mode waveguide, with a slightly lower directional contrast, as the confinement in one dimension does not substantially influence the behaviour of the mode along the orthogonal dimension. This assumption is of course subject, as we said, to the requirement of the waveguide being single-mode. An example of this is shown in our paper [Paper A], in which a waveguide with a non-analytical cross-section is excited directionally with a very high directionality contrast, by a simple circular dipole. On the other hand, if our goal is to excite a specific guided mode unidirectionally, independently of the source required to do so, we would better adopt Fermi's golden rule and optimise the source's parameter to find that which maximises directionality for that desired guided mode. The advantage of Fermi's golden rule, in this case, is clear, as it provides an *exact* value for the coupling in every scenario, regardless of the complexity of the waveguide, as opposed to the angular spectrum approach which is rigorously exact only for planar structures.

2.5 Unidirectionality of guided modes: State of the art

Unidirectional excitation of guided modes was realised, in the last few years, in a variety of different setups, using paraxial and nonparaxial fields and regardless of the complexity of the structures involved, from simple planar waveguides to photonic crystals or metamaterials. This highlights the robustness and universality of the phenomenon, proving that eventually it boils down to an intrinsic property of dipolar sources, independently of the means by which they are realised. Different approaches are currently exploited to obtain unidirectional excitation of guided modes and, eventually, they all rely on the symmetry of the system being broken. After the description of transverse spin of surface plasmons given by Bliokh and colleagues in 2012 [139], who later also unveiled the spin momentum locking of surface modes we discussed earlier [114–116], many groups have successfully managed to couple the spin of electric dipolar sources to the transverse spin of guided modes. The first realisation was made by Rodriguéz Fortuño *et al.* [136], using a narrow slit to induce the dipole and couple its scattered light to directional surface plasmons. This work was published simultaneously with a work by Lin *et al.* [140], in which also subwavelength slits are used to control directionality but without making use of spin-momentum locking. Lin and colleagues implemented an arrangement of subwavelength apertures, each of which scattered as a linear electric dipole. Finely designing the spacing and relative orientation between the slits, the interference between the light scattered by each slit, including the propagation phases acquired due to the distance between the slits, resulted in an overall directionality. In [136], instead, the group used a single slit but this time illuminated it with elliptically polarised light. The slit, embedded in a thin gold film and shown in figure 2.3 (a), under elliptically polarised illumination, scatters light as an elliptical dipole would. For a specific polarisation of the source the transverse spin of the dipole will match that of a surface plasmon propagating in a specific direction at the gold-air interface. Changing the handedness of the polarisation inverts the propagation direction of the surface plasmon, as it is also shown in figure 2.3 (a). After the initial implementations using nanometric slits, circular electric dipole sources have been demonstrated using small gold nanoparticles. Representative examples of this can be found in Refs. [134, 137, 138] and summaries of their experimental setups and results are show in figure 2.3 (b), (c) and (d), respectively. Petersen and colleagues in [134] illuminated

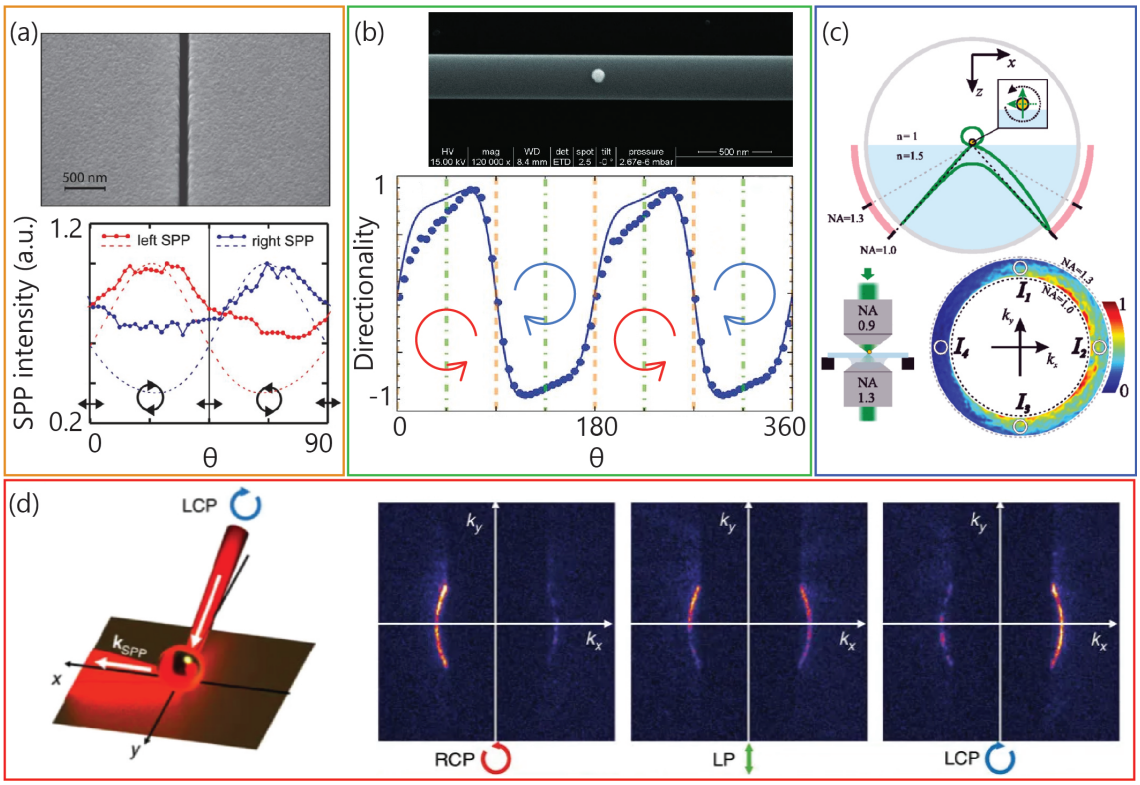

Figure 2.3: Experimental realisations of unidirectional guided modes via circular electric dipoles. In (a), taken from Ref. [136], a single slit is used as a circular dipole to excite directional surface plasmon polaritons. Panel (b) summarises the experimental results from Ref. [134], in which a circular electric dipole is induced in a gold nanoparticle and the fields it scatters are coupled directionally inside a single-mode nanofiber. In panel (c) a schematics of the setup and the experimental near-field angular spectrum measured in Ref. [137] are reported. The group uses high numerical aperture microscopy to single out the near-field of the circularly polarised dipole induced in a gold nanoparticle on a glass substrate. Finally, in (d), the results from Ref. [138] are reprinted, showing the directional excitation of surface plasmons induced by the scattering from a gold nanoparticle.

a gold spherical nanoparticle placed on top of a single mode nanofiber and showed a polarisation-controlled excitation of the guided mode inside the fiber. Near-unity directionality is achieved for the two counter-rotating circular polarisations, corresponding to a circular electric dipole being induced in the scattering nanoparticle. A scanning electron microscope image of the particle sitting on the nanofiber and the measured the polarisation-dependent directionality are plotted in figure 2.3 (b), taken from their paper [134]. In figure 2.3 (c), we report the findings of Neugebauer and colleagues published in [137]. In this paper the group directly measures the near field scattered by a gold nanoparticle sitting on a glass substrate. To do so, they implement a high-numerical aperture microscope which only collects the radiation scattered at angles larger than the critical angle, hence limiting their observation to the near-field part of the angular spectrum. The near field radiation is then converted into a far-field pattern by oil-matching the glass substrate with the detection objective. Being the refractive index of glass higher than air, the near-field evanescent components scattered by the nanoparticle become propagating inside glass. The characteristic p-polarised near field angular spectrum of a circular electric dipole is hence directly measured. This experiment is particularly important as it shows the inherent directionality of the circular electric dipole's fields themselves, without the need of measuring the directionality via a matched waveguide. We will see later that Neugebauer and colleagues have experimentally measured the angular spectrum of a Janus dipole, presented in our paper [Paper D], implementing a similar setup. Finally, in Ref. [138], O'Connor and colleagues proved the directional excitation of surface plasmons obtained illuminating a gold spherical nanoparticle on a gold substrate, together with the reciprocal effect: exciting a surface plasmon propagating towards the nanosphere from a given direction, they could detect the far field scattering from the nanoparticle, in an orthogonal direction to the surface plasmon, to be circularly polarised. The directionality in the surface plasmons excitation, together with a schematic of the experimental system under study, are depicted in figure 2.3 (d).
Implementation of circular electric dipoles by means of scattering nanostructures were the first attempts at verifying the predicted unidirectionality but, however common in literature, they are not the only ones. Rauschenbeutel's group, for example, has demonstrated the possibility of using the circularly polarised emission by trapped ultracold cesium atoms to match the transverse spin of guided modes [141, 142].

Another formalism often adopted to study unidirectionality requires writing the coupling amplitude between a point source and a guided mode using the Green's

function analysis. As we have seen previously in section 1.5, the Green's function of the mode describes the response of the system at any point $\mathbf{r}$ to a source placed in $\mathbf{r}'$. Analogously to Fermi's golden rule approach, the degree of similarity between the dipolar source and the excited mode, hence their coupling amplitude, can be estimated by means of a product between the dipole moment and the Green's function [135, 143]. This becomes significantly relevant when the guided mode is not translationally invariant across the length of the guide such as in photonic crystal waveguides. In these guides, in fact, the polarisation, which is mostly elliptical, becomes linear or circular in specific locations, denoted as "L-points" and "C-points", respectively [144]. When a circularly polarised dipolar source is placed in a C-point, the coupling amplitude between the dipole and the mode becomes unitary for one propagation direction and goes to zero for the counterpropagating one, ensuring the unidirectional excitation of the guided mode. This method clearly requires a precise engineering of the waveguiding structure and a highly accurate placing of the dipolar source [145]. Unlike the scattering nanostructures, however, the coupling efficiency between the source and the waveguide is incredibly high so that most of the light emitted by the source actually couples to the guided mode [146, 147]. To overcome the difficulty of positioning the source, different strategies have been devised, such as inducing circular dipoles in AFM tips or using quantum dots as sources [135, 143, 148–151], all of which achieve almost completely unidirectional excitations. Apart from the high level of directionality it provides, this approach is currently being pursued in the quantum optics community as a concrete method for the generation of spin-path entangled states with a large number of photons [143, 152, 153] and the realisation of all-optical non-reciprocal elements [148] .
The vast development of this field over the last five years has also led to numerous applications, such as polarimeters [154–158], nanorouters [134, 138, 159], photon emitters [141, 148].
Moreover, as a result of unidirectional excitation of guided modes, novel near-field optical forces have been observed [160–167].

2.6 Our work: Paper A

In this framework, we have extended the theoretical description of the unidirectional excitation of guided modes by means of circular electric dipoles to reveal the near field directionality of circular magnetic dipoles. We have used the angular spectrum

approach to determine a strong directionality in the near fields of circularly polarised dipolar sources which is then translated into directional excitation of a guided mode once the source is placed in close proximity of a waveguide. Circularly polarised electric and magnetic dipoles possess a unidirectional angular spectrum in free space, however, when we want to use these source to excite a guided mode, the dipoles need not to be exactly circular but elliptical and the degree of ellipticity depends on the wavevector of the mode that we are exciting. We have determined the optimisation conditions that are required for the unidirectional excitation of any guided mode and shown that elliptical electric dipole sources unidirectionally excite p-polarised guided modes, while elliptical magnetic dipoles do so for s-polarised modes. In this paper, I performed the analytical calculations of the fields generated by a magnetic dipole, derived a unified formalism which allowed to describe the fields of electric and magnetic dipoles with the simple notation presented, performed the numerical simulations and prepared the first draft for the main text, the figures and the appendices.

2.7 Paper A

Phys. Rev .B ***95****, 245416 (2017)*

Unidirectional evanescent-wave coupling from circularly polarized electric and magnetic dipoles: An angular spectrum approach

Michela F. Picardi, Alejandro Manjavacas, Anatoly V. Zayats and Francisco J. Rodríguez-Fortuño

---

Unidirectional evanescent-wave coupling from circularly polarized electric and magnetic dipoles: An angular spectrum approach

Michela F. Picardi[1], Alejandro Manjavacas[2], Anatoly V. Zayats[1] and Francisco J. Rodríguez-Fortuño[1]

[1] *Department of Physics, King's College London, Strand, London WC2R 2LS, United Kingdom*
[2] *Department of Physics and Astronomy, University of New Mexico, Albuquerque, New Mexico 87131, United States*

Unidirectional evanescent-wave coupling from circularly polarized dipole sources is one of the most striking types of evidence of spin-orbit interactions of light and an inherent property of circularly polarized dipoles. Polarization handedness self-determines propagation direction of guided modes. In this paper, we compare two different approaches currently used to describe this phenomenon: the first requires the evaluation of the coupling amplitude between dipole and waveguide modes, while the second is based on the calculation of the angular spectrum of the dipole. We present an analytical expression of the angular spectrum of dipole radiation, unifying the description for both electric and magnetic dipoles. The symmetries unraveled by the implemented formalism show the existence of specific terms in the dipole spectrum which can be recognized as being directly responsible for directional evanescent-wave coupling. This provides a versatile tool for both a comprehensive understanding of the phenomenon and a fully controllable engineering of directionality of guided modes.

I. INTRODUCTION

The nanophotonics and quantum-optics communities have recently shown strong interest in the fascinating scenario of a photonic waveguide being excited by a circularly polarized electric dipole source showing strong directionality [1–8]. The practical importance of the unidirectional excitation by circularly polarized dipoles

is evident in quantum optics, as it provides a means of mapping quantum spin states into different free photon states [7–13]. It is also extremely interesting in classical nanophotonics, where the dipole scattering can be imitated by a small illuminated particle in the Rayleigh limit. Small particles illuminated with circularly polarized light behave as circularly polarized dipolar scatterers and, thus, exhibit directional excitation of modes in nearby waveguides [14–17]. The effect is an example of spin-orbit interaction (SOI) of light, where light polarization determines light propagation trajectory [18, 19]. SOI effects are generally believed to be small (unless enhanced with artificial materials [20, 21]). However, in the present case, illuminated particles scatter light into completely opposite directions, constituting a remarkably simple yet drastic example of SOI, providing a unique opportunity for robust, integrated, ultrafast light nano-routing based on polarization [15, 22–25]. The effect can also have important consequences in the optical manipulation of chiral [26, 27] and non-chiral nanoparticles [28–31], giving rise to unintuitive lateral forces, as well as applications in optical isolation [13, 32].

Different approaches are commonly used to explain the unidirectionality effect of dipolar scattering. A very general and simple one relies on the fact that the coupling strength of a dipole to any photonic mode is proportional to the similarity between the electric dipole vector $\mathbf{p}$ and the electric field vector of the photonic mode at the location of the dipole $\mathbf{E}(\mathbf{r}_0)$. Therefore, the dipole can be made to match the fields of the mode propagating in one direction, but not the opposite one [3–9]. This line of thought can be equally well applied to magnetic dipoles [5, 7]. Another approach relies on the asymmetric near-field angular spectrum of dipole fields themselves, together with considerations of momentum conservation [1, 2, 15, 16]. This approach applies only to the case of planar waveguides, but provides a very valuable physical insight. It shows that the directionality of a circularly polarized dipole is a property of its evanescent components that can be observed only when the dipole is placed in close proximity to a structure. The case of magnetic dipole directionality, although already considered in the first approach, has never been treated analytically with spectral calculations. The knowledge of the angular spectra of magnetic dipoles is important for the design of dielectric-based nanophotonic systems, since magnetic dipoles can experimentally be achieved by illuminating high-index spheres of dimensions comparable to fractions of a wavelength [33, 34], whose lowest order resonance have a magnetic dipole character. In this paper, we derive the analytical angular spectra of both electric and magnetic dipoles in a

concise nomenclature, which provides an intuitive straightforward understanding of their scattering directionality. We also show in a simple way how both explanations discussed above: (i) mode-coupling and (ii) dipole angular spectrum, are ultimately equivalent in the scenarios where both apply.

II. MODE COUPLING AND SPIN-DIRECTION LOCKING

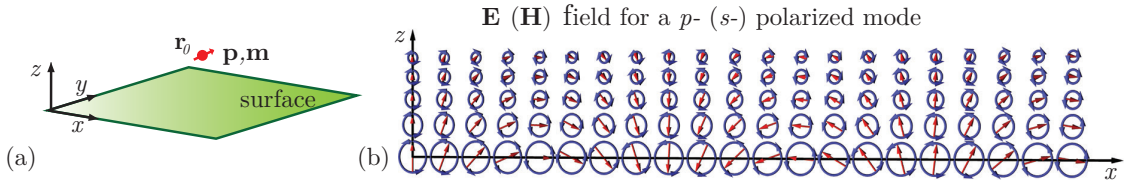

Figure 1: (a) Schematic of an electric or magnetic dipole placed near a surface. (b) Electric (magnetic) field of a p-polarized (s-polarized) evanescent wave propagating in the $+x$ direction. It corresponds, for example, to the electric field of surface plasmon polaritons, which is p-polarized, or to the magnetic field of an s-polarized guided mode on a dielectric slab. Red arrows depict the instantaneous field amplitude, while blue lines show the corresponding polarization ellipses.

We start with a very brief overview of the mode coupling explanation of directional scattering of circularly polarized dipoles [4–9]. Consider a dipolar emitter located in $\mathbf{r}_0$ close to a waveguide interface (outside or inside the waveguide). In the most general case, the emitter can have non-zero both electric $\mathbf{p}$ and magnetic $\mathbf{m}$ dipole moments.

The probability that photons emitted by the source couple to a certain waveguide mode is proportional to the square modulus of the coupling amplitude between the dipole moments and the mode fields in the waveguide [3–5]

$$P \propto |\mathbf{p}^* \cdot \mathbf{E}(\mathbf{r}_0) + \mathbf{m}^* \cdot \mu \mathbf{H}(\mathbf{r}_0)|^2, \tag{1}$$

where $\mathbf{p}$ and $\mathbf{m}$ are electric and magnetic dipole moments, μ is the magnetic permeability of the medium, $\mathbf{E}(\mathbf{r}_0)$ and $\mathbf{H}(\mathbf{r}_0)$ electric and magnetic fields calculated at $\mathbf{r} = \mathbf{r_0}$, respectively. This expression is valid for any type of waveguided mode, provided that fields at $\mathbf{r}_0$ are known. It can be verified that there are positions at which the modes of a waveguide display circularly (or more generally, elliptically) polarized fields with a handedness that depends on the propagation direction. These

positions can either lie inside the waveguide [6–8] or be in its close proximity, in the regions of evanescent tails that surround it [3–5, 9, 35]. Hence it follows that circularly (or elliptically) polarized dipoles with opposite handedness will couple into opposite propagating directions of the modes, while linearly polarized dipoles will excite them equally in both directions [9]. This can occur for modes of optical fibers [14, 36, 37], integrated optical waveguides [4, 6], plasmonic waveguides [1] and photonic crystal waveguides for both electric and magnetic dipole sources [7].

We consider the simple scenario of a dipole near planar waveguides, slabs or surfaces, with faces perpendicular to the z axis (see Fig.1 (a)). In this simple case, the modes supported by the structure can be analytically described. Furthermore we can assume $k_y = 0$ without loss of generality and, therefore, deal with a two-dimensional problem. The guided modes of such systems, in the region $z > 0$, are time-harmonic evanescent waves oscillating at a frequency ω and characterized by a wavevector $\mathbf{k}^{\pm} = (k_x, k_y = 0, \pm k_z)$, where $k_z = \sqrt{k^2 - k_x^2}$, $k = n\omega/c$ and $n = \sqrt{\varepsilon\mu}$ is the refractive index of the surrounding medium. The positive sign in k_z assumes evanescent decay in the $+\hat{\mathbf{z}}$ direction (the opposite case can be obtained by reversing the sign of k_z). If we assume a real n, evanescent waves fulfill $\mathrm{Re}(k_x) > k$, resulting in k_z having an imaginary component. The evanescent wave field is written as

$$\mathbf{E}(\mathbf{r}) = \mathbf{E}_0 e^{i\mathbf{k}^{\pm}\cdot\mathbf{r}}.$$

Using the expressions $\mathbf{H} = \frac{1}{\omega\mu}(\mathbf{k}^{\pm} \times \mathbf{E})$, $\mathbf{E} = -\frac{1}{\omega\varepsilon}(\mathbf{k}^{\pm} \times \mathbf{H})$, directly derived from Maxwell's equations, and the subsequent transversality conditions $\mathbf{E} \cdot \mathbf{k}^{\pm} = 0$ and $\mathbf{H} \cdot \mathbf{k}^{\pm} = 0$, we obtain the electric and magnetic fields of p-polarized (TM) and s-polarized (TE) evanescent modes [2, 5, 38, 39]:

$$\mathbf{E}^p = \begin{pmatrix} \pm k_z A_{\mathrm{TM}} \\ 0 \\ -k_x A_{\mathrm{TM}} \end{pmatrix}; \qquad \mathbf{H}^p = \frac{k^2}{\omega\mu} \begin{pmatrix} 0 \\ A_{\mathrm{TM}} \\ 0 \end{pmatrix},$$

$$\mathbf{E}^s = -\frac{k^2}{\omega\varepsilon} \begin{pmatrix} 0 \\ A_{\mathrm{TE}} \\ 0 \end{pmatrix}; \qquad \mathbf{H}^s = \begin{pmatrix} \pm k_z A_{\mathrm{TE}} \\ 0 \\ -k_x A_{\mathrm{TE}} \end{pmatrix}, \tag{2}$$

with A_{TM} and A_{TE} being the amplitudes of the fields.

It is evident that for $\mathrm{Re}(k_x) \gg k$ the vectors associated with the complex numbers k_x and k_z become almost orthogonal to one another in the complex plane, so that $\mathbf{E}^p$ and $\mathbf{H}^s$ fields are elliptically polarized (see Fig.1(b)). In the limit in which $k_x \to \infty$, $k_z \to ik_x$ and the polarization becomes purely circular. Therefore, the basic electromagnetic equations above require that the polarization of evanescent waves is elliptical or circular in the plane of propagation. While this is not new [40], only recently it was pointed out that it implies a transverse spin angular momentum with a handedness that depends only on the propagation direction (called spin-direction or spin-momentum locking) [37, 38, 41, 42]. This provides a very intuitive explanation for the directional excitation of evanescent waves [3, 5, 9, 38]. If we consider an electric dipole circularly polarized in the xz plane, with the sign of the z-component determining the handedness:

$$\mathbf{p}_{L,R} = \begin{pmatrix} 1 \\ 0 \\ \pm i \end{pmatrix},$$

for a p-polarized evanescent wave, when $k_x \to \infty$ with the evanescent decay in the $+z$ direction (taking the positive root for $k_z \approx ik_x$), the value of $|\mathbf{p}^* \cdot \mathbf{E}^p|$ is equal to

$$|\mathbf{p}^* \cdot \mathbf{E}^p| = \begin{cases} 0 & \text{for the propagation direction} \mp x \\ 2E_x & \text{for the propagation direction} \pm x \end{cases}$$

with the sign depending only on the sign of p_z and, therefore, explaining the directionality. It is interesting to verify that the value of the product $|\mathbf{p}^* \cdot \mathbf{E}^p|$ does not result in directional emission if the wave is propagating ($|k_x| < k$) instead of evanescent ($|k_x| > k$) or, likewise, if the dipole is linearly polarized. Similar considerations apply to the case of a circularly polarized magnetic dipole coupled with the magnetic field $\mathbf{H}^s$ of an s-polarized evanescent wave.

III. DIPOLE ANGULAR SPECTRUM APPROACH

The focus of this work is on an alternative explanation for the directionality of the emission of circularly polarized dipoles based on the angular spectrum (momentum representation) of the emitted waves. This explanation was introduced in [1] for electric dipoles only. Here we provide a new simplified analytical formulation of this approach that presents advantages both in terms of physical intuition and system design engineering. Also, we extend it to the case of magnetic dipoles.

We start by considering an arbitrary electric dipole $\mathbf{p}$ located at $\mathbf{r}_0 = (0, 0, z_0)$ within a homogeneous medium with permittivity ε, permeability μ and wave number $k = \omega\sqrt{\varepsilon\mu}$. The electric field $\mathbf{E}^{\mathrm{ED}}$ generated by the dipole can be expressed using the angular spectrum as [43]:

$$\mathbf{E}^{\mathrm{ED}}(x, y, z) = \iint \mathbf{E}^{\mathrm{ED}}(k_x, k_y)|_{z=z_0} \times \\ \times e^{i(k_x x + k_y y + k_z |z - z_0|)} dk_x dk_y.$$

We can project $\mathbf{E}^{\mathrm{ED}}(k_x, k_y)|_{z=z_0}$ on $\hat{\mathbf{e}}_s$ and $\hat{\mathbf{e}}_p^{\pm}$ [44], which are the unit vectors of the electric field of s-polarized and p-polarized waves, defined as (see Appendix 1):

$$\hat{\mathbf{e}}_s(k_x, k_y) = \left(-\frac{k_y}{k_t}, \frac{k_x}{k_t}, 0 \right), \\ \hat{\mathbf{e}}_p^{\pm}(k_x, k_y) = \left(\pm\frac{k_x k_z}{k k_t}, \pm\frac{k_y k_z}{k k_t}, -\frac{k_t}{k} \right),$$

where $k_t = \sqrt{k_x^2 + k_y^2}$ and the $\pm$ accounts for fields calculated above or below $z = z_0$ respectively.

Applying this decomposition (see Appendix 2 for details), it is possible to write the angular spectrum of the field as the sum of $s-$ and $p-$polarized components:

$$\mathbf{E}^{\mathrm{ED}}(k_x, k_y)|_{z=z_0} = \frac{ik^2}{8\pi^2\varepsilon} \frac{1}{k_z} \left[(\hat{\mathbf{e}}_s \cdot \mathbf{p}) \hat{\mathbf{e}}_s + (\hat{\mathbf{e}}_p^{\pm} \cdot \mathbf{p}) \hat{\mathbf{e}}_p^{\pm} \right]. \tag{3}$$

In the same way, for a magnetic dipole with arbitrary dipole moment $\mathbf{m}$ (see Appendix 3), we can write its electric field angular spectrum as:

$$\mathbf{E}^{\mathrm{MD}}(k_x, k_y)|_{z=z_0} = -\frac{ik^2}{8\pi^2\varepsilon} \frac{1}{k_z} \frac{1}{c} \left[(\hat{\mathbf{e}}_p^{\pm} \cdot \mathbf{m}) \hat{\mathbf{e}}_s - (\hat{\mathbf{e}}_s \cdot \mathbf{m}) \hat{\mathbf{e}}_p^{\pm} \right]. \tag{4}$$

These compact equations are the main result of this work, written in vector form, independent of basis representation. In previous works [43–45], the angular spectra of dipoles are calculated in terms of matrix elements of the Green tensor in a given coordinate system. These matrix elements are difficult to associate with an intuitive interpretation. Equations (3) and (4), instead, provide physical insight, unravel symmetries in the fields, and prove to be useful design rules. They allow for a direct understanding of the effect of spin-momentum locking in relation to dipole evanescent-wave excitation. Examining them we see that the p-polarized angular spectrum of an electric dipole $\mathbf{p}$ is given directly (up to a constant prefactor) by $(\hat{\mathbf{e}}_p^{\pm}/k_z)\cdot\mathbf{p}$, identical in form to the s-polarized field of a magnetic dipole $(\hat{\mathbf{e}}_p^{\pm}/k_z)\cdot\mathbf{m}$. Analogously, the s-polarized field of an electric dipole is given by $(\hat{\mathbf{e}}_s/k_z)\cdot\mathbf{p}$ while the p-polarized field of a magnetic dipole reads $(\hat{\mathbf{e}}_s/k_z)\cdot\mathbf{m}$. Therefore, the simple operations $\left[(\hat{\mathbf{e}}_p^{\pm}/k_z)\cdot\right]$ and $[(\hat{\mathbf{e}}_s/k_z)\cdot]$ acting on electric and magnetic dipole moments provide all the information about their near-field and far-field directionality.

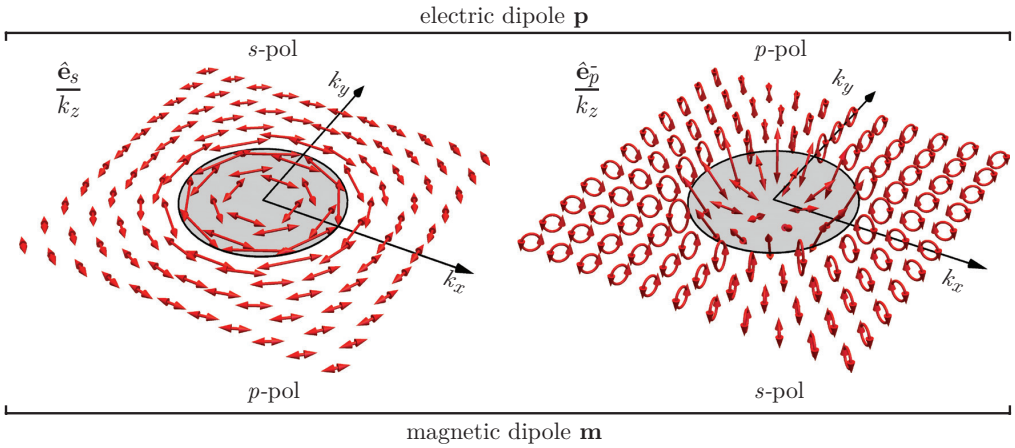

Figure 2: Electric field polarization associated to $(\hat{\mathbf{e}}_s/k_z)$ and $(\hat{\mathbf{e}}_p^{-}/k_z)$ as function of k_x and k_y. The shaded areas correspond to the propagating components $k_x^2+k_y^2<k^2$. The polarization ellipse associated with a complex vector $\mathbf{v}$ is computed as the parametric curve defined by $\mathrm{Re}(\mathbf{v}e^{-i\omega t})$. While $\hat{\mathbf{e}}_s$ is associated with linear polarization for any value of k_x and k_y, and does not give rise to any directionality, $\hat{\mathbf{e}}_p^{\pm}$ is associated with elliptical polarization for the evanescent components ($|k_t|>k$) and linear polarization for propagating components ($|k_t|<k$).

In Fig. 2, we plot the polarization ellipse associated with the complex vectors $(\hat{\mathbf{e}}_s/k_z)$ and $(\hat{\mathbf{e}}_p^{-}/k_z)$ as functions of k_x and k_y. The figure provides a simple guideline for the design of dipole directionality at a glance. It also unifies the spectra of electric and magnetic dipoles, highlighting that they have identical directionality but

applied to different mode polarizations. Applying the dot product between these vectors and the dipole moments $\mathbf{p}$ or $\mathbf{m}$, following Eqs. (3) and (4), we obtain the p-polarized and s-polarized components of the electric and magnetic dipoles. The dot product between two complex vectors $\mathbf{u} \cdot \mathbf{v}$ is maximum when $\mathbf{u} \propto \mathbf{v}^*$, as derived by Schwarz's inequality. Therefore it is possible to engineer the dipole moment $\mathbf{p}$ or $\mathbf{m}$ to maximize (minimize) its angular spectrum components at a specific transverse wave-vector (k_x, k_y), simply by maximizing (minimizing) its scalar product with the unit vector $(\hat{\mathbf{e}}_p^{\pm}/k_z)$.

The spectra of a circularly polarized dipole is shown in Fig. 3, calculated by applying the $\left[(\hat{\mathbf{e}}_p^{-}/k_z)\cdot\right]$ and $[(\hat{\mathbf{e}}_s/k_z)\cdot]$ operations to the dipole vector $\mathbf{p}$ or $\mathbf{m} = (1, 0, i)$, respectively. When $k_t \to \infty$, $(\hat{\mathbf{e}}_p^{\pm}/k_z)$ approaches circular polarization, which in turn means that the circularly polarized dipole will maximize the scalar product along one direction while simultaneously minimizing it along the exactly opposite one. This happens only for the p-polarized fields of an electric dipole or the s-polarized fields of a magnetic one (*i.e.* the terms that involve $\hat{\mathbf{e}}_p^{\pm}$). No directionality can be observed in the other terms, (*i.e.* those that involve $\hat{\mathbf{e}}_s$) which is true in general because the vector $(\hat{\mathbf{e}}_p^{\pm}/k_z)$ changes under the inversion $(k_x, k_y) \to (-k_x, -k_y)$ while the vector $(\hat{\mathbf{e}}_s/k_z)$ does not, except for a global phase factor. Therefore this inversion does not affect the polarization associated with $\hat{\mathbf{e}}_s$, indeed modifying the one associated with $\hat{\mathbf{e}}_p^{\pm}$

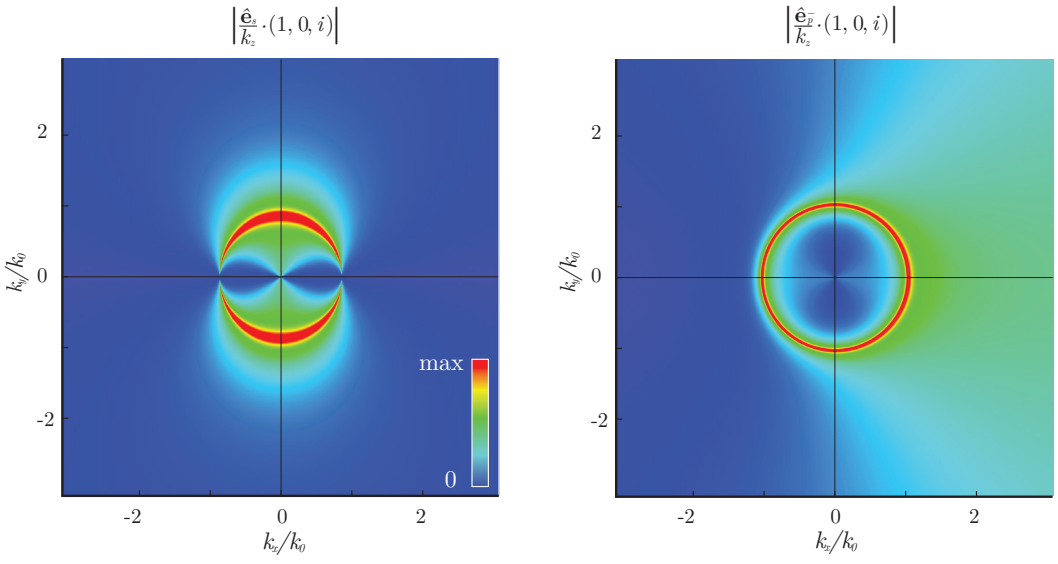

Figure 3: Angular spectrum of $s-$ and $p-$ polarized components of the electric field on the plane (k_x, k_y) generated by a circularly polarized dipole $\mathbf{p} = [1, 0, i]$.

We would like to emphasize that all the discussion above relates only to the angular components of the dipole itself, in a homogeneous medium, with no mention being made to nearby surfaces or waveguides. Yet, when a dipole is placed in close proximity of a surface, it is clear that, due to the conservation of transverse momentum, the probability of excitation of the waveguide modes will necessarily be proportional to the amplitude of the angular spectrum of the dipole at the specific (k_x, k_y) of each waveguide mode [1], weighted by the corresponding Fresnel reflection coefficients containing information about the s-polarized and p-polarized modes existing at the surface. The precise mathematical formulation of this is given in Appendix 4. This means that when a dipole displaying a strongly asymmetric spectrum in its evanescent components (such as that in Fig. 3) is placed in near-field proximity to a surface or planar waveguide, unidirectional excitation of guided modes will take place. This conclusion is reached independently of the field structure of the guided modes. A similar argument can be made in a non-planar waveguide in which only one direction of space is translationally invariant, such as an optical fiber. In that case, only one wave-vector component (along the waveguide direction, e.g., k_x) is conserved, but we can use similar logic as above, to conclude that directional excitation will take place due to the asymmetry of the spectrum in k_x. An example of this can be seen in fig. 4, where a waveguide with a non-analytical cross section is directionally excited by a circular dipole.
One of the advantages of knowing the angular spectrum is the possibility to calculate the fields at every point of space by integrating the expressions above, added with the reflected counterparts given in Appendix 4. As an example, in Fig. 5 we show the electric field, magnetic field and time-averaged Poynting vector for a circular electric dipole placed in close proximity to a metallic surface supporting surface plasmon polariton modes. An animated version is provided as Supplementary Movie M1.

Far-field and near-field directionality

The asymmetry in the evanescent angular spectrum components of circular dipoles ($|k_x| > k$) is in strong contrast with the symmetry of the propagating angular spectrum components ($|k_x| < k$). In fact, circular dipole antennas are commonly used in radio-frequency to avoid directional emission, not presenting any preferred radiation direction in the plane of the dipole. The sharp contrast in the behaviour

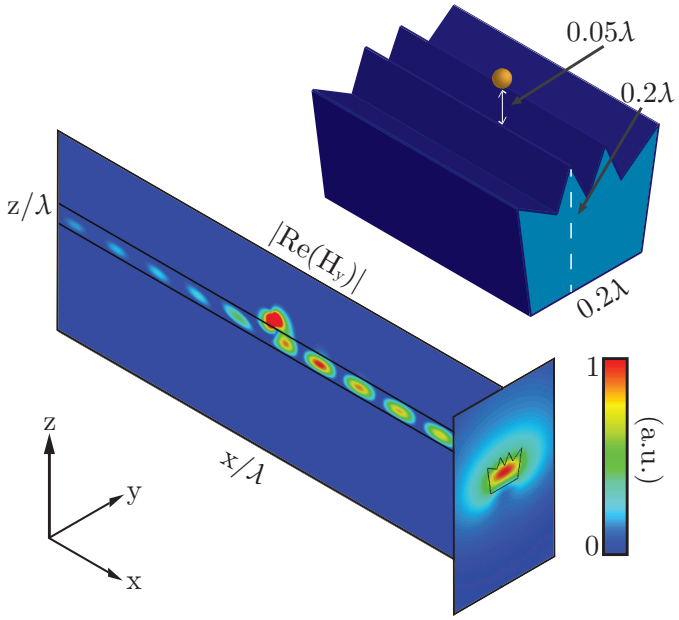

Figure 4: Directional excitation of guided modes in a non-planar waveguide with a non analytically solvable cross-section. The refractive index of the waveguide is $n = 3$ and the surrounding medium is air. A circular dipole $\mathbf{p} = [1, 0, i]$ is placed between the central crests of the waveguide, and the smallest distance between the dipole and the waveguide is 0.05λ

between the evanescent and propagating components can be explained by simple superposition arguments.

In Fig. 6 we plot the $p(s)$-polarized angular spectra of electric (magnetic) dipoles along k_x, assuming $k_y = 0$. This corresponds to the term responsible for unidirectionality, given by $[\hat{\mathbf{e}}_p^-(k_x, k_y = 0)/k_z] \cdot \mathbf{p} = (1/k)(-1, 0, -k_x/k_z) \cdot (p_x, p_y, p_z)$. We can easily see that the angular spectrum of a vertical dipole is an odd function of k_x [Fig. 6(a)], while that of a horizontal dipole is even [Fig. 6(b)]. The superposition of both components can therefore be a strongly asymmetric function of k_x. However, the superposition gives completely different results depending on the phase difference between the two of them. For instance, in a diagonal linearly polarized dipole $\mathbf{p} = (1, 0, 1)$ the evanescent angular frequency spectrum components ($|k_x| > k$) have the same amplitude in both directions ($\pm k_x$). On the other hand, a circularly polarized dipole as discussed above introduces a $\pi/2$ phase between the two components, $\mathbf{p} = (1, 0, i)$, and the resulting evanescent angular frequency spectrum ($|k_x| > k$) is highly non-symmetric, accounting for circular dipole directionality [Fig. 6(c)]. It should be noticed that the exact opposite behaviour takes place for the propagating components ($|k_x| < k$), where the spectrum of the circular dipole has a symmetric

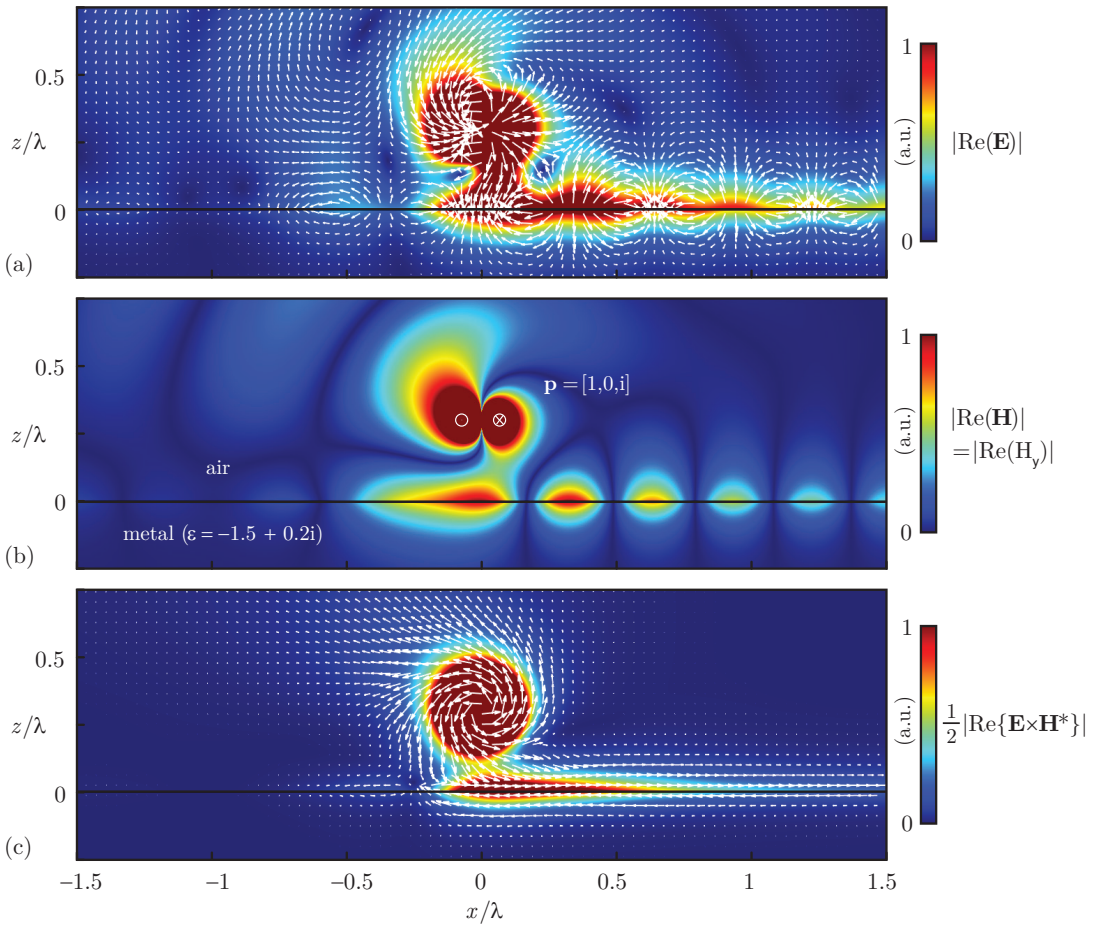

Figure 5: (a,b) Electromagnetic field and (c) power flow induced by a circularly polarized electric (magnetic) dipole in close proximity to an interface of a material with $\varepsilon = -1.5+0.2i$ and $\mu = 1$ ($\mu = -1.5+0.2i$ and $\varepsilon = 1$), calculated by integration of the angular spectra of the dipole field given by Eq.(3) added to the reflected fields given by equations (2.7). Colormap represents amplitude, and white arrows represent direction of (a) instantaneous electric (magnetic) field, (b) instantaneous magnetic (electric) field, and (c) time-averaged Poynting vector. Snapshot from Supplementary Movie M1 [46].

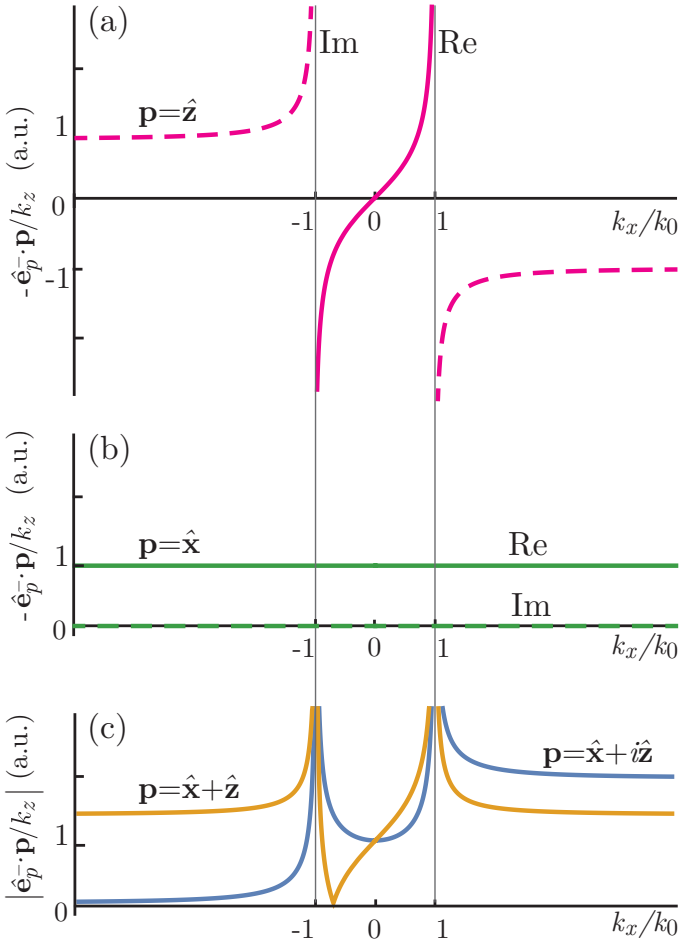

Figure 6: Angular spectra along k_x ($k_y = 0$) of (a) vertically polarized, (b) horizontally polarized, (c) diagonally polarized (yellow) and circularly polarized (blue) dipoles. In panel (c) the absolute values of the angular spectra are plotted. Note that the spectra plotted represent the amplitude density per unit k_x/k_0. To obtain the radiation diagram it should be converted to amplitude density per unit angle, using the relation: $dk_x = k_0 \cos\theta d\theta$.

amplitude in k_x while that of a linear dipole is strongly asymmetric (corresponding to the radiation diagrams of circular and linear dipoles).

The different behaviour in the spectra of evanescent and propagating components of a dipole intuitively allows for a complete understanding of the reason why directionality of circularly polarized dipoles is observed only when the waveguide is placed in a region of near fields, where the evanescent components are non-negligible. In fact, the directionality is a property belonging only to the evanescent part of the dipole angular spectrum and can therefore be observed when the evanescent components are coupled to a waveguide mode. Further evidence of directionality of the dipole near fields can be seen in the time-averaged Poynting vector of a circularly polarized electric dipole (Fig. 5(c)). We can see that the energy flow is circulating around the dipole in its near field region, in the same sense as the dipole rotation, intuitively explaining why surface waves will be excited directionally in the nearby plasmonic surface. In contrast, the Poynting vector becomes radial in the far field of the dipole.

CONCLUSIONS

We compared two different descriptions of the phenomenon of directional excitation of guided modes driven by electric and magnetic dipoles. The two explanations look profoundly different in nature, because the first one depends explicitly on the waveguide mode field structure, while the second one depends only on the dipole fields and on momentum conservation. The second description has the advantage of showing explicitly that the circularly polarized dipole directionality is a universal phenomenon, in the sense that the same dipole can unidirectionally excite any waveguide mode with the appropriate wave-vector, as directionality is determined by the dipole itself. Both considered approaches lead to identical results. The reason behind this equivalence lies in the fact that, as shown in equations (2), for guided modes the field structure can be completely described once its wavevector has been specified and, vice versa, given the field structure, the associated wave-vector is completely determined. While the mode-coupling explanation focuses on how the field vector structure of the modes matches with the field of the dipole, the angular spectrum explanation focuses on how the wave-vector of the modes matches those of the dipole. Ultimately, the two explanations of the phenomenon are formally equivalent. Other explanations of the effect have been proposed considering

quantum spin Hall effect as intrinsic properties of the Maxwell's equations [38]. Controlling directionality exclusively with light polarization allows ultra-high speed modulation and switching of light, with broadband behaviour, opening new avenues for light nano-routing based on a very fundamental concept that works in a variety of platforms ranging from microwaves to nanophotonics and plasmonics. Dipole directionality also provides a method for readout of quantum spin states mapped into photons propagating on different directions. The knowledge of the angular spectrum of dipoles in the form presented here greatly helps in understanding their directionality properties and provides a simple recipe for engineering the required electric or magnetic dipole moments to achieve directional excitation of any mode in planar waveguides by simply knowing the dispersion of the mode and its polarization (s- or p-). By including the magnetic dipole in our analysis, we enable the analytical design of applications requiring directional excitation of s-polarized modes. The simultaneous excitation of electric and magnetic dipoles in a single particle is known to enable remarkable directionality properties such as reduced backscattering, and can be experimentally achieved in particles with overlapping electric and magnetic resonances using high index dielectric particles [47–50]. Our compact notation allows the straightforward calculation of the angular spectrum in both propagating and evanescent components of simultaneous electric and magnetic dipoles with arbitrary polarizations.

ACKNOWLEDGMENTS

This work was supported by European Research Council project ERC-2016-STG-714151-PSINFONI and EPSRC (UK). A.M. acknowledges financial support from the Department of Physics and Astronomy and the College of Arts and Sciences of the University of New Mexico. A.Z. acknowledges support from the Royal Society and the Wolfson Foundation. All data supporting this research are provided in full in the results section and Appendices.

APPENDIX A: POLARIZATION VECTOR BASIS

For our calculations we always use vectors $\hat{\mathbf{e}}_s(k_x, k_y)$ and $\hat{\mathbf{e}}_p^{\pm}(k_x, k_y)$ as our basis [39]. These vectors are related to the electric field polarization in s-polarized and p-polarized fields, respectively, and can be defined as:

$$\begin{aligned}\hat{\mathbf{e}}_s &= \frac{\hat{\mathbf{z}} \times \mathbf{k}^{\pm}}{\sqrt{(\hat{\mathbf{z}} \times \mathbf{k}^{\pm}) \cdot (\hat{\mathbf{z}} \times \mathbf{k}^{\pm})}} \\ &= (-\sin\phi, \cos\phi, 0) \\ &= \frac{1}{\sqrt{k_x^2 + k_y^2}}(-k_y\hat{\mathbf{x}} + k_x\hat{\mathbf{y}}),\end{aligned} \tag{A1}$$

$$\begin{aligned}\hat{\mathbf{e}}_p^{\pm} &= \hat{\mathbf{e}}_s \times \frac{\mathbf{k}^{\pm}}{k} \\ &= (\pm\cos\theta\cos\phi, \pm\cos\theta\sin\phi, -\sin\theta) \\ &= \frac{1}{k\sqrt{k_x^2 + k_y^2}}[\pm k_x k_z\hat{\mathbf{x}} \pm k_y k_z\hat{\mathbf{y}} - (k_x^2 + k_y^2)\hat{\mathbf{z}}].\end{aligned} \tag{A2}$$

where k is the wavenumber of the medium, $\mathbf{k}^{\pm} = (k_x, k_y, \pm k_z)$ is the wavevector with the $\pm$ accounting for fields calculated above or below $z = z_0$ respectively, and $\hat{\mathbf{z}}$ is the unit vector normal to the plane in which we choose to expand the angular spectrum. Importantly, these vectors are valid for both near-field evanescent waves $|k_t| > k$ and far-field propagating waves $|k_t| < k$. In the propagating lossless case, $\mathbf{k}^{\pm}$ is purely real and its magnitude is $|\mathbf{k}^{\pm}|^2 = k^2$, so following the definition in Eqs.(A1,A2), vectors $\hat{\mathbf{e}}_s$ and $\hat{\mathbf{e}}_p^{\pm}$ are purely real unit vectors forming an orthonormal basis, as pictured in Fig. A1.

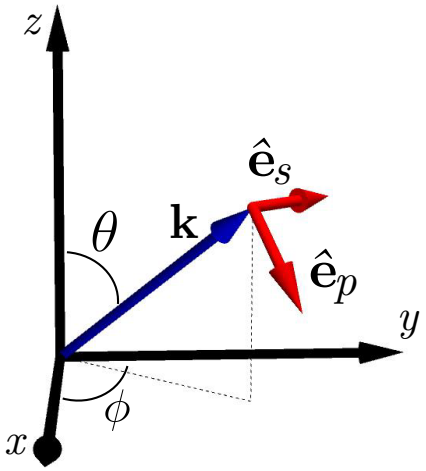

Figure A1: Coordinate system and polarization basis used.

In the evanescent case, $\mathbf{k}^{\pm}$ becomes complex, and $|\mathbf{k}^{\pm}|^2 = \mathbf{k}^{\pm} \cdot \mathbf{k}^{\pm *} > k^2$, which translates into the vector $\hat{\mathbf{e}}_p^{\pm}$ becoming complex and no longer having unit magnitude. However, equation $\mathbf{k}^{\pm} \cdot \mathbf{k}^{\pm} = k_x^2 + k_y^2 + k_z^2 = k^2$ always holds [5, 39], and so $\hat{\mathbf{e}}_s$ and

$\hat{\mathbf{e}}_p^{\pm}$ are still an "orthonormal basis" in the special sense that $\hat{\mathbf{e}}_s \cdot \hat{\mathbf{e}}_s = \hat{\mathbf{e}}_p^{\pm} \cdot \hat{\mathbf{e}}_p^{\pm} = 1$, and $\hat{\mathbf{e}}_s \cdot \hat{\mathbf{e}}_p^{\pm} = 0$, with no complex conjugation. This means that we can always use $\hat{\mathbf{e}}_s$ and $\hat{\mathbf{e}}_p^{\pm}$ as a valid geometrical orthonormal basis, as long as we remember that, if $\mathbf{f} = a\hat{\mathbf{e}}_s + b\hat{\mathbf{e}}_p^{\pm}$ then $a = \mathbf{f} \cdot \hat{\mathbf{e}}_s$ and $b = \mathbf{f} \cdot \hat{\mathbf{e}}_p^{\pm}$, with no complex conjugation. Also notice the simple relations $\hat{\mathbf{e}}_p^{\pm} \times \hat{\mathbf{e}}_s = (\mathbf{k}^{\pm}/k)$, $(\mathbf{k}^{\pm}/k) \times \hat{\mathbf{e}}_p^{\pm} = \hat{\mathbf{e}}_s$ and $(\mathbf{k}^{\pm}/k) \times \hat{\mathbf{e}}_s = -\hat{\mathbf{e}}_p^{\pm}$. From these relations and the requirement $\mathbf{H} = \frac{1}{\eta}\left[\frac{\mathbf{k}^{\pm}}{k} \times \mathbf{E}\right]$ derived from Maxwell's equations for plane waves it follows that any electric field $\mathbf{E} = \left[A\hat{\mathbf{e}}_s + B\hat{\mathbf{e}}_p^{\pm}\right] e^{i\mathbf{k}^{\pm}\cdot\mathbf{r}}$ is associated with a magnetic field $\mathbf{H} = \left[\frac{B}{\eta}\hat{\mathbf{e}}_s - \frac{A}{\eta}\hat{\mathbf{e}}_p^{\pm}\right] e^{i\mathbf{k}^{\pm}\cdot\mathbf{r}}$ with $\eta = (\mu/\varepsilon)^{1/2}$. This mathematical relation always holds and can be generalized to evanescent waves.

APPENDIX B: THE ANGULAR SPECTRUM OF AN ELECTRIC DIPOLE

An electric dipole, in the time harmonic case, can be described in terms of a dipole moment $\mathbf{p}$, associated to an electric current density $\mathbf{J} = -i\omega\delta^3(\mathbf{r} - \mathbf{r_0})\mathbf{p}$, where we assume a $e^{-i\omega t}$ time dependence. The electric and magnetic fields generated by this dipole in a homogeneous medium can be written as [51]:

$$\mathbf{E}^{\mathrm{ED}} = k^2\pi + \boldsymbol{\nabla}(\boldsymbol{\nabla} \cdot \boldsymbol{\pi}), \tag{B1}$$

$$\mathbf{H}^{\mathrm{ED}} = -i\omega\varepsilon\boldsymbol{\nabla} \times \boldsymbol{\pi}, \tag{B2}$$

with k being the wavenumber of the medium and π being a vector potential, often referred to as the Hertz potential [51], which can be calculated as the product of $\mathbf{p}$ and the scalar Green function for the Helmholtz operator [43]:

$$\boldsymbol{\pi} = \frac{\mathbf{p}}{4\pi\varepsilon}\frac{e^{ik|\mathbf{r}-\mathbf{r_0}|}}{|\mathbf{r} - \mathbf{r_0}|}.$$

Using the well known Weyl's identity [52]:

$$\frac{e^{i\mathbf{k}\cdot\mathbf{r}}}{|\mathbf{r}|} = \frac{i}{2\pi}\iint \frac{1}{k_z} e^{i(k_x x + k_y y)} e^{ik_z|z|} dk_x dk_y,$$

assuming that the electric dipole (ED) is located in the z- axis, $\mathbf{r}_0 = z_0\hat{\mathbf{z}}$, we can write $\boldsymbol{\pi}$ as:

$$\boldsymbol{\pi} = \frac{i}{8\pi^2\varepsilon}\iint \frac{\mathbf{p}}{k_z} e^{i(k_x x + k_y y)} e^{ik_z|z-z_0|} dk_x dk_y. \tag{B3}$$

By applying eqs (B1) and (B2) to (B3) (note that this is equivalent to the substitution $\boldsymbol{\nabla} \rightarrow i\mathbf{k}^{\pm}$), the electric field $\mathbf{E}^{\mathrm{ED}}$ and the magnetic field $\mathbf{H}^{\mathrm{ED}}$ can be written as [44]:

$$\mathbf{E}^{\mathrm{ED}} = \frac{i}{8\pi^2\varepsilon} \iint \frac{1}{k_z} e^{i(k_x x + k_y y)} e^{ik_z|z-z_0|} \mathbf{g}_E dk_x dk_y,$$
$$\mathbf{H}^{\mathrm{ED}} = \frac{i\omega}{8\pi^2} \iint \frac{1}{k_z} e^{i(k_x x + k_y y)} e^{ik_z|z-z_0|} \mathbf{g}_H dk_x dk_y,$$

where $\mathbf{g}_E$ and $\mathbf{g}_H$ are given by:

$$\mathbf{g}_E = k^2\mathbf{p} - \mathbf{k}^{\pm}(\mathbf{k}^{\pm} \cdot \mathbf{p}),$$
$$\mathbf{g}_H = \mathbf{k}^{\pm} \times \mathbf{p},$$

with $\mathbf{k}^{\pm}$ being

$$\mathbf{k}^{+} = (k_x, k_y, k_z) \qquad \text{when } z > z_0$$
$$\mathbf{k}^{-} = (k_x, k_y, -k_z) \qquad \text{when } z < z_0.$$

Following Ref.[44], we can then project the function $\mathbf{g}_E(k_x, k_y)$ along the two directions $\hat{\mathbf{e}}_s$ and $\hat{\mathbf{e}}_p^{\pm}$ relative to the s and p polarizations (see Appendix 1):

$$\mathbf{g}_E = \gamma_s \hat{\mathbf{e}}_s + \gamma_p^{\pm} \hat{\mathbf{e}}_p^{\pm},$$

Therefore:

$$\begin{aligned}
\gamma_s &= \mathbf{g}_E \cdot \hat{\mathbf{e}}_s \\
&= [k^2\mathbf{p} - (\mathbf{p} \cdot \mathbf{k}^{\pm})\mathbf{k}^{\pm}] \cdot \frac{1}{\sqrt{k_x^2 + k_y^2}}(-k_y\hat{\mathbf{x}} + k_x\hat{\mathbf{y}}) \\
&= \frac{k^2}{\sqrt{k_x^2 + k_y^2}}(-k_y p_x + k_x p_y) = k^2 \hat{\mathbf{e}}_s \cdot \mathbf{p},
\end{aligned}$$

$$\begin{aligned}\gamma_p^{\pm} &= \mathbf{g}_E \cdot \hat{\mathbf{e}}_p^{\pm} = \\ &= [k^2\mathbf{p} - (\mathbf{p}\cdot\mathbf{k}^{\pm})\mathbf{k}^{\pm}]\cdot \\ &\frac{1}{k\sqrt{k_x^2+k_y^2}}(\pm k_x k_z\hat{\mathbf{x}} \pm k_y k_z\hat{\mathbf{y}} - (k_x^2+k_y^2)\hat{\mathbf{z}}) = \\ &= \pm\frac{k_z k}{\sqrt{k_x^2+k_y^2}}(k_x p_x + k_y p_y) - k\sqrt{k_x^2+k_y^2}p_z = \\ &= k^2\hat{\mathbf{e}}_p^{\pm}\cdot\mathbf{p}.\end{aligned}$$

Analogously, we decompose $\mathbf{g}_H$ along the directions $\hat{\mathbf{e}}_s$ and $\hat{\mathbf{e}}_p^{\pm}$ and it can be easily checked that $\mathbf{g}_H \cdot \hat{\mathbf{e}}_s = \frac{\gamma_p^{\pm}}{k}$ and $\mathbf{g}_H \cdot \hat{\mathbf{e}}_p^{\pm} = -\frac{\gamma_s}{k}$ so that we can write:

$$\mathbf{g}_H = \frac{\gamma_p^{\pm}}{k}\hat{\mathbf{e}}_s - \frac{\gamma_s}{k}\hat{\mathbf{e}}_p^{\pm}.$$

With all of the above we have all the ingredients required to compose the angular spectrum of the dipole field, defined as [43]:

$$\begin{aligned}\mathbf{E}^{\mathrm{ED}}(x,y,z) = \iint \mathbf{E}^{\mathrm{ED}}(k_x,k_y)|_{z=z_0}\times \\ \times e^{i(k_x x + k_y y + k_z|z-z_0|)}dk_x dk_y,\end{aligned}$$

which can be further decomposed into p- and s-polarizations:

$$\mathbf{E}^{\mathrm{ED}}(k_x,k_y)|_{z=z_0} = \mathbf{E}_p^{\mathrm{ED}}(k_x,k_y)|_{z=z_0} + \mathbf{E}_s^{\mathrm{ED}}(k_x,k_y)|_{z=z_0},$$

and identically for the magnetic field. Putting all together, the p-polarized fields of the electric dipole are given by:

$$\mathbf{E}_p^{\mathrm{ED}}(k_x,k_y)|_{z=z_0} = \frac{i}{8\pi^2\varepsilon}k\left[\pm\frac{1}{\sqrt{k_x^2+k_y^2}}(k_x p_x + k_y p_y) - \frac{1}{k_z}\sqrt{k_x^2+k_y^2}p_z\right]\hat{\mathbf{e}}_p^{\pm},$$

$$\mathbf{H}_p^{\mathrm{ED}}(k_x,k_y)|_{z=z_0} = \frac{i\omega}{8\pi^2}\left[\pm\frac{1}{\sqrt{k_x^2+k_y^2}}(k_x p_x + k_y p_y) - \frac{1}{k_z}\sqrt{k_x^2+k_y^2}p_z\right]\hat{\mathbf{e}}_s,$$

while the s-polarized fields are:

$$\mathbf{E}_s^{\mathrm{ED}}(k_x,k_y)|_{z=z_0}=\frac{i}{8\pi^2\varepsilon}k\left[\frac{k}{k_z\sqrt{k_x^2+k_y^2}}(-k_yp_x+k_xp_y)\right]\hat{\mathbf{e}}_s,$$

$$\mathbf{H}_s^{\mathrm{ED}}(k_x,k_y)|_{z=z_0}=-\frac{i\omega}{8\pi^2}\left[\frac{k}{k_z\sqrt{k_x^2+k_y^2}}(-k_yp_x+k_xp_y)\right]\hat{\mathbf{e}}_p^{\pm}.$$

This can be written in a compact notation as:

$$\begin{aligned}\mathbf{E}^{\mathrm{ED}}(k_x,k_y)|_{z=z_0}&=\frac{i}{8\pi^2\varepsilon}\frac{k^2}{k_z}\left[(\hat{\mathbf{e}}_s\cdot\mathbf{p})\hat{\mathbf{e}}_s+(\hat{\mathbf{e}}_p^{\pm}\cdot\mathbf{p})\hat{\mathbf{e}}_p^{\pm}\right],\\ \mathbf{H}^{\mathrm{ED}}(k_x,k_y)|_{z=z_0}&=\frac{i\omega}{8\pi^2}\frac{k}{k_z}\left[(\hat{\mathbf{e}}_p^{\pm}\cdot\mathbf{p})\hat{\mathbf{e}}_s-(\hat{\mathbf{e}}_s\cdot\mathbf{p})\hat{\mathbf{e}}_p^{\pm}\right].\end{aligned}$$

APPENDIX C: THE ANGULAR SPECTRUM OF A MAGNETIC DIPOLE

A magnetic dipole can be described, in the time-harmonic case ($e^{-i\omega t}$ time dependence), in terms of a magnetic dipole moment $\mathbf{m}$, associated to a magnetic current density $\mathbf{J_m}=-i\omega\mu\delta^3(\mathbf{r}-\mathbf{r_0})\mathbf{m}$. The electric and magnetic fields generated by this dipole in a homogeneous medium are given by expressions analogous to eqs. (B1) and (B2) applied to the magnetic dipole case [51]:

$$\begin{aligned}\mathbf{H}^{\mathrm{MD}}&=\boldsymbol{\nabla}(\boldsymbol{\nabla}\cdot\boldsymbol{\pi}_m)+k^2\boldsymbol{\pi}_m,\\ \mathbf{E}^{\mathrm{MD}}&=i\omega\mu\boldsymbol{\nabla}\times\boldsymbol{\pi}_m,\end{aligned}$$

where this time $\boldsymbol{\pi}_m$ is the magnetic Hertz potential [51] and it can be calculated to be:

$$\boldsymbol{\pi}_m=\mathbf{m}\frac{e^{ik|\mathbf{r}-\mathbf{r_0}|}}{4\pi|\mathbf{r}-\mathbf{r_0}|}.$$

Proceeding as with the electric dipole, the magnetic field $\mathbf{H}^{\mathrm{MD}}$ and the electric field $\mathbf{E}^{\mathrm{MD}}$ can then be written as:

$$\mathbf{H}^{\mathrm{MD}} = \frac{i}{8\pi^2}\iint \frac{1}{k_z} e^{i(k_x x + k_y y)} e^{ik_z|z-z_0|}\mathbf{f}_H dk_x dk_y,$$
$$\mathbf{E}^{\mathrm{MD}} = -\frac{i\omega\mu}{8\pi^2}\iint \frac{1}{k_z} e^{i(k_x x + k_y y)} e^{ik_z|z-z_0|}\mathbf{f}_E dk_x dk_y,$$

where:

$$\mathbf{f}_H = k^2\mathbf{m} - \mathbf{k}^{\pm}(\mathbf{k}^{\pm}\cdot\mathbf{m}),$$
$$\mathbf{f}_E = \mathbf{k}^{\pm}\times\mathbf{m},$$

with the same definition for $\mathbf{k}^{\pm}$ as given before. In the same manner as for the electric dipole, we can then project the functions $\mathbf{f}_E$ and $\mathbf{f}_H$ along the two directions relative to the s and p polarizations so that they can be expressed as:

$$\mathbf{f}_E = \nu_s^{\pm}\hat{\mathbf{e}}_s + \nu_p\hat{\mathbf{e}}_p^{\pm},$$
$$\mathbf{f}_H = k\nu_p\hat{\mathbf{e}}_s - k\nu_s^{\pm}\hat{\mathbf{e}}_p^{\pm},$$

where:

$$\nu_s^{\pm} = \mathbf{f}_E\cdot\hat{\mathbf{e}}_s = \pm\frac{(k_x m_x + k_y m_y)k_z}{\sqrt{k_x^2+k_y^2}} - \sqrt{k_x^2+k_y^2}\,m_z,$$
$$\nu_p = \mathbf{f}_E\cdot\hat{\mathbf{e}}_p^{\pm} = \frac{k}{\sqrt{k_x^2+k_y^2}}(k_y m_x - k_x m_y).$$

The s-polarized fields of the magnetic dipole are then given by:

$$\mathbf{H}_s^{\mathrm{MD}}(k_x,k_y)|_{z=z_0} = \frac{i}{8\pi^2}k\left[\pm\frac{1}{\sqrt{k_x^2+k_y^2}}(k_x m_x + k_y m_y) - \frac{1}{k_z}\sqrt{k_x^2+k_y^2}\,m_z\right]\hat{\mathbf{e}}_p^{\pm},$$
$$\mathbf{E}_s^{\mathrm{MD}}(k_x,k_y)|_{z=z_0} = -\frac{i\omega\mu}{8\pi^2}\left[\pm\frac{1}{\sqrt{k_x^2+k_y^2}}(k_x m_x + k_y m_y) - \frac{1}{k_z}\sqrt{k_x^2+k_y^2}\,m_z\right]\hat{\mathbf{e}}_s,$$

and the p-polarized fields are given by:

$$\mathbf{H}_p^{\mathrm{MD}}(k_x,k_y)|_{z=z_0} = -\frac{i}{8\pi^2}k\left[\frac{k}{k_z\sqrt{k_x^2+k_y^2}}(-k_y m_x + k_x m_y)\right]\hat{\mathbf{e}}_s,$$
$$\mathbf{E}_p^{\mathrm{MD}}(k_x,k_y)|_{z=z_0} = \frac{i\omega\mu}{8\pi^2}\left[\frac{k}{k_z\sqrt{k_x^2+k_y^2}}(-k_y m_x + k_x m_y)\right]\hat{\mathbf{e}}_p^{\pm}.$$

Notice that this can be written as:

$$\mathbf{E}^{\mathrm{MD}}(k_x,k_y)|_{z=z_0} = \frac{i}{8\pi^2\varepsilon}\frac{k^2}{k_z}\frac{1}{c}\left[-(\hat{\mathbf{e}}_p^{\pm}\cdot\mathbf{m})\hat{\mathbf{e}}_s + (\hat{\mathbf{e}}_s\cdot\mathbf{m})\hat{\mathbf{e}}_p^{\pm}\right],$$

$$\mathbf{H}^{\mathrm{MD}}(k_x,k_y)|_{z=z_0} = \frac{i\omega}{8\pi^2}\frac{k}{k_z}\frac{1}{c}\left[(\hat{\mathbf{e}}_p^{\pm}\cdot\mathbf{m})\hat{\mathbf{e}}_p^{\pm} + (\hat{\mathbf{e}}_s\cdot\mathbf{m})\hat{\mathbf{e}}_s\right].$$

As expected [51], going from the electric dipole to the magnetic one we obtain the same result that we would obtain simply performing the following substitutions:

- $\varepsilon \to \mu$,
- $\mathbf{p} \to \mu\mathbf{m}$,
- $\mathbf{H} \to -\mathbf{E}$,
- $\mathbf{E} \to \mathbf{H}$.

APPENDIX D: REFLECTED FIELDS

The fields reflected from a surface can be easily calculated starting from the fields radiated by the dipole in a homogeneous medium. In fact, retrieving the reflected fields once the angular spectrum has been determined only requires the knowledge of Fresnel's reflection coefficients $r_s(\omega,k_x,k_y)$ and $r_p(\omega,k_x,k_y)$, characteristic of the specific reflective material or layered media. The reflected electric and magnetic fields, both of electric and magnetic dipole, can therefore be written as:

$$\mathbf{E}^{\mathrm{ED}}_{\mathrm{ref}}(k_x,k_y,z) = \frac{i}{8\pi^2\varepsilon}\frac{k^2}{k_z}\left[r_s(\hat{\mathbf{e}}_s\cdot\mathbf{p})\hat{\mathbf{e}}_s + r_p(\hat{\mathbf{e}}_p^-\cdot\mathbf{p})\hat{\mathbf{e}}_p^+\right]e^{ik_z(z+z_0)},$$
$$\mathbf{H}^{\mathrm{ED}}_{\mathrm{ref}}(k_x,k_y,z) = \frac{i\omega}{8\pi^2}\frac{k}{k_z}\left[r_p(\hat{\mathbf{e}}_p^-\cdot\mathbf{p})\hat{\mathbf{e}}_s - r_s(\hat{\mathbf{e}}_s\cdot\mathbf{p})\hat{\mathbf{e}}_p^+\right]e^{ik_z(z+z_0)},$$
$$\mathbf{E}^{\mathrm{MD}}_{\mathrm{ref}}(k_x,k_y,z) = \frac{i}{8\pi^2\varepsilon}\frac{k^2}{k_z}\frac{1}{c}\left[-r_s(\hat{\mathbf{e}}_p^-\cdot\mathbf{m})\hat{\mathbf{e}}_s + r_p(\hat{\mathbf{e}}_s\cdot\mathbf{m})\hat{\mathbf{e}}_p^+\right]e^{ik_z(z+z_0)},$$
$$\mathbf{H}^{\mathrm{MD}}_{\mathrm{ref}}(k_x,k_y,z) = \frac{i\omega}{8\pi^2}\frac{k}{k_z}\frac{1}{c}\left[r_p(\hat{\mathbf{e}}_s\cdot\mathbf{m})\hat{\mathbf{e}}_s + r_s(\hat{\mathbf{e}}_p^-\cdot\mathbf{m})\hat{\mathbf{e}}_p^+\right]e^{ik_z(z+z_0)}. \tag{D1}$$

If the surface or layered media is rotationally symmetric around z, the reflection coefficients will have the same symmetry. They will depend only on k_t, independent of the angle, and therefore the directionality of the fields reflected by the surface (which includes any excited guided modes) will not be affected by the surface. The directionality will be entirely determined by that of the dipole in the homogeneous medium. It is worth noticing that these expressions are mathematically general and allow using any Fresnel reflection coefficients. In particular, no assumption is made on the value of frequency ω radiated by the dipole, so we can consider the response to complex frequencies for which the guided modes can show interesting effects such as the no back-bending of surface plasmons [53, 54]. These properties are fully described via Fresnel's coefficient of the surface using a complex ω.

REFERENCES

1. Rodríguez-Fortuño, F. J. *et al.* Near-field interference for the unidirectional excitation of electromagnetic guided modes. *Science* **340.** doi:10.1126/science.1233739 (2013).
2. Kapitanova, P. V. *et al.* Photonic spin Hall effect in hyperbolic metamaterials for polarization-controlled routing of subwavelength modes. *Nature Communications* **5.** doi:10.1038/ncomms4226 (2014).
3. Aiello, A., Banzer, P., Neugebauer, M. & Leuchs, G. From transverse angular momentum to photonic wheels. *Nature Photonics* **9.** doi:10.1038/nphoton.2015.203 (2015).
4. Espinosa-Soria, A. & Martinez, A. Transverse Spin and Spin-Orbit Coupling in Silicon Waveguides. *IEEE Photonics Technology Letters* **28.** doi:10.1109/LPT.2016.2553841 (2016).
5. Van Mechelen, T. & Jacob, Z. Universal spin-momentum locking of evanescent waves. *Optica* **3.** doi:10.1364/OPTICA.3.000118 (2016).

6. Coles, R. J. *et al.* Chirality of nanophotonic waveguide with embedded quantum emitter for unidirectional spin transfer. *Nature Communications* **7.** doi:10.1038/ncomms11183 (2016).
7. Le Feber, B., Rotenberg, N. & Kuipers, L. Nanophotonic control of circular dipole emission. *Nature Communications* **6.** doi:10.1038/ncomms7695 (2015).
8. Luxmoore, I. J. *et al.* Interfacing Spins in an InGaAs Quantum Dot to a Semiconductor Waveguide Circuit Using Emitted Photons. *Physical Review Letters* **110.** doi:10.1103/PhysRevLett.110.037402 (2013).
9. Marrucci, L. Quantum optics: Spin gives direction. *Nature Physics* **11.** doi:10.1038/nphys3198 (2015).
10. Coles, R. J. *et al.* Waveguide-coupled photonic crystal cavity for quantum dot spin readout. *Optics Express* **22.** doi:10.1364/OE.22.002376 (2014).
11. Mitsch, R., Sayrin, C., Albrecht, B., Schneeweiss, P. & Rauschenbeutel, A. Quantum state-controlled directional spontaneous emission of photons into a nanophotonic waveguide. *Nature Communications* **5.** doi:10.1038/ncomms6713 (2014).
12. Young, A. B. *et al.* Polarization Engineering in Photonic Crystal Waveguides for Spin-Photon Entanglers. *Physical Review Letters* **115.** doi:10.1103/PhysRevLett.115.153901 (2015).
13. Lodahl, P. *et al. Chiral quantum optics* 2017. doi:10.1038/nature21037.
14. Petersen, J., Volz, J. & Rauschenbeutel, A. Chiral nanophotonic waveguide interface based on spin-orbit interaction of light. *Science* **346.** doi:10.1126/science.1257671 (2014).
15. O'Connor, D., Ginzburg, P., Rodríguez-Fortuño, F. J., Wurtz, G. A. & Zayats, A. V. Spin-orbit coupling in surface plasmon scattering by nanostructures. *Nature Communications* **5.** doi:10.1038/ncomms6327 (2014).
16. Neugebauer, M., Bauer, T., Banzer, P. & Leuchs, G. Polarization tailored light driven directional optical nanobeacon. *Nano letters* **14.** doi:10.1021/nl5003526 (2014).
17. Neugebauer, M., Bauer, T., Aiello, A. & Banzer, P. Measuring the Transverse Spin Density of Light. *Physical Review Letters* **114.** doi:10.1103/PhysRevLett.114.063901 (2015).
18. Bliokh, K. Y., Rodríguez-Fortuño, F. J., Nori, F. & Zayats, A. V. Spin-orbit interactions of light. *Nature Photonics* **9.** doi:10.1038/nphoton.2015.201 (2015).
19. Cardano, F. & Marrucci, L. Spin-orbit photonics. *Nature Photonics* **9.** doi:10.1038/nphoton.2015.232 (2015).
20. Marrucci, L. *et al.* Spin-to-orbital conversion of the angular momentum of light and its classical and quantum applications. *Journal of Optics* **13.** doi:10.1088/2040-8978/13/6/064001 (2011).

21. Yin, X., Ye, Z., Rho, J., Wang, Y. & Zhang, X. Photonic Spin Hall Effect at Metasurfaces. *Science* **339.** doi:10.1126/science.1231758 (2013).

22. Espinosa-Soria, A., Rodríguez-Fortuño, F. J., Griol, A. & Martínez, A. On-Chip Optimal Stokes Nanopolarimetry Based on Spin-Orbit Interaction of Light. *Nano Letters* **17.** doi:10.1021/acs.nanolett.7b00564 (2017).

23. Rodríguez-Fortuño, F. J. *et al.* Universal method for the synthesis of arbitrary polarization states radiated by a nanoantenna. *Laser & Photonics Reviews* **8.** doi:10.1002/lpor.201300184 (2014).

24. Rodríguez-Fortuño, F. J., Barber-Sanz, I., Puerto, D., Griol, A. & Martínez, A. Resolving Light Handedness with an on-Chip Silicon Microdisk. *ACS Photonics* **1.** doi:10.1021/ph500084b (2014).

25. Rodríguez-Fortuño, F. J. *et al.* Sorting linearly polarized photons with a single scatterer. *Optics Letters* **39.** doi:10.1364/OL.39.001394 (2014).

26. Wang, S. B. & Chan, C. T. Lateral optical force on chiral particles near a surface. *Nature communications* **5.** doi:10.1038/ncomms4307 (2014).

27. Hayat, A., Mueller, J. P. B. & Capasso, F. Lateral chirality-sorting optical forces. *Proceedings of the National Academy of Sciences.* doi:10.1073/pnas.1516704112 (2015).

28. Rodríguez-Fortuño, F. J., Engheta, N., Martínez, A. & Zayats, A. V. Lateral forces on circularly polarizable particles near a surface. *Nature Communications* **6.** doi:10.1038/ncomms9799 (2015).

29. Sukhov, S., Kajorndejnukul, V., Naraghi, R. R. & Dogariu, A. Dynamic consequences of optical spin-orbit interaction. *Nature Photonics* **9.** doi:10.1038/nphoton.2015.200 (2015).

30. Scheel, S., Buhmann, S. Y., Clausen, C. & Schneeweiss, P. Directional spontaneous emission and lateral Casimir-Polder force on an atom close to a nanofiber. *Physical Review A* **92.** doi:10.1103/PhysRevA.92.043819 (2015).

31. Kalhor, F., Thundat, T. & Jacob, Z. Universal spin-momentum locked optical forces. *Applied Physics Letters* **108.** doi:10.1063/1.4941539 (2016).

32. Sayrin, C. *et al.* Nanophotonic Optical Isolator Controlled by the Internal State of Cold Atoms. *Physical Review X* **5.** doi:10.1103/PhysRevX.5.041036 (2015).

33. Kuznetsov, A. I., Miroshnichenko, A. E., Fu, Y. H., Zhang, J. & Luk, B. Magnetic light. *Scientific Reports.* doi:10.1038/srep00492 (2012).

34. Zywietz, U., Evlyukhin, A. B., Reinhardt, C. & Chichkov, B. N. Laser printing of silicon nanoparticles with resonant optical electric and magnetic responses. *Nature Communications* **5.** doi:10.1038/ncomms4402 (2014).

35. Kien, F. L., Balykin, V. I. & Hakuta, K. Angular momentum of light in an optical nanofiber. *Physical Review A - Atomic, Molecular, and Optical Physics* **73.** doi:10.1103/PhysRevA.73.053823 (2006).

36. Le Kien, F. & Rauschenbeutel, A. Anisotropy in scattering of light from an atom into the guided modes of a nanofiber. *Physical Review A* **90.** doi:10.1103/PhysRevA.90.023805 (2014).

37. Junge, C., O'Shea, D., Volz, J. & Rauschenbeutel, A. Strong Coupling between Single Atoms and Nontransversal Photons. *Physical Review Letters* **110.** doi:10.1103/PhysRevLett.110.213604 (2013).

38. Bliokh, K. Y., Smirnova, D. & Nori, F. Quantum spin Hall effect of light. *Science* **348.** doi:10.1126/science.aaa9519 (2015).

39. Jackson, J. D. *Classical Electrodynamics, 3rd Edition* doi:10.1002/3527600434.eap109 (1998).

40. Sund, S. E., Swanson, J. A. & Axelrod, D. Cell membrane orientation visualized by polarized total internal reflection fluorescence. *Biophysical Journal* **77.** doi:10.1016/S0006-3495(99)77066-9 (1999).

41. Bliokh, K. Y. & Nori, F. Transverse spin of a surface polariton. *Physical Review A* **85.** doi:10.1103/PhysRevA.85.061801 (2012).

42. Bliokh, K. Y., Bekshaev, A. Y. & Nori, F. Extraordinary momentum and spin in evanescent waves. *Nature communications* **5.** doi:10.1038/ncomms4300 (2014).

43. Novotny, L. & Hecht, B. *Principles of Nano-Optics* doi:10.1017/CBO9780511794193 (Cambridge University Press, Cambridge, 2012).

44. Rotenberg, N. *et al.* Plasmon scattering from single subwavelength holes. *Physical Review Letters* **108.** doi:10.1103/PhysRevLett.108.127402 (2012).

45. Scheel, S. & Buhmann, S. Y. Macroscopic Quantum Electrodynamics—Concepts and Applications. *Acta Physica Slovaca* **58.** doi:10.2478/v10155-010-0092-x (2008).

46. See Supplemental Material at http://link.aps.org/supplemental/10.1103/PhysRevB.95.245416 for the animated version of Fig. 5.

47. García-Cámara, B., Moreno, F., González, F. & Martin, O. J. F. Light scattering by an array of electric and magnetic nanoparticles. *Optics Express* **18.** doi:10.1364/OE.18.010001 (2010).

48. Person, S. *et al.* Demonstration of Zero Optical Backscattering from Single Nanoparticles. *Nano Letters* **13.** doi:10.1021/nl4005018 (2013).

49. Staude, I. *et al.* Tailoring directional scattering through magnetic and electric resonances in subwavelength silicon nanodisks. *ACS Nano* **7.** doi:10.1021/nn402736f (2013).

50. Evlyukhin, A. B. & Bozhevolnyi, S. I. Resonant unidirectional and elastic scattering of surface plasmon polaritons by high refractive index dielectric nanoparticles. *Physical Review B* **92.** doi:10.1103/PhysRevB.92.245419 (2015).

51. Ishimaru, A. *Electromagnetic wave propagation, radiation, and scattering* doi:10.1002/9781119079699 (Prentice Hall, 1991).

52. Mandel, L. & Wolf, E. *Optical coherence and quantum optics* (Cambridge university press, 1995).

53. Archambault, A., Besbes, M. & Greffet, J. J. Superlens in the time domain. *Physical Review Letters* **109.** doi:10.1103/PhysRevLett.109.097405 (2012).

54. Tsakmakidis, K. L., Pickering, T. W., Hamm, J. M., Page, A. F. & Hess, O. Completely stopped and dispersionless light in plasmonic waveguides. *Physical Review Letters* **112.** doi:10.1103/PhysRevLett.112.167401 (2014).

Chapter 3

Near-field directionality beyond spin-momentum locking

In the previous chapter we have seen that circularly polarised dipoles can directionally excite a guided mode via evanescent coupling, when their spin matches the transverse spin of the evanescent wave. This happens because the direction of the spin is locked with the propagation direction, hence inverting one of them implies the inversion of the other as well. In this chapter we will describe two more quantities that, just like spin, can be associated to any guided mode, one of which is momentum locked, while the other is momentum independent. Like we did with circularly polarised dipoles, we can find dipolar sources that match each of these vectors and will therefore excite the associated guided modes. Therefore, in this chapter we will derive the triad of vectors associated to a guided mode: spin, time averaged Poynting vector and reactive power, and find the three elemental dipoles which match them: circular, Huygens and Janus dipoles, respectively. We will then review the theory of scattering from nanostructures and show that small nanoparticles are experimentally suitable to realise dipolar sources. Moreover, we will describe the analytical solution to the scattering from a nanosphere by means of Mie theory. Finally, we will present the results of three of our papers: [Paper B] in which the three elemental sources are predicted and their near field directionality is revealed, [Paper C] in which the behaviour of these source between two waveguiding structures is numerically simulated for realistic waveguides' parameters and [Paper D] in which the first experimental realisation of a Janus dipole is presented, together with the prediction and experimental measurement of its spinning version.

3.1 Spin, Poynting vector and reactive power

From electric and magnetic fields numerous conserved quantities can be derived each of which, due to Noether's theorem, is associated with a specific symmetry transformation. It was recently proposed that the electromagnetic field actually carries an infinite number of associated conserved quantities [168], which clearly determines that the decision on which of these is relevant depending on the physics of the system under study. We will discuss in more detail the meaning and description of some conserved electromagnetic quantities in chapter 5. Here, we will consider three vectors, which can be built from the electric and magnetic fields, which are orthogonal to each other and associated with guided modes. The first one is the time averaged Poynting vector, which is proportional to $\mathrm{Re}[\mathbf{E}^* \times \mathbf{H}]$ [17]. This vector is aligned along the direction of the electromagnetic power flow and determines its intensity. It is maximum when the electric and the magnetic fields are orthogonal and oscillating in phase. The second quantity is the spin vector, which is proportional to $\varepsilon_0 \mathrm{Im}[\mathbf{E}^* \times \mathbf{E}] + \frac{1}{\mu_0}\mathrm{Im}[\mathbf{H}^* \times \mathbf{H}]$. It is maximum when two components of the electric (magnetic) field are orthogonal and 90° out of phase, so it is associated to a rotation of the field. Finally, the third quantity is the reactive power [34], which is proportional to $\mathrm{Im}[\mathbf{E}^* \times \mathbf{H}]$. As it is clear, this vector is the imaginary part of the Poynting vector and is, therefore, maximum when the electric and magnetic fields are orthogonal to each other and 90° out of phase.

A free-propagating plane wave has zero reactive power as the Poynting vector associated with it is purely real since the electric and magnetic fields are orthogonal and in phase. Conversely, a standing wave with equal incident and reflected amplitudes has a purely imaginary Poynting vector, as $\mathbf{E}$ and $\mathbf{H}$ are in quadrature phase.

For evanescent waves the three vectors can all be simultaneously nonzero, with the power flow along the propagation direction, the reactive power along the direction of evanescent decay and the spin orthogonal to them both and transverse to the propagation direction. Since all three of the vectors are orthogonal and defined via a cross product, we can build each of them using two components of the electric and/or magnetic field with a given phase difference. If we fix the polarisation of the mode, to be either s or p, the number of field components that we have available to build these vectors is reduced to three. It is important, in this case, that the reader refers to our definition of the s- (2.3) and p- polarised fields (2.4), which, in the case of guided modes, correspond to TE and TM polarised modes, respectively. We can, therefore, pair the field components in a cyclic fashion and obtain the aforementioned quantities.

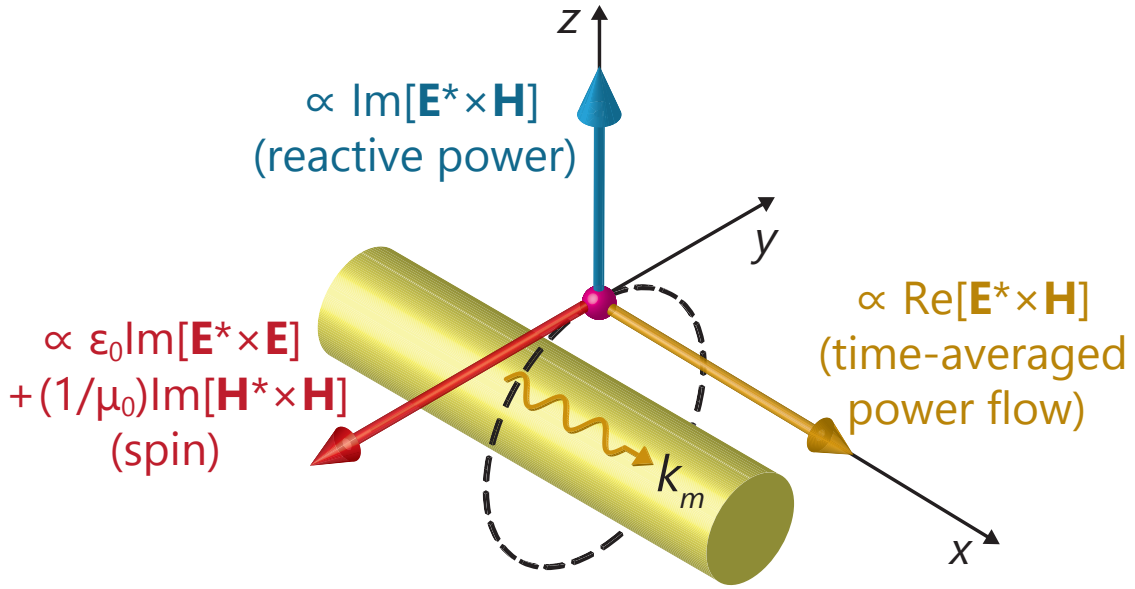

Figure 3.1: The three vectors associated to any guided mode. The red arrow depicts the spin vector, the yellow arrow the Poynting vector and the blue arrow the reactive power.

For example, for a p-polarised mode of a waveguide oriented as in figure 3.1, at the location of the pink sphere ($y = 0$), the electric field has two nonzero components $\mathbf{E} = (E_x, 0, E_z)$ and the magnetic field is transverse to the propagation direction, $\mathbf{H} = (0, H_y, 0)$. In such a p-polarised mode, E_x and H_y are in phase, while E_z, which is along the direction of evanescent decay, is 90° out of phase with the former two, as we saw in equations (1.32) and (1.33). Therefore, the real part of the Poynting vector will be proportional to the product between E_z and H_y, the imaginary part will be proportional to the product between E_x and H_y, the spin to the product between the two electric field components E_x and E_z. The three vectors discussed form an interesting triad also in terms of the symmetries associated to them. We can consider their behaviour under time (T) and parity (P) transformations, $t \to -t$ and $\mathbf{r} \to -\mathbf{r}$, respectively. To do so, we have to keep in mind that, with respect to time reversal, $\mathbf{E}$ fields are even while $\mathbf{H}$ fields are odd. Furthermore, the operations of taking the real and imaginary parts are time even and time odd, respectively. This is summarised in Table 3.1.

Table 3.1: Parity (P) and time reversal (T) symmetries for the tern of vector quantities associated with guided modes.

	P-symmetry $\mathbf{r} \to -\mathbf{r}$	T-symmetry $t \to -t$
Poynting vector	odd	odd
Spin	even	odd
Reactive power	odd	even

3.2 Elemental dipoles

We saw in section 2.2 that we can realise a circularly polarised dipolar source that matches the spin of the guided mode leading to undirectional excitation of said mode. Analogously, we can design dipolar sources that will match the Poynting vector and reactive power of the mode to excite. A dipolar source that matches the Poynting vector of a p-polarised guided mode is a superposition of an electric dipole along the z-axis, $\mathbf{p} = (0, 0, p_z)$ and a magnetic one along the y-axis, $\mathbf{m} = (0, m_y/c, 0)$, both oscillating in phase. This source, called a Huygens dipole, satisfies Kerker's condition [169, 170]: $p = \frac{m}{c}$. In 1983, in fact, Kerker and coworkers found two conditions to nullify the scattering from spherical objects in the backward and forward directions, respectively [169]. Known as Kerker's first condition ever since, the requirement to suppress backward scattering from a spherical nanoparticle is that its electric permittivity ε and magnetic permeability μ are equal. Later [126], this condition was extended to high-index nanoparticle having $\mu = 1$, $\varepsilon \neq 1$ but specific electric and magnetic polarisabilities α_{E} and α_{M}, respectively. In a plane wave, the relation $\mathbf{H} = \frac{\mathbf{E}}{\eta}$ holds, with $\eta = \frac{\varepsilon}{c}$. Since the magnitude of the induced electric p and magnetic m dipole moments in the nanoparticle is dictated by $p = \alpha_{\mathrm{E}}|\mathbf{E}|$ and $m = \alpha_{\mathrm{M}}|\mathbf{H}|$, for plane wave illumination Kerker's first condition $p = \frac{m}{c}$ is satisfied in particles which have $\alpha_{\mathrm{E}} = \varepsilon\alpha_{\mathrm{M}}$ [171]. Similarly to spin, Poynting vector is momentum locked, which means that a source matching a given Poynting vector will excite guided modes unidirectionally. This is justified by the fact that both spin and Poynting vectors are odd with respect to time-reversal symmetry, as can be seen in table 3.1. A Huygens dipole is then another type of electromagnetic source which is capable of achieving unidirectional excitation of guided modes. Inverting the polarisation of the source, which corresponds to changing the orientation of either the electric or the magnetic dipole, the mode will match the Poynting vector in the opposite direction,

therefore flipping the propagation direction of the light in the waveguide. This is shown in further detail in papers [Paper B] and [Paper C]. The electric and magnetic angular spectra of this source, likewise those of the circular dipole, are strongly asymmetric: their amplitude is much higher in the direction which matches the Poynting vector than it is in the opposite direction. A Huygens source that satisfies Kerker's condition without any scaling coefficient on the amplitudes of m or p will have the point of zero amplitude lying exactly on the lightline. Together with the perfectly circular dipole, such Huygens dipoles are the sources we refer to when we talk about the "ideal" dipoles: the amplitude of the electric and the magnetic dipole moments are equal, of course taking the scaling factor of c into account. To obtain unidirectionality for a given guided mode (characterised by a specific wavevector outside of the lightline) we can engineer the Huygens dipole's relative amplitudes between the electric and the magnetic dipole, in an analogous fashion to what we did for with the ellipticity of the circular dipole. These sources can then be tailored to optimise the directionality for any guided mode. The optimisation procedure of dipolar sources is detailed in paper [Paper B], and relies on imposing the coupling amplitude given by Fermi's golden rule to be zero for the wavevector of the mode we do *not* want the source to excite. Such sources have different amplitudes for the electric and magnetic dipole moments and we refer to them as "optimised" dipoles. Unlike the circular dipole, the Huygens dipole is also directional in the far field, so this source is commonly used as a highly directional antenna [172–175].

Furthermore, we can match the reactive power of the guided mode using an electric dipole along x, $\mathbf{p} = (p_x, 0, 0)$ and a magnetic dipole along y, $\mathbf{m} = (0, m_y/c, 0)$, this time satisfying Kerker's condition with an i phase difference: $p = \frac{im}{c}$. The reactive power is even under time-reversal, hence a source matching it will excite a given guided mode but propagating in both directions, so there is not any form of locking with the propagation direction. However, interestingly, when the source's reactive power *opposes* the reactive power of the guided mode, the source will not couple to the mode *at all*. Drawing from Roman mythology, we named the source that matches or opposes the reactive power of a guided mode a Janus dipole, due to its dual face behaviour: from one side its reactive power will match that of the guided mode, hence coupling to the waveguide, from the other side it will not excite the mode. The coupling/noncoupling behaviour of the Janus dipole is revealed in our works [Paper B] and [Paper C], while its first experimental realisation is described in [Paper D]. In figure 3.2 the electric field angular spectra of circular, Huygens and noncoupling Janus dipoles are plotted. In the left column of the figure the free-space angular

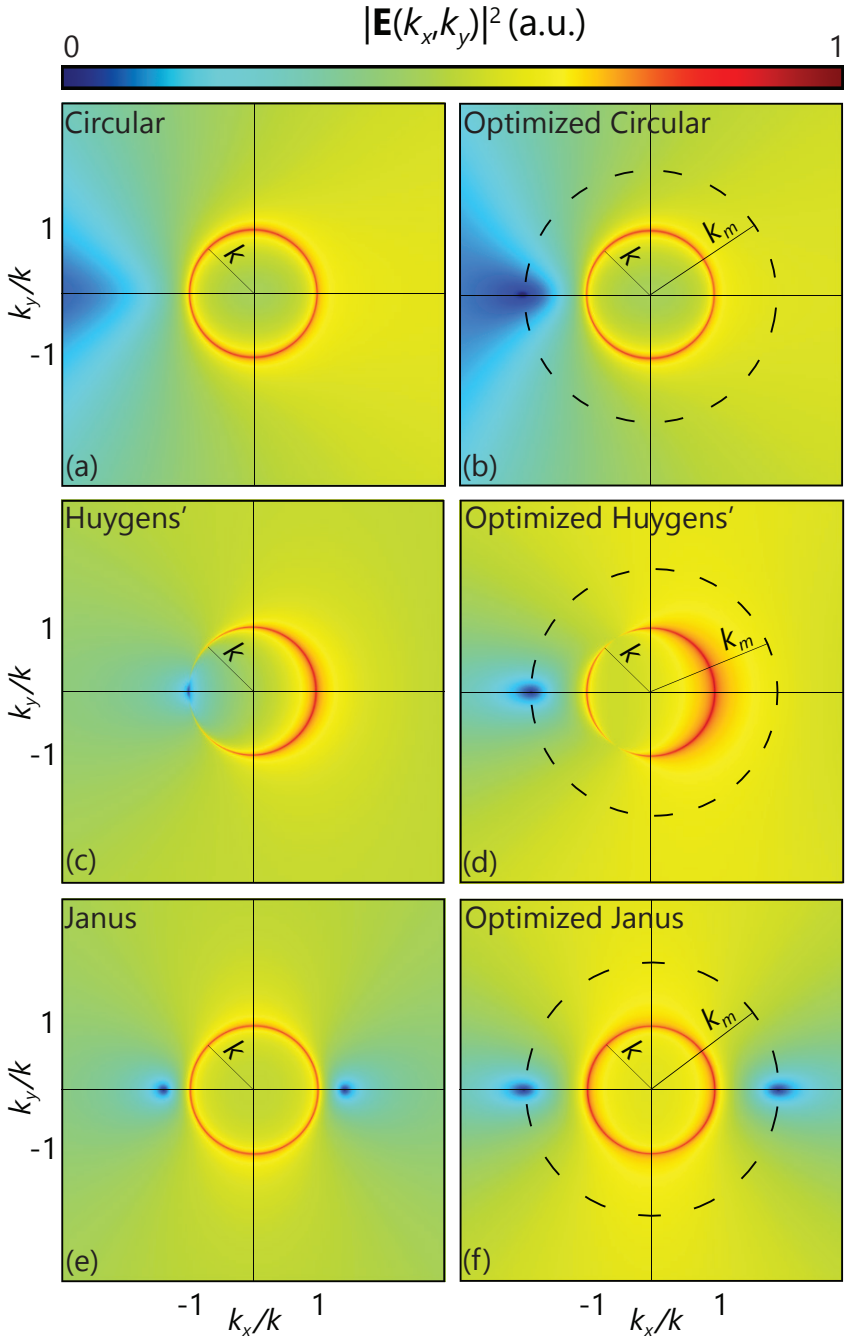

Figure 3.2: Angular spectra of the three elemental dipolar sources, (a, b) circular, (c, d) Huygens and (e, f) Janus dipoles. In (a, c, e) the ideal free space dipoles are plotted, corresponding to: (a) $\mathbf{p} = (-1, 0, i)$, $\mathbf{m} = 0$; (c) $\mathbf{p} = (0, 0, -1)$, $\mathbf{m} = (0, c, 0)$; (e) $\mathbf{p} = (1, 0, 0)$, $\mathbf{m} = (0, ic, 0)$. In (b, d, f) the sources are optimized for a wavevector $k_m = 1.5k$: (b) $\mathbf{p} = (-1.34i, 0, 1)$, $\mathbf{m} = 0$; (d) $\mathbf{p} = (0, 0, -0.7)$, $\mathbf{m} = (0, c, 0)$; (f) $\mathbf{p} = (0.89, 0, 0)$, $\mathbf{m} = (0, ic, 0)$.

spectra of the ideal dipoles are plotted, while in the right one the sources have been optimised to match a specific mode with wavevector k_m. It is clear that in each of the spectra there is at least one point corresponding to a specific wavevector in which the amplitude of the field goes to zero. In the case of the optimised circular and Huygens dipoles, explicitly, these points are in $k_x = -1.5k$, while for the noncoupling Janus dipole the spectrum is zero in both directions, so for $k_x = \pm 1.5k$.

3.3 Scattering from nanostructures

The dipolar sources that we discussed can be realised experimentally in various different ways, all of which share a common feature: they are small compared to the wavelength. Particularly, there have been interesting realisations of electric and magnetic dipolar sources leading to unidirectional guided modes using quantum dots [143, 150, 176–178], atoms [142, 179], near-field tips [135, 180] and scattering nanostructures [126, 134, 172, 181–183]. The latter is the approach we are going to focus on in this thesis work, since it is the one employed in our work [Paper D] to experimentally observe a Janus dipole.

The scattering from small objects is the subject of numerous textbooks [119, 120, 184]. The idea is the following: a given nanoparticle of specified size, shape and material is illuminated by a monochromatic plane wave. Although the problem examined is simple and apparently straightforward, it can seldom be solved analytically. The field inside the particle is given by $(\mathbf{E}_p, \mathbf{H}_p)$, the field outside of the particle is the superposition of the incident field $(\mathbf{E}_i, \mathbf{H}_i)$ and the field scattered by the nanoparticle $(\mathbf{E}_s, \mathbf{H}_s)$. We can impose two conditions on all these fields: they must satisfy Maxwell's equations, both inside and outside the particle, and their tangential components must be continuous at the interface between two different media, so that energy is conserved across the boundary [119].

Three concepts which are worth explaining in this context are those of extinction, scattering and absorption. Consider a plane wave incident on a particle and a detector placed after it. The power impinging on the detector *without* the particle is larger than the power that the detector receives once the particle is between it and the plane wave source. This is because the particle can both absorb part of the light, transforming it into other forms of energy such as heat, and scatter it, changing the light's trajectory so that it does not hit the detector anymore. The combination of these two phenomena is called extinction. These three quantities are

usually treated in terms of their cross sections: the extinction cross section being the sum of the scattering and absorption ones. These two cross sections are calculated as the rate of energy scattered and absorbed by the particle, respectively, over the incident irradiance.
The scattering from small nanoparticles can, in many cases, be approximated by the fields of the first orders of multipoles, electric and magnetic dipoles and quadrupoles. In general, the following rule of thumb applies: the smaller the particle compared to the incident wavelength, the less number of multipoles required to describe the scattering accurately. Care is necessary though when adopting this rule, as material and shape can remarkably influence the scattering behaviour of a small particle. This is, however, the reason why it is common practice to *induce* dipole moments inside nanoparticles: the illuminated particle will scatter light as if a dipolar source was to be positioned in its place. There is a considerable amount of control which can be achieved while inducing dipole moments in a nanoparticle, both tailoring the design of the particle itself (size, shape, material), but also engineering the illumination (polarisation, wavelength, angular momentum, angle of incidence). These optimisations usually require numerical techniques, since the scattering from arbitrarily shaped particles is not solvable analytically, however algorithms to perform these calculations are becoming more and more common, also thanks to powerful machine learning techniques [185–188]. There are, however, scattering problems which can be solved analytically, the most important of which is undoubtedly that of a sphere of arbitrary radius and refractive index. The solution of this problem is commonly attributed to Gustav Mie and goes under the name of Mie theory.

3.4 Mie theory

The algebraic manipulations required to derive Mie theory are almost universally accepted as some of the most pedantic and boring calculations the human mind has ever devised [119, 120]. Luckily, there are plenty of textbooks which perform them thoroughly [119, 120, 189], allowing us to glance over the derivation and focus on the physics that this theory provides us with. It is worth, however, to answer the question *"Why can the scattering problem be solved analytically for spherical objects?"*. The key to the analytical solution of the scattering from a sphere lies in the choice of spherical polar coordinates. In these coordinates, in fact, the fields that satisfy Helmholtz equation (1.17) can be expanded in terms of spherical

harmonics. Spherical harmonics are a very well known set of orthogonal functions, employed in the most diverse branches of physics, being the eigenvectors of the angular momentum operator. They can be expressed in terms of spherical Bessel functions which have easy recurrent relations that allow to derive subsequent terms in the series in a simple way, making them an ideal basis to adopt for computations. Adopting spherical coordinates to describe the problem becomes very handy when imposing the boundary condition which requires the tangential components of the fields to be continuous across the interface between the particle and the surrounding medium. In fact, in such a reference system, the normal to the surface is always along the radial component, which simplifies the calculations significantly. Once the fields are written in this way, both inside and outside the particle, and the boundary conditions have been imposed, the coefficients of the expansion can be calculated. The scattering cross section is then derived as a sum of these coefficients and the amplitudes and phases of the coefficients are related to the amplitudes and phases of the multipolar components in which the scattering can be decomposed. Mie theory then gives us an analytical way to determine the multipolar behaviour from the scattering of a spherical nanoparticle. The particle's refractive index and radius are the tunable parameters that we can employ in engineering the multipolar response of the sphere, as they influence the number of multipoles present in a given frequency range and the frequency at which each multipolar resonance appears.

The nanoparticle, illuminated by an external plane wave, behaves as a resonant cavity. For some frequencies, the plane wave will excite resonant modes inside the cavity. There are two types of modes in a spherical cavity, usually called transverse magnetic (TM) and transverse electric (TE). The TM modes are so called because the magnetic field does not have any component along the radial direction of the sphere. Conversely, in TE modes, the magnetic field is radial while the electric field is circulating. This can be seen in figure 3.3 in which the fields corresponding to these two resonances, excited in a silicon nanoparticle with a radius of 88 nm, are plotted, together with the scattering efficiency. The first resonance is centered about 565 nm and corresponds to a TM resonant mode inside the cavity. The electric field is linear, lying along the polarisation direction of the plane wave illuminating the particle, while the magnetic field is circulating around it. At this resonant condition the particle scatters like a linear electric dipole, oriented along the direction of the electric field. At the second resonance, centered about 680 nm, the behaviour of the electric and magnetic fields is reversed, the magnetic field has only radial

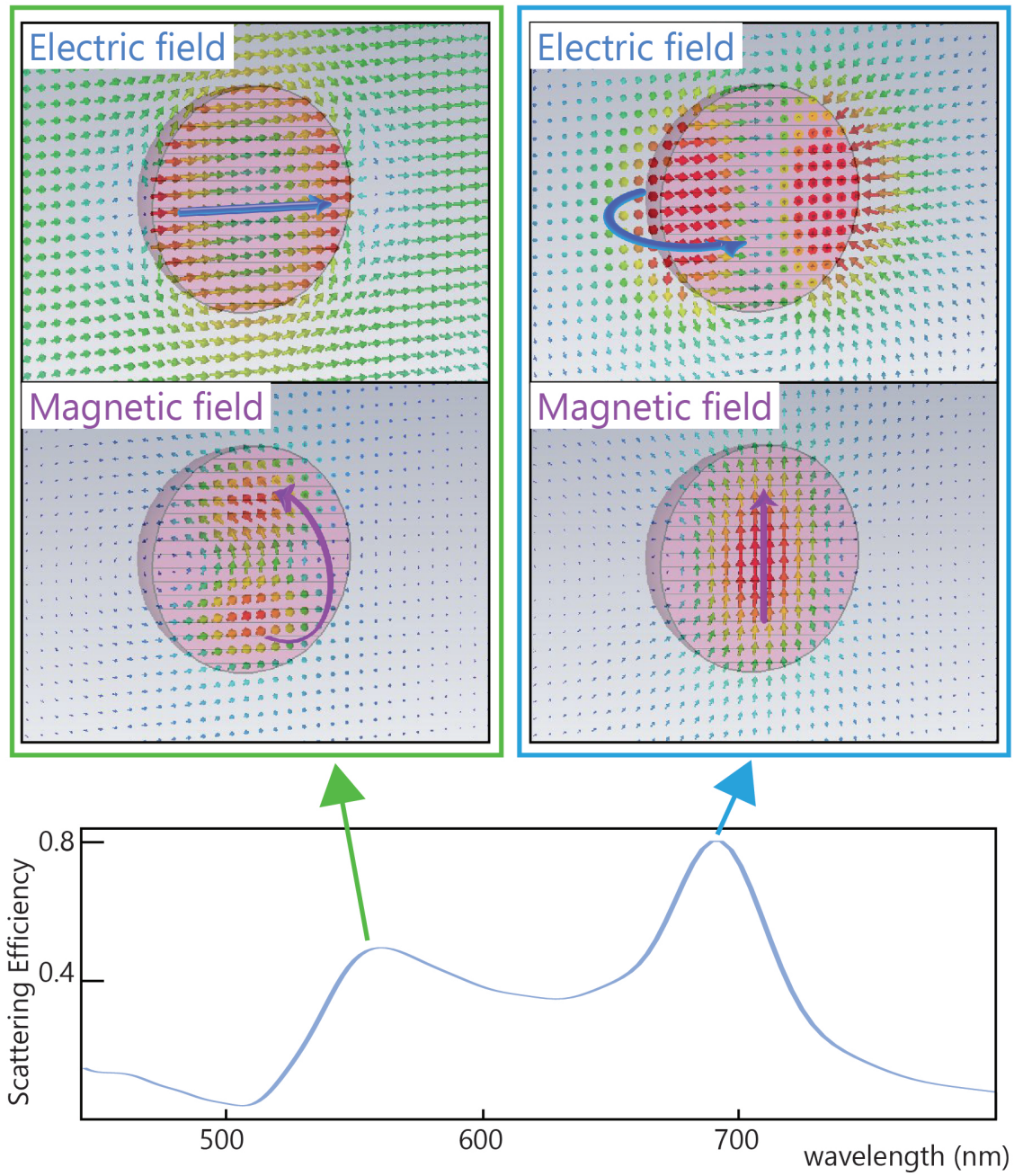

Figure 3.3: Scattering efficiency and numerically calculated scattered fields of a Si spherical nanoparticle with radius $r = 88\,\text{nm}$. The scattering efficiency is calculated as the scattering cross section divided by the surface area of the sphere. The arrows depict the instantaneous orientation of the electric and magnetic fields at the resonant wavelengths.

components and the electric field is circulating around it. When illuminated at this wavelength, the particle then scatters like a magnetic dipole, oriented along

the direction of the magnetic field in the illuminating plane wave. Changing the radius of the nanoparticle shifts the spectral position of the resonances, like in every cavity, and in larger nanoparticles (compared to the wavelength) other resonances can be excited, such as those corresponding to higher order multipoles, i.e. electric or magnetic quadrupole, octupole, etc. While solving Helmholtz equation (1.17) and applying boundary conditions for a dielectric nanoparticle allows for two sets of solutions, TE and TM modes, the situation is different for metallic nanoparticles. In fact, since metals are conductors, the field inside them must be zero and normal to the surface. This means that, unlike what happens with dielectric nanoparticles, only TM modes are excitable in metallic ones, which can then be used as electric only multipolar sources. As an example, in figure 3.4, the scattered field and scattering efficiency of a gold spherical nanoparticle with a radius of 88 nm are depicted. Even

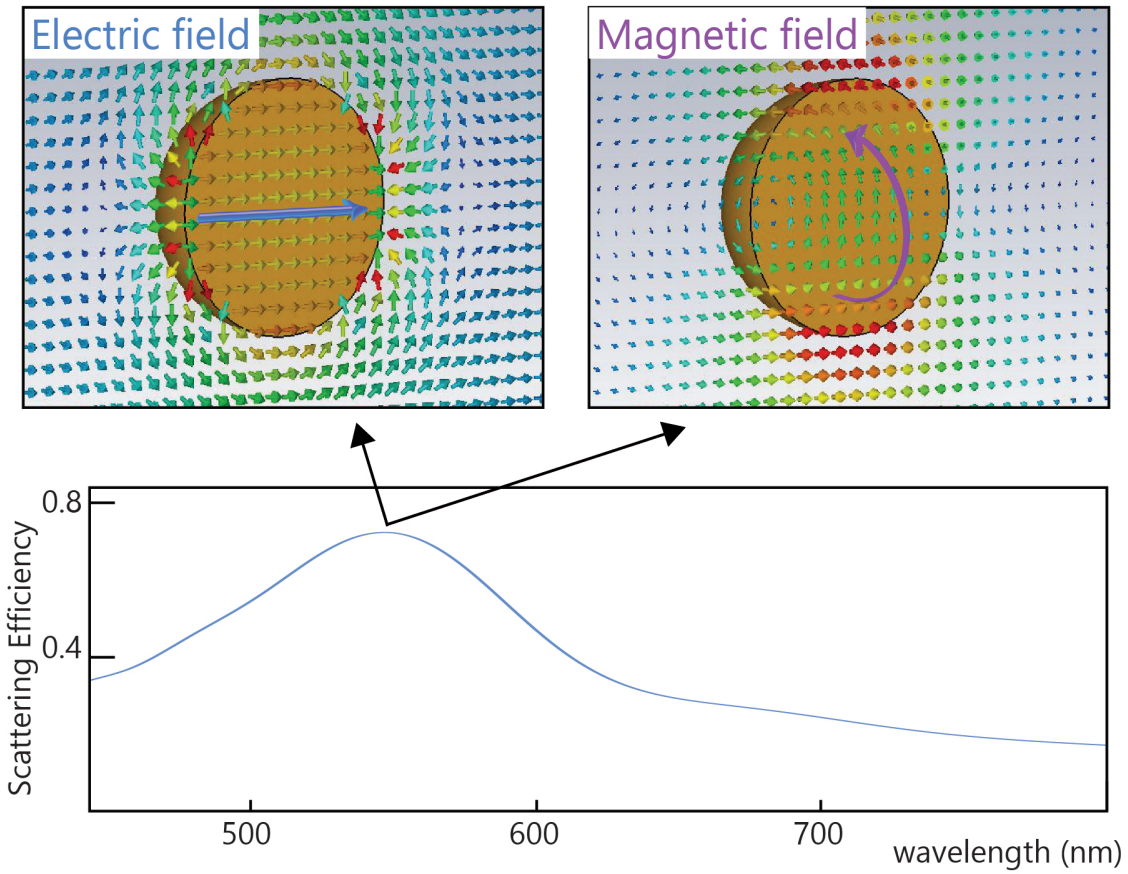

Figure 3.4: Scattering efficiency and numerically calculated scattered fields of an Au spherical nanoparticle with radius $r = 88\,\text{nm}$. The scattering efficiency is calculated as the scattering cross section divided by the surface area of the sphere. The arrows depict the instantaneous orientation of the electric and magnetic field at the resonant wavelength.

though the radius of the gold nanoparticle is the same as the silicon nanoparticle of figure 3.3, in this case we clearly see that the scattering efficiency only presents one resonance peak. The fields calculated at the resonant wavelength are those of an electric dipole oriented along the electric field polarisation of the illuminating plane wave.

3.5 Our work: Paper B

In this work we present the three elemental dipolar sources explained in section 3.2, describing the Janus dipole for the first time and unveiling the near-field directionality of the Huygens dipole. We show the near-field properties of these sources and derive them starting from Fermi's golden rule (as seen in section 2.4) and imposing a null coupling amplitude between an unknown electro-magnetic dipole and a given guided mode. For this work, I developed the calculations, performed the numerical simulations, realised the 3D rendering from the simulation data (Figure S1) and prepared the first draft for both the main text, the figures and the appendices.

3.6 Our work: Paper C

In this work we present a review of the various approaches to describe dipole's near-field directionality and properties. Moreover, we simulate the three elemental dipoles between two commercially available standard silicon waveguides. The waveguides are designed for telecom wavelength ($\lambda = 1550\,\text{nm}$) and the behaviour of the three sources embedded between them is revealing of their associated symmetries, which were summarised in 3.1. For this work, I performed the numerical simulations of the three elemental dipoles between waveguides and rendered each of them via the 3D graphics software *Blender*.

3.7 Our work: Paper D

Finally, in this work an experimental realisation of the Janus dipole is presented. The measurements, performed by Martin Neugebauer and Jörg Eismann at the Max

Planck Institute in Erlangen, consisted in illuminating a silicon nanoparticle with a plane wave, at a wavelength for which the amplitude of the electric and magnetic responses are comparable and the phase between the two resonances is close to $\pi/2$, accounting for the necessary phase shift between the two dipoles required for a Janus source. The near fields scattered by the particle are collected via near-field microscopy and Fourier transformed to obtain the angular spectrum of the source. In the angular spectrum we observe a full circle of zeros for the noncoupling Janus dipole, whose radius corresponds to the spectral component that the dipole is lacking. Moreover, in this paper, we introduce the spinning Janus dipole. This has been obtained illuminating the nanoparticle with circularly polarised light, at the same wavelength at which the Janus condition is satisfied for the linear illumination. My contribution to this paper consists of the theoretical work and the numerical simulations. Furthermore I prepared the first draft of the main text, all the figures in the main text, and appendix 1.

3.8 Paper B

Phys. Rev. Lett. ***120****, 117402 (2018)*

Janus and Huygens Dipoles: Near-Field Directionality Beyond Spin-Momentum Locking

Michela F. Picardi, Anatoly V. Zayats
and Francisco J. Rodríguez-Fortuño

Janus and Huygens Dipoles: Near-Field Directionality Beyond Spin-Momentum Locking

Michela F. Picardi[1], Anatoly V. Zayats[1]
and Francisco J. Rodríguez-Fortuño[1]

[1] *Department of Physics, King's College London, Strand, London WC2R 2LS, United Kingdom*

Unidirectional scattering from circularly polarized dipoles has been demonstrated in near-field optics, where the quantum spin-Hall effect of light translates into spin-momentum locking. By considering the whole electromagnetic field, instead of its spin component alone, near-field directionality can be achieved beyond spin-momentum locking. This unveils the existence of the Janus dipole, with side-dependent topologically protected coupling to waveguides, and reveals the near-field directionality of Huygens dipoles, generalizing Kerker's condition. Circular dipoles, together with Huygens and Janus sources, form the complete set of all possible directional dipolar sources in the far- and near-field. This allows the designing of directional emission, scattering, and waveguiding, fundamental for quantum optical technology, integrated nanophotonics, and new metasurface designs.

Nanoscale emitters, scatterers and their assemblies have been recently considered for quantum optical technologies, metasurface designs enabling flat lenses and holograms, and scalable photonic circuitry, where the requirements on miniaturization and efficient coupling to photonic modes are strict [1–3]. Scatterers can be realised as strongly resonant plasmonic or high-index dielectric nanoparticles supporting electric and/or magnetic dipolar resonances, while emitters can be quantum dots or atoms. Near field interference and related directional excitation of fields from circularly polarized electric and magnetic dipoles [4–13] have proven to have fascinating applications in quantum optics [14–16] and in novel experimental nanophotonic devices such as nanorouters, polarimeters, and non-reciprocal optical components [17–25]. These effects rely on the photonic quantum spin-Hall effect exploiting the phenomenon of spin-momentum locking in evanescent and guided waves [26–31]: in

essence, the spin of the dipole can be matched to the inherent spin of confined fields to be directionally excited. Electromagnetic spin accounts for the rotation of the electric **E** and magnetic **H** field vectors, however it does not account for the relative amplitude and phases *between* electric and magnetic components. By engineering superpositions of electric and magnetic dipoles and their interference [32–35] we can exploit these relations to achieve near-field directionality beyond spin-momentum locking. An example of a well-known dipolar source which exploits these relations to achieve *far-field* directionality is the Huygens antenna. This source combines two orthogonal linearly polarized electric p and magnetic m dipoles satisfying Kerker's condition [36, 37]:

$$p = \frac{m}{c}, \tag{1}$$

with c being the speed of light. Its radiation diagram is highly directional and has zero back-scattering, due to the interference of magnetic and electric dipole radiation. These antennas are attracting great attention due to the feasibility of implementing them using high-index dielectric nanoparticles [38–41], with applications in null back-scattering metasurfaces, and all-dielectric mirrors [42–48].

Here we show that Huygens sources can be generalized to achieve near-field directionality, and that there exists a dipolar source complementary to a Huygens dipole, which we term Janus dipole, with a different relation between the phases of electric and magnetic dipoles, which is not directional in the far-field, but has unique near-field properties allowing side-dependent coupling to guided modes. Together, Huygens, Janus, circular electric and magnetic dipoles (as well as the infinite spectrum of their linear combinations) provide a general closed solution to dipolar far- and near-field directionality that takes into account the topology of the vector structure of free space and guided electromagnetic fields. These dipolar sources can be experimentally realised as plasmonic, dielectric and hybrid nanoparticles. We consider three elemental dipole sources for near-field directionality: circularly polarized dipoles have spinning electric or magnetic dipole moments, while Huygens and Janus sources combine orthogonal electric and magnetic dipoles that are in phase or 90° out of phase to each other, respectively. Each can be introduced from their close relation to well known electromagnetic quantities (Fig. 1). Firstly, Huygens sources are often explained in terms of the time-averaged Poynting vector $\propto \mathrm{Re}\,[\mathbf{E}^* \times \mathbf{H}]$. This vector represents intensity and direction of the electromagnetic power flow. It arises wherever electric and magnetic field are in phase and orthogonal to each other. It

(a)

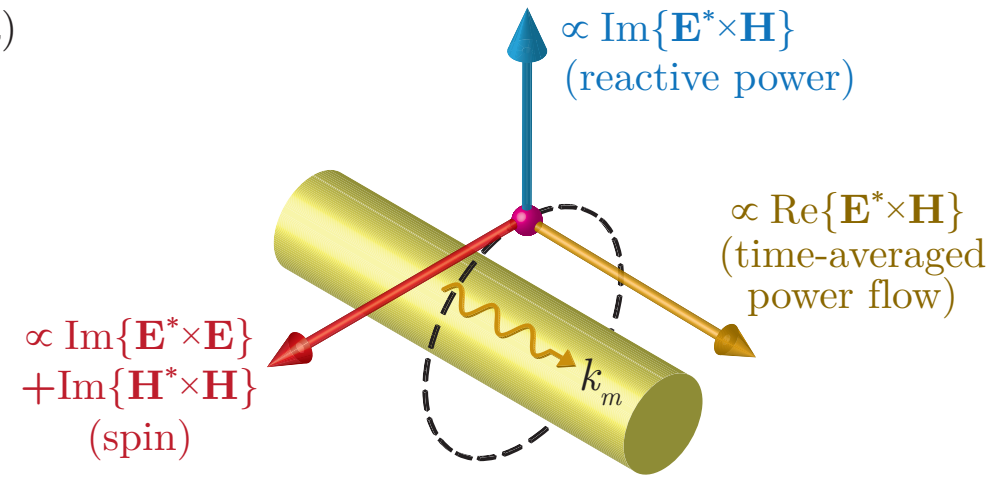

(b)

	Circular source	Huygens' source	Janus source
p-polarized	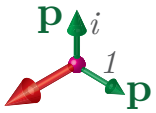 Im{E*×E}	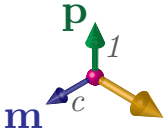 Re{E*×H}	Im{E*×H} 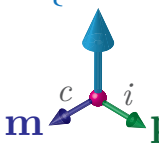
s-polarized	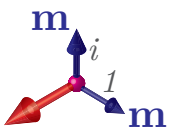 Im{H*×H}	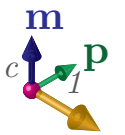 Re{E*×H}	Im{E*×H} 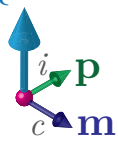
symmetry	P-even T-odd	P-odd T-odd	P-odd T-even

Figure 1: (a) Triad of vectors (time-averaged power flow, reactive power and spin vector) associated to any guided mode, each related to one of the three sources in the schematics (b). (b) Schematics of the sources and their relative vectors. The top left panel depicts a circularly polarized electric dipole, superposition of two orthogonal linear electric dipoles **p** with complex amplitudes 1 and i, representing their quadrature phase relation. This circular dipole is associated with a transverse spin vector shown in the panel. A similar notation is used throughout the table, using **m** for magnetic dipole moments. The spin (red), Poynting (yellow) and reactive power (blue) vectors are associated to different directional dipolar sources and each of them behaves differently under parity (P) and time-reversal (T) symmetry transformations. Notice that, with respect to time-reversal, **E** fields are even while **H** fields are odd. Moreover, the operation of taking the real part of respective vectors is time-even while taking the imaginary part is time-odd.

follows that, when electric and magnetic dipoles are orthogonal and in phase –a Huygens source–, they produce fields associated with a net power flow in a given direction. This gives rise to directionality in the far-field [42–48], but we can exploit the same idea in the near-field of a waveguide (Fig. 1). Secondly, circularly polarized dipole directionality can be explained by means of the spin angular momentum [49] $\propto \mathrm{Im}\left[\mathbf{E}^* \times \mathbf{E}\right] + \mathrm{Im}\left[\mathbf{H}^* \times \mathbf{H}\right]$, which accounts for the rotation of the vectors $\mathbf{E}$ and $\mathbf{H}$. Owing to the existence of out-of-phase *longitudinal* components of the fields in guided modes, this spin can be transverse to the propagation direction. Circularly polarized dipoles –two orthogonal electric or magnetic dipole moments, 90° out of phase– exploit this well-known transverse spin-momentum locking [6, 28–31], exciting the guided mode in one direction only. Finally, we can consider a third quantity $\propto \mathrm{Im}\left[\mathbf{E}^* \times \mathbf{H}\right]$. This expression resembles spin angular momentum, but it mixes electric and magnetic components. It arises when $\mathbf{E}$ and $\mathbf{H}$ are orthogonal but 90° out of phase. This phase shift results in harmonic oscillations of the instantaneous power flow, with a zero time-averaged net flow. This is the imaginary part of the complex Poynting vector, and is known as *reactive power*. It points in the direction of evanescent gradient: away from or towards the nearby waveguide, depending on the mode. We thus propose the Janus source, using orthogonal electric and magnetic dipoles with a 90° phase shift to match or oppose this vector, accounting for its two 'faces': one face couples into the mode, while the other is non-coupling. The three vector quantities, each associated with one of the sources, form a triad at each point near a waveguide [31] (Fig. 1).

As a simple example, Fig. 2 shows the fields generated by (a) a circular dipole, (b) a Huygens antenna, and (c,d) a Janus dipole for its two orientations, all placed over a dielectric slab waveguide. We used a planar slab as an example, but the directionality of the dipoles is universal and completely independent of the waveguide's nature. The first two sources lead to directional evanescent wave excitation of guided modes. While this is known for circular dipoles [4–13, 29, 31], Huygens antennas have been extensively studied for their strong directional radiation diagram, but their near-field directionality had not been explored. The direction of excitation of these sources can be switched by flipping the sign of one of their two dipole components, which can be experimentally achieved tuning polarization and wavelength of the light illuminating the nanoparticle, with respect to its electric and magnetic resonances.

The Janus dipole has an intriguing property: by opposing or matching the direction of reactive power, perpendicular to the waveguide, it either shows (c) a

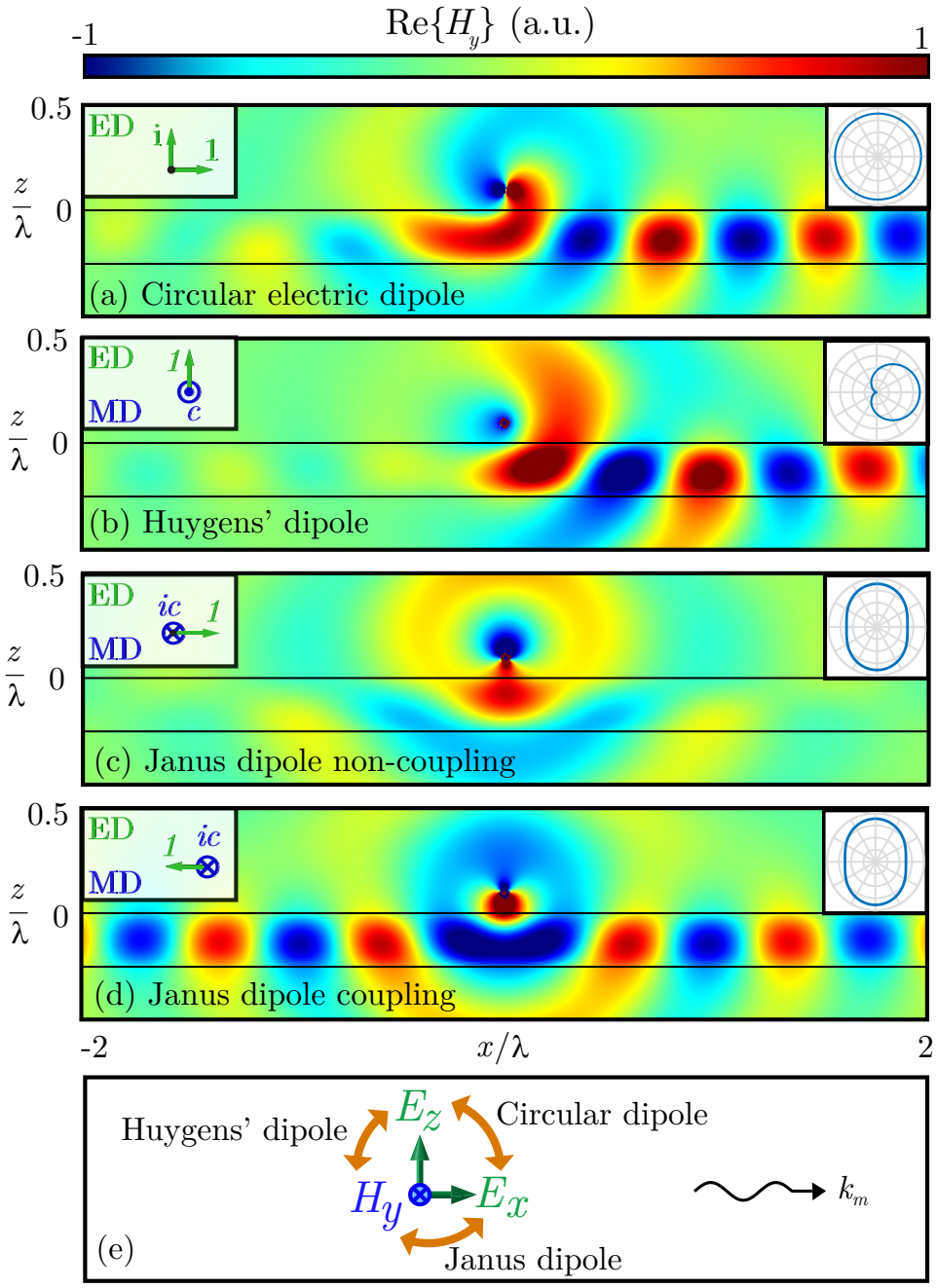

Figure 2: Magnetic field radiated by (a) a circularly polarized electric dipole $\mathbf{p} = (1, 0, i)$, $\mathbf{m} = (0, 0, 0)$; (b) a Huygens antenna $\mathbf{p} = (0, 0, 1)$, $\mathbf{m} = (0, -c, 0)$; (c,d) a Janus dipole $\mathbf{p} = (\pm 1, 0, 0)$, $\mathbf{m} = (0, ic, 0)$ in non-coupling (c) and coupling (d) orientation, in close proximity ($z_0 = 0.1\lambda$) to a dielectric slab (index $n = 2$ and thickness $t = \lambda/4$) (e) Schematic of field components excited by each source. The insets show the orientation of the dipoles and the far field radiation diagrams. These fields have been simulated using Comsol Multiphysics.

complete absence of coupling, not exciting waveguide modes at all or (d) excitation of the guided mode in both directions. This is determined by which 'side' of the dipole is facing the waveguide. Inverting the sign of one component in the Janus dipole will change the side facing the waveguide, like when flipping a coin, and this will switch the coupling on and off [Figs. 2(c,d)]. Alternatively, the dipole's behaviour depends on which side of the waveguide it is placed. Each of these three elemental sources possesses the same symmetries as the vector it is associated with, sharing its behaviour under parity (P) and time-reversal (T) symmetry transformations [50], as summarized in Fig. 1(b). A quantitative explanation of the three sources can be obtained from Fermi's golden rule [6–9, 14, 15, 31]. This rule dictates that the coupling efficiency between an electric $\mathbf{p}$ and magnetic $\mathbf{m}$ dipole source and a waveguide mode is proportional to $|\mathbf{p}\cdot\mathbf{E}^* + \mathbf{m}\cdot\mu\mathbf{H}^*|^2$, where $\mathbf{E}$ and $\mathbf{H}$ are the electric and magnetic fields, respectively, of the mode calculated at the location of the dipoles, and μ is the permeability of the medium. In Fig. 2, the dipoles are interacting with a p-polarized waveguide mode, so the only non-zero field components are the transverse electric and magnetic fields E_z and H_y, and the longitudinal field E_x. The circular dipole exploits spin-momentum locking [6, 28–31] to achieve $\mathbf{p}\cdot\mathbf{E}^* = p_x E_x^* + p_z E_z^* = 0$ for the mode propagating to the left or right, thereby showing unidirectional excitation in the opposite direction. Analogously, circular magnetic dipoles directionally excite s-polarized modes when $\mathbf{m}\cdot\mu\mathbf{H}^* = 0$.

To describe the nature of the other two sources, however, we must also take into account the relative phase and amplitude between $\mathbf{E}$ and $\mathbf{H}$. Their relation can be exploited such that the electric and magnetic coupling terms interfere destructively between each other $\mathbf{p}\cdot\mathbf{E}^* + \mathbf{m}\cdot\mu\mathbf{H}^* = 0$. In other words, the mode excited by the electric dipole $\mathbf{p}$ in a given direction is exactly cancelled out by the one excited by the magnetic dipole $\mathbf{m}$ after their superposition. The Huygens source exploits the fixed relative amplitude and phase that exists between the transverse field components E_z and H_y, which depends on the propagation direction of the mode, as dictated by the Poynting vector. This relation is a well-known property of plane waves which extends directly into evanescent and guided waves. The Janus dipole exploits the locked amplitude and phase relation that exists between H_y and the longitudinal electric field E_x. The unique feature of the Janus dipole, which distinguishes it from the other two, is that the modes excited by the electric p_x and magnetic m_y dipoles simultaneously interfere destructively for *both* propagation directions. This is possible because the ratio between E_x and H_y is dictated by the reactive power

flow vector, and is independent of the mode's left or right propagation direction (time-reversal). This is universally true, at any location, on any waveguide, as follows from the even time-reversal (T) symmetry of the reactive power flow (see Fig. 1(b)). Thus, a Janus dipole can be designed to achieve polarization and position-dependent "non-coupling" in *every scenario where longitudinal fields are present*, such as *inside* nanowires and photonic crystal waveguides, not being limited to external evanescent coupling as illustrated here. This is a remarkable topological property of near-field polarization in addition to transverse spin [28]. Both the circular and Janus dipole rely on the longitudinal component of the field, while the Huygens source does not. This explains why circular and Janus dipoles are not directional in the far field [4, 13], as plane waves have no longitudinal field.

Figure 3 shows the three dipole sources embedded between two waveguides, metal-air interfaces supporting surface plasmons as an example, at a distance such that light from the dipole can couple to both waveguides, but with negligible coupling between the waveguides for the propagation distances considered. The circular dipole couples into opposite directions for the waveguides placed above or below the dipole, while the Huygens dipole couples in the same direction for both. Most interestingly, while these two sources exhibit left-right directionality, the Janus dipole exhibits a front-back directionality. While it does not excite the waveguide placed below, it does however excite both directions in the waveguide above it, *regardless of its distance to either*. In this way, the Janus dipole is topologically protected from coupling into the waveguide facing its non-coupling side. This arises because the ratio between E_x and H_y in evanescent waves is independent of the propagation direction but does depend on the *direction of evanescent decay*. This remarkable and inherently broadband behaviour suggests novel potential applications in optical nanorouting and signal processing. Importantly, all the directionality properties described in Fig. 3 are robust and independent of the distance of the dipoles to the waveguides. The symmetry of excitations follows directly from that of the sources themselves. A numerical simulation of a Janus dipole between two nanophotonic silicon waveguides is provided in the Supplemental Materials (SM) [51].

The design of dipoles exhibiting near-field interference can be done in a general case using Fermi's golden rule, as long as the modal fields are known. However, we now provide a simple complete theory for the specific case of dipoles coupling into *evanescent fields* of planar waveguides, as in Figs. 2 and 3, showing how the three elemental dipoles arise as complete solutions to a single equation. We align

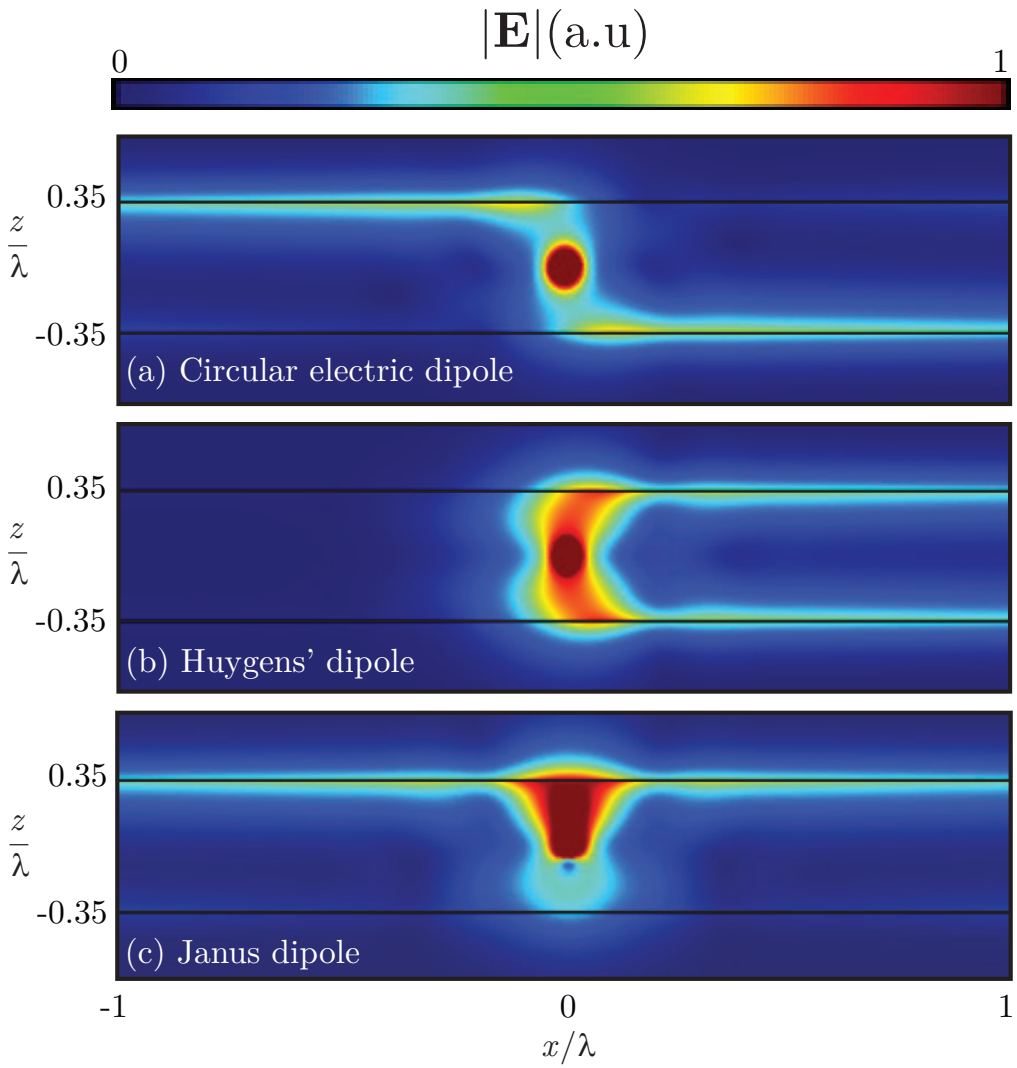

Figure 3: Amplitude of the electric field generated by (a) a circular dipole, (b) a Huygens antenna and (c) a Janus dipole embedded in the centre of a metal-air-metal waveguide, with $\varepsilon = -1.5 + 0.02i$ and $\mu = 1$. The distance between the two waveguides is 0.7λ. These fields have been simulated using Comsol Multiphysics.

our reference system with the propagation direction of the mode, such that the wave-vector of the evanescent field is given by $\mathbf{k} = (k_x, k_y, k_z) = (\pm k_m, 0, \pm i\alpha_m)$, where k_m is the propagation constant of the mode, $\alpha_m = (k_m^2 - k^2)^{1/2}$ accounts for the evanescent nature and k is the wave-number of the medium. The sign of $\pm k_m$ determines the propagation direction, while the sign of $\pm i\alpha_m$ gives the direction of evanescent decay, which depends on whether the waveguide is below (positive) or above (negative) the dipole. We can write the three field components of p-polarized modes in a vector of the form $\mathbf{F}_p = (E_x, c\mu H_y, E_z)$ and the corresponding dipole moment components as $\mathbf{q}_p = (p_x, m_y/c, p_z)$ so that Fermi's golden rule reduces to a simple scalar product $\left|\mathbf{q}_p \cdot \mathbf{F}_p^*\right|^2$. Maxwell's equations demand that p-polarized fields with $k_y = 0$ are always given by $\mathbf{F}_p \propto (\frac{\pm i\alpha_m}{k}, 1, -\frac{\pm k_m}{k})$ [13, 28], irrespective of the nature of the waveguide. The key aspect underpinning all phenomena described in this work is that each pair of these three components has a fixed amplitude and phase relation between them. Indeed, each of the three elemental dipole sources is derived from the relationship between each of the three possible pairs of field components [Fig. 2(e)].

To obtain near-field interference effects, we solve the equation that achieves zero coupling of the dipoles into a given mode:

$$\mathbf{q}_p \cdot \mathbf{F}_p^* = \left(p_x, \frac{m_y}{c}, p_z\right) \cdot \left(\frac{\pm i\alpha_m}{k}, 1, -\frac{\pm k_m}{k}\right)^* = 0. \tag{2}$$

Mathematically, this simple equation defines a geometric plane of solutions given by the sub-space of dipole vectors $\mathbf{q}_p$ which are orthogonal to $\mathbf{F}_p$. This unifies all possible ways to achieve directional evanescent coupling of p-polarized modes from electric and magnetic dipole sources, providing a general framework for near-field directionality in planar geometries. Each of the sources discussed above corresponds to intersections of this plane with the p_x, m_y, or $p_z = 0$ planes. Alternatively, each dipole corresponds to the intersection of two planes given by Eq. 2 but for different pairs of sign combinations in k_m and α_m, explaining why each case shows zero excitation of exactly two directions in Fig. 3. A summary of all possible mathematical solutions to this equation is given in Table 3.2. Notice that the dipoles are fine-tuned to achieve a perfect contrast ratio for a specific mode k_m, but the simplest versions, in which $(p_x, m_y/c, p_z) \propto (1, 0, \pm i)$, $(0, \pm 1, 1)$ and $(1, \pm i, 0)$, also work remarkably well as shown in Fig. 2. The optimized Huygens dipole $\frac{\pm k_m^*}{k} p = \frac{m}{c}$ constitutes a generalized Kerker's condition that works for both propagating and

Table 3.2: Elemental dipole sources for near-field directionality in planar waveguides. Optimized dipoles use $\hat{k}_m = k_m^*/k$ and $\hat{\alpha}_m = \alpha_m^*/k$, while the simplest dipoles use $\hat{\alpha}_m, \hat{k}_m \approx 1$. In the general solution, $\mathbf{q}_{p/s}^i$ and $\mathbf{q}_{p/s}^j$ stand for any two of the three elemental dipoles with a, b arbitrary complex coefficients.

	p-polarization $\mathbf{q}_p = (p_x, m_y/c, p_z)$	s-polarization $\mathbf{q}_s = (m_x/c, p_y, m_z/c)$
Elliptical	$(\pm\hat{k}_m, 0, \mp i\hat{\alpha}_m)$	$(\pm\hat{k}_m, 0, \mp i\hat{\alpha}_m)$
Huygens	$(0, \pm\hat{k}_m, 1)$	$(0, \pm\hat{k}_m, -1)$
Janus	$(1, \pm i\hat{\alpha}_m, 0)$	$(-1, \pm i\hat{\alpha}_m, 0)$
General	$\mathbf{q}_p = a\mathbf{q}_p^i + b\mathbf{q}_p^j$	$\mathbf{q}_s = a\mathbf{q}_s^i + b\mathbf{q}_s^j$

evanescent waves, and reduces to Eq. 1 when $k_m = k$. Each of the three elemental sources is obtainable as a linear superposition of the other two. Finally, we can consider the entire geometric plane of solutions obtained by linear combinations of the elemental sources, resulting in an infinite range of electric and magnetic dipoles that verify Eq. 2.

Analogous considerations are valid for $s-$ polarized modes (see SM [51] for details). Solutions are given in Table 3.2. In complete physical analogy to the p-polarized case, the same three elemental dipoles can be derived, but swapping the roles of the electric and magnetic moments. Tab. 3.2 therefore provides all possible solutions for near-field directionality from a dipole source in the general case of planar geometries, but we would like to emphasize that following a spectral interpretation [52] (see SM [51]), all dipoles derived in Table 3.2 are excellent approximations to their optimum when placed near arbitrary waveguides, as was shown in Ref. [13]. In conclusion, previous approaches to guided optics directionality from dipolar sources made use of the spin of the guided mode's fields **E** and **H**, neglecting their mutual amplitude and phase relations. By considering the complete vector structure of electromagnetic fields, we provide a unified theory describing all possible dipole sources exhibiting far- and near-field directionality with planar structures; these considerations can

be applied to arbitrary geometries once the modes supported by the waveguide are known. The implementation of these new sources using resonant plasmonic or dielectric nanoparticles and their integration in photonic circuitry will provide a step change in the already broad range of near-field directionality applications, currently based on circular dipoles exclusively. We expect novel ideas to emerge in quantum optics, photonic nano-routing, photonic logical circuits, optical forces and torques of particles in near-field environments, inverse and reciprocal scenarios for polarization synthesis, integrated polarimeters, and other unforeseen devices throughout the whole electromagnetic spectrum.

This work was supported by European Research Council Starting Grant ERC-2016-STG-714151-PSINFONI and EPSRC (UK). A.Z. acknowledges support from the Royal Society and the Wolfson Foundation. All data supporting this research is provided in full in the main text and Supplementary Materials.

REFERENCES

1. Editorial. Not so small. *Nature Photonics* **8.** doi:10.1038/nphoton.2014.282 (2014).
2. Yu, N. & Capasso, F. Flat optics with designer metasurfaces. *Nature Materials* **13.** doi:10.1038/nmat3839 (2014).
3. Chang, D. E., Vuletić, V. & Lukin, M. D. Quantum nonlinear optics - photon by photon. *Nature Photonics* **8.** doi:10.1038/nphoton.2014.192 (2014).
4. Rodríguez-Fortuño, F. J. *et al.* Near-field interference for the unidirectional excitation of electromagnetic guided modes. *Science* **340.** doi:10.1126/science.1233739 (2013).
5. Kapitanova, P. V. *et al.* Photonic spin Hall effect in hyperbolic metamaterials for polarization-controlled routing of subwavelength modes. *Nature Communications* **5.** doi:10.1038/ncomms4226 (2014).
6. Aiello, A., Banzer, P., Neugebauer, M. & Leuchs, G. From transverse angular momentum to photonic wheels. *Nature Photonics* **9.** doi:10.1038/nphoton.2015.203 (2015).

7. Espinosa-Soria, A. & Martinez, A. Transverse Spin and Spin-Orbit Coupling in Silicon Waveguides. *IEEE Photonics Technology Letters* **28.** doi:10.1109/LPT.2016.2553841 (2016).
8. Coles, R. J. *et al.* Chirality of nanophotonic waveguide with embedded quantum emitter for unidirectional spin transfer. *Nature Communications* **7.** doi:10.1038/ncomms11183 (2016).
9. Le Feber, B., Rotenberg, N. & Kuipers, L. Nanophotonic control of circular dipole emission. *Nature Communications* **6.** doi:10.1038/ncomms7695 (2015).
10. Zharov, A. A., Zharov, A. A. & Zharova, N. A. Control of surface plasmon excitation via the scattering of light by a nanoparticle. *Journal of Experimental and Theoretical Physics* **123.** doi:10.1134/S1063776116070268 (2016).
11. Wang, Y.-H. *et al.* Photonic spin Hall effect by the spin-orbit interaction in a metasurface with elliptical nano-structures. *Applied Physics Letters* **110.** doi:10.1063/1.4978520 (2017).
12. Garoli, D., Zilio, P., De Angelis, F. & Gorodetski, Y. Helicity locking of chiral light emitted from a plasmonic nanotaper. *Nanoscale* **9.** doi:10.1039/C7NR01674C (2017).
13. Picardi, M. F., Manjavacas, A., Zayats, A. V. & Rodríguez-Fortuño, F. J. Unidirectional evanescent-wave coupling from circularly polarized electric and magnetic dipoles: An angular spectrum approach. *Physical Review B* **95.** doi:10.1103/PhysRevB.95.245416 (2017).
14. Marrucci, L. Quantum optics: Spin gives direction. *Nature Physics* **11.** doi:10.1038/nphys3198 (2015).
15. Luxmoore, I. J. *et al.* Interfacing Spins in an InGaAs Quantum Dot to a Semiconductor Waveguide Circuit Using Emitted Photons. *Physical Review Letters* **110.** doi:10.1103/PhysRevLett.110.037402 (2013).
16. Mitsch, R., Sayrin, C., Albrecht, B., Schneeweiss, P. & Rauschenbeutel, A. Quantum state-controlled directional spontaneous emission of photons into a nanophotonic waveguide. *Nature Communications* **5.** doi:10.1038/ncomms6713 (2014).
17. Petersen, J., Volz, J. & Rauschenbeutel, A. Chiral nanophotonic waveguide interface based on spin-orbit interaction of light. *Science* **346.** doi:10.1126/science.1257671 (2014).
18. Neugebauer, M., Bauer, T., Banzer, P. & Leuchs, G. Polarization tailored light driven directional optical nanobeacon. *Nano letters* **14.** doi:10.1021/nl5003526 (2014).
19. Espinosa-Soria, A., Rodríguez-Fortuño, F. J., Griol, A. & Martínez, A. On-Chip Optimal Stokes Nanopolarimetry Based on Spin-Orbit Interaction of Light. *Nano Letters* **17.** doi:10.1021/acs.nanolett.7b00564 (2017).

20. O'Connor, D., Ginzburg, P., Rodríguez-Fortuño, F. J., Wurtz, G. A. & Zayats, A. V. Spin-orbit coupling in surface plasmon scattering by nanostructures. *Nature Communications* **5.** doi:10.1038/ncomms6327 (2014).

21. Rodríguez-Fortuño, F. J. *et al.* Universal method for the synthesis of arbitrary polarization states radiated by a nanoantenna. *Laser & Photonics Reviews* **8.** doi:10.1002/lpor.201300184 (2014).

22. Rodríguez-Fortuño, F. J., Barber-Sanz, I., Puerto, D., Griol, A. & Martínez, A. Resolving Light Handedness with an on-Chip Silicon Microdisk. *ACS Photonics* **1.** doi:10.1021/ph500084b (2014).

23. Rodríguez-Fortuño, F. J. *et al.* Sorting linearly polarized photons with a single scatterer. *Optics Letters* **39.** doi:10.1364/OL.39.001394 (2014).

24. Sayrin, C. *et al.* Nanophotonic Optical Isolator Controlled by the Internal State of Cold Atoms. *Physical Review X* **5.** doi:10.1103/PhysRevX.5.041036 (2015).

25. Ma, J., Xi, X., Yu, Z. & Sun, X. Hybrid graphene/silicon integrated optical isolators with photonic spin-orbit interaction. *Applied Physics Letters* **108.** doi:10.1063/1.4945715 (2016).

26. Bliokh, K. Y. & Nori, F. Transverse and longitudinal angular momenta of light. doi:10.1016/j.physrep.2015.06.003 (2015).

27. Bliokh, K. Y., Rodríguez-Fortuño, F. J., Nori, F. & Zayats, A. V. Spin-orbit interactions of light. *Nature Photonics* **9.** doi:10.1038/nphoton.2015.201 (2015).

28. Bliokh, K. Y., Smirnova, D. & Nori, F. Quantum spin Hall effect of light. *Science* **348.** doi:10.1126/science.aaa9519 (2015).

29. Junge, C., O'Shea, D., Volz, J. & Rauschenbeutel, A. Strong Coupling between Single Atoms and Nontransversal Photons. *Physical Review Letters* **110.** doi:10.1103/PhysRevLett.110.213604 (2013).

30. Bliokh, K. Y., Bekshaev, A. Y. & Nori, F. Extraordinary momentum and spin in evanescent waves. *Nature communications* **5.** doi:10.1038/ncomms4300 (2014).

31. Van Mechelen, T. & Jacob, Z. Universal spin-momentum locking of evanescent waves. *Optica* **3.** doi:10.1364/OPTICA.3.000118 (2016).

32. Sinev, I. S. *et al.* Chirality Driven by Magnetic Dipole Response for Demultiplexing of Surface Waves. *Laser & Photonics Reviews* **11.** doi:10.1002/lpor.201700168 (2017).

33. Lee, S.-Y. *et al.* Role of Magnetic Induction Currents in Nanoslit Excitation of Surface Plasmon Polaritons. *Physical Review Letters* **108.** doi:10.1103/PhysRevLett.108.213907 (2012).

34. Evlyukhin, A. B. & Bozhevolnyi, S. I. Resonant unidirectional and elastic scattering of surface plasmon polaritons by high refractive index dielectric nanoparticles. *Physical Review B* **92.** doi:10.1103/PhysRevB.92.245419 (2015).

35. Neugebauer, M., Woźniak, P., Bag, A., Leuchs, G. & Banzer, P. Polarization-controlled directional scattering for nanoscopic position sensing. *Nature Communications* **7.** doi:10.1038/ncomms11286 (2016).

36. Kerker, M., Wang, D.-S. & Giles, C. L. Electromagnetic scattering by magnetic spheres. *Journal of the Optical Society of America* **73.** doi:10.1364/JOSA.73.000765 (1983).

37. Zambrana-Puyalto, X., Fernandez-Corbaton, I., Juan, M. L., Vidal, X. & Molina-Terriza, G. Duality symmetry and Kerker conditions. *Optics Letters* **38.** doi:10.1364/OL.38.001857 (2013).

38. Evlyukhin, A. B. *et al.* Demonstration of Magnetic Dipole Resonances of Dielectric Nanospheres in the Visible Region. *Nano Letters* **12.** doi:10.1021/nl301594s (2012).

39. Fu, Y. H., Kuznetsov, A. I., Miroshnichenko, A. E., Yu, Y. F. & Luk'yanchuk, B. Directional visible light scattering by silicon nanoparticles. *Nature Communications* **4.** doi:10.1038/ncomms2538 (2013).

40. Permyakov, D. *et al.* Probing magnetic and electric optical responses of silicon nanoparticles. *Applied Physics Letters* **106.** doi:10.1063/1.4919536 (2015).

41. Kuznetsov, A. I., Miroshnichenko, A. E., Brongersma, M. L., Kivshar, Y. S. & Luk'yanchuk, B. Optically resonant dielectric nanostructures. *Science* **354.** doi:10.1126/science.aag2472 (2016).

42. Geffrin, J. *et al.* Magnetic and electric coherence in forward- and back-scattered electromagnetic waves by a single dielectric subwavelength sphere. *Nature Communications* **3.** doi:10.1038/ncomms2167 (2012).

43. Person, S. *et al.* Demonstration of Zero Optical Backscattering from Single Nanoparticles. *Nano Letters* **13.** doi:10.1021/nl4005018 (2013).

44. Staude, I. *et al.* Tailoring directional scattering through magnetic and electric resonances in subwavelength silicon nanodisks. *ACS Nano* **7.** doi:10.1021/nn402736f (2013).

45. Nieto-Vesperinas, M., Gomez-Medina, R. & Saenz, J. J. Angle-suppressed scattering and optical forces on submicrometer dielectric particles. *Journal of the Optical Society of America A* **28.** doi:10.1364/JOSAA.28.000054 (2011).

46. Coenen, T., Bernal Arango, F., Femius Koenderink, A. & Polman, A. Directional emission from a single plasmonic scatterer. *Nature Communications* **5.** doi:10.1038/ncomms4250 (2014).

47. Wei, L., Bhattacharya, N. & Paul Urbach, H. Adding a spin to Kerker's condition: angular tuning of directional scattering with designed excitation. *Optics Letters* **42.** doi:10.1364/OL.42.001776 (2017).

48. Paniagua-Domínguez, R. *et al.* Generalized Brewster effect in dielectric metasurfaces. *Nature Communications* **7.** doi:10.1038/ncomms10362 (2016).

49. Bliokh, K. Y., Bekshaev, A. Y. & Nori, F. Optical Momentum, Spin, and Angular Momentum in Dispersive Media. *Physical Review Letters* **119.** doi:10.1103/PhysRevLett.119.073901 (2017).

50. Bliokh, K. Y., Kivshar, Y. S. & Nori, F. Magnetoelectric Effects in Local Light-Matter Interactions. *Physical Review Letters* **113.** doi:10.1103/PhysRevLett.113.033601 (2014).

51. See Supplemental Material at http://link.aps.org/supplemental/10.1103/PhysRevLett.120.117402 for a numerical simulation of a Janus dipole between 3D silicon waveguides; and the description of *s*-polarized evanescent fields; and the angular spectrum appro.

52. Saleh, B. E. A. & Teich, M. C. *Fundamentals of Photonics* doi:10.1002/0471213748 (John Wiley & Sons, Inc., New York, USA, 1991).

Janus and Huygens' dipoles: near-field directionality beyond spin-momentum locking Supplementary Materials

S1. Numerical simulations of the Janus dipole between three-dimensional waveguides

In the main text, we described the simple case of a dipole near planar waveguides. Here we consider the placement of a Janus dipole between realistic three-dimensional (3D) silicon waveguides. The simulations were performed using the commercial CST Microwave Studio software. Electric and magnetic dipole sources were modelled as linear and loop currents, respectively. A Janus dipole was placed between two standard silicon nanowire waveguides optimized for TM-polarized mode at a telecommunication wavelength of $\lambda = 1,550$ nm. The Janus dipole having a magnetic component normal to the plane in which waveguides are situated excites the mode of the upper waveguide in both directions, while not coupling to the lower waveguide. The simulated spatial distribution of the magnetic field amplitude is shown in Fig. S1. The effect is robust with respect to the distance between the waveguides and the distance between the dipole and each waveguide, as long as it is small enough to allow near-field coupling.

S2. General equation for *s*-polarized evanescent fields

In the case of s-polarized fields, Maxwell's equations imply that the electromagnetic fields when $k_y = 0$ are given by $\mathbf{F}_s = (c\mu H_x, E_y, c\mu H_z) \propto (\frac{\pm i\alpha_m}{k}, -1, -\frac{\pm k_m}{k})$, and writing the relevant dipole components as $\mathbf{q}_s = (m_x/c, p_y, m_z/c)$, the near-field destructive interference condition based on Fermi's golden rule can be written as $\mathbf{q}_s \cdot \mathbf{F}_s^* = 0$. The solutions to this equation are summarised in Table I of the main text.

S3. Optimization of dipoles and their angular spectrum visualization

As derived in the main text and summarized in Table I, the optimized conditions for Huygens' and Janus dipoles to achieve zero coupling to a mode with wavenumber k_m can be written compactly as:

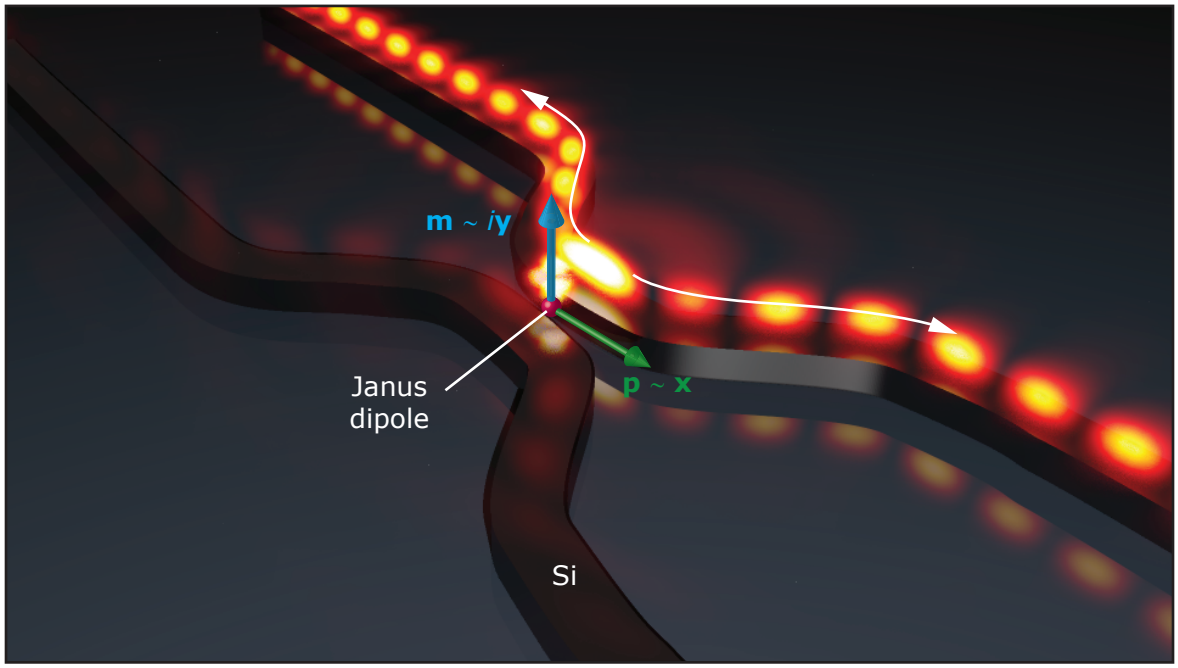

Figure S1: Three dimensional rendering of the simulated magnetic field amplitude of the modes in the system of two identical Si-waveguides excited by an optimized Janus dipole. The fields have been shifted in space so that they appear above the waveguides. The cross section of silicon waveguides is $(0.2 \times 0.16)\lambda$. The refractive index of silicon at $\lambda = 1,550$ nm was taken as $n = 3.45$. An animated version of the field evolution is available as Supplementary Video.

$$\frac{\pm k_m^*}{k} p = \frac{m}{c} \qquad \text{and} \qquad \frac{\pm i\alpha_m^*}{k} p = \frac{m}{c}, \tag{S1}$$

respectively. The first equation corresponds to the Huygens' dipole and constitutes a generalized Kerker's condition which works for both evanescent and propagating waves. It, in fact, reduces to the *conventional* Kerker's condition for $k_m = k$, corresponding to propagating radiated waves:

$$p = \frac{m}{c}. \tag{S2}$$

Note that Eq. S2 corresponds to Eq. 1 in the main text. The angular spectrum of the source provides a convincing visual explanation of this optimization. In Fig. S2, we plot the angular spectra of the fields below the three elemental sources in two

different cases: the blue spectra are for the simplest dipoles, while the red ones have been optimized so that the dipoles match the mode supported by the waveguide.

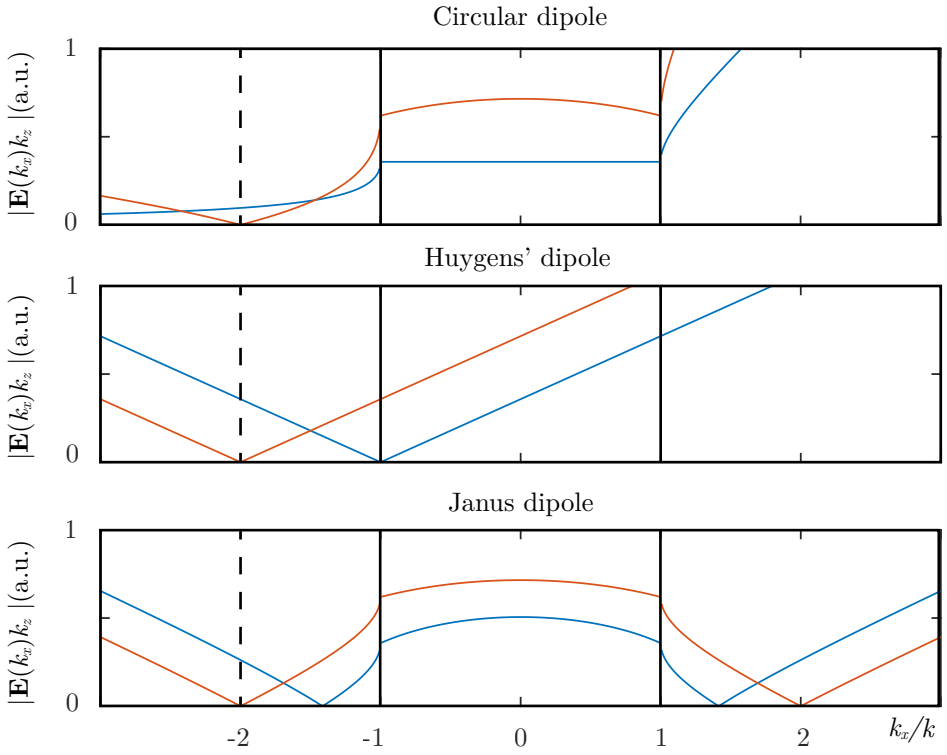

Figure S2: Electric field amplitude angular spectra of dipolar sources in a homogeneous medium as a function of spatial frequency k_x with $k_y = 0$, for the case of (blue) the simplest dipoles and (red) the optimized dipoles, optimized for zero coupling to a mode with $k_m = -2k$. The simplest dipoles are given by $(p_x, m_y/c, p_z) \propto (1, 0, i)$, $(0, -1, 1)$ and $(1, i, 0)$ for circular, Huygens' and Janus sources, respectively, while their optimized versions can be found in Table I in the main text.

S4. Deriving directionality from the angular spectrum of electric and magnetic dipole fields

In the main text, we derived the condition for directionality using the Fermi's golden rule. Here, we show that the same result can be obtained exploiting the angular spectrum representation of electric and magnetic dipoles sources.

We start from our results in Ref. [1] where we derived the angular spectra amplitudes

of the electric field generated by electric and magnetic dipoles as:

$$\mathbf{E}^{\mathrm{ED}}(k_x,k_y)|_{z=z_0} = \frac{ik^2}{8\pi^2\varepsilon}\frac{1}{k_z}\left[(\hat{\mathbf{e}}_s\cdot\mathbf{p})\hat{\mathbf{e}}_s + (\hat{\mathbf{e}}_p\cdot\mathbf{p})\hat{\mathbf{e}}_p\right],$$
$$\mathbf{E}^{\mathrm{MD}}(k_x,k_y)|_{z=z_0} = -\frac{ik^2}{8\pi^2\varepsilon}\frac{1}{k_z}\frac{1}{c}\left[(\hat{\mathbf{e}}_p\cdot\mathbf{m})\hat{\mathbf{e}}_s - (\hat{\mathbf{e}}_s\cdot\mathbf{m})\hat{\mathbf{e}}_p\right],$$

these can be summed to give:

$$\mathbf{E}(k_x,k_y)|_{z=z_0} = \frac{ik^2}{8\pi^2\varepsilon}\frac{1}{k_z}\left[\left(\hat{\mathbf{e}}_s\cdot\mathbf{p} - \hat{\mathbf{e}}_p\cdot\frac{\mathbf{m}}{c}\right)\hat{\mathbf{e}}_s + \left(\hat{\mathbf{e}}_p\cdot\mathbf{p} + \hat{\mathbf{e}}_s\cdot\frac{\mathbf{m}}{c}\right)\hat{\mathbf{e}}_p\right]. \tag{S3}$$

The unit vectors $\hat{\mathbf{e}}_s$ and $\hat{\mathbf{e}}_p$ are the ones corresponding to s- and p-polarized fields, respectively, and are given by:

$$\begin{aligned}\hat{\mathbf{e}}_s &= \frac{\hat{\mathbf{z}}\times\hat{\mathbf{k}}}{\sqrt{(\hat{\mathbf{z}}\times\hat{\mathbf{k}})\cdot(\hat{\mathbf{z}}\times\hat{\mathbf{k}})}},\\ \hat{\mathbf{e}}_p &= \hat{\mathbf{e}}_s\times\hat{\mathbf{k}},\end{aligned} \tag{S4}$$

where $\hat{\mathbf{k}} = \mathbf{k}/k$ is the normalized wave-vector, with the property that $\hat{\mathbf{k}}\cdot\hat{\mathbf{k}} = \hat{\mathbf{e}}_s\cdot\hat{\mathbf{e}}_s = \hat{\mathbf{e}}_p\cdot\hat{\mathbf{e}}_p = 1$ and $\hat{\mathbf{e}}_s\cdot\hat{\mathbf{e}}_p = 0$. Using Eq. S4, we can then substitute $\hat{\mathbf{e}}_p$ into Eq. S3, obtaining:

$$\mathbf{E}(k_x,k_y)|_{z=z_0} = \frac{ik^2}{8\pi^2\varepsilon}\frac{1}{k_z}\left\{\left[\hat{\mathbf{e}}_s\cdot\mathbf{p} - (\hat{\mathbf{e}}_s\times\hat{\mathbf{k}})\cdot\frac{\mathbf{m}}{c}\right]\hat{\mathbf{e}}_s + \left[(\hat{\mathbf{e}}_s\times\hat{\mathbf{k}})\cdot\mathbf{p} + \hat{\mathbf{e}}_s\cdot\frac{\mathbf{m}}{c}\right]\hat{\mathbf{e}}_p\right\}. \tag{S5}$$

Applying the scalar triple product cyclic property, we can finally arrive at a compact exact mathematical expression that describes any arbitrary dipole source angular spectrum:

$$\mathbf{E}(k_x,k_y)|_{z=z_0} = \frac{ik^2}{8\pi^2\varepsilon}\frac{1}{k_z}\left\{\left[\hat{\mathbf{e}}_s\cdot\left(\hat{\mathbf{k}}\times\mathbf{p} + \frac{\mathbf{m}}{c}\right)\right]\hat{\mathbf{e}}_p + \left[\hat{\mathbf{e}}_s\cdot\left(\mathbf{p} - \hat{\mathbf{k}}\times\frac{\mathbf{m}}{c}\right)\right]\hat{\mathbf{e}}_s\right\}, \tag{S6}$$

from which the directional properties of any dipole source immediately follow, both in propagating and evanescent components. Eq. S6 is plotted in Fig. S2 for different sources, clearly showing the directionality properties.

Equation S6 describes the fields of the isolated source in a homogeneous medium. We would like to consider the effects of placing this dipole in near proximity to a

waveguide. Let's consider, for simplicity, a planar waveguide along the xy plane, supporting a guided mode with propagation constant k_m. The fraction of power generated by the source that is coupled to this mode on each direction depends on the overlap between the source's angular spectra and the waveguide mode angular spectra [1, 2]. The angular distribution of excitation of the mode in the waveguide will thus be proportional to the amplitude of the spectral component having the transverse wavevector $\mathbf{k}_t = (k_m \cos\phi,\, k_m \sin\phi)$ at each angle ϕ. To determine the contrast ratio between light coupled in two opposite directions, we can reorient our axes such that $k_y = 0$ without loss of generality, and compare the $\mathbf{k}_t = (-k_m, 0)$ and $(+k_m, 0)$ dipole components. In particular, we can make one of them identically zero. To achieve this, we simply have to equate the field angular spectrum (Eq. S6) to zero at a certain $\hat{\mathbf{k}}$, i.e. forcing an evanescent component to be zero. We only need to do this for the term in Eq. S6 corresponding to the same polarization as the mode we are interested in. For example, if the mode is p-polarized, we take the term polarized along $\hat{\mathbf{e}}_p$ and equate it to zero:

$$\hat{\mathbf{y}} \cdot \left(\hat{\mathbf{k}} \times \mathbf{p} + \frac{\mathbf{m}}{c} \right) = 0, \tag{S7}$$

where we used the fact that $\hat{\mathbf{e}}_s = \hat{\mathbf{y}}$ when $k_y = 0$. Notice that by substituting $\hat{\mathbf{k}} = (1/k)(\pm k_m, 0, \pm i\alpha_m)$, Eq. S7 can be written as $p_x(\pm i\alpha_m/k) - p_z(\pm k_m/k) + m_y/c = 0$ which is exactly the same condition as in the main text when k_m is real. In contrast to the equation derived from Fermi's golden rule, this time the positive (negative) sign in α_m corresponds to the fields above (below) the dipole, because $\hat{\mathbf{k}}$ refers to the wave-vector of the dipole fields, and not those of the waveguide mode. Curiously, substituting $\hat{\mathbf{e}}_p = \hat{\mathbf{e}}_s \times \hat{\mathbf{k}}$, in the s-polarized component of Eq. S3, and $\hat{\mathbf{e}}_s = -\hat{\mathbf{e}}_p \times \hat{\mathbf{k}}$ in the p-polarized one, the two components can be written in a very convenient way:

$$\begin{aligned}
\mathbf{E}(k_x, k_y)|_{z=z_0} &= \frac{ik^2}{8\pi^2\varepsilon}\frac{1}{k_z}\left\{ \left[\hat{\mathbf{e}}_s \cdot \mathbf{p} - (\hat{\mathbf{e}}_s \times \hat{\mathbf{k}}) \cdot \frac{\mathbf{m}}{c} \right] \hat{\mathbf{e}}_s + \left[\hat{\mathbf{e}}_p \cdot \mathbf{p} - (\hat{\mathbf{e}}_p \times \hat{\mathbf{k}}) \cdot \frac{\mathbf{m}}{c} \right] \hat{\mathbf{e}}_p \right\} \\
&= \frac{ik^2}{8\pi^2\varepsilon}\frac{1}{k_z}\left\{ \left[\hat{\mathbf{e}}_s \cdot \left(\mathbf{p} - \hat{\mathbf{k}} \times \frac{\mathbf{m}}{c} \right) \right] \hat{\mathbf{e}}_s + \left[\hat{\mathbf{e}}_p \cdot \left(\mathbf{p} - \hat{\mathbf{k}} \times \frac{\mathbf{m}}{c} \right) \right] \hat{\mathbf{e}}_p \right\} \\
&= \frac{ik^2}{8\pi^2\varepsilon}\frac{1}{k_z}\left(\mathbf{p} - \hat{\mathbf{k}} \times \frac{\mathbf{m}}{c} \right) \left[(\cdot\, \hat{\mathbf{e}}_s)\, \hat{\mathbf{e}}_s + (\cdot\, \hat{\mathbf{e}}_p)\, \hat{\mathbf{e}}_p \right].
\end{aligned}$$

In this way, the amplitude of the s-polarized component is given by the dot product of $\hat{\mathbf{e}}_s$ with the vector $\mathbf{v} = \mathbf{p} - \left(\hat{\mathbf{k}} \times \frac{\mathbf{m}}{c} \right)$, and the amplitude of the p-polarized component

is given by the dot product of $\hat{\mathbf{e}}_p$ with the same vector $\mathbf{v}$. This is even more compact than Eq. S6 but is slightly less convenient for the derivation of optimized dipoles.

3.9 Paper C

Europhysics News ***49***, *14-18 (2018)*

Not every dipole is the same: the hidden patterns of dipolar near fields

Michela F. Picardi, Anatoly V. Zayats
and Francisco J. Rodríguez-Fortuño

Not every dipole is the same: the hidden patterns of dipolar near fields

Michela F. Picardi[1], Anatoly V. Zayats[1]
and Francisco J. Rodríguez-Fortuño[1]

[1] *Department of Physics, King's College London, Strand, London WC2R 2LS, United Kingdom*

Nanophotonics is a fast-evolving scientific field studying light at the nanoscale. Its fascinating advances typically stem from concepts in modern physics, such as quantum optics, photonic crystals and optomechanics [1]. Occasionally, new insights appear even from the classical Maxwell's equations of electromagnetism themselves [2].

Here we outline recently uncovered features of dipoles, the humblest among electromagnetic sources, whose interactions with a nearby structure can nevertheless be unexpectedly rich in terms of their selective excitation of guided modes. This has important applications throughout nanophotonics, from optical information technologies to the design of advanced photonic devices. Dipolar sources are ubiquitous in every branch of nanophotonics due to their universality. Atoms, quantum dots and other point-like sources, when emitting light, behave as dipoles. Light scattered off any small illuminated particle also does. Matter itself, in its interaction with light, can be regarded as a collection of point dipoles. Dipoles are technologically important; in nanophotonics they are a fundamental tool for the analysis and design of experiments involving near-field instrumentation such as the detector tips in near field optical microscopy or the optical excitations caused by incident electron beams in a cathodoluminescence scanning electron microscope. These kinds of equipment rely on their interaction with optical near-fields of structures - for which the dipole model is perfectly suited. In fact, it is in the properties of these near-field interactions that new behaviours have recently been observed.

Fundamentals of dipolar sources

Unlike classical gravitational fields, which can be well approximated to first order with knowledge of the total mass of objects, electromagnetic fields may originate from sources with a net zero charge, and so one looks at the next dominant term in the series expansion: the dipole. As we all know, electromagnetic dipoles come in two varieties: electric and magnetic (Fig. 1). Electric and magnetic dipole moments $\mathscr{p}(t)$ and $\mathscr{m}(t)$ vary with time. Fortunately, the superposition principle allows us to consider the monochromatic constituents of any time dependent dipole, such that we may study a harmonically oscillating dipolar source radiating fields of a given, fixed, wavelength. This allows us to eliminate the time-dependence in the dipole moments, at the expense of using complex vectors $\mathbf{p}$ and $\mathbf{m}$ with real and imaginary components accounting for the amplitude and phase of their sinusoidal oscillation. For example, $\mathbf{p} = (1, 1, 0)$ corresponds to a linearly polarized dipole, oscillating parallel to the $x = y$ line, while $\mathbf{p} = (1, i, 0)$ corresponds to a circularly polarized electric dipole, rotating anticlockwise in the xy plane. The complex nature of the dipole moment, which fully determines its phase, amplitude and polarization, is at the heart of the dipole's remarkable directionality properties. The experimental realization in optical laboratories of electric and magnetic dipoles with determined polarizations is simple. One way is via illumination of small particles which become electrically and magnetically polarized [Fig. 1(c)]. The polarization of the dipolar source that can be generated with this method depends on two factors, the first being the polarization of the fields incident on the particle, which can be easily manipulated. The second factor is the polarizability response of the nanoparticle, which varies in amplitude and phase depending on particle geometry and working wavelength. A fine control on these elements can ensure the possibility to generate any desired dipolar source with an arbitrary polarization.

Directionality of circularly polarized dipoles

A first hint that not all dipoles are equal came from the stunning, elegant behaviour of circularly polarized dipoles. We always resort to linearly polarized dipoles when we learn, think, and teach about them, with the assumption that any other polarized dipole is just a superposition of linear ones: while true, this neglects the fact that superposition and interference can yield interesting physical effects. Interference is usually associated with the propagation phase acquired by light along different

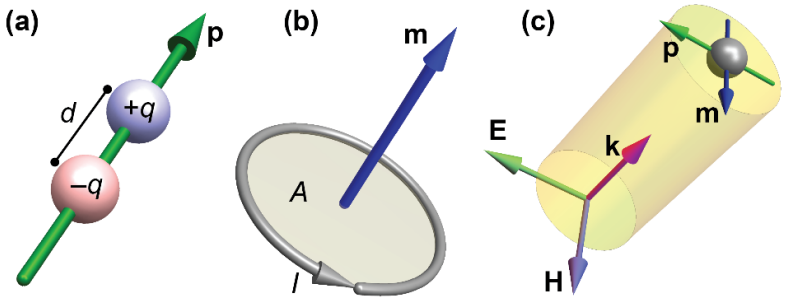

Figure 1: (a) The electric dipole moment vector **p** is the product between the charge constituting each of its poles q, and their separation distance **d**. (b) The magnetic dipole moment vector m is the product between the amplitude of a circulating current I and the area it encloses $A\hat{n}$, in a direction $\hat{n}$ normal to the area. Both converge to point sources in the appropriate limit. (c) A polarizable particle being illuminated by an incident beam with wave-vector **k**, electric field **E**, and magnetic field **H**. The particle becomes polarized and behaves like a dipolar source with dipole moments proportional to the incident fields $\mathbf{p} = \alpha_e \mathbf{E}$ and $\mathbf{m} = \alpha_m \mathbf{H}$ with $\alpha_{e/m}$ representing complex proportionality constants, which are the particle's electric and magnetic polarizability.

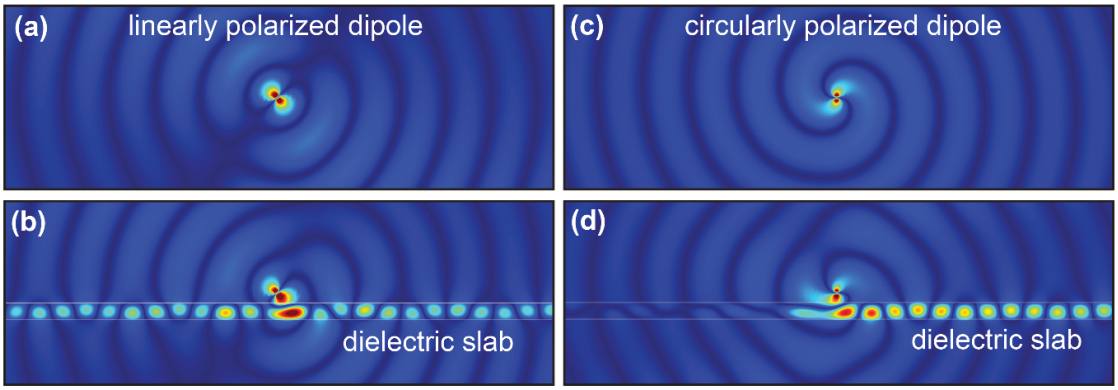

Figure 2: Snapshot of radiated magnetic field amplitude of a linearly (a,b) and circularly (c,d) polarized electric dipole radiating either in freespace (a,c) or at a sub-wavelength distance 0.1λ near a dielectric waveguide (b,d). The phenomenon exists for any kind of waveguide. In this figure we chose a dielectric slab with refractive index $n = 3$ and thickness $t = 0.2\lambda$.

trajectories, but it also applies to the near fields. Fig. 2(a) depicts a linearly polarized dipole $\mathbf{p} = (1, 1, 0)$ radiating in free space, with its familiar radiation diagram. Fig. 2(b) shows this same dipole placed close to an optical waveguide - and we see that optical modes are excited. This is possible thanks to the dipole nearfields. The coupling interaction between point dipoles and nearby waveguides is a well-known property of dipolar sources. Fig. 2(c) shows a circularly polarized dipole $\mathbf{p} = (1, i, 0)$ radiating in free space, and Fig. 2(d) shows the same dipole near an optical waveguide [3]. We see that, surprisingly and despite the mirror symmetry of this structure, the circularly polarized dipole excites modes in a single direction of the waveguide. This is a fundamental behaviour of the dipole, inherently broadband, robust to losses and imperfections. Remarkably, it admits many different but equivalent explanations, detailed in Box 1. The excitation of light modes from this circularly polarized dipole resembles a water wheel for light. When a circularly polarized dipole is sandwiched between two waveguides [Fig 3(a)], both are excited in opposite directions. Known for a few years now, this unique directionality has yielded fascinating applications such as ultracompact broadband optical nanorouting [3, 4], polarization analysers [5], quantum optical applications [6] including non-reciprocal nanophotonic devices [7], exotic lateral optical and Casimir forces [8, 9], generation of polarized light [10], and many others. And yet this dipole is but a first taste of how not every dipole is the same.

Box 1. A variety of explanations for the near-field directionality of dipoles can be given, all being ultimately equivalent, but each highlighting different aspects.

Phase matching between the dipole fields and the waveguide: The phase matching of fields along smooth interfaces requires that the moving wave-fronts of a source must match the moving wavefronts of the mode being excited. Consider the fields radiated from the circular dipole depicted in Fig. 2(c). Its wave-fronts are counterclockwise rotating spirals. Clearly, if a waveguide is placed below the dipole as in Fig. 2(d), the wave-fronts sweep the waveguide from left to right, matching the wave-fronts of the guided mode propagating in the waveguide in the left to right direction, which gets excited. Indeed, placing the waveguide above the dipole would switch the directionality to the left, in agreement with a waterwheel analogy.

Superposition of excitations with different symmetries: Consider a vertically polarized dipole $\mathbf{p} = a\hat{\mathbf{y}}$, over a dielectric waveguide. Due to the complete mirror symmetry of the problem, modes are excited in the waveguide in both directions, exactly in phase. The field will have an even symmetry with respect to the mirror-symmetry plane. Now consider a horizontal dipole $\mathbf{p} = b\hat{\mathbf{x}}$. This dipole is oscillating, alternatively pointing left and right, and this will evidently excite modes in both directions with identical amplitude, but exactly out of phase, constituting an odd symmetry of excitation. By a judicious superposition of both, horizontal and vertical components of the dipole result in the addition of an even and an odd function, which may produce a highly asymmetrical total field resulting in unidirectional excitation. This is the case for the circular dipole. In general, any dipole $\mathbf{p}$ and $\mathbf{m}$ is a superposition of six components, which can all interfere between each other.

Overlap of the dipole's fields with the guided fields: The amount of coupling between a dipolar source $\mathbf{p}$ and $\mathbf{m}$, and a waveguided mode with electric and magnetic fields $\mathbf{E}$ and $\mathbf{B}$ (evaluated at the location of the dipole) is given by Fermi's golden rule $|\mathbf{p}^* \cdot \mathbf{E} + \mathbf{m}^* \cdot \mathbf{B}|^2$ involving dot products between dipole moments and fields, where $*$ signifies complex conjugation [11]. In the case of the circularly polarized electric dipole, the excitation along one direction is zero because $\mathbf{p}^* \cdot \mathbf{E} = 0$ for the field of the mode in that direction. For example, $(1, i, 0)^* \cdot (1, -i, 0) = 0$. This happens because the electric field of the waveguided mode indeed has a near circular polarization $\approx (1, \pm i, 0)$ whose handedness depends on its propagation direction, a phenomenon named spin-momentum locking [12, 13]. In a more general case, the expression $\mathbf{p}^* \cdot \mathbf{E} + \mathbf{m}^* \cdot \mathbf{B}$ is composed of the sum of six different terms, corresponding to how each component of the dipole excites each mode: this sum may easily interfere destructively for certain dipoles and waveguide modes [14]. This explanation gives an equal focus to both the dipoles and the fields of the specific waveguide, betraying the fact that the directionality is a universal property of the dipole, valid for any waveguide. It has the advantage of being an exact valid explanation in any scenario, such as dipolar sources inside photonic crystals.

Angular spectrum of the dipolar fields: This explanation mathematically fleshes-out the simple phase matching argument given above. It is most powerful when the dipole is placed near smooth interfaces which conserve momentum

and thus allow us to apply phase matching arguments. With it, we realize that the directionality of the dipole is a property of the dipole itself, universal for any waveguide [15]. It is based on a careful analysis of the fields produced by a dipole [16], whose exact analytical form has been known for as long as Maxwell's equations themselves. The amplitude and phase of the electric field $\mathbf{E}(\mathbf{r})$ originating from a dipole, at any point in space $\mathbf{r}$, can be written in a short single-line equation. We may then analyse this field by means of its spatial Fourier transform $\mathbf{E}(\mathbf{r}) = \iiint d\mathbf{k}\mathbf{E}(\mathbf{k})e^{i\mathbf{k}\cdot\mathbf{r}}$, where $\mathbf{E}(\mathbf{k})$ is the constant electric field amplitude of a plane wave or evanescent wave with wave-vector $\mathbf{k} = (k_x, k_y, k_z)$ and $e^{i\mathbf{k}\cdot\mathbf{r}}$ describes its propagation or attenuation through space. We have "spread out" the field into its spatial components, called its spatial or angular spectrum. In the phase matching argument above, we pointed out from an intuitive and hand-wavy argument that the phase fronts of a circularly polarized dipole sweep from left to right when looking below the dipole, explaining its directionality. Indeed, the angular spectrum of such dipole reveals the dominance of evanescent components with wave-vectors $\mathbf{k}$ pointing from left to right when looking from below the dipole [15], providing a solid quantitative foundation to our intuitive notion. Janus and Huygens dipoles exhibit similar imbalances in their angular spectra, fully explaining their behaviour and symmetries.

Beyond circularly polarized dipoles: a zoo of directional dipoles

Using the analysis techniques described in Box 1, we recently asked ourselves what other unconventional dipolar sources could be found. By combining electric and magnetic dipoles together, new directional dipolar source behaviours are revealed [14]. The idea of combining electric and magnetic dipoles to obtain distinct functionality is not new. The Huygens dipole is a source which combines two linearly polarized orthogonal electric $\mathbf{p}$ and magnetic $\mathbf{m}$ dipoles with an amplitude ratio of $p = m/c$, where c is the speed of light, such that their combined radiation is directional in the far-field in the $\mathbf{p} \times \mathbf{m}$ direction. For example, $\mathbf{p} = (1, 0, 0)$ and $\mathbf{m} = (0, c, 0)$ show complete far field directionality in the $+z$ direction. The radiations of the electric and magnetic dipoles, omnidirectional when on their own, interfere destructively in one direction but constructively in the opposite one, resulting in unidirectionality. This has been used to create engineered surfaces with perfect reflection, and all-dielectric

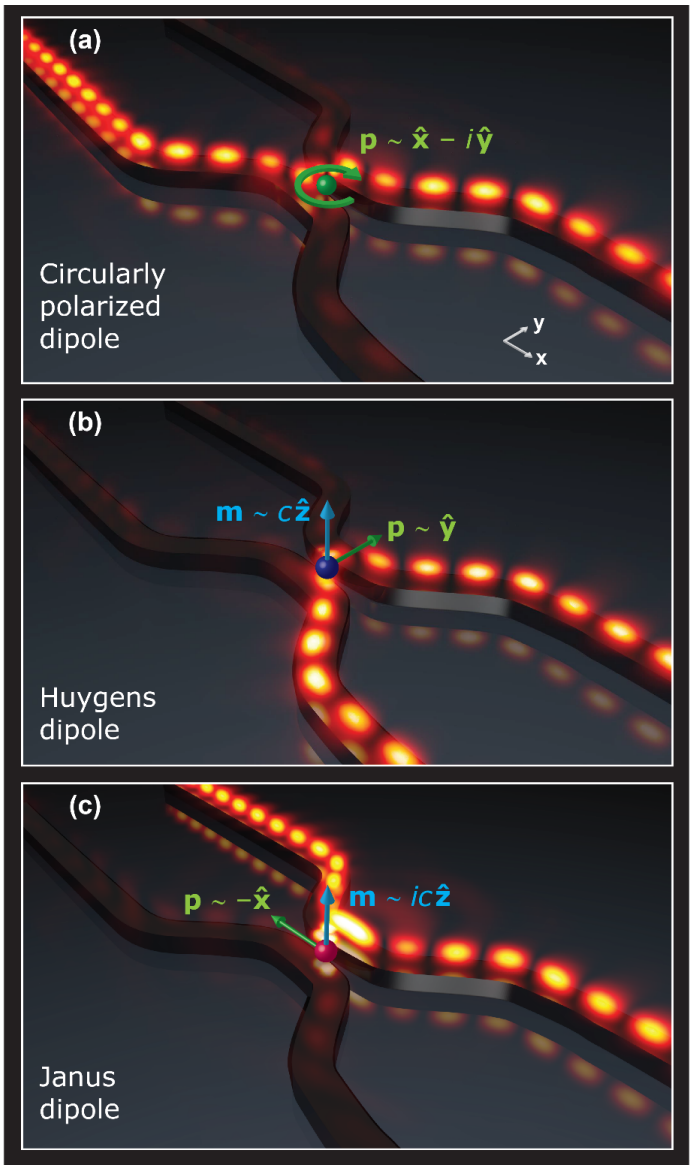

Figure 3: Behaviour of three different dipolar sources: (a) circular (b) Huygens and (c) Janus dipoles, sandwiched between two standard silicon nanophotonic waveguides. The dipole moments where optimized for optimal directionality contrast as described in Ref. [14]. The figure renders a snapshot of the field intensity of a real three dimensional numerical simulation. The simulation was performed in the commercial electromagnetic solver CST Microwave Studio. The fields are shown shifted in space so that they appear above the waveguides instead of inside. The cross section of these silicon waveguides is $(0.2 \times 0.16)\lambda$. The refractive index of silicon at $\lambda = 1550nm$ was taken as $n = 3.45$. Notice that the three sources are intimately related to the three spatial symmetries of the underlying structure: two mirror symmetries along orthogonal planes, and a half-turn rotational symmetry.

mirrors among other applications [17]. It turns out that the same phenomenon exists in the dipole's near-field [14]. The Huygens dipole exhibits a different symmetry of near-field excitation compared to the circular one: when sandwiched between waveguides, it couples to the modes in the waveguides along the same direction for both [Fig. 3(b)]. Both circular and Huygens dipoles appear as solutions of a single equation, yet a third solution completes the set [14]. This novel dipole greatly resembles the Huygens dipole, in that it too is a combination of linearly polarized and orthogonal dipoles, but its electric and magnetic dipoles are in quadrature phase, that is, with a $\pi/2$ phase difference between dipole moment amplitudes. It does not show any directional behaviour in the far-field, and yet it shows unique and surprising properties in its near field coupling. This source, like its namesake ancient Roman god Janus, has two faces. One face enables coupling into nearby waveguides, while the opposite face is non-coupling to them. Therefore, flipping the Janus dipole's face as if it were a coin, enables switching the coupling on or off. Equivalently, the binary state of the coupling depends on which side of the dipole the waveguide is placed. When sandwiched between two waveguides, the Janus dipole couples to both directions on the same waveguide, the one facing its coupling side, while blatantly ignoring the other one [Fig. 3(c)]. These new near-field dipolar sources all follow the same explanations given in Box 1, ultimately relying on near-field interference between distinct dipolar components.

Conclusions

The three elemental dipoles shown in Fig. 3 arise as solutions from one same equation, describing dipole directionality in a simplified planar waveguide scenario [14]. In fact, any linear combination of the three elemental sources results in an infinite range of possible directional dipole sources. More complex three-dimensional scenarios and more complex waveguide geometries will enable even further examples of directional dipoles, opening a zoo of possibilities. The behaviour is fundamental and robust. Given the amount of applications that arose from circularly polarized dipoles alone, we expect these new dipolar possibilities to give rise to a plethora of new ideas. As a simple example, the directionality of circularly polarized dipoles was used as a method for local measurement of the transverse electric field polarization: the generalization of the concept will allow local measurement of all spatial components of both electric and magnetic fields in complex structured electromagnetic beams. New ideas can

arise in a wide array of areas such as quantum optics, optical logical circuits, photonic nanorouting, polarization detection and synthesis, novel optical forces and torques in nanoparticles, and hopefully in as yet unforeseen devices throughout nanophotonics and other regions of the electromagnetic spectrum.

REFERENCES

1. Heber, J. & Trabesinger, A. Nature Milestones Photons. *Nature* (2010).
2. Engheta, N. 150 years of Maxwell's equations. *Science.* doi:10.1126/science.aaa7224 (2015).
3. Rodríguez-Fortuño, F. J. *et al.* Near-field interference for the unidirectional excitation of electromagnetic guided modes. *Science* **340.** doi:10.1126/science.1233739 (2013).
4. Petersen, J., Volz, J. & Rauschenbeutel, A. Chiral nanophotonic waveguide interface based on spin-orbit interaction of light. *Science* **346.** doi:10.1126/science.1257671 (2014).
5. Espinosa-Soria, A., Rodríguez-Fortuño, F. J., Griol, A. & Martínez, A. On-Chip Optimal Stokes Nanopolarimetry Based on Spin-Orbit Interaction of Light. *Nano Letters* **17.** doi:10.1021/acs.nanolett.7b00564 (2017).
6. Marrucci, L. Quantum optics: Spin gives direction. *Nature Physics* **11.** doi:10.1038/nphys3198 (2015).
7. Scheucher, M., Hilico, A., Will, E., Volz, J. & Rauschenbeutel, A. Quantum optical circulator controlled by a single chirally coupled atom. *Science* **354.** doi:10.1126/science.aaj2118 (2016).
8. Rodríguez-Fortuño, F. J., Engheta, N., Martínez, A. & Zayats, A. V. Lateral forces on circularly polarizable particles near a surface. *Nature Communications* **6.** doi:10.1038/ncomms9799 (2015).
9. Manjavacas, A., Rodríguez-Fortuño, F. J., Javier García De Abajo, F. & Zayats, A. V. Lateral Casimir Force on a Rotating Particle near a Planar Surface. *Physical Review Letters.* doi:10.1103/PhysRevLett.118.133605 (2017).
10. Rodríguez-Fortuño, F. J. *et al.* Universal method for the synthesis of arbitrary polarization states radiated by a nanoantenna. *Laser & Photonics Reviews* **8.** doi:10.1002/lpor.201300184 (2014).
11. Le Feber, B., Rotenberg, N. & Kuipers, L. Nanophotonic control of circular dipole emission. *Nature Communications* **6.** doi:10.1038/ncomms7695 (2015).
12. Aiello, A., Banzer, P., Neugebauer, M. & Leuchs, G. From transverse angular momentum to photonic wheels. *Nature Photonics* **9.** doi:10.1038/nphoton.2015.203 (2015).

13. Bliokh, K. Y., Smirnova, D. & Nori, F. Quantum spin Hall effect of light. *Science* **348.** doi:10.1126/science.aaa9519 (2015).

14. Picardi, M. F., Zayats, A. V. & Rodríguez-Fortuño, F. J. Janus and Huygens Dipoles: Near-Field Directionality Beyond Spin-Momentum Locking. *Physical Review Letters* **120.** doi:10.1103/PhysRevLett.120.117402 (2018).

15. Picardi, M. F., Manjavacas, A., Zayats, A. V. & Rodríguez-Fortuño, F. J. Unidirectional evanescent-wave coupling from circularly polarized electric and magnetic dipoles: An angular spectrum approach. *Physical Review B* **95.** doi:10.1103/PhysRevB.95.245416 (2017).

16. Jackson, J. D. *Classical Electrodynamics, 3rd Edition* doi:10.1002/3527600434.eap109 (1998).

17. Geffrin, J. *et al.* Magnetic and electric coherence in forward- and back-scattered electromagnetic waves by a single dielectric subwavelength sphere. *Nature Communications* **3.** doi:10.1038/ncomms2167 (2012).

3.10 Paper D

Light: Science & Applications ***8***, *52 (2019)*

Experimental demonstration of linear and spinning Janus dipoles for polarisation- and wavelength-selective near-field coupling

Michela F. Picardi, Martin Neugebauer, Jörg S. Eismann, Gerd Leuchs, Peter Banzer, Francisco J. Rodríguez-Fortuño and Anatoly V. Zayats

---

Experimental demonstration of linear and spinning Janus dipoles for polarisation- and wavelength-selective near-field coupling

Michela F. Picardi[1], Martin Neugebauer[2,3], Jörg S. Eismann[2,3], Gerd Leuchs[2,3], Peter Banzer[2,3], Francisco J. Rodríguez-Fortuño[1] and Anatoly V. Zayats[1]

[1] *Department of Physics, King's College London, Strand, London WC2R 2LS, United Kingdom*
[2] *Max Planck Institute for the Science of Light, Staudtstr. 2, D-91058, Erlangen, Germany*
[3] *Institute of Optics, Information and Photonics, University Erlangen-Nuremberg, Staudtstr. 7/B2, D-91058, Erlangen, Germany*

The electromagnetic field scattered by nano-objects contains a broad range of wavevectors and can be efficiently coupled to waveguided modes. The dominant contribution to scattering from subwavelength dielectric and plasmonic nanoparticles is determined by electric and magnetic dipolar responses. Here, we experimentally demonstrate spectral and phase selective excitation of Janus dipoles, sources with electric and magnetic dipoles oscillating out of phase, in order to control near-field interference and directional coupling to waveguides. We show that by controlling the polarisation state of the dipolar excitations and the excitation wavelength to adjust their relative contributions, directionality and coupling strength can be fully tuned. Furthermore, we introduce a novel spinning Janus dipole featuring cylindrical symmetry in the near and far field, which results in either omnidirectional coupling or noncoupling. Controlling the propagation of guided light waves via fast and robust near-field interference between polarisation components of a source is required in many applications in nanophotonics and quantum optics.

Scattered fields from plasmonic and dielectric nanostructures contain a broad range of wavevectors [1], which makes them suitable for efficient coupling to waveguided modes. Such nanostructures underpin applications in photonic data manipulation, quantum technologies and precision metrology. Nanoparticle scattering is often dominated by lowest-order multipoles, electric and magnetic dipoles, whose near-

and far-field interference can be controlled at ultrafast speeds by tuning the amplitudes and phases between dipolar components [2–4]. For example, spin-momentum locking of guided light that is excited by circularly polarised dipoles [5–10] has led to numerous applications in quantum optics [11–13] and optical manipulation [14–16]. Recently, a dipolar source that exhibits a face-dependent coupling behaviour was theoretically predicted, the "Janus dipole", which is composed of out-of-phase electric and magnetic dipoles [17]. Here, we experimentally demonstrate the excitation of such a Janus dipole using a silicon nanoparticle and measure its characteristic near-field angular spectral signature. Furthermore, we introduce a spinning Janus dipole that features cylindrical symmetry, which provides either omnidirectional coupling or noncoupling.

Previous experimental demonstrations of near-field directional coupling of dipolar sources have been realised with circularly polarised dipoles. While circularly polarised electric dipoles, which are comprised of two orthogonal linear electric dipoles that oscillate with a phase difference of $\pm\pi/2$, excite unidirectionally p-polarised waveguide modes, circular magnetic dipoles can be used to excite s-polarised modes [18]. By superimposing electric and magnetic dipole contributions, additional degrees of freedom in engineering directionality can be harnessed via their interference [19–21]. For example, the well-known Huygens dipole is a combination of orthogonally oriented, in-phase electric $\mathbf{p}$ and magnetic $\mathbf{m}$ dipoles that satisfy Kerker's scattering condition, which is expressed as $p = m/c$, where c denotes the speed of light. This source has been experimentally demonstrated to exhibit directionality in the far-field [22–24] and is employed in reflectionless dielectric metasurfaces [25, 26]. However, when the electric and magnetic dipoles are perpendicular to each other, as in the Huygens dipole, but $\pm\pi/2$ out of phase, the resulting source is the so-called Janus dipole, which has only recently been predicted theoretically [17]. The Janus dipole earns its name from the dependence of its observed behaviour on which side of this source faces a nearby waveguide. One face will couple to guided modes, while the opposite one will exhibit a complete absence of coupling. This behaviour is reversed by flipping the polarisation of the dipole by switching between the two faces. Unlike circular dipoles, whose directionality can be switched experimentally by changing the polarisation of the plane wave illuminating the nanoparticle, the Janus and Huygens dipoles' directionalities cannot be controlled in this way using spherical, isotropic nanoparticles as scatterers [17]. Janus, Huygens, and circularly polarised dipoles were identified as the three elemental dipolar sources for directional mode excitation

in planar geometries [17]. All these sources are based on the same fundamental principles of near-field interference and provide broadband operation.

Here, we experimentally demonstrate wavelength-selective excitation of Janus dipole sources, along with their directional coupling properties, by tailoring the near-field interference between the electric and magnetic dipole moments that are induced in dielectric nanoparticles. We demonstrate that by tuning the polarisation state of the excited dipoles and the excitation wavelength to adjust their relative contributions, various dipolar sources can be realised, including the linear Janus dipole. In addition, we discuss and experimentally demonstrate the possibility of realising omnidirectional coupling or noncoupling with a novel spinning Janus dipole.

A dipolar source can be realised experimentally by illuminating any small nanostructure which scatters in the lowest-order Mie regime [8, 22]. Simultaneous electric and magnetic dipolar excitations will be realised if both its electric and magnetic polarisabilities are nonzero [23, 25, 27, 28]. Plane-wave illumination conveniently provides orthogonal electric E and magnetic H fields, which match the p and m dipole moment directions that are required for the linear Janus dipole. However, the orthogonal fields of plane waves are always in phase. To obtain a Janus source for which the electric and magnetic dipole moments are phase shifted, we can exploit the intrinsic wavelength-dependent phase difference between the electric and magnetic polarisabilities of the particle [8]. When this phase difference equals $\pm\pi/2$ and the amplitudes of the electric and magnetic dipole moments are comparable, a Janus dipole is realised (Fig. 1 a).

High-index dielectric nanoparticles, such as silicon particles, are suitable for this purpose since they possess both electric and magnetic Mie resonances [2]. For small enough nanoparticles, higher order multipole resonances can be safely neglected in the visible spectrum [27]. By tuning the wavelength and polarisation of the illumination, we can select the amplitudes, directions, and phase difference of the electric and magnetic dipole moments in the nanoparticle; hence, it is the ideal candidate for experimentally realising a Janus dipole source.

The unique coupling behaviour of a Janus dipole with a waveguide is closely related to the reactive power of the evanescent tails in the mode that is being excited

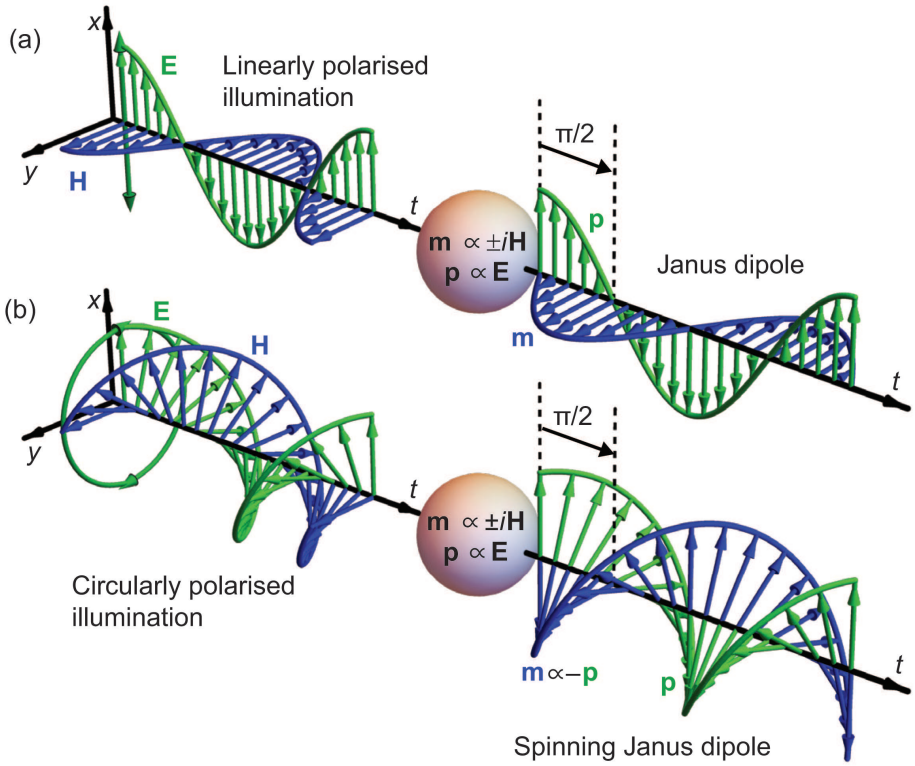

Figure 1: Linear and spinning Janus dipoles. A nanoparticle whose electric and magnetic polarisabilities have a fixed phase difference at a specified wavelength scatters light like a dipolar source with electric and magnetic dipole moments that feature a phase difference determined by the intrinsic polarisabilities. Left: incident **E** and **H** fields as functions of time. Right: dipole moments **p** and **m** of the nanoparticle as functions of time. When the phase difference between the two polarizabilities is $\pi/2$, (a) the nanoparticle under linearly polarised plane wave illumination will scatter like a linear Janus dipole. (b) The same nanoparticle under circularly polarised plane wave illumination will scatter like a spinning Janus dipole (the electric and magnetic fields rotate in the same way and are oriented antiparallel at all times). An additional global phase-delay between the excitation fields and the resulting dipoles is omitted in the sketch.

[17]. The reactive power is the vector $\mathrm{Im}\{\mathbf{E}^* \times \mathbf{H}\}$, namely, the imaginary part of the Poynting vector. The coupling or noncoupling behaviour of the Janus dipole depends on whether the corresponding vector quantity, $\mathrm{Im}\{\mathbf{p}^* \times \mathbf{m}\}$, of the source is pointing in the same or opposite direction as the reactive power of the mode, which gives rise to its two faces. The direction of the reactive power of an evanescent wave depends on its polarisation [29]: s-polarised waves (also called transverse electric waves, with no electric field component in the direction of propagation) have a reactive power that points in the direction of the evanescent decay, while the reactive power of p-polarised modes (transverse magnetic modes) is opposite the direction of decay. Therefore, the definitions of coupling and noncoupling faces of a Janus dipole depend on the polarisation of the excited mode. In this work, we experimentally generate both a linear and a spinning Janus dipole with $\mathrm{Im}\{\mathbf{p}^* \times \mathbf{m}\}$ pointing towards a nearby medium of higher optical density (glass with a refractive index of 1.5), thereby resulting in preferred p-polarised and strongly suppressed s-polarised evanescent coupling between the dipole and the medium. We observe this behaviour by measuring the angular spectrum of the sources in the glass half-space (similar to the measurements in [8]; see SM for details).

Because of the small distance between the dipolar source and the substrate, both the propagating and evanescent wavevector components of the source can couple into propagating waves inside the glass, which can be measured. We are interested in the emission that corresponds to evanescent fields in free-space, which is responsible for the near-field directionality of the Janus dipole, with $\frac{k_t}{k_0} > 1$, where k_t is the transverse wavevector that is perpendicular to the optical axis (z) and k_0 is the wavenumber in free space. These fields, which are evanescent in free space and become propagating in optically denser media, are sometimes referred to as "forbidden light" [30]. Although the amplitude of the measured spectrum will be a modified version of the near-field spectrum of the isolated Janus source in free space, the difference can be calculated via a multiplicative transfer function that accounts for the polar-angle dependence of the Fresnel transmission coefficients through the high-index substrate interface. Therefore, any zeroes in the angular spectrum of the free-space source will also be present in the measured angular spectra, which follows directly from the conservation of transverse momentum. The arrangement of zeroes in the spectra are a clear signature of a Janus dipole (see SM). For instance, a Janus dipole with $\frac{p_x}{m_y} = -\frac{iR}{c}$, where R is a normalised measure of the ratio of electric to magnetic components, shows zero amplitude for the s-polarised evanescent

components with $k_t = k_0\sqrt{R^2+1}$ on its noncoupling side ($z > 0$), which is due to the destructive interference between the electric and magnetic dipole fields after their superposition. Then, a Janus dipole that satisfies $px/my = -i/c$ would lead to a ring of zero intensity at the transverse k-vector, that corresponds to $k_t = \sqrt{2}k_0$ [17]. However, this would exceed the angular range of our experimental setup. Thus, our ideal Janus dipole condition is $p_x/m_y = -i0.75/c$, which is optimised for $k_t = 1.25k_0$.

For our experiment, we place an individual silicon nanosphere (diameter approximately 176 nm) on a glass substrate (see Fig. 2 a) on the optical axis of a linearly x-polarised Gaussian beam (focused with an effective NA of 0.5) that is used for excitation. For this configuration, due to the linearly polarised illumination, we excite an x-polarised electric dipole, namely, p_x, and a y-polarised magnetic dipole, m_y. Then, we can control the amplitudes of and the relative phase between the two dipole moments by selecting the wavelength of the excitation field. Between the magnetic and electric dipole resonances (Fig. 2 b,) we expect two wavelengths for which the relative phase between my and p_x is close to $\pi/2$ (the Janus dipole condition) with both dipole amplitudes being of comparable strength. Due to the presence of the substrate, these will differ slightly from those that are predicted by free-space Mie theory. Nonetheless, the free-space scattering cross-section provides a range within which the wavelength can be fine-tuned experimentally. Then, we measure the intensity distribution in the back focal plane (BFP) of an oil immersion objective (NA=1.3) that is placed below the glass substrate to capture the near- and far-field parts of the angular spectrum of the Janus dipole for $0.6 < k_t/k_0 < 1.3$. The angular range below an NA of 0.6 is also collected but discarded because it contains the transmitted input beam. The collected spectrum is analysed with a linear polariser to retrieve its s- and p-polarisation components.

Figure 3 shows the results of the measurements, together with the calculated dipoles, that were obtained for three wavelengths of illumination: (a) $\lambda = 520\,\text{nm}$, (b) $\lambda = 640\,\text{nm}$, and (c) $\lambda = 700\,\text{nm}$. We observe a striking agreement between the measured data and the results of the numerical calculations. At $\lambda = 640\,\text{nm}$, we are very close to the linear Janus dipole condition (Fig. 3), for which the electric and magnetic dipole moments have a relative phase that is close to $\pi/2$ and an amplitude ratio of $|p_x/m + y| \approx 0.75/c$. A ring of zero amplitude outside the light cone (which corresponds to near fields) in the s-polarised angular spectrum of Fig. 3 b is a clear signature of the noncoupling face of the Janus dipole. Our measurements reveal that

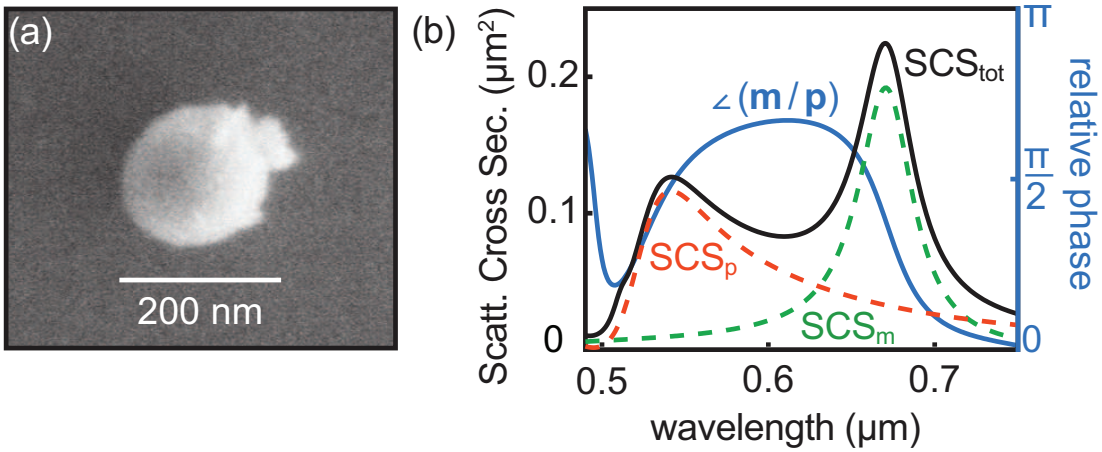

Figure 2: Nanoparticle properties. (a) A SEM image of a spherical Si particle with core radius $r \approx 84$ nm and oxide shell thickness $s \approx 4$ nm. (b) The total scattering cross-section (solid black line) and the relative phase between the resonances (solid blue line) calculated using Mie theory for the nanoparticle in (a). The dashed orange and green lines represent the electric and magnetic dipole scattering cross-sections, which are proportional to $|\mathbf{p}|^2$ and $(|\mathbf{m}/c|^2)$, respectively.

the amplitude of its angular spectrum is zero for a circle with transverse wavevector $k_t = 1.25k_0$ as analytically expected. Hence, if placed near a waveguide that is supporting an s-polarised mode with this or a similar propagation constant, this source will not be able to excite it in any direction due to a momentum mismatch. In contrast, the p-polarised component is non-zero everywhere except for the $k_x = 0$ line. The source will excite p-polarised modes in all directions except for the $\pm y$-direction. These are trivial zeroes because they result from a polarisation mismatch: the dipole has components p_x and m_y; however, p-polarised modes that are propagating parallel to the y-direction do not feature the corresponding E_x and H_y field components for coupling. Reversing the Janus dipole reverses the coupling/noncoupling behaviour: the s-polarised component becomes non-zero everywhere and, hence, coupling, while the p-polarised component features the noncoupling spectrum. To reverse the Janus dipole, one must change the relative phase between $\mathbf{p}$ and $\mathbf{m}$ by 180°. One way of reversing a Janus dipole that is induced via plane-wave illumination would be to invert the illumination direction. Due to the relation $(\mathbf{E} \times \mathbf{H}) \propto \mathbf{k}$ in plane waves, changing the direction of k corresponds to a sign change of either E or H, but not of both simultaneously. Thus, polarisation that was coupling would become non-coupling and vice versa.

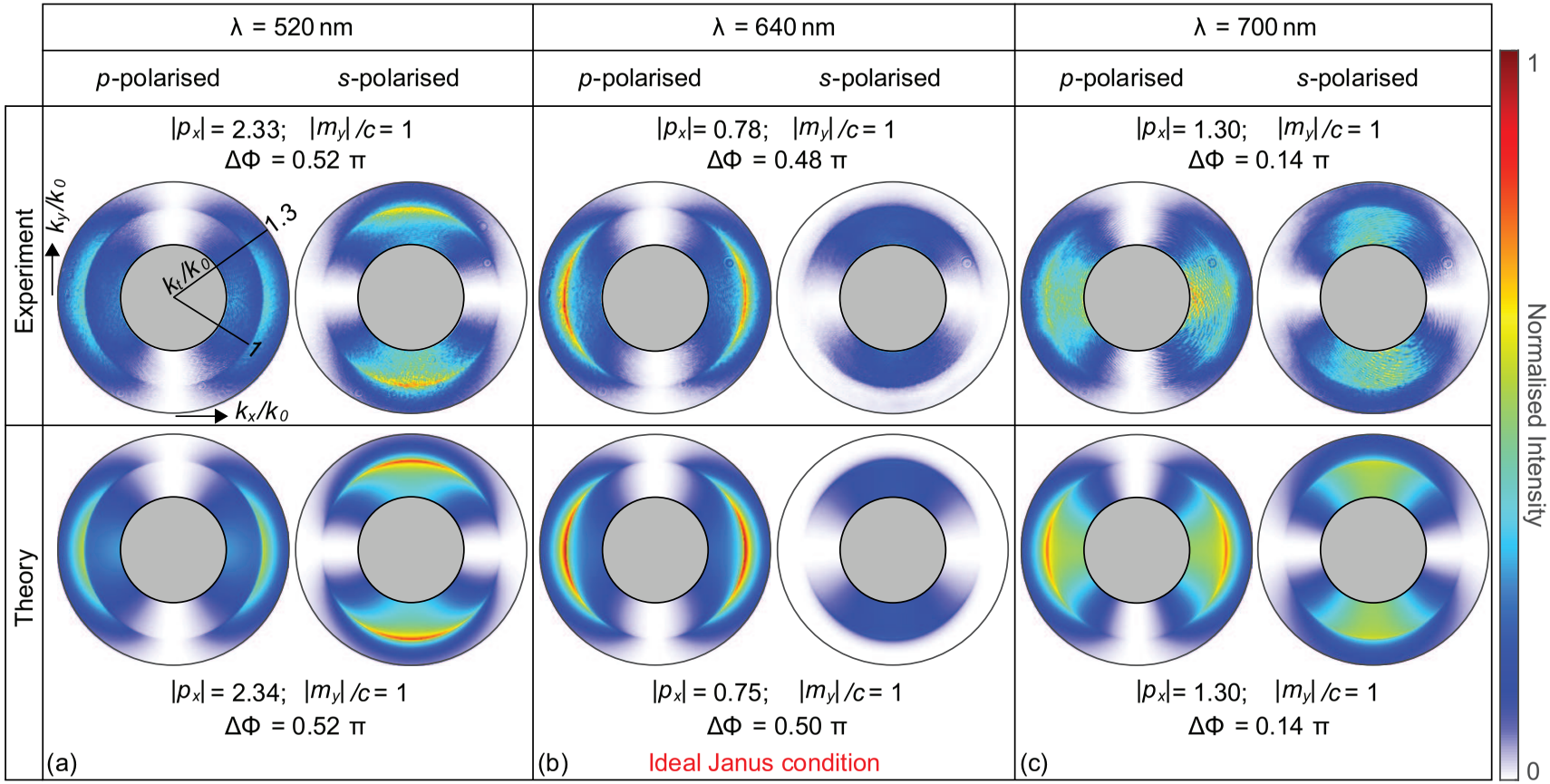

Figure 3: Near-field scattering of dipolar sources and their spectral dependence. Measured (top) and calculated (bottom) BFP intensities of s- and p-polarised near-field angular distributions for (a) $\lambda = 520\,\text{nm}$, (b) $\lambda = 640\,\text{nm}$, (c) $\lambda = 700\,\text{nm}$ that correspond to various relative contributions of electric and magnetic dipoles and their relative phases. The sets of s- and p-polarised intensity distributions are normalised to their common maximum value. For $\lambda = 640\,\text{nm}$, the Janus condition ($|p_x/m_y| = 0.75/c$ and $\Delta\Phi = \arg(m_y/p_x) = \pi/2$) is theoretically satisfied. The s-polarised component of the light that is scattered by the Janus dipole presents a full ring of zero intensity at the locations $k_x^2 + k_y^2 = k_t^2 = k_0^2(R^2+1)$ which correspond to the noncoupling condition for a given *amplitude* of the wavevector k_t, in *any* direction. In (a) and (c), the dipole moments and phase difference used in the theoretical plots are the same as the experimental ones, while in (b) the simulation shows the ideal Janus dipole, with $|p_x/m_y| = 0.75/c$ and $\Delta\Phi = \pi/2$.

Figure 3 a, c show the angular spectra that were obtained at two other wavelengths, namely, 520nm and 700nm, respectively, for which the Janus condition is not fulfilled and, therefore, the aforementioned feature of noncoupling cannot be realised. From the measured angular spectra, we determine the corresponding dipole moments that are induced in the nanoparticle [3, 21]. For this purpose, we performed a nonlinear least-square fit of theoretically calculated far fields to our measured angular spectra. A more detailed description of the retrieval of the dipole moments is provided in the supplementary material. At $\lambda = 520$nm, the amplitude of the magnetic dipole moment is substantially smaller than that of the electric dipole moment ($|p_x/m_y| \approx 2.3/c$). Hence, even if the phase between them is close to $\pi/2$, the destructive interference condition is satisfied at transverse wavevectors, namely, $k_t/k_0 \gg \mathrm{NA}$, which well exceeds the available numerical aperture in the experiment. In the measured angular region, the electric dipole behaviour will be dominant and the nanoparticle will scatter like an electric dipole that is polarised along x. In contrast, for $\lambda = 700$nm, the amplitudes of the two dipole moments are comparable, namely, $|p_x/m_y| \approx 1.3/c$; however, the phase between the two is almost zero: $\Delta\Phi = 0.14\,\mathrm{rad}$. To quantitatively compare all three excited dipoles and their polarisation-dependent coupling to evanescent waves, we further investigate the measured angular spectra in the region above the critical angle ($k_t/k_0 < 1.3$). The ratios between the integrated *p*- and *s*-polarised intensities are 1.5 : 1 (520nm), 11.5 : 1 (640nm) and 1.8 : 1 (700nm). These results highlight again the noncoupling nature of the *s*-polarised light of the Janus dipole. The overall scattering efficiency into the super-critical angular regime of our system can be defined as the ratio between the power of the light that is scattered into this region and the power of the angular spectrum of the incoming beam of light. For the three wavelengths, we acquired similar values of $\sim 1.6\%$, $\sim 1.7\%$, and $\sim 1.4\%$. In principle, these numbers can be increased by using tightly focused beams with a higher effective NA for excitation.

Due to the linearly polarised illumination, **p** and **m** are always pointing along x and y, respectively (Fig. 1 a), which is the reason for the lines of zero amplitude ($k_y = 0$ for *s*-polarised light and $k_x = 0$ for *p*-polarised light) that are clearly visible in all angular spectra in Fig. 3. These zeroes are caused by a polarisation mismatch between the dipole and the modes, as described above, rather than the destructive interference between p and m that is characteristic of the Janus dipole.

These trivial lines of zero amplitude in the spectra can be removed via illumination with circularly polarised light, which should result in the excitation of $\mathbf{p}$ and $\mathbf{m}$ with the same time-dependence as the illuminating $\mathbf{E}$ and $\mathbf{H}$ fields, but with a phase delay that corresponds to $\pi/2$, as a direct consequence of the particle's response (Fig. 1 b.) This illumination induces electric and magnetic dipoles that are circularly polarised and spin together in the xy plane but are oriented antiparallel at all times, such that $\mathbf{p} = (1, -i, 0)$ and $\mathbf{m}/c = -\mathbf{p}/R$. This source constitutes a novel "spinning" Janus dipole, with a non-zero associated vector $\mathrm{Im}\{\mathbf{p}^* \times \mathbf{m}\}$ that is directed along $+z$ towards the substrate, as required for noncoupling to s-polarised modes. The angular spectrum intensity of this dipole is rotationally symmetric, as it exhibits no polarisation mismatch to modes in any direction. The stark contrast between p-polarised coupling and s-polarised noncoupling in the evanescent region is even clearer in the experiment. The full ring of zeroes is caused purely by the interference of $\mathbf{p}$ and $\mathbf{m}$, which is characteristic of the Janus dipole (Fig. 4). The source couples to p-polarised evanescent waves in all directions, while it does not couple to s-polarised evanescent waves with a fixed $k_t > k_0$ at any angle. This behaviour would be reversed for an opposite sign of the $\pi/2$ phase difference between the electric and magnetic polarisabilities that are induced by the nanoparticle. In this case, the induced electric and magnetic dipoles are spinning parallel to each other and the source is noncoupling for p-polarised modes.

In conclusion, the experimental measurement of the Janus dipole supports the theoretical predictions of a source with a polarisation-dependent omnidirectional absence of coupling to evanescent waves, which adds to the already widely used circular and Huygens dipoles as an extra source with a polarisation-controllable near field. The striking agreement between the dipoles that are obtained from the scattering from the silicon nanoparticle and the theoretical point sources demonstrates the effectiveness of the utilised dipolar approximation. Moreover, the sensitivity of the response to the illumination parameters leaves room for applications in which a different phase and amplitude ratio between the dipole components may be required, including guided modes with different transverse wavevectors, which can be matched to the source by properly tuning the dipole components. This experimental demonstration highlights the feasibility of the Janus source, thereby paving the way towards novel applications in nanophotonics, quantum information and plasmonics, which might include the Janus dipole and its spinning version.

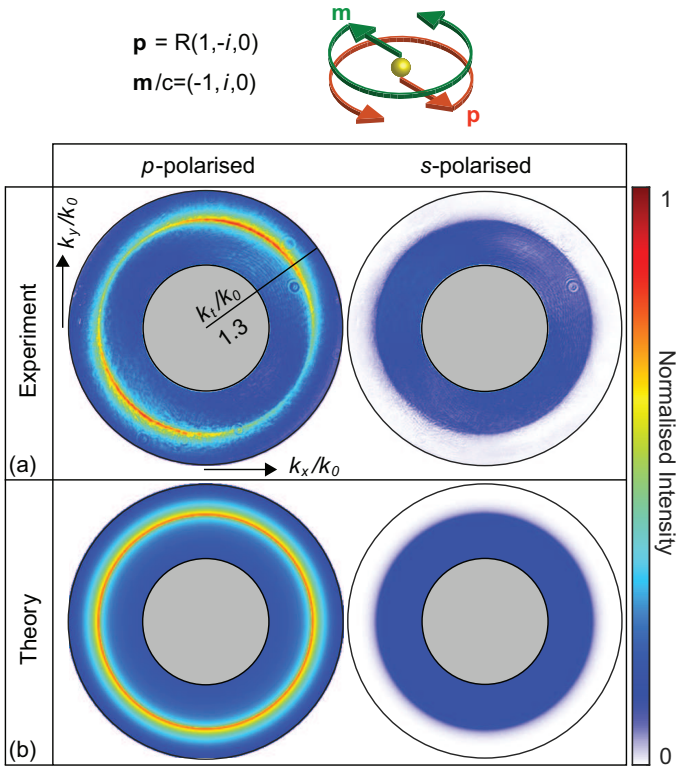

Figure 4: Spinning Janus dipole. Measured (a) and calculated (b) BFP intensities of the p- and s- polarised scattering from a spinning Janus dipole. The experimental and theoretical distributions are normalised to their common maximum value. The retrieved experimental dipole moments are $\mathbf{p} = (0.61 - 0.11i, -0.01 - 0.75i, 0)$ and $\mathbf{m}/c = (-1, 0.30 + 0.84i, 0)$, while the theoretical ones are $\mathbf{p} = 0.75(1, -i, 0)$ and $\mathbf{m}/c = (-1, i, 0)$. The slight asymmetry in the experimental results can be attributed to the experimental dipole moments not matching exactly the ideal ones for which the spinning Janus dipole is cylindrically symmetric.

REFERENCES

1. Bohren, C. F. & Huffman, D. R. Absorption and scattering of light by small particles (1983).
2. Woźniak, P., Banzer, P. & Leuchs, G. Selective switching of individual multipole resonances in single dielectric nanoparticles. *Laser & Photonics Reviews* **9.** doi:10.1002/lpor.201400188 (2015).
3. Eismann, J. S., Neugebauer, M. & Banzer, P. Exciting a chiral dipole moment in an achiral nanostructure. *Optica* **5.** doi:10.1364/OPTICA.5.000954 (2018).
4. Wei, L., Miroshnichenko, A. E. & Kivshar, Y. S. Control of light scattering by nanoparticles with optically-induced magnetic responses. *Chinese Physics B* **23** (2014).
5. Bliokh, K. Y., Smirnova, D. & Nori, F. Quantum spin Hall effect of light. *Science* **348.** doi:10.1126/science.aaa9519 (2015).
6. Rodríguez-Fortuño, F. J. *et al.* Near-field interference for the unidirectional excitation of electromagnetic guided modes. *Science* **340.** doi:10.1126/science.1233739 (2013).
7. O'Connor, D., Ginzburg, P., Rodríguez-Fortuño, F. J., Wurtz, G. A. & Zayats, A. V. Spin-orbit coupling in surface plasmon scattering by nanostructures. *Nature Communications* **5.** doi:10.1038/ncomms6327 (2014).
8. Neugebauer, M., Bauer, T., Banzer, P. & Leuchs, G. Polarization tailored light driven directional optical nanobeacon. *Nano letters* **14.** doi:10.1021/nl5003526 (2014).
9. Kapitanova, P. V. *et al.* Photonic spin Hall effect in hyperbolic metamaterials for polarization-controlled routing of subwavelength modes. *Nature Communications* **5.** doi:10.1038/ncomms4226 (2014).
10. Petersen, J., Volz, J. & Rauschenbeutel, A. Chiral nanophotonic waveguide interface based on spin-orbit interaction of light. *Science* **346.** doi:10.1126/science.1257671 (2014).
11. Coles, R. J. *et al.* Chirality of nanophotonic waveguide with embedded quantum emitter for unidirectional spin transfer. *Nature Communications* **7.** doi:10.1038/ncomms11183 (2016).
12. Le Feber, B., Rotenberg, N. & Kuipers, L. Nanophotonic control of circular dipole emission. *Nature Communications* **6.** doi:10.1038/ncomms7695 (2015).
13. Lodahl, P. *et al. Chiral quantum optics* 2017. doi:10.1038/nature21037.
14. Hayat, A., Mueller, J. P. B. & Capasso, F. Lateral chirality-sorting optical forces. *Proceedings of the National Academy of Sciences.* doi:10.1073/pnas.1516704112 (2015).

15. Rodríguez-Fortuño, F. J., Engheta, N., Martínez, A. & Zayats, A. V. Lateral forces on circularly polarizable particles near a surface. *Nature Communications* **6.** doi:10.1038/ncomms9799 (2015).

16. Sukhov, S., Kajorndejnukul, V., Naraghi, R. R. & Dogariu, A. Dynamic consequences of optical spin-orbit interaction. *Nature Photonics* **9.** doi:10.1038/nphoton.2015.200 (2015).

17. Picardi, M. F., Zayats, A. V. & Rodríguez-Fortuño, F. J. Janus and Huygens Dipoles: Near-Field Directionality Beyond Spin-Momentum Locking. *Physical Review Letters* **120.** doi:10.1103/PhysRevLett.120.117402 (2018).

18. Picardi, M. F., Manjavacas, A., Zayats, A. V. & Rodríguez-Fortuño, F. J. Unidirectional evanescent-wave coupling from circularly polarized electric and magnetic dipoles: An angular spectrum approach. *Physical Review B* **95.** doi:10.1103/PhysRevB.95.245416 (2017).

19. Rolly, B., Stout, B. & Bonod, N. Boosting the directivity of optical antennas with magnetic and electric dipolar resonant particles. *Optics Express* **20.** doi:10.1364/OE.20.020376 (2012).

20. Coenen, T., Bernal Arango, F., Femius Koenderink, A. & Polman, A. Directional emission from a single plasmonic scatterer. *Nature Communications* **5.** doi:10.1038/ncomms4250 (2014).

21. Hancu, I. M., Curto, A. G., Castro-López, M., Kuttge, M. & van Hulst, N. F. Multipolar Interference for Directed Light Emission. *Nano Letters* **14.** doi:10.1021/nl403681g (2014).

22. Evlyukhin, A. B. & Bozhevolnyi, S. I. Resonant unidirectional and elastic scattering of surface plasmon polaritons by high refractive index dielectric nanoparticles. *Physical Review B* **92.** doi:10.1103/PhysRevB.92.245419 (2015).

23. Staude, I. *et al.* Tailoring directional scattering through magnetic and electric resonances in subwavelength silicon nanodisks. *ACS Nano* **7.** doi:10.1021/nn402736f (2013).

24. Alaee, R., Filter, R., Lehr, D., Lederer, F. & Rockstuhl, C. A generalized Kerker condition for highly directive nanoantennas. *Optics Letters* **40.** doi:10.1364/OL.40.002645 (2015).

25. Kuznetsov, A. I., Miroshnichenko, A. E., Brongersma, M. L., Kivshar, Y. S. & Luk'yanchuk, B. Optically resonant dielectric nanostructures. *Science* **354.** doi:10.1126/science.aag2472 (2016).

26. Liu, S. *et al.* Huygens' metasurfaces enabled by magnetic dipole resonance tuning in split dielectric nanoresonators. *Nano letters* **17** (2017).

27. Evlyukhin, A. B. *et al.* Demonstration of Magnetic Dipole Resonances of Dielectric Nanospheres in the Visible Region. *Nano Letters* **12.** doi:10.1021/nl301594s (2012).

28. Zywietz, U., Evlyukhin, A. B., Reinhardt, C. & Chichkov, B. N. Laser printing of silicon nanoparticles with resonant optical electric and magnetic responses. *Nature Communications* **5.** doi:10.1038/ncomms4402 (2014).

29. Wei, L., Picardi, M. F., Kingsley-Smith, J. J., Zayats, A. V. & Rodríguez-Fortuño, F. J. Directional scattering from particles under evanescent wave illumination: the role of reactive power. *Optics Letters* **43.** doi:10.1364/OL.43.003393 (2018).

30. Novotny, L. Allowed and forbidden light in near-field optics I A single dipolar light source. *Journal of the Optical Society of America A* **14.** doi:10.1364/JOSAA.14.000091 (1997).

Experimental demonstration of linear and spinning Janus dipoles for polarisation- and wavelength-selective near-field coupling Supplementary Materials

S1. The angular spectrum

In order to characterise the fields radiated by a Janus dipole and its behaviour when coupling to nearby waveguides, we can use the angular spectrum representation. This is a convenient approach to predict and optimise directionality in near field coupling [1]. The fields from the source are written as a sum of all its spectral components, both propagating plane waves and non-propagating evanescent waves, each corresponding to a transverse wavevector in the plane $\mathbf{k}_t = (k_x, k_y)$ and each with a given amplitude and phase. In free space, the radiation of a source located at $\mathbf{r} = 0$ is simply the superposition of all these contributions:

$$\mathbf{E}(x, y, z) = \iint \mathbf{E}(\mathbf{k}_t)|_{z=0} e^{i(k_x x + k_y y + k_z |z|)} dk_x dk_y, \tag{S1}$$

where $k_z = \sqrt{k^2 - k_x^2 - k_y^2}$ taking always the positive root, and $k = \omega/c$ is the wavenumber of free space.

This corresponds to the fields of the source in free space. However, whenever we wish to study the coupling of a source to a waveguide, thanks to the conservation of momentum parallel to interfaces, the only relevant spectral components are the ones whose transverse wavevector matches those of the modes supported by the waveguide. In other words, what matters in the coupling is the similarity between the k-spaces spanned by the source fields and by the waveguide mode fields. With these assumptions it is then clear that in order for a mode to be excited by the source, the source must have the spectral component with the same wavevector of the mode and, therefore, to achieve non-coupling between a source and a guided mode it is sufficient to remove that spectral component from the source. Then, if a source "lacks" some spectral components it will not be possible to excite the waveguide modes with the corresponding wavevector, independently of the distance between the source and the waveguide.

The key to achieve near-field destructive interference for a given mode is, therefore, to engineer a source “lacking" the spectral component corresponding to the mode. To achieve the omnidirectional noncoupling of the s-polarised modes on a planar waveguide with propagation constant k_m, a Janus dipole can be used, with the amplitude of all the spectral components of the dipole source being zero on a circumference of radius $|\mathbf{k}_t| = k_m$. Therefore, we can focus our analysis on the free-space angular spectrum of the source and this will straightforwardly determine directional excitation of guided modes if the source was placed in close proximity of a waveguiding structure. In a most general case, the free-space electric field angular spectrum amplitudes of any dipolar source, generated by a superposition of an electric and a magnetic dipole, can be written as (see [1] and supplementary information of [2]):

$$\mathbf{E}(\mathbf{k}_t)|_{z=0} = \frac{ik^2}{8\pi^2\varepsilon}\frac{1}{k_z}\left[(\mathbf{v}\cdot\hat{\mathbf{e}}_s)\,\hat{\mathbf{e}}_s + \left(\mathbf{v}\cdot\hat{\mathbf{e}}_p^{\pm}\right)\hat{\mathbf{e}}_p^{\pm}\right], \tag{S2}$$

with $\mathbf{v} = \mathbf{p} - \hat{\mathbf{k}} \times (\mathbf{m}/c)$, $\hat{\mathbf{k}} = \frac{\mathbf{k}}{k} = (k_x, k_y, \pm k_z)/k$ is the normalised wavevector, and $\hat{\mathbf{e}}_s = \frac{1}{k_t}(-k_y, k_x, 0)$ and $\hat{\mathbf{e}}_p^{\pm} = \frac{1}{k}\left(\frac{\pm k_z k_x}{k_t}, \frac{\pm k_z k_y}{k_t}, -k_t\right)$ are the unit vectors relative to s- and p-polarisations respectively. Notice that the terms $\hat{\mathbf{e}}_s$, $\hat{\mathbf{e}}_p^{\pm}$ and $\mathbf{v}$ are all functions of $\mathbf{k}_t$, and the last two have a sign choice in k_z, so the angular spectrum Eq. (S2) depends on whether we are calculating the field at $z > 0$ or $z < 0$ respectively. This difference is crucial as it is the origin of the Janus dipole having two “faces”. Also notice that Eq. (S2) decomposes the angular spectrum vector into a superposition of two complex amplitudes scaling the two unit vectors corresponding to s- and p-polarisations.

In order to analyse the near-field non-coupling behaviour of a source, we can plot the locus of values of $\mathbf{k}_t$ for which $\mathbf{E}(\mathbf{k}_t) = 0$ for each of the two polarisation components. Fig. S1 depicts these locations of the zeros in the angular spectrum of a linear Janus dipolar source with dipole moments $p_x/m_y = -iR/c$ and $R > 0$ following Eq. (S2). The figure plots the p-polarised and s-polarised spectral planes of the source on its two “faces”, corresponding to $z > 0$ and $z < 0$. The angular spectra for $z > 0$ and $z < 0$ swap places if $R < 0$, corresponding to “flipping the face” of the Janus dipole. For the spinning Janus dipole described in the main text, $\mathbf{p} = (1, -i, 0)$

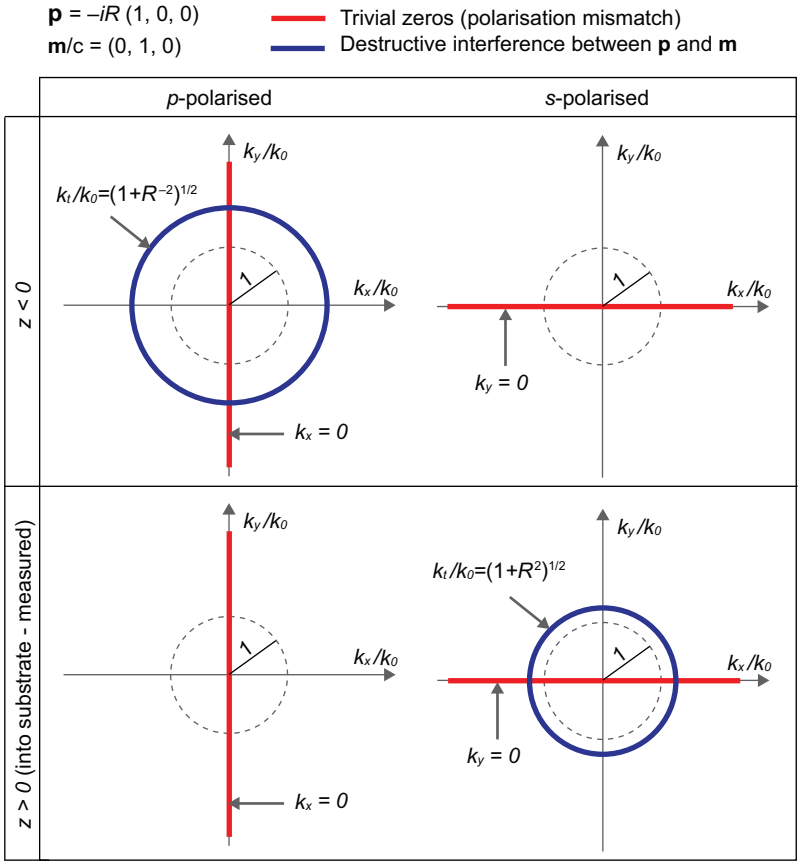

Figure S1: Schematic representation of the zeros in the angular spectrum of a linear Janus dipole, for both polarisations, and for propagation both above and below the source. The zeros in the angular spectrum will be preserved even after transmission through the planar substrate, due to conservation of transverse momentum.

and $\mathbf{m}/c = -\mathbf{p}/R$, the lines of trivial zeros disappear from the spectrum, while the circles of destructive interference between $\mathbf{p}$ and $\mathbf{m}$ remain unaltered.

S2. Experimental setup

A simplified version of the experimental arrangement utilised for measuring the angular spectra of the individual dipole moment combinations is sketched in Fig. S2(a). An incoming monochromatic collimated Gaussian beam of light passes through a linear polariser (transmission axis defined as x-axis, power of the transmitted beam of the order of $1\,\mu$W) and is focused by a first microscope objective with a numerical aperture (NA) of 0.6 (aperture filling factor ≈ 0.8). The focused beam impinges onto a silicon nanosphere (core radius $r = 84\,$nm and estimated oxide shell

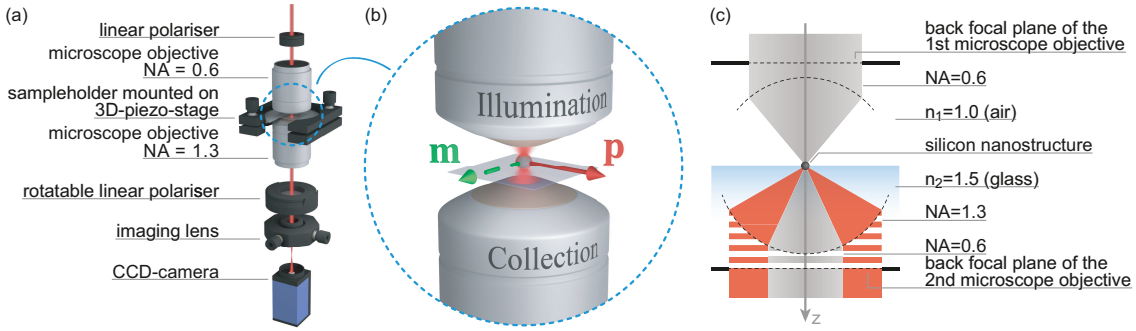

Figure S2: Experimental concept and setup. (a) Simplified sketch of the main components of the experimental setup. (b) Magnified central part. The electric and magnetic dipole moments (**p** and **m**) induced in the silicon nano sphere are indicated as red and green arrows, respectively. (c) Excitation and detection geometry.

thickness $s = 4\,\text{nm}$, see Fig.2 of the manuscript) sitting on a glass-substrate, which is attached to a 3D-piezo-stage. The particle is placed on the optical axis of the beam, which results in the excitation of an x-oriented electric and a y-oriented magnetic dipole moment [Fig. S2(b)]. A second microscope objective (immersion-type with NA = 1.3, index-matched to the glass substrate) is attached from below, collecting the transmitted beam and the light scattered by the particle. The polarisation of the transmitted light is analyzed using a second rotatable polariser. Finally, the back focal plane of the second objective is imaged onto a CCD-camera.

In order to adapt the setup for the excitation of a spinning Janus dipole moment, an additional $\lambda/4$-retarder needs to be introduced between the linear polariser and the first objective, converting the linear polarisation of the incoming beam into circularly polarised light.

Since the first objective used for focusing has a smaller NA than the second objective used for collecting the light, in a certain angular range it is possible to detect the scattered light only. The principle is similar to a dark field microscope [Fig. S2(c)]. The incoming and transmitted beam corresponding to an NA of 0.6 is depicted in gray. The red circular sectors indicate the angular range in which we detect only the light scattered by the particle. Within the angular range defined by $1.0 \geq k_t/k_0 \geq 0.6$, we detect the scattered light associated with the propagating part of the angular spectrum above the glass interface. In the range $1.3 \geq k_t/k_0 > 1.0$, we detect the initially evanescent part of the angular spectrum. The upper limit of 1.3 represents the NA of the collecting objective.

S3. Fitting of dipole moments

In the manuscript, we plot experimentally measured and theoretically calculated polarisation resolved back focal plane intensity distributions for linear and spinning Janus dipoles [see Figs. 3(b) and 4], respectively. For the theoretical distributions, we thereby assume ideal dipole moments, with a relative phase of $\pi/2$ and an amplitude ratio of $|\mathbf{p}| \,/\, |\mathbf{m}| = 0.75/c$. In addition, we provide the experimental dipole moment ratios, which we acquired by fitting theoretical s- and p-polarised intensity patterns to the experimental data, obtaining $(p_x, m_y) \propto (0.77, 0.07 + 1.00i)$ for the linear *Janus* dipole and $(p_x, p_y, m_x, m_y) \propto (1, 0.19 - 1.19i, -1.58 - 0.27i, 0.25 + 1.41i)$ for the spinning *Janus* dipole. This is done by utilizing a nonlinear least square fit where we used the amplitudes and phases of the Cartesian dipole moments $(p_x, p_y, p_z, m_x, m_y, m_z)$ of the calculated far fields as free parameters. Dipole moments which are expected to be of negligible strength are excluded from the fit and their corresponding amplitudes are set to zero, e.g. for the linear Janus dipole excited on-axis with a linearly x-polarised beam, we set p_y, p_z, m_x and m_z to zero. For the sake of completeness, we show the fitted back focal plane intensity distributions in Figs. S3(a) and (b). The first and third rows represent the experimental and the ideal theoretical results as depicted in the manuscript. The second row corresponds to the fitted distributions (not shown in the manuscript).

For the linear Janus dipole, experiment, fit, and ideal theory are all in very good agreement. However, in case of the spinning Janus dipole we see a mismatch between the ideal theory and the experimental data. In the experiment we observe an asymmetric scattering pattern, whereas the theoretical calculations predict a perfectly symmetric angular spectrum. The fitted distributions, however, show a very good overlap with the experimental data. This indicates that the minor aberrations of the experimental data can be explained by an amplitude and phase mismatch of the individual components of the experimental dipole moment with respect to the ideal dipole moment.

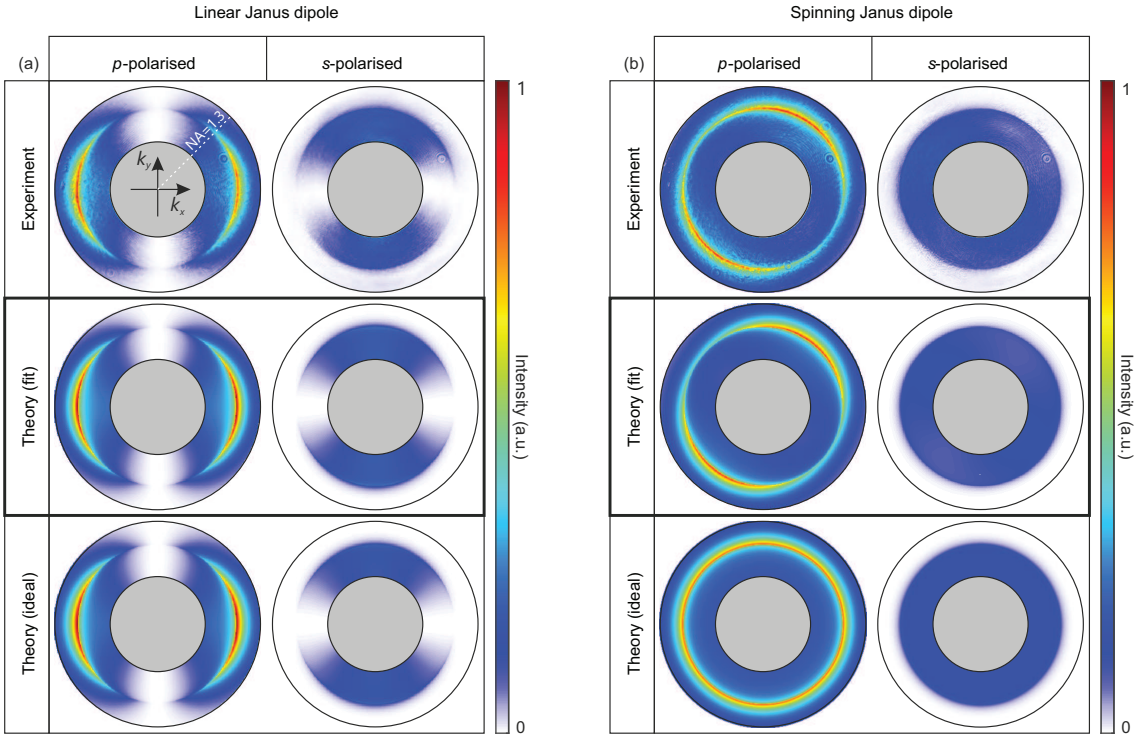

Figure S3: Linear and spinning Janus dipoles. The first and third rows in (a) and (b) depict the measured and the theoretical (ideal) *p*- and *s*-polarised intensities of a linear and a circular polarised Janus dipole, respectively. The results are shown in Figs.3 and 4 of the main text. The back focal plane intensity distributions in the second rows depict the intensity distributions for the dipole moments fitted to the experimental observations. Each set of *p*- and *s*-polarised intensities is normalised to its common maximum value.

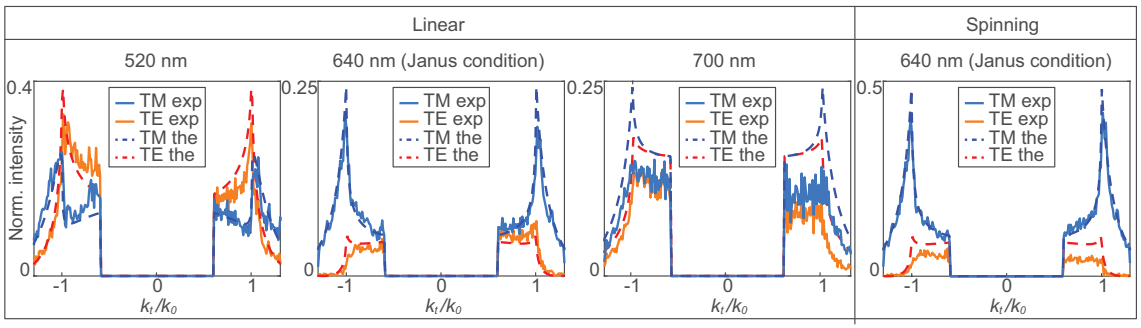

Figure S4: Scattered intensity profiles. The intensity profiles obtained from the cross-sections of the experimental (solid lines) and theoretical (dashed lines) intensity maps of Figs. 3 and 4 in the main text. The cross-sections are performed along the line $k_x = k_y$ to avoid measuring any of the trivial zeros along the k_x and k_y axes.

REFERENCES

1. Picardi, M. F., Manjavacas, A., Zayats, A. V. & Rodríguez-Fortuño, F. J. Unidirectional evanescent-wave coupling from circularly polarized electric and magnetic dipoles: An angular spectrum approach. *Physical Review B* **95.** doi:10.1103/PhysRevB.95.245416 (2017).
2. Picardi, M. F., Zayats, A. V. & Rodríguez-Fortuño, F. J. Janus and Huygens Dipoles: Near-Field Directionality Beyond Spin-Momentum Locking. *Physical Review Letters* **120.** doi:10.1103/PhysRevLett.120.117402 (2018).

Chapter 4

Multimode control

In the previous chapters we designed dipoles to achieve the directional excitation of a single mode. In order to do so, we specifically looked at the near fields of dipolar sources that had a zero amplitude of a single component of the angular spectrum. The question we wish to address in this chapter is whether this approach can be generalised and extended to engineer the controlled excitation of multiple guided modes. A single mode waveguide only supports one mode at a given frequency with wavevector $\pm k_m$, where the $\pm$ accounts for the two directions of propagation inside the waveguide, assumed the source is placed somewhere between the ends of the guide, either inside or close to it. For this type of waveguide, then, imposing that the spectrum of the source is zero for either $+k_m$ or $-k_m$ ensures that the propagation is bound to be unidirectional, with the direction determined by the wavevector for which the angular spectrum is nonzero. For waveguides supporting more than one mode, however, it is not sufficient to cancel a mode propagating in one direction to ensure unidirectionality, but we need to take into account all the possible modes. A simultaneous control of more than one mode can be obtained exploiting the totality of the degrees of freedom of dipoles. In fact, each dipolar source can be described in terms of a dipole moment $\mathbf{p} = (p_x, p_y, p_z)$ for an electric dipole and $\mathbf{m} = (m_x, m_y, m_z)$ for a magnetic one. While, as we saw in chapter 3, two dipole moment components are needed to impose the unidirectionality of a single guided mode, four remaining degrees of freedom can also be exploited to concurrently control the excitation of more than one mode. The possibility of engineering more than one mode simultaneously opens up new interesting scenarios. For example, one might be interested in controlling, not only the direction, but also the relative amplitudes and phases between the modes excited in the multimode waveguide using

a single dipolar source. In this chapter we will describe the way in which up to six complex conditions (one per complex degree of freedom) can be imposed on the propagation of modes in a waveguide, to tailor the angular spectrum of a dipolar source, superposition of an electric and a magnetic dipole, that achieves the fully controllable excitation of said modes.

4.1 A simplified picture

Let us start with a somewhat simplified description of the engineering procedure to quickly convey the main idea behind it. The idea of engineering the spectrum of a source, selectively nullifying specific components, is somewhat more intuitive in the temporal domain. In fact, if a waveguide supports two modes at different wavelengths, then a source whose frequency spectrum lacks one of the two wavelengths will not excite the corresponding mode. In the same way as a time-invariant waveguide will conserve the frequency spectrum of the source, a translationally-invariant one will conserve the wavevector components parallel to the translation symmetry axes. A waveguide may support two modes with different wavevectors, so a source whose wavevector spectrum lacks one of the two components will not excite the corresponding mode. Consider the fields of a dipolar source in a given z-plane, $\mathbf{E}^{\text{dipole}}(x, y, t)$ as shown in figure 4.1(a). We only look at the fields radiated by the dipole, its primary fields, not including the scattering by the waveguide. These fields can be Fourier-transformed to momentum-frequency space $\mathbf{E}^{\text{dipole}}(k_x, k_y, \omega)$, see figure 4.1(b). As the dipole is monochromatic, its spectrum is limited to a single frequency $\omega = \omega_0$ plane (although this could be generalised even further for time-varying sources). The dipole fields can now be represented together with the dispersion relation of the waveguide in the same momentum-frequency plot as in figure 4.1(b): the intersection between the waveguide mode and the dipole fields is a requirement for matching the dipolar radiation to the modes. The dipole in this example has been engineered to exhibit zero amplitude exactly at certain points of intersection with the dispersion relation of the waveguide, which are the points highlighted in figure 4.1(b). Thus, this dipole will neither excite mode 1 to the right nor mode 2 to the left. As a result, each of the two modes will be excited, from the *same* dipolar source, into different directions of the waveguide. This is confirmed in real space, as shown in panel (c) of figure 4.1. This description is exact in the case of a slab waveguide, in which guided modes have a single momentum value (k_x, k_y) and transverse momentum is conserved.

The model is not exact for one-dimensional waveguides such as that in the figure, because guided modes will have a spread of wave-vector k_y values caused by the mode confinement along y, and the non-translational-invariance of the waveguide along y will allow scattering along k_y. However, our simulations show that these effects are negligible for our purposes, and the model above becomes an excellent design principle even for one-dimensional waveguides.

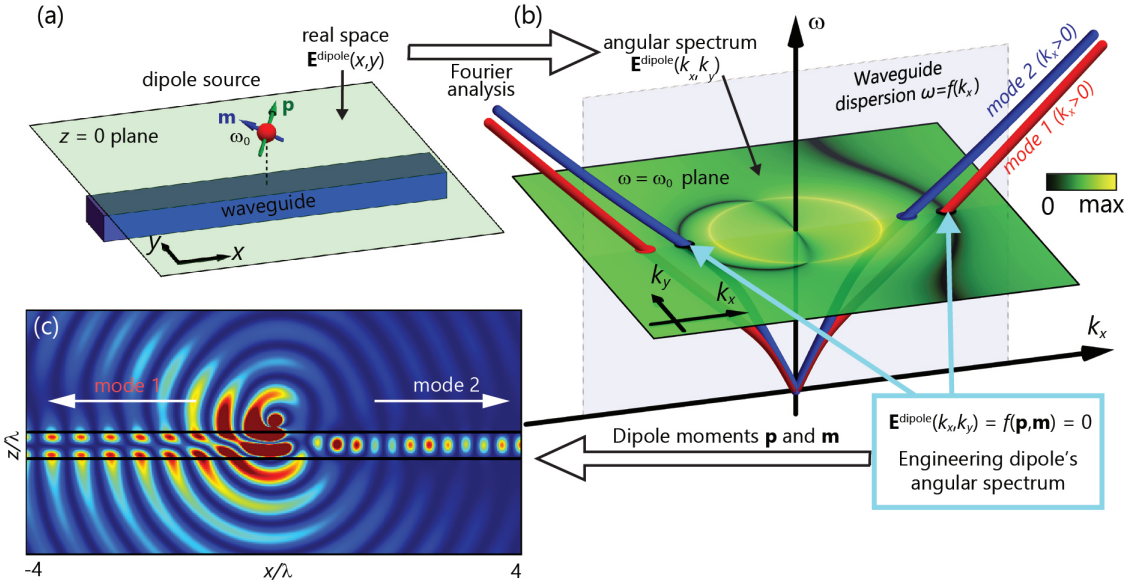

Figure 4.1: Concept of dipolar angular spectra tailored to a nearby waveguide. (a) Schematic depiction of a dipole source placed near a waveguide. The $z = 0$ plane, in which the waveguide lies, is the plane in which the fields of the dipole are calculated. (b) The dipolar angular spectrum and the waveguide's dispersion relation plotted together in the frequency-momentum space. The dipole's angular spectrum can be engineered so that the spectral position of features of interest, such as zeros required for cancelling mode excitation, match the k-vector of guided modes. A multimode waveguide of thickness $t = 0.6\lambda$ and refractive index $n = 2$ surrounded by air, and dipole moments $p_x = -0.84i$, $p_z = -0.164$, and $m_y/c = 1$ have been simulated. (c) Excitation of 2 different modes in opposite directions in the multimode waveguide obtained by cancelling required components of the dipolar fields as shown in (b). The plot corresponds to the dipole and waveguide parameters as in Fig. 4.4 (c).

4.2 Complete model of angular spectrum

When dealing with the angular spectrum of a dipole, the simple picture suggested by figure 4.1 must be revised for two reasons. Firstly, we have to distinguish between the two angular spectra [131], $\mathbf{E}(k_x, k_y, z) = \mathbf{E}^+(k_x, k_y)e^{ik_z z} + \mathbf{E}^-(k_x, k_y)e^{-ik_z z}$, corresponding to waves propagating towards the positive and negative z direction (we always define $k_z = \sqrt{k^2 - k_t^2}$ as the positive root, with positive imaginary part if $k_t > k$). In chapter 2 we showed that this is accounted for by the $\pm$ sign in equation (2.12). When dealing with a dipolar source, only the upwards propagating part $\mathbf{E}^+(k_x, k_y)$ will exist in the upper half space $z > 0$, and only the downwards propagating part $\mathbf{E}^-(k_x, k_y)$ will exist in the lower half space $z < 0$, since all waves must be propagating away from the source plane at $z = 0$.

Secondly, each of these angular spectra $\mathbf{E}^\pm(k_x, k_y)$ is not a scalar function, as suggested by figure 4.1, but instead is a vector function. Despite being a three dimensional vector field, the divergence-free condition imposed by Maxwell's equations on each angular component which we derived in chapter 1, equation (1.18), reduces by one the degrees of freedom, allowing the angular spectrum vector function to be written using a two-dimensional basis. A convenient choice of basis is to use again s- and p-polarisation: $\mathbf{E}^\pm(k_x, k_y) = E_s^\pm \hat{\mathbf{e}}_s^\pm + E_p^\pm \hat{\mathbf{e}}_p^\pm$, where the two unit vectors are the same defined in equations (2.3) and (2.4).

Evidently, the spectra for s- or p- polarised fields will couple to the corresponding s- or p-polarised waveguided modes in nearby waveguides, respectively. This is an exact statement in slabs, but the deviation from this rule for typical one-dimensional waveguides is negligible.

Therefore, a complete description of an arbitrary source requires different spectra to account for the waves with the two polarisations s- and p-, each defined on the half-spaces above and below the dipole, constituting *four* different angular spectra in total. For example, figure 4.1 shows a waveguide supporting p-polarised modes placed below the dipole, so the relevant scalar angular spectrum is $E_p^-(k_x, k_y)$, which is the one shown.

4.3 The angular spectra of the three elemental sources

As we saw in chapter 2, we can write the angular spectra of electric and magnetic dipoles in terms of their dipole moments. We can start from the electric field in equation (2.12) and rewrite it as:

$$\mathbf{E}^{\pm}(k_x, k_y) = \frac{ik^2}{8\pi^2\varepsilon}\left[(\mathbf{v}^{\pm}\cdot\hat{\mathbf{e}}_s)\hat{\mathbf{e}}_s + (\mathbf{v}^{\pm}\cdot\hat{\mathbf{e}}_p^{\pm})\hat{\mathbf{e}}_p^{\pm}\right], \tag{4.1}$$

where $\mathbf{v}^{\pm}$ depends on the wavevector and on both the electric $\mathbf{p}$ and magnetic $\mathbf{m}$ dipole moments of the source:

$$\mathbf{v}^{\pm} = \frac{1}{k_z}\left[\mathbf{p} - \left(\hat{\mathbf{e}}_k^{\pm}\times\frac{\mathbf{m}}{c}\right)\right], \tag{4.2}$$

where $\hat{\mathbf{e}}_k^{\pm} = \mathbf{k}^{\pm}/k$ and $\mathbf{k}^{\pm} = (k_x, k_y, \pm k_z)$. The unit vectors $\hat{\mathbf{e}}_s$, $\hat{\mathbf{e}}_p^{\pm}$ and $\hat{\mathbf{e}}_k^{\pm}$ are the same we defined in chapter 2 and follow the cyclic relations we presented in (2.5). When equation (4.1) is applied to a given dipole $\mathbf{p}$ and $\mathbf{m}$, four spectra may be calculated and plotted, corresponding to E_p^+, E_s^+, E_p^- and E_s^-. As an example of something the reader will now be surprisingly familiar with, in figure 4.2 we have plotted the four angular spectra associated with the three elemental dipoles described in section 3.2.

4.4 Engineering dipolar angular spectra

So far, we have described the direct problem: given dipoles $\mathbf{p} = (p_x, p_y, p_z)$ and $\mathbf{m} = (m_x, m_y, m_z)$, we obtain the four relevant angular spectra which are a unique signature of this dipole via equation (4.1). The equation is linear, so coherent superposition of dipoles will result in the linear combination of their fields and spectra. Now, we want to solve the inverse problem. Our aim is to design a dipole whose angular spectra takes prescribed complex scalar values at designed points (specifying both amplitude *and* phase of the spectrum at each point), distributed throughout the four scalar spectra, as shown for example in figure 4.3. Each condition is expressed by equating equation (4.1) to the desired value. This forms a system of equations with 6 complex-valued unknowns $(p_x, p_y, p_z, m_x, m_y, m_z)$ and as many

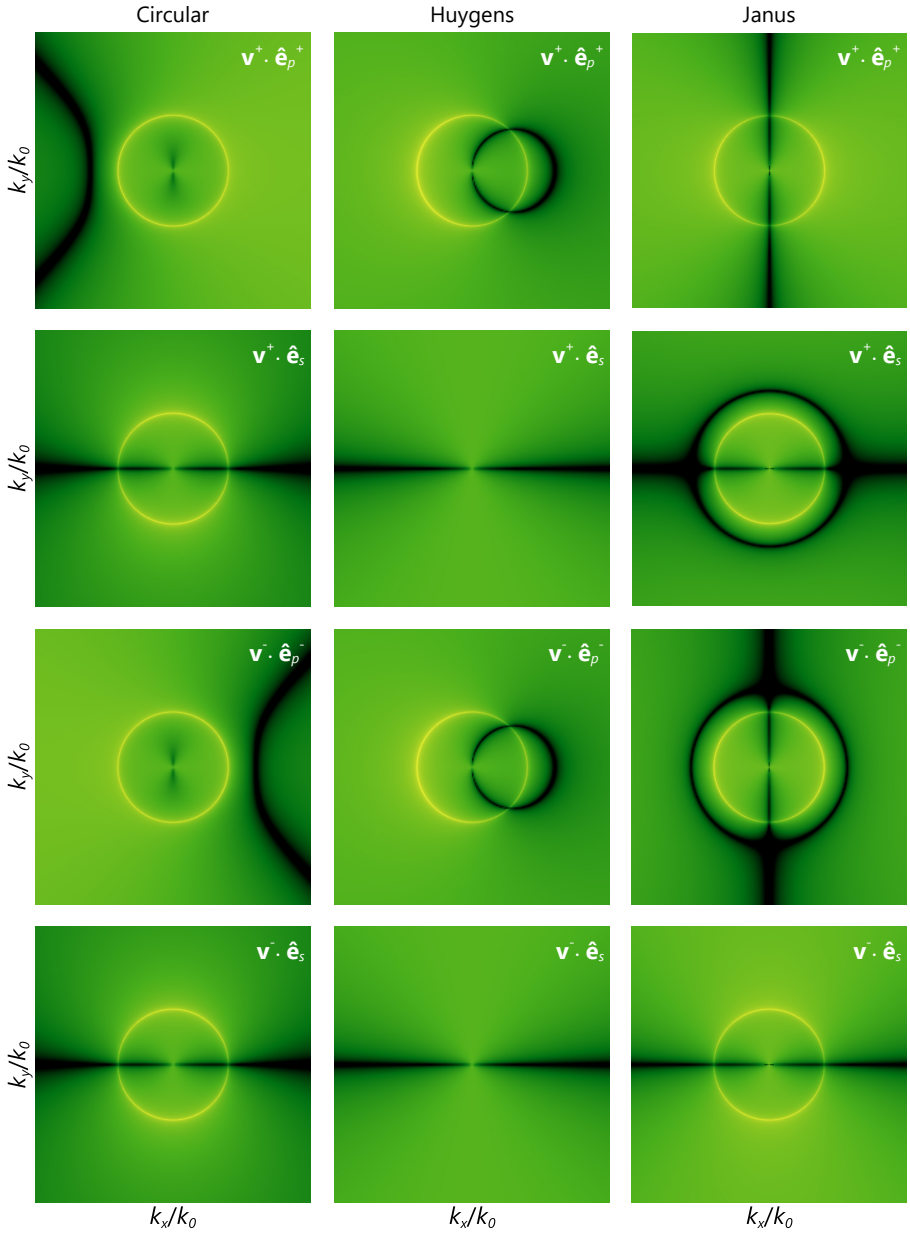

Figure 4.2: Angular spectra of the three elemental dipolar sources, circular, Huygens and Janus dipoles in four different planes corresponding to the two polarisations, s and p, and to fields radiated above and below the source. The three elemental dipoles correspond to different solutions when a single condition is imposed (in this case, the condition is that the p-polarised angular spectra for $z < 0$ must have a zero at the location $(k_x, k_y) = (a, 0)$ with $a > k$). For the circular dipole $\mathbf{p} = (\frac{a}{\sqrt{1-a^2}}, 0, -i)$, for the Huygens $\mathbf{p} = (0, 0, \frac{1}{a})$, $\mathbf{m} = (0, c, 0)$ and for the Janus $\mathbf{p} = (\frac{1}{\sqrt{1-a^2}}, 0, 0)$, $\mathbf{m} = (0, ic, 0)$.

equations as specific conditions that we impose onto the angular spectra. Expressed in matrix notation, basic linear algebra provides us with the solution(s). The dot

products $\mathbf{v}^{\pm}\cdot\hat{\mathbf{e}}_s$ and $\mathbf{v}^{\pm}\cdot\hat{\mathbf{e}}_p^{\pm}$ determine the amplitudes and phases of the s- and p-polarised components, respectively. Substituting the expressions for $\mathbf{v}^{\pm}$, $\hat{\mathbf{e}}_s$ and $\hat{\mathbf{e}}_p^{\pm}$ the dot products can be written, in matrix form, as:

$$\mathbf{v}^{\pm}\cdot\hat{\mathbf{e}}_s = \frac{1}{k_z k_t}\begin{bmatrix}-k_y & k_x & 0 & \mp k_z k_x & \mp k_z k_y & k_t^2\end{bmatrix}\cdot\begin{bmatrix}p_x\\ p_y\\ p_z\\ m_x/c\\ m_y/c\\ m_z/c\end{bmatrix},$$

$$\mathbf{v}^{\pm}\cdot\hat{\mathbf{e}}_p^{\pm} = -\frac{1}{k k_z k_t}\begin{bmatrix}\pm k_x k_z & \pm k_y k_z & -k_t^2 & -k_y(k_z^2+k_t^2) & -k_x(k_z^2+k_t^2) & 0\end{bmatrix}\cdot\begin{bmatrix}p_x\\ p_y\\ p_z\\ m_x/c\\ m_y/c\\ m_z/c\end{bmatrix}. \quad (4.3)$$

We can, therefore, build a matrix which contains up to six rows. Each row is going to be either of the two row vectors of equation 4.3 (depending on the polarization), and each row is calculated for a given point in k-space $\mathbf{k}_n = (k_{xn}, k_{yn}, k_{zn})$ with $k_{zn} = (k^2 - k_{xn}^2 - k_{yn}^2)^{1/2}$ and for a given half space (by deciding on the $\pm$ sign choices shown in equation 4.3). The resulting matrix forms a linear system of equations in the six complex incognitas p_x, p_y, p_z, m_x/c, m_y/c and m_z/c where the independent coefficients are the amplitude and phase for each of the selected points in k space. In this way we find all solutions corresponding to those superpositions of electric and magnetic dipoles whose angular spectrum has the desired amplitudes and phases for all locations in the angular spectrum. The solution might be a unique solution or might have infinite solutions with one or more degrees of freedom, following the usual rules of linear algebra. For example, specifying a single condition in the spectra will result in infinite solutions written as the linear combination of five different combinations of electric and magnetic dipoles. Since we have 6 complex degrees of freedom in our dipole, we can specify up to 6 complex amplitudes at distinct points in k-space, distributed throughout the four scalar spectra. An example of such 6 conditions is shown in figure 4.3. In this example we fixed amplitude and phase of

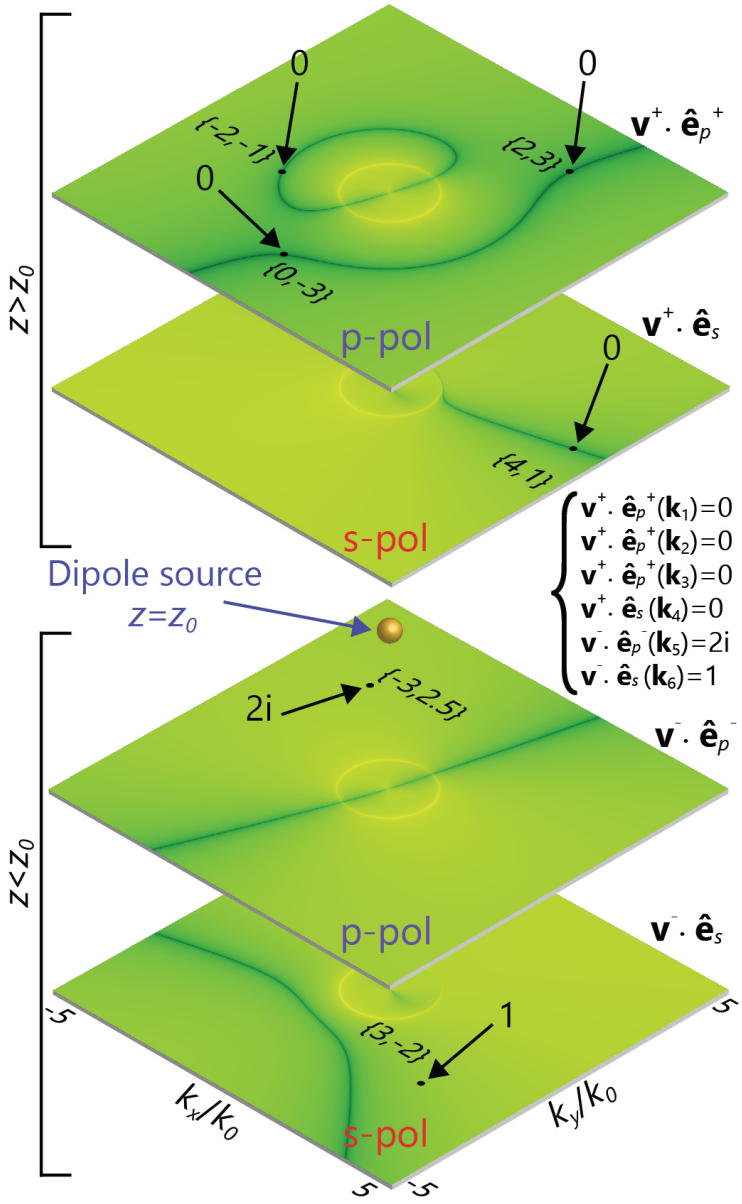

Figure 4.3: Every dipolar source can be defined using four angular spectra, each specified by one of the two orthogonal polarisation states, s or p, and by the propagation direction along z, i.e. fields radiated above or below the source. The plot shows the four angular spectra of a single dipolar source, together with six chosen values of the electric field amplitude and phase (four of them being zero, and the other two being 1 and $2i$) placed in the four planes at different locations in k-space (indicated with arrows). The dipole moment components required to achieve this combination were found to be $\mathbf{p} = (3.10, -1.00, 0.26i)$ and $\mathbf{m}/c = (-2.03i, -6.88i, 3.95)$.

three points in the $z > z_0$ p-polarised plane, and one in each of the three remaining

planes. The resulting linear system is then:

$$\frac{ik^2}{8\pi^2\varepsilon}\begin{bmatrix} \frac{k_{x1}}{kk_{t1}} & \frac{k_{y1}}{kk_{t1}} & -\frac{k_{t1}}{k_{z1}k} & -\frac{k_{y1}}{kk_{z1}k_{t1}}(k_{z1}^2+k_{t1}^2) & -\frac{k_{x1}}{kk_{z1}k_{t1}}(k_{z1}^2+k_{t1}) & 0 \\ \frac{k_{x2}}{kk_{t2}} & \frac{k_{y2}}{kk_{t2}} & -\frac{k_{t2}}{k_{z2}k} & -\frac{k_{y2}}{kk_{z2}k_{t2}}(k_{z2}^2+k_{t2}^2) & -\frac{k_{x2}}{kk_{z2}k_{t2}}(k_{z2}^2+k_{t2}) & 0 \\ \frac{k_{x3}}{kk_{t3}} & \frac{k_{y3}}{kk_{t3}} & -\frac{k_{t3}}{k_{z3}k} & -\frac{k_{y3}}{kk_{z3}k_{t3}}(k_{z3}^2+k_{t3}^2) & -\frac{k_{x3}}{kk_{z3}k_{t3}}(k_{z3}^2+k_{t3}) & 0 \\ \frac{k_{y4}}{k_{z4}k_{t4}} & -\frac{k_{x4}}{k_{z4}k_{t4}} & 0 & +\frac{k_{x4}}{k_{t4}} & +\frac{k_{y4}}{k_{t4}} & -\frac{k_{t4}}{k_{z4}} \\ -\frac{k_{x5}}{kk_{t5}} & -\frac{k_{y5}}{kk_{t5}} & -\frac{k_{t5}}{k_{z5}k} & -\frac{k_{y5}}{kk_{z5}k_{t5}}(k_{z5}^2+k_{t5}^2) & -\frac{k_{x5}}{kk_{z5}k_{t5}^2}(k_{z5}^2+k_{t5}^2) & 0 \\ -\frac{k_{y6}}{k_{z6}k_{t6}} & \frac{k_{x6}}{k_{z6}k_{t6}} & 0 & -\frac{k_{x6}}{k_{t6}} & -\frac{k_{y6}}{k_{t6}} & +\frac{k_{t6}}{k_{z6}} \end{bmatrix} \cdot \begin{bmatrix} p_x \\ p_y \\ p_z \\ m_x/c \\ m_y/c \\ m_z/c \end{bmatrix} = \begin{bmatrix} 0 \\ 0 \\ 0 \\ 0 \\ 2i \\ 1 \end{bmatrix} \tag{4.4}$$

We provide an online dipole calculator [190] to retrieve the dipole moments that achieve user-specified amplitudes in arbitrary points on the angular spectra. If our conditions are all placing zeroes, then we are limited to 5, because we need one degree of freedom in the solution to act as an arbitrary scaling coefficient of the dipolar solution (requiring 6 zeroes simply yields the trivial solution $\mathbf{p} = \mathbf{m} = 0$). Other limitations apply: for example, if we try to place all our conditions in the same polarisation or in the same angular direction, we will be limited in the number of conditions that we can place, because only a subset of the 6 dipole components are involved in that specific polarisation and/or direction.

Overall, with this technique we acquire enormous design power. We can freely decide, within the above limitations, the amplitude and phase of excitation of nearby waveguided modes, even in multimode waveguides. Two such examples are shown in figure 4.4 and confirmed by electromagnetic simulations. In figure 4.4 (a), the *p*-polarised mode of the waveguide is selectively excited in opposite directions with different amplitudes and phases, while at the same time a zero scattering is imposed in the far field in a specified direction. In figure 4.4 (b), the directionality of two different modes of the same bimodal waveguide is designed so that each of the modes propagates unidirectionally in different directions. Furthermore, figure 4.5 shows the flexibility of the method to engineer direction and opening angle of the mode in the plane of the slab waveguide, by placing zeroes at required angles in the radiation diagram. The design space is enormous if multiple waveguides with different orientations and modes of different polarisations are considered.

With this method, we can design the outside of the light cone, for engineering of evanescent guided mode excitation, as well as the inside, engineering the far-field radiation diagrams and radiated polarizations. The concept presented here is very

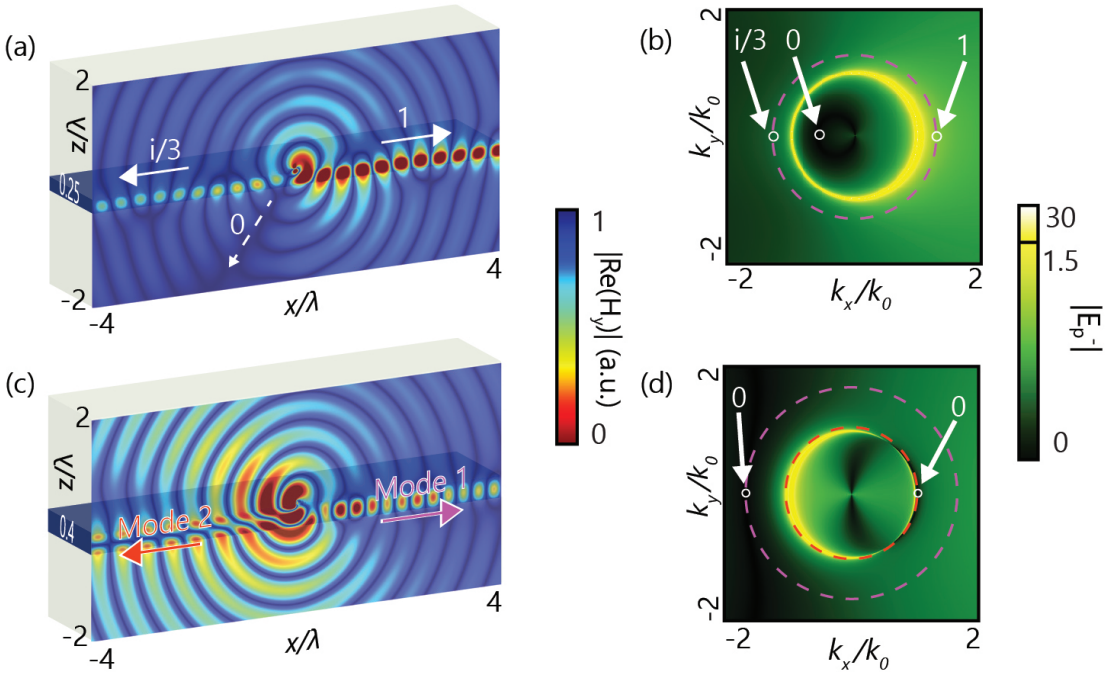

Figure 4.4: Universal tunability: By suitably designing the amplitude and phase of the dipole at $k_y = 0$ and $k_x = \pm k_{\text{mode}}$, excitation of various waveguided and free-space modes can be obtained. (a, b) The same mode is coupled in opposite directions with different amplitudes and 90° out-of-phase, and a far-field direction of zero radiation is imposed below the source for an angle of 37°, [$\mathbf{p} = (1 - 0.03i, 0, 0.41 - 1.22i)$, $\mathbf{m} = (0, 0.56 - 0.76i, 0)$]. (c,d) Two different modes are coupled into opposite directions [$\mathbf{p} = (1i, 0, -0.39)$,$\mathbf{m}/c = (0, -0.69, 0)$]. (a, c) $\text{Re}\{H_y\}$. (b, d) E_p^- angular spectra of each dipole source. The radii of the dashed circles correspond to the wavevectors of the waveguide modes. The distance between the dipole and the waveguide is $0.05\,\lambda$. The refractive index of the waveguide is $n = 2.2$ and the surrounding material is air. The thickness of the waveguide is $0.25\,\lambda$ in (a, b) and $0.4\,\lambda$ in (c,d)

general and its application can be extended in many ways, for instance, to time-varying sources in which the frequency dimension can also play a role, to higher order multipoles to gain more degrees of freedom, or to collections of sources such as arrays, which will further modify the angular spectra. In the case of arrays, the angular spectra will be discretized into diffraction orders both inside and outside the lightcone, introducing the possibility of metasurfaces aimed at near-field engineering. With this work we demonstrate an enormous design power for the nanophotonic control of finely-tailored waveguide excitations via the three-dimensional electric and magnetic polarization of single sources. With recent advances in the synthesis of complex beams, the required fine tuning of exotic electric and magnetic field polarizations to

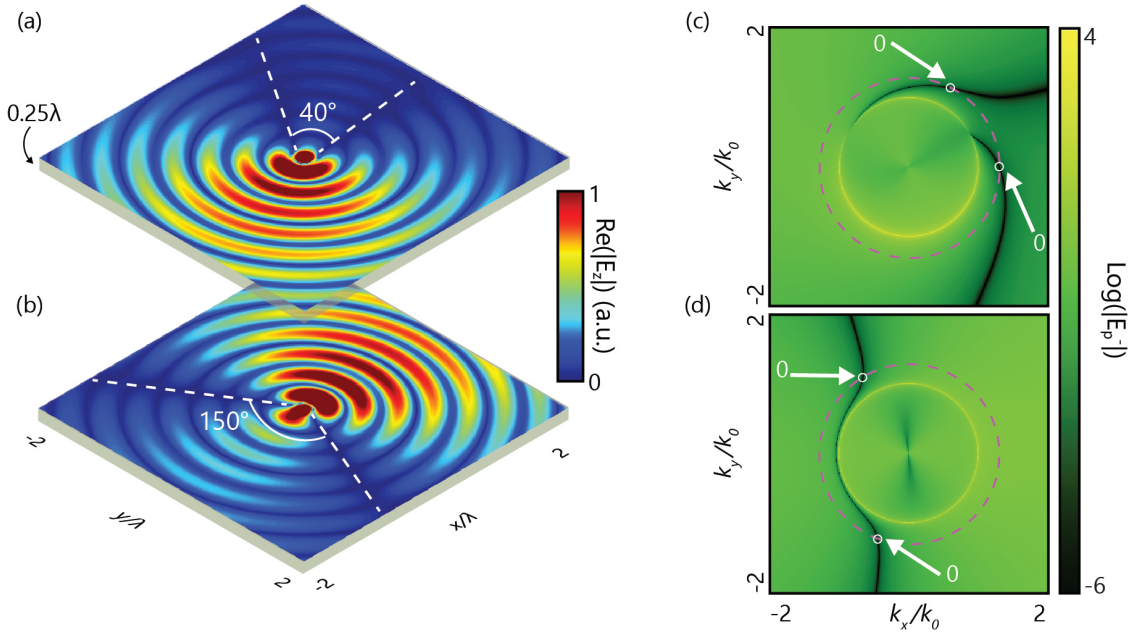

Figure 4.5: Engineering the in-plane steering of the guided mode in a planar waveguide in arbitrary directions. (a, c) The near-field electric field amplitude is designed to have two zeros separated by 40° [$\mathbf{p} = (1.56i, 0.90i, 1)$]. (b,d) The zeros are separated by 150° [$\mathbf{p} = (3.30i, 0, 2.11)$, $\mathbf{m} = (-1, 0, 0)$]]. The position of zeros controls the orientation and opening angle of the radiation pattern. (a, b) $\mathrm{Re}\{E_z\}$. (c, d) E_p^- angular spectra of each dipole source. The radii of the dashed circles correspond to the wavevectors of the waveguide modes. The distance between the dipole and the waveguide is $0.05\,\lambda$, while the thickness of the waveguide is $0.25\,\lambda$. The refractive index of the waveguide is $n = 2.2$ and the surrounding material is air.

electrically and magnetically polarize nanoparticles in three dimensions is now an experimental reality [191–194].

4.5 Far-field amplitudes

The description of the angular spectra engineering we provided is valid both for the near- and the far-fields of dipolar sources, as we showed in figure 4.4, in which amplitudes, phases and directions in the near- and far-fields are tuned simultaneously. However, when considering the far-field radiation ($k_x^2 + k_y^2 < k_0^2$), the mathematical value of the spectrum $\mathbf{E}^{\pm}(k_x, k_y)$ does not allow an intuitive comparison between amplitudes radiated in different directions. For instance, $\mathbf{E}^{\pm}(k_x, k_y)$ shows a singularity on the circle $k_x^2 + k_y^2 = k_0^2$, when $k_z = 0$, preventing an evaluation of the

radiation along the xy plane. It is worth then spending a few words on how to make the description intuitive both for points inside and outside the lightcone. To address this problem, consider the change of variables into spherical coordinates $\{k_x = k_0 \sin\theta\cos\phi;\ k_y = k_0 \sin\theta \sin\phi;\ k_z = k_0\cos\theta\}$, where θ is the polar angle measured from the z axis, and ϕ is the azimuthal angle. The double integral can be transformed into spherical angular coordinates via the corresponding Jacobian $dk_x\, dk_y = k_0^2 \cos\theta \sin\theta\, d\theta\, d\phi$. Substituting the differential solid angle $d\Omega = \sin\theta\, d\theta\, d\phi$ and using $\cos\theta = k_z/k_0$ we may rewrite the angular spectrum as an integration over the solid angle:

$$\mathbf{E}(x,y,z) = \iint \left[k_0 k_z \mathbf{E}^{\pm}(k_x,k_y)\right] e^{i(k_x x + k_y y \pm k_z z)} d\Omega, \tag{4.5}$$

The quantity in square brackets may be considered an improved angular spectrum function $\mathbf{F}(\theta,\phi) = k_0 k_z \mathbf{E}^{\pm}(k_x,k_y)|_{\{k_x = k_0\sin\theta\cos\phi;\ k_y = k_0\sin\theta\cos\phi\}}$ because it represents the amplitude of the electric field radiated along any angular direction. The spectrum $\mathbf{F}(\theta,\phi)$ has no singularity and the far-field radiation in the xy plane is simply given by $\mathbf{F}(\frac{\pi}{2},\phi)$.

Although the above arguments were reasoned for real-valued angles, the multiplication times $k_0 k_z$ can be extended to the entire angular spectrum, including the near-field region with imaginary k_z. The resulting function $\mathbf{F}(k_x,k_y)$ is continuous across the boundary $k_x^2 + k_y^2 = k_0^2$, and is a suitable angular spectrum for simultaneous design of far-field and near-field radiation.

Therefore, in the online dipole designer tool [190], the amplitude at any point in the angular spectrum is defined as $E_{p,s}(k_x,k_y) = \frac{A+iB}{k_0 k_z}$, where $A+iB$ is an arbitrary complex amplitude specified by the user which corresponds to the more intuitive amplitude of the modified spectrum $F_{p,s}(k_x,k_y) = A + iB$.
All the results presented in this chapter have been collected in a manuscript which is currently under review and available as a preprint [Paper 10].

Chapter 5

Nanofibers and nanowires

While the previous chapters were mainly devoted to the study and engineering of electromagnetic sources, the other fundamental element towards achieving controllable guiding of modes is clearly the waveguide itself. Waveguiding structures come in a multitude of shapes and materials, and each of them is based on different working principles and suited for specific applications. The physics behind the light confining and guiding that is achieved in these structures is very different. For example dielectric optical fibers, as we saw in previous chapters, confine light by means of total internal reflection [89, 195, 196], photonic crystal fibers do so based on photonic bandgaps [197–201], combinations of photonic crystal can achieve topologically protected confinement of light [202–204] and plasmonic waveguides convert and transport the incident light via surface plasmon polaritons [55, 205–207], to name a few of the possible waveguiding mechanism known. Among the vast collection of possible waveguides, in this chapter we focus our attention on cylindrical dielectric nanofibers and their metallic counterpart: nanowires. These structures are particularly interesting because, due to their cylindrical symmetry, they guide vortex modes carrying nonzero angular momentum. In this final chapter we will then describe the different angular momenta which can be observed in guided modes of nanofibers and nanowires, together with the degree of chirality of light, usually referred to as helicity. We will also discuss the so-called "Abraham-Minkowski debate", which has been a long standing controversy regarding the correct description of light's momenta. Moreover, we will describe the fields of the guided modes supported by cylindrical waveguides, which differ substantially from the modes of planar structures that we adopted as test bench for our theories in the rest of this thesis. Finally, some properties of dielectric nanofibers and metallic nanowires are explored in our paper

[Paper E], in which analytical and numerical calculations of spin, angular momenta and helicity are performed, uncovering, among other things, the quantization of the canonical total angular momentum of cylindrical guided modes outside of the paraxial approximation.

5.1 Angular momenta, spin and helicity inside a medium

In chapter 1 we have introduced and defined the angular momenta of light in free space (see section 2.1), with a particular attention to spin angular momentum (SAM), intrinsic and extrinsic orbital angular momenta (IOAM and EOAM, respectively) and total angular momentum (TAM). Another quantity that should be mentioned is helicity. Helicity is actually only one of the quantities which are capable of characterising the degree of chirality of light, together with others among which, unsurprisingly, the best known is called "chirality" [208–211]. This shall not surprise us as we discussed in chapter 3 that the amount of conserved quantities in electromagnetism is infinite. Fortunately, in monochromatic fields, as are the ones we study throughout this thesis, helicity and chirality are proportional to one another [212]. While in time-dependent fields care is then required while dealing with helicity and chirality, for monochromatic fields the choice boils down to what the experimental setup actually measures and, for the theorists, personal taste. The electromagnetic helicity corresponds to the projection of the SAM along the direction of linear momentum [213]. Helicity is clearly also a conserved quantity in electromagnetism. The rigorous derivation of all these quantities has not followed a straightforward path. While, in fact, it is easy to define them for free-space and monochromatic fields in homogeneous, isotropic and nondispersive materials [214–216], their definition in complex media has required considerable efforts. Self-consistent and physically meaningful expressions for SAM and OAM in complex media have been provided by Bliokh and colleagues in 2017 [217, 218], followed immediately by the helicity [213]. However, the theoretical studies regarding these quantities cannot be considered concluded by any means, as the transfer of angular momenta between light and matter is strongly dependent on the geometry of the structures involved and said quantities must then be recalculated for each specific case. Our contribution to this was the calculation, both analytical and numerical, of angular momenta and helicity in nanofibers and nanowires, which

is reported in [Paper E].
It is interesting, though, to spend a few words reflecting on why it has been so difficult to establish exact expressions for these quantities, even though they are experimentally measured routinely. The key to the problem is most likely to lie in a 100-years old debate, the so called "Abraham-Minkowski controversy", which we will briefly describe.

5.2 Abraham and Minkowski debate

In classical Newtonian mechanics, the linear momentum of a moving object is defined by the product of its mass m with its velocity $\mathbf{v}$. This linear momentum, bound to the motion of the object only and attached to Cartesian coordinates, is known as the kinetic momentum. Lagrangian mechanics refines this definition by introducing generalised coordinates and defining the canonical momentum as the derivative of the Lagrangian with respect to the generalised velocity. Whenever the Lagrangian depends only on the position, the two momenta are equal. However, in Lagrangians which have velocity-dependent terms, such as the electromagnetic potential, the two momenta differ from each other [219, 220]. We can easily see how different these two momenta can be for something as simple as a charged particle with mass m, charge q in an electromagnetic field. The kinetic momentum of the charged particle is simply given by the product between its mass and its velocity $\mathbf{v}$, so:

$$\mathbf{p}_{\mathrm{K}} = m\mathbf{v}.$$

A Lagrangian that describes this system is given by:

$$\mathscr{L} = \frac{1}{2}mv^2 - qV + q\mathbf{A}\cdot\mathbf{v},$$

where V and $\mathbf{A}$ are the scalar and vector potentials, respectively. Taking the derivative of this Lagrangian with respect to velocity gives us the canonical momentum:

$$\mathbf{p}_{\mathrm{C}} = \frac{\partial\mathscr{L}}{\partial\mathbf{v}} = m\mathbf{v} + q\mathbf{A}.$$

Applying Euler-Lagrange equation:

$$\frac{d}{dt}\left(\frac{\partial \mathscr{L}}{\partial \mathbf{v}}\right) = \frac{\partial \mathscr{L}}{\partial \mathbf{r}},$$

we can immediately see that the right-hand side of the equation is zero, since the Lagrangian does not depend on the position $\mathbf{r}$. Therefore Euler-Lagrange equation simplifies to:

$$\frac{\partial}{\partial t}\mathbf{p}_{\mathrm{C}} = 0. \tag{5.1}$$

Equation 5.1 shows us that, for the simple system we described, canonical momentum is a constant of motion and is, therefore, a conserved quantity. This also means that it is the canonical momentum which is associated with the translational invariance of such a physical system via Noether's theorem [221]. The kinetic momentum then, in Lagrangian classical mechanics, is a conserved quantity only when it matches the canonical one. What happens now when, instead of looking at a charged particle with mass m we consider the linear momentum of a massless object such as a photon? Things get complicated and it is no longer straightforward to calculate the two momenta classically for a photon inside a medium. Complicated enough to give rise to an actual debate. From De Broglie's relation [222], we can write the linear momentum of a photon in free space as $\hbar\mathbf{k}$, with $\hbar$ being the reduced Planck's constant and $\mathbf{k}$ the wavevector in vacuum. The question that generated the controversy, however, is an apparently trivial one: *"How does this momentum change in a material with refractive index n?"*. It is clear that the free-space momentum must be somehow weighted by the refractive index of the material. However, since the refractive index is a pure number, dimensional analysis is of no help in deciding if the new momentum will have to be the free-space one *multiplied* by n or *divided* by it. The two momenta $\mathbf{p}_A = \frac{\hbar\mathbf{k}}{n}$ and $\mathbf{p}_M = n\hbar\mathbf{k}$ are what Abraham and Minkowski, respectively, derived at the beginning of the twentieth century, each of them starting from first principles [223]. Following reference [224], we will present an argument in favour of each, deriving the momentum of a photon in a medium. Let us consider a single photon with energy $\hbar\omega$, travelling with speed c in the z-direction. Along this direction the photon encounters a block of transparent medium with refractive index n, thickness L and mass M. The total energy of the system can be written

via Einstein's equation:

$$E = Mc^2 + \hbar\omega.$$

On entering the medium, the velocity of the photon is reduced from c to c/n. To travel the same length L in free space the photon would take a time $t_0 = L/c$, while in the medium this time needed is n times bigger, i.e. $t_n = nL/c$. Upon leaving the box, the path difference between what the photon would have travelled in free space and what it actually travels passing through the medium, $(n-1)L$, is compensated by the push that the photon exerts on the block, so the block moves in the z-direction by an amount Δz. The motion of the centre of mass-energy is uniform if the following condition is satisfied:

$$\Delta z Mc^2 = (n-1)L\hbar\omega \Rightarrow \Delta z = (n-1)L\frac{\hbar\omega}{Mc^2}.$$

The momentum acquired from the photon by the block to move a distance Δz is:

$$p_{\text{block}} = \frac{1}{M}\frac{\Delta z}{L(n/c)} = \left(1 - \frac{1}{n}\right)\frac{\hbar\omega}{c}.$$

Conservation of momentum then requires the total momentum to be equal to that of the photon before hitting the block $p_{tot} = \frac{\hbar\omega}{c} = \hbar k$, hence the momentum in the medium must be:

$$p_n = \frac{\hbar\omega}{nc} = \frac{\hbar k}{n}.$$

This derivation, therefore, gives us Abraham momentum.
Let us now, instead, consider a plane wave travelling in the z-direction towards a single slit in the xy-plane. In the far field, after the slit, we will see the characteristic single slit's diffraction pattern. It is possible to determine the width of the central peak making use of Heisenberg's uncertainty principle. In fact, the finite width of the slit Δx, determines a spread in the value of the momentum in the x direction after the slit Δp_x, such that $\Delta x \Delta p_x \approx \hbar$. We can then derive the angular width of the central peak θ as:

$$\theta \approx \frac{\Delta p_x}{p_z} \approx \frac{\hbar}{\Delta x}\frac{c}{\hbar\omega} = \frac{c}{\omega\Delta x}.$$

Replicating the experiment with the same slit inside a medium with refractive index n, the width of the central peak is reduced by n. Since Δp_x depends solely on the width of the slit, the only way to reduce the value of θ is for p_z to increase inside the medium. Therefore:

$$p_n = \frac{\hbar\omega n}{c} = \hbar k n.$$

This second derivation gives us Minkowski momentum.
The indisputable correctness of the arguments for both derivations meant that an experimental measurement was left, as the only feasible option, to determine who was right. However the experiments failed to clearly crown a winner in the dispute, as some of them reported measuring Minkowski momentum [225–228], while others claimed the measurement of Abraham momentum [229–231]. The incontrovertible answer expected from the experimental results failed to manifest itself, powering both sides of the controversy. After a century of debates and experimental attempts the dilemma was solved in a draw [224, 232–236]. Both momenta, in fact, are correct, because they are the two different linear momenta for light. The formalism adopted by Abraham describes the kinetic momentum while that employed by Minkowski derives the canonical one. Both these momenta are conserved and both are perfectly valid descriptions of momentum, but they are different between each other. A similar issue of course arose while calculating the angular momenta as well, which was finally resolved in 2017 [217, 218] with a similar conclusion, relating the two different formalisms to distinct momenta. These two momenta are both useful when evaluating specific properties of the fields. As an example, in paper [Paper E], we show that the canonical (Minkowski) momentum can be associated with the propagation constant of a guided mode in a cylindrical guide, while the kinetic (Abraham) is related to its group velocity.

5.3 Hybrid modes in cylindrical waveguides

Before we can proceed with the calculations of momenta and helicity in cylindrical waveguiding structures, it is important to spend a few words on the modes of these structures. Differently from the guided modes of planar slabs which we saw in (1.8), modes of cylindrical waveguides cannot be separated into s- and p-polarised. The simplicity of the modes in planar slabs comes from the assumption that the

slab is infinite in the two directions in which the field is not confined, one being the propagation direction and the other being transverse to it. In a cylindrical waveguide, however, this assumption does not hold, and the mode is confined along two directions at the same time, requiring more convoluted boundary conditions. The propagation constant of the modes of such a structure does not have an analytical closed-form as it is the solution of a transcendental equation, but the method to retrieve it numerically is very well documented in several textbooks [89, 195, 237–239]. The fields calculated are written in terms of Bessel and Hankel functions inside and outside the waveguide, respectively, satisfying Maxwell's equations in each medium and the boundary conditions on the surface of the waveguide. These functions are characterised by two numbers: the radial wavenumber which describes the radial profile of the mode and the azimuthal wavenumber which describes its angular profile. The fundamental mode of the waveguide is characterised by a null azimuthal number and does not carry angular momentum. However, higher order modes have azimuthal numbers which are different from zero. The value of this number corresponds to the total angular momentum carried by these modes. In our work [Paper E] we propose a set of three quantum numbers which unambiguously identify any higher order mode of cylindrical waveguides. The modes of cylindrical structures have, in general, all six electromagnetic field components, unlike *s*- and *p*-polarised ones which only have three. This is why, in contrast to TE and TM modes, these are usually referred to as *hybrid* modes. We derive the field of cylindrical guided modes and their propagation constants in the paper [Paper E]. It is worth pointing out that, even though the geometry of the problem would make it very natural to calculate the fields in cylindrical coordinates, the basis of circular polarisations in Cartesian coordinates presents some advantages. This basis is chosen transverse to the propagation direction, say the z-axis, and the electric and magnetic fields in said basis are given by: $E^{\pm} = (E_x \mp iE_y)/\sqrt{2}$ and $H^{\pm} = (H_x \mp iH_y)/\sqrt{2}$. The advantage of choosing this basis is that the quantities that we calculate acquire very natural forms when we write them in term of their components in this basis plus their component along the propagation direction.

5.4 Our work: Paper E

In this work, we calculate the guided modes of cylindrical nanofibers (dielectric) and nanowires (metallic). While for the dielectric nanofibers the material is assumed

to be non-dispersive, the metallic case is treated as dispersive and the dielectric constant used is calculated using Drude model (1.35). We propose a set of quantum numbers to characterise unequivocally each of the modes supported by the guiding nanostructures. From the fields, we derive, both analitically and numerically, the spin angular momentum, the orbital angular momentum and the helicity associated with each mode. Remarkably, we find the quantization of the total angular momentum, when calculating it using Minkowski's approach. We relate the results found for the angular momenta to the dynamical and geometrical phases in inhomogeneously polarised fields. Finally, we show that, in the geometrical optics approximation, the spin angular momentum of the metallic nanowires modes can be determined by the transverse spin of surface plasmons propagating along helical trajectories. My contribution to this work consisted of performing all the numerical calculations both for the metallic and dielectric cases, from the dispersion relations to the angular momenta. I also prepared the first draft of figures 2, 3 and 4 and of the appendix.
In the past, doctoral theses have been used as the mean by which authors would defend their ideas from the community's criticisms and rebate points raised by other authors. Adopting this exquisitely old-fashioned interpretation of what a doctoral dissertation is, I would like to use this space to reply to an issue that was anonymously raised on Wikipedia (https://en.wikipedia.org/wiki/Abraham-Minkowski_controversy#Theoretical_basis) regarding this work. The author of the comment, whom I personally thank for reading our work and considering it a valuable enough source to deserve citation in Wikipedia, states:

«Recently, Picardi and coworkers emphasized the physical difference between the kinetic-Abraham and canonical-Minkowski quantities, arguing that "the former ones describe the properties of electromagnetic fields only, while the latter ones characterize properties of the whole wave mode (i.e., a polariton, which involves, on the microscopic level, oscillations of both fields and electrons in matter)" [Paper E]. However the EM fields can be divided into two kinds: radiation field (made up of photons) and non-radiation field (such as the self-field carried by a charged particle). Picardi and coworkers did not explain whether or not the "electromagnetic fields only" include the non-radiation field carried by "electrons in matter", thus leading to an ambiguous implication.».

In our formalism we did not separate the self-consistent electromagnetic fields produced by charges in the material from the radiation fields, hence our calculations include those fields. Therefore, when we consider the electromagnetic fields *only*, we are taking into consideration the aforementioned non radiative fields. Hopefully this thesis ends up in the right hands and "Smithwikilover" does not consider our claims ambiguous anymore.

5.5 Paper E

Optica ***5****, 8, 1016-1026 (2018)*

Angular momenta, helicity, and other properties of dielectric-fiber and metallic-wire modes

Michela F. Picardi, Konstantin Y. Bliokh, Francisco J. Rodríguez-Fortuño, Filippo Alpeggiani and Franco Nori

---

Angular momenta, helicity, and other properties of dielectric-fiber and metallic-wire modes

Michela F. Picardi[1], Konstantin Y. Bliokh[2,3], Francisco J. Rodríguez-Fortuño[1], Filippo Alpeggiani[4] and Franco Nori[2,5]

[1] *Department of Physics, King's College London, Strand, London WC2R 2LS, United Kingdom*
[2] *Theoretical Quantum Physics Laboratory, RIKEN Cluster for Pioneering Research, Wako-shi, Saitama 351-0198, Japan*
[3] *Nonlinear Physics Centre, RSPE, The Australian National University, Canberra, Australia*
[4] *Kavli Institute of Nanoscience, Delft University of Technology, 2600 GA Delft, The Netherlands*
[5] *Physics Department, University of Michigan, Ann Arbor, Michigan 48109-1040, USA*

Spin and orbital angular momenta (AM) of light are well studied for *free-space* electromagnetic fields, even nonparaxial. One of the important applications of these concepts is the information transfer using AM modes, often via optical fibers and other guiding systems. However, the self-consistent description of the spin and orbital AM of light in *optical media* (including dispersive and metallic cases) was provided only recently [K.Y. Bliokh *et al.*, *Phys. Rev. Lett.* 119, 073901 (2017)]. Here we present the first accurate calculations, both analytical and numerical, of the spin and orbital AM, as well as the helicity and other properties, for the full-vector eigenmodes of cylindrical dielectric and metallic (nanowire) waveguides. We find remarkable fundamental relations, such as the *quantization of the canonical total AM* of cylindrical guided modes in the general nonparaxial case. This quantization, as well as the noninteger values of the spin and orbital AM, are determined by the generalized *geometric and dynamical phases* in the mode fields. Moreover, we show that the spin AM of metallic-wire modes is determined, in the geometrical-optics approximation, by the *transverse spin* of surface plasmon-polaritons propagating along helical trajectories on the wire surface. Our work provides a solid platform for future studies and applications of the AM and helicity properties of guided optical and plasmonics waves.

1. INTRODUCTION

Spin and orbital angular momentum (AM) of light are well-established concepts in modern optics (see, e.g., books [1–3] and reviews [4–6]). Despite some subtle issues originating from quantum and field-theory aspects [7–9], the spin and orbital AM, as well as their local densities, are well-defined for monochromatic electromagnetic fields (even nonparaxial) *in free space* [6, 10–14]. In parallel with theoretical studies, the spin and orbital AM were intensively explored experimentally. In the past decades, these have found numerous applications in diverse areas including optical manipulations [15–18], quantum optics [19–21], information transfer and communications [22–24].

Importantly, vortex modes carrying AM naturally appear in cylindrically-symmetric waveguides, such as dielectric fibers [25, 26] or metallic wires [27, 28]. Moreover, one of the important applications of the optical AM is the multi-channel information transfer via optical fibers [29, 30]. However, the rigorous characterization of the spin and orbital AM of a multimode waveguide still remains an unsolved problem involving nonparaxial electromagnetic fields in *inhomogeneous media*. It is known that fiber modes exhibit various spin-orbit interaction phenomena [31–35], i.e., coupling between the polarization and orbital degrees of freedom [36]. Furthermore, the total AM must be conserved due to the cylindrical symmetry of the system [37, 38]. However, none of these studies answers the question *"what are the spin and orbital AM values?"* for the cylindrical guided modes.

The only work that properly addressed the above question [39] did this for the simplest situation of a single fundamental mode of a nondispersive (dielectric) nanofiber. Moreover, only the electric-field (but not the magnetic-field) contributions to the energy, spin, and orbital AM of the fiber mode were considered there. Importantly, Ref. [39] demonstrated that the problem of the characterization of the AM of the guided modes is closely related to the *Abraham-Minkowski dilemma* in the characterization of the momentum of light in a medium [40–44]. Traditionally, this dilemma discussed only the linear momentum of plane waves in homogeneous media, and only very recently it was solved for the momentum, spin, and orbital AM of arbitrary monochromatic fields in inhomogeneous and dispersive (but isotropic and lossless) media [45, 46]. In particular, it was shown that the canonical (Minkowski-type)

momentum, spin and orbital AM acquire very natural forms similar to the well-known Brillouin energy density [47, 48].

In this work, we show that the general description [45, 46] of the momentum and AM of light works perfectly for cylindrical modes in both dielectric and metallic (plasmonics) waveguides. This allows one to unambiguously quantify all dynamical properties of complex eigenmodes in inhomogeneous dispersive structures. In particular, we find a very simple yet fundamental result: the canonical total (spin + orbital) AM of the eigenmodes of cylindrical waveguides always takes on *integer values* ℓ (the topological charge of the vortex in the longitudinal field components) in units of $\hbar$ per photon. Note that this simple result cannot be obtained within the usual Poynting-vector-based (i.e., kinetic or Abraham) formalism [47, 48], where the total AM is non-integer. Thus, our approach allows one to extend the results and intuition developed for free-space fields (where the total AM of cylindrical modes is integer [10, 11, 14]) to the fields in inhomogeneous dispersive media. Remarkably, we show that, akin to earlier free-space results [11], the non-integer spin and orbital AM values for guided modes is closely related to the generalized *geometric phases* in the mode fields. Moreover, for metallic-wire modes we provide a simple geometrical-optics model based on the helical rays of surface plasmon-polaritons. It shows that the longitudinal spin AM of the metallic-wire modes originates from the transverse spin [6, 45, 46, 49, 50] of skew surface plasmon-polaritons.

We also show that the canonical [45, 46] and kinetic (Poynting-Abraham) [47, 48] momentum of the guided modes can be associated with the propagation constant β and the group velocity $\partial\omega/\partial\beta$, respectively. Last but not least, we also examine the *helicity* of guided modes. This is an independent fundamental quantity (conserved in free space), which is equivalent to the spin AM only in the simplest plane-wave case, but generally it characterizes *the degree of chirality* of the electromagnetic field [51–55]. Akin to the AM, the description of the optical helicity was extended from free space to dispersive inhomogeneous media only very recently [56, 57]. We show that the helicity of guided modes differs from their spin AM and can take any values in the $(-1, 1)$ range (in units of $\hbar$ per photon). This shows that the cylindrical guided modes are the eigenmodes of the longitudinal component of the total AM (with integer eigenvalues), but not helicity eigenstates.

We perform both analytical and numerical calculations for dielectric multimode fibers, as well as for metallic wires supporting plasmonic modes. Our results reveal fundamental features of the momentum, AM, and helicity properties, universal for electromagnetic modes in various complex media.

2. BASIC EQUATIONS AND GUIDED-MODE PROPERTIES

A. Energy, momentum, spin and helicity

Recently, an efficient formalism describing canonical dynamical properties (momentum, angular momentum, etc.) of monochromatic electromagnetic fields in isotropic dispersive media was developed [45, 46]. According to this, the cycle-averaged energy (Brillouin expression [47, 48]), momentum, spin, orbital, and total AM densities in the field can be written as:

$$\begin{aligned} W &= \frac{1}{4}\left(\tilde{\varepsilon}|\mathbf{E}|^2 + \tilde{\mu}|\mathbf{H}|^2\right), \\ \mathbf{P} &= \frac{1}{4\omega}\mathrm{Im}\left[\tilde{\varepsilon}\mathbf{E}^*\cdot(\nabla)\mathbf{E} + \tilde{\mu}\mathbf{H}^*\cdot(\nabla)\mathbf{H}\right], \\ \mathbf{S} &= \frac{1}{4\omega}\mathrm{Im}\left[\tilde{\varepsilon}\mathbf{E}^*\times\mathbf{E} + \tilde{\mu}\mathbf{H}^*\times\mathbf{H}\right], \\ \mathbf{L} &= \mathbf{r}\times\mathbf{P}, \quad \mathbf{J} = \mathbf{L} + \mathbf{S}. \end{aligned} \tag{1}$$

Here, $\mathbf{E}(\mathbf{r})$ and $\mathbf{H}(\mathbf{r})$ are the complex electric and magnetic field amplitudes, ω is the frequency, and $(\tilde{\varepsilon}, \tilde{\mu} = (\varepsilon, \mu) + \omega d(\varepsilon, \mu)/d\omega$ are the dispersion-modified permittivity ε and permeability μ of the medium, which are assumed to be real. In Eqs. 1 and in what follows we neglect inessential common factors and use the dimensionless parameters (ε, μ) in Gaussian units [which should be understood as $(\varepsilon, \mu) \to (\varepsilon_0\varepsilon, \mu_0\mu)$ in SI units].

The quantities (1) represent *canonical Minkowski-type* properties of the field [45, 46]. In particular, the canonical momentum density $\mathbf{P}$ can naturally be associated with the local wavevector (phase gradient) in the field: $\mathbf{P}/W = \mathbf{k}_{loc}/\omega$. In turn, the *kinetic Abraham* momentum density is given by the Poynting vector [47, 48]:

$$\boldsymbol{\mathscr{P}} = \frac{1}{2c}\mathrm{Re}\left(\mathbf{E}^{*} \times \mathbf{H}\right). \tag{2}$$

($c \to 1$ in SI units). The Poynting-Abraham momentum density actually describes the energy flux and the *group velocity* of the wave propagation. For localized modes with well-defined real wave vector (phase gradient) $\mathbf{k}$, the group velocity is given by the ratio of the integral Poynting vector and Brillouin energy [25, 26, 45–47]: $\mathbf{v}_g = \partial\omega/\partial\mathbf{k} = c^2 \langle \boldsymbol{\mathscr{P}} \rangle / \langle W \rangle$, where $\langle ... \rangle$ denotes the integration over the corresponding coordinates. Note that the Poynting vector 2 also determines the *kinetic* (Abraham-type) total AM density [46, 47]:

$$\boldsymbol{\mathscr{J}} = \mathbf{r} \times \boldsymbol{\mathscr{P}}. \tag{3}$$

As we show below, for the waveguide modes its properties differ considerably from the canonical AM (eq. 1). In particular, even their integral values differ, $\langle \boldsymbol{\mathscr{J}} \rangle \neq \langle \boldsymbol{J} \rangle$, in contrast to the free-space situation [54]. The physical difference between the kinetic-Abraham and canonical-Minkowski quantities is that the former ones describe the properties of *electromagnetic fields only*, while the latter ones characterize properties of the *whole wave mode* (i.e., a polariton, which involves, on the microscopic level, oscillations of both fields and electrons in matter) [46, 58]. In fact, the concept of "photon in a medium" implies such polariton excitation characterized by Minkowski-type quantities. Moreover, it is the canonical-Minkowski quantities that are *conserved* in media with the corresponding symmetries [45, 46, 59, 60].

The electromagnetic *helicity* is an independent important property of electromagnetic fields, which is related to the "dual symmetry" between the electric and magnetic fields [51–56]. It quantifies the chirality of the field, and generally differs from the spin AM. Recently, it was shown [57] that the helicity density in dispersive inhomogeneous dielectrics and metals can be written as:

$$\mathfrak{S} = \frac{1}{2\omega}|\tilde{n}|\mathrm{Im}\left[\mathbf{H}^* \cdot \mathbf{E}\right] = \frac{1}{4\omega}\left|\tilde{\varepsilon}\sqrt{\frac{\mu}{\varepsilon}} + \tilde{\mu}\sqrt{\frac{\varepsilon}{\mu}}\right| \mathrm{Im}\left[\mathbf{H}^* \cdot \mathbf{E}\right], \tag{4}$$

where $\tilde{n} = \sqrt{\varepsilon\mu} + d\sqrt{\varepsilon\mu}/d\omega$ is the group refractive index of the medium. For dispersionless dielectrics, $\tilde{n} = \sqrt{\varepsilon\mu}$, while for Drude-model metals with $\varepsilon = 1 - \omega_p^2/\omega^2$, $\tilde{\varepsilon} = 2 - \varepsilon$ (ω_p is the plasma frequency), and $\tilde{\mu} = \mu$, one has $|\tilde{n}| = \sqrt{|\mu/\varepsilon|}$.

Below we investigate the momentum, AM, and helicity properties of the eigenmodes of cylindrical dielectric fibers and metallic wires. We will calculate the normalized values "per photon in units of $\hbar$ ", which are given by the local density ratios $\omega\mathbf{S}/W$, $\omega\mathbf{L}/W$, $\omega\mathfrak{S}/W$, etc., and by the corresponding integral ratios $\omega\left\langle\mathbf{S}\right\rangle / \left\langle W\right\rangle$, etc.

B. Eigenmodes of cylindrical fibers and wires

We consider a cylindrical non-magnetic medium of radius r_0 in vacuum, which is characterized by the permittivity and permeability:

$$\varepsilon = \begin{cases} \varepsilon_1, & \text{for } r < r_0 \\ \varepsilon_2, & \text{for } r > r_0 \end{cases} \quad \text{and } \mu = 1.$$

(We, however, keep μ in the equations to facilitate the transition to SI units: $\varepsilon \to \varepsilon_0\varepsilon$, $\mu \to \mu_0$.) In dielectric waveguides the dispersion is neglected, so that $\tilde{\varepsilon} = \varepsilon$ and $\varepsilon_1 > \varepsilon_2$, while in metallic wires $-\varepsilon_1 > \varepsilon_2 > 0$, but $\tilde{\varepsilon_1} > \varepsilon_2 > 0$. In what follows, we assume the Drude plasma dispersion for the metal: $\varepsilon_1(\omega) = 1 - \omega_p^2/\omega^2$.

The eigenmodes of cylindrical waveguides are well studied [25–28], and are schematically shown in Fig. 1.

Usually, the mode fields are presented using the components attached to the cylindrical coordinates (r, ϕ, z). However, we found that these acquire a particularly laconic form in the basis of circular polarizations attached to the transverse Cartesian coordinates: $E^{\pm} = (E_x \mp iE_y)/\sqrt{2}$, $H^{\pm} = (H_x \mp iH_y)/\sqrt{2}$. Namely, the eigenmode field inside the waveguide ($r < r_0$) can be written as:

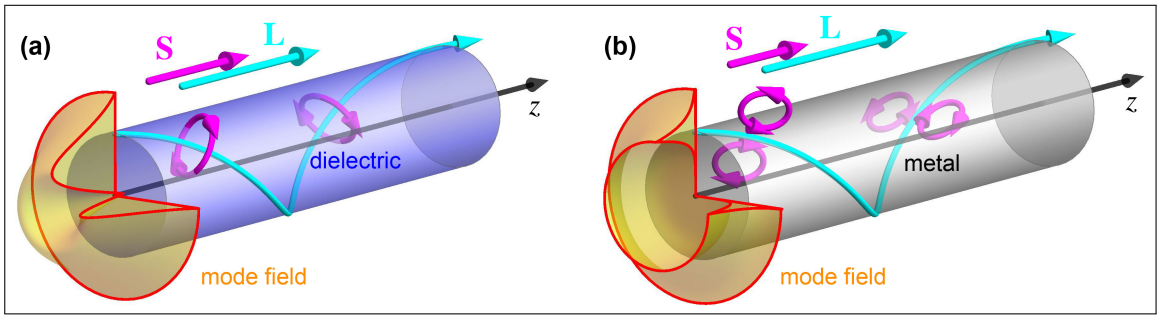

Figure 1: Schematic pictures of the eigenmodes of a dielectric fiber (a) and a metallic wire (b). The geometrical-optics skew rays with their polarizations (transverse circular in dielectrics and in-plane elliptical for surface plasmon-polaritons [6, 36, 49, 50]) are shown by cyan and magenta, respectively. These helical rays and their corresponding polarizations illustrate the origin of the orbital (**L**) and spin (**S**) AM of the cylindrical guided modes.

$$E^{\pm} = -\frac{i}{\sqrt{\varepsilon}\kappa}(\pm\beta A + ikB)J_{\ell\mp1}(\rho)e^{i(\ell\mp1)\phi+i\beta z},$$
$$H^{\pm} = -\frac{i}{\sqrt{\mu}\kappa}(\pm\beta B - ikA)J_{\ell\mp1}(\rho)e^{i(\ell\mp1)\phi+i\beta z},$$
$$E_z = \sqrt{\frac{2}{\varepsilon}}AJ_{\ell}(\rho)e^{i\ell\phi+i\beta z}, \quad H_z = \sqrt{\frac{2}{\mu}}BJ_{\ell}(\rho)e^{i\ell\phi+i\beta z}. \tag{5}$$

Here, $k = \sqrt{\varepsilon\mu}\omega/c$ is the wave number in the medium, $\beta > k_0$ is the mode propagation constant (k_0 is the wave number in vacuum), $\kappa = \sqrt{k^2 - \beta^2}$ is the radial wave number, $\rho = \kappa r$, $\ell = 0, \pm1, \pm2, ...$ is the azimuthal quantum number, and $J_\alpha(\rho)$ is the Bessel function of the first kind. The values of the propagation constant β for given other parameters (ω, r_0, etc.) are found from the transcendental characteristic equation, whereas the complex constants A and B are determined from the boundary conditions at $r = r_0$ (See Appendix A) [26]. The eigenmode fields outside the fiber are given by (5) with the substitution:

$$J_\alpha(\rho) \to H_\alpha^{(1)}(\rho), \quad (A, B) \to (C, D), \tag{6}$$

where $H_\alpha^{(1)}(\rho)$ is the Hankel function, the radial wave number becomes imaginary, $\kappa = \sqrt{k^2 - \beta^2} = i\sqrt{\beta^2 - k^2}$, whereas the complex constants C and D are determined from the boundary conditions (see Appendix A). Equations (5) and (6) describe the

eigenmodes of dielectric fibers [25, 26] and metallic wires [27, 28]. In the latter case, $\varepsilon_1 < 0$, and both k and κ become imaginary inside the wire.

C. Labelling the modes with quantum numbers

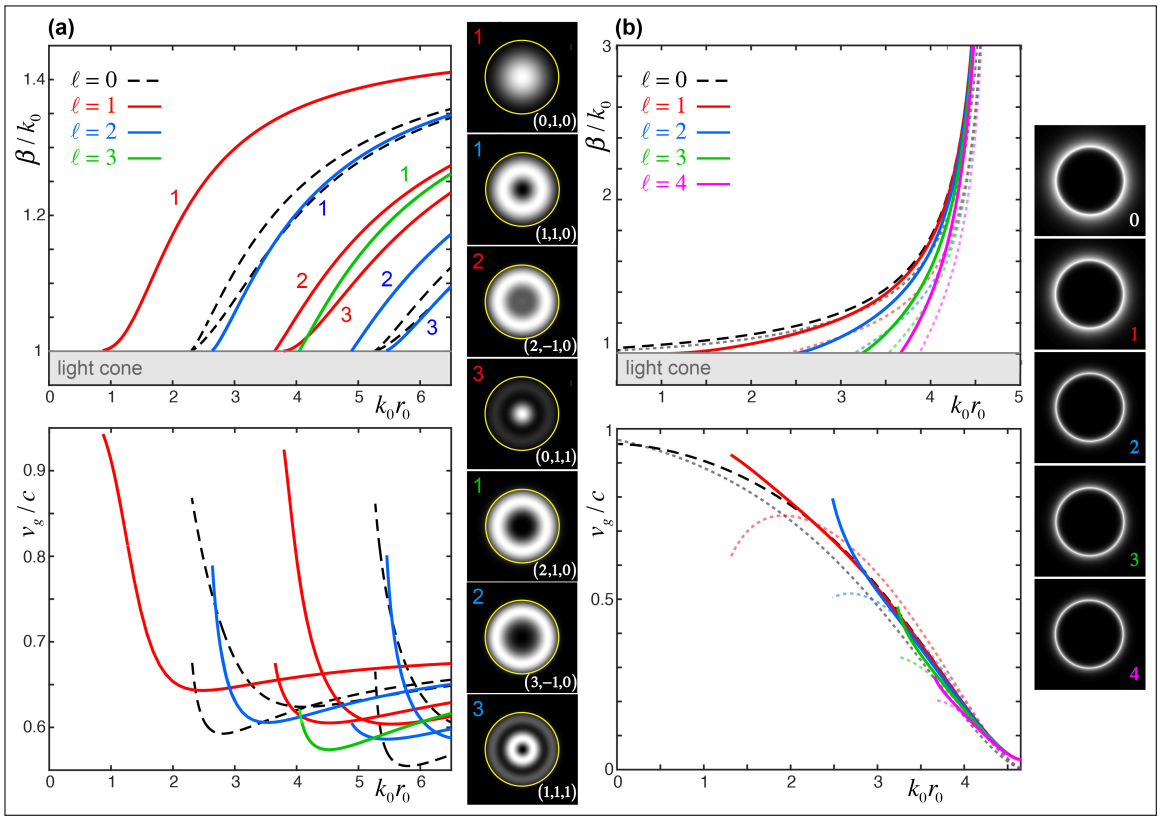

Figure 2: Numerically calculated eigenmodes of a multimode dielectric fiber with parameters $r_0 = 200$ nm, $\varepsilon_1 = 2.1$, $\varepsilon_2 = 1$ (a) and of a metallic wire with parameters $r_0 = 150$ nm, $\varepsilon_1 = 1 - \omega_p^2/\omega^2$, $\omega_p = 1.3262 \times 10^{16} s^{-1} \simeq 6.63\ c/r_0$, $\varepsilon_2 = 1$ (b). The frequency ω was varied in these calculations. The upper panels depict the normalized propagation constants β , which characterize the canonical momentum (9) of the modes (exceeding $\hbar k_0$ per photon). The lower panels show the subluminal group velocities (9) of the modes. The small greyscale panels show typical transverse energy distributions $W(x, y)$ in different modes. The dielectric fiber modes are marked by the total-AM quantum number $\ell = m + \sigma$, as well as by the three (orbital, spin, and radial) quantum numbers (m, σ, n) Eq. (8). The metallic-wire modes are marked by the single total-AM quantum number ℓ. The dotted curves in (b) correspond to the surface-plasmon geometrical-optics model, Eqs. (21) and (22).

The transcendental characteristic equation for β and cumbersome relations for the constants (A,B,C,D) require numerical calculations. Figure 2 shows examples

of the numerically-calculated dispersions $\beta(\omega)$ and energy distributions $W(x,y)$ for the eigenmodes of multimode dielectric fibers and metallic wires. These modes can be classified via their *quantum numbers*. As we show below, the main azimuthal quantum number ℓ characterizes the *total AM*. The $\ell = 0$ modes are pure TE (with $A = C = 0$) and TM waves (with $B = D = 0$) (see Appendix A) [26], for which the AM and helicity vanish identically:

$$L_z = S_z = \mathfrak{S} = J_z = \mathscr{J}_z = 0 \quad \text{for} \quad \ell = 0. \tag{7}$$

Therefore, in what follows, we are interested only in the $\ell \neq 0$ modes, which are *mixed* (i.e., neither TE, nor TM). Importantly, in dielectric fibers, these modes (including the fundamental mode with $\ell = 1$) have circular polarizations in the paraxial limit [25, 31]. This corresponds to geometrical-optics rays propagating inside the dielectric due to the total internal reflection and having circular polarizations, as shown in Fig 1(a)[25]. Therefore, one can introduce the *spin quantum number* $\sigma = \pm 1$, characterizing the sign of this polarization, spin AM, and helicity of the mode in the paraxial limit (where the geometrical-optics rays are practically aligned with the z-axis). Accordingly, the orbital AM of the mode in the paraxial approximation is described by *the orbital AM quantum number* $m = \ell - \sigma$, which corresponds to the orbital AM carried by helical geometrical-optics rays, Fig. 1 (a) [25]. Finally, the dielectric-fiber modes with the same AM numbers can have different radial profiles, which are characterized by the *radial quantum number* $n = 0, 1, 2, ...$, counting the number of additional maxima of $W(r)$ and corresponding to the fact that the geometrical-optics rays can propagate at different angles with respect to the dielectric interface [25]. Thus, a set of three quantum numbers,

$$(n, \sigma, n) = (\text{orbital, spin, radial}), \tag{8}$$

labels the $\ell \neq 0$ modes of a dielectric fiber, as shown in Fig 2(a) [25, 31]. Due to the mirror symmetry of the waveguide, the modes with opposite total AM $\ell = \pm 1, \pm 2, ...$ are double-degenerate, and we restrict our analysis to the $\ell > 0$ case. At the same time, the modes with opposite spin quantum numbers $\sigma = \pm 1$ (and the same orbital and radial quantum numbers) are not degenerate, which indicates the *spin-orbit*

interaction in optical fibers [31–36, 61].

The situation is much simpler in the case of metallic wires. There, the eigenmodes have a *surface plasmon-polariton* origin [27, 28, 62, 63]. Therefore, the mode is localized near the metal-dielectric interface [all geometrical-optics rays lie on the cylindrical surface, Fig. 1 (b), and its radial profile is fixed for each ℓ, i.e., effectively $n \equiv 0$. Furthermore, the polarization is also fixed, locally tending to the TM surface-plasmon mode in the large-radius limit $k_0 r_0 \gg 1$; i.e., there are no circularly-polarized modes and effectively $\sigma \equiv 0$. Thus, the metallic-wire modes are labelled by a single *total AM quantum number* ℓ, as shown in Fig. 2 (b). Nonetheless, the AM and helicity properties of the metallic-wire modes are generally nontrivial. Akin to the dielectric fiber case, the fundamental $\ell = 0$ mode has pure TM polarization with $B = D = 0$ and vanishing AM and helicity, Eq. (7). However, the higher-order modes are mixed, and, as we show below, their spin and orbital AM, as well as helicity, are nonzero. Notably, the nonzero spin AM of the metallic-wire modes can be explained by the fact that even locally-TM-polarized surface-plasmon waves possess an elliptical polarization in the propagation plane [see Fig. 1 (b)] and therefore carries the *transverse spin* [45, 46, 49], a phenomenon which is currently attracting considerable attention [6, 36, 50]. For the modes with $\ell > 0$, the geometrical-optics surface-plasmon rays are *helical* [64], as shown in Fig. 1 (b), and the locally-transverse spin acquires a nonzero z component [65]. In Section 4.B, we will show that this geometrical-optics ray picture, supplied by the known surface-plasmon-polariton properties, perfectly describes properties of higher-order metallic-wire modes and enables one to derive analytical expressions for the dispersion and AM quantities. To the best of our knowledge, the nonzero spin AM of higher-order metallic-wire modes and its relation to the transverse spin of surface plasmon-polaritons has never been described before.

3. Angular momenta and momenta of guided modes

A. Momentum, spin, orbital, and total angular momenta

Some important momentum and AM properties of the cylindrical modes can be found analytically from Eqs. (5) and (6), without numerically calculating their parameters. In this section, we describe these universal momentum and AM features,

independent of the dielectric or metallic waveguide properties. We first note that all field components Eq. (5) share the same z-dependent factor $\exp(i\beta z)$. From here, it is easy to see that the z-component of the canonical momentum Eq. (1) is naturally associated with the propagation constant of the mode, β. At the same time, the integral Poynting vector Eq. (2) provides the group velocity of the modes [25, 26, 47]. These momentum and velocity properties read:

$$\frac{\langle P_z \rangle}{\langle W \rangle} = \frac{P_z}{W} = \frac{\beta}{\omega}, \quad v_g = \frac{c^2 \langle \mathscr{P}_z \rangle}{\langle W \rangle} = \frac{\partial \omega}{\partial \beta}, \tag{9}$$

where $\langle ... \rangle$ denotes the integration over the transverse (x,y)-plane. Note that since $\beta > k_0$, the canonical momentum per photon always exceeds the photon momentum in vacuum. In other words, the guided modes carry "*supermomentum*" larger than $\hbar k_0$ per photon [45, 46, 66–68]. At the same time, the group velocity is always subluminal: $v_g < c$. This imposes the following inequality on the Poynting and canonical momenta: $c \langle P_z \rangle / \langle W \rangle > 1 > c \langle \mathscr{P}_z \rangle / \langle W \rangle$, which seem to be universal for any guided modes [45, 46], while for free-space localized solutions $c \langle P_z \rangle / \langle W \rangle = c \langle \mathscr{P}_z \rangle / \langle W \rangle < 1$ [54, 67]. Figure 2 shows these dimensionless canonical-momentum and group-velocity characteristics for the numerically-calculated modes of dielectric fibers and metallic wires, confirming that these are restricted by 1 from below and above, respectively.

The eigenmodes fields Eq. (5) and Eq. (6) are written in a form convenient for the AM analysis. Indeed, each field component has a well-defined vortex phase factor $\exp(i\alpha\phi)$. In turn, the z-component of the orbital AM Eq. (1) is determined by the operator $\hat{L}_z = -i(\mathbf{r} \times \boldsymbol{\nabla})_z = -i\partial/\partial\phi$. However, the whole field Eq. (5) is not an orbital AM eigenmode, because different components have different azimuthal numbers α. This is typical for nonparaxial vortex fields with intrinsic spin-orbit coupling [10, 11, 36].

For the analysis of the AM properties of the modes, it is instructive to write the energy density Eq. (1) as a sum of the energies of the right-hand circular (+), left hand circular (−), and longitudinal (z) field components: $W = W^+ + W^- + W_z$, where $W^\pm = \left(\tilde{\varepsilon} |E^\pm|^2 + \tilde{\mu} |H^\pm|^2\right)/4$ and $W_z = \left(\tilde{\varepsilon} |E_z|^2 + \tilde{\mu} |H_z|^2\right)/4$. Substituting now the fields (5) and (6) into Eqs. (1), we find that the z-components of the spin and orbital AM can be written as:

$$\frac{\omega L_z}{W} = \frac{(\ell-1)W^+ + (\ell+1)W^- + \ell W_z}{W}, \qquad \frac{wS_z}{W} = \frac{W^+ - W^-}{W}. \tag{10}$$

Most importantly, it follows from these relations that the total AM of the eigenmodes is always an *integer*:

$$\frac{\omega \langle J_z \rangle}{\langle W \rangle} = \frac{\omega J_z}{W} = \frac{\omega L_z}{W} + \frac{\omega S_z}{W} = \ell. \tag{11}$$

To the best of our knowledge, this remarkably simple result has not been derived before.

Moreover, it is by no means trivial. On the one hand, a cylindrically-symmetric stationary system must possess eigenmodes, simultaneously, of the energy ($i\partial/\partial t$) and total AM ($\hat{J}_z$) operators, with the corresponding eigenvalues ω and ℓ. One the other hand, until recently, we have not had expressions for the total AM of light in a medium, which would yield the integer value Eq. (11). In particular, the often-used Poynting-Abraham total AM Eq. (3) is not an integer for cylindrical guided waves (see [39] and Figs. 3 and 4 below):

$$\frac{\omega \langle \mathscr{J}_z \rangle}{\langle W \rangle} \neq \ell. \tag{12}$$

It is only the recently-derived canonical Minkowski-type AM [45, 46] that yields the proper integer value Eq. (11). We also emphasize the importance of the *dual-symmetric* form of the canonical energy, momentum, and AM expressions Eq. (1), which can be written as a sum of the electric and magnetic contributions: $\mathbf{P} = \mathbf{P}^e + \mathbf{P}^m$, $\mathbf{L} = \mathbf{L}^e + \mathbf{L}^m$, $\mathbf{S} = \mathbf{S}^e + \mathbf{S}^m$. The simple results Eqs. (9)-(11) would not be obtained for the pure-electric definitions $\mathbf{P}' = 2\mathbf{P}^e$, $\mathbf{L}' = 2\mathbf{L}^e$, $\mathbf{S}' = 2\mathbf{S}^e$. Obtaining the values (9)-(11) for the electric-biased definitions would require to also use the pure-electric energy definition $W' = 2W^e$, as was done in [39]. However, such definition is physically inconsistent because such energy is not a conserved quantity,

even in free space. The fundamental importance and consistency of the canonical Minkowski-type dual-symmetric definitions (Eq. 1) is discussed in detail in [45, 46]. The natural and laconic form of Eqs (9)-(11) fairly supports this approach.
As we will see in Section 4, the dielectric-fiber modes become paraxial and circularly-polarized, with $\omega \langle S_z \rangle / \langle W \rangle \simeq \omega \langle \mathfrak{S} \rangle / \langle W \rangle \simeq \sigma = \pm 1$ and $\omega \langle L_z \rangle / \langle W \rangle \simeq m = \ell - \sigma$ in the $k_0 r_0 \gg 1$ limit. This determines the spin and orbital quantum numbers (8). In the nonparaxial regime, these values are not integer but the sign of the spin AM and helicity still determines the quantum number σ. For the metallic-wire modes, $\omega \langle S_z \rangle / \langle W \rangle \simeq \omega \langle \mathcal{S} \rangle / \langle W \rangle \simeq 0$ in the $k_0 r_0 \gg 1$ limit. Note also that the vanishing spin and orbital AM of pure TE and TM modes with $\ell = 0$, Eq. (7), follows from Eqs. (10), (11) and Eqs. (5), (6) with $A = C = 0$ or $B = D = 0$, when we notice that $|E^+|^2 = |E^-|^2$, $|H^+|^2 = |H^-|^2$, and hence $W^+ = W^-$.

B. Relation to the dynamical and geometric phases

Remarkably, the values of the angular momenta Eqs. (10) and (11), and the quantization of the total AM are closely related to the *dynamical and geometric phases* in inhomogeneous polarized fields. To start with, we would like to characterize the phase difference in a complex vector field $\boldsymbol{\psi}(\mathbf{r})$ between two $\mathbf{r}$-points connected by a contour C. For a scalar field $\psi(\mathbf{r})$, the only natural definition of the phase is $\Phi = \int_C \nabla \mathrm{Arg}\psi \cdot d\mathbf{r} = \mathrm{Im} \int_C \frac{\psi^*(\nabla)\psi}{|\psi|^2} \cdot d\mathbf{r}$. However, the vector field $\boldsymbol{\psi}(\mathbf{r})$ has more degrees of freedom: for example, it can be factorized into a complex scalar amplitude and a unit direction (polarization) vector. One way to introduce the phase is to use the scalar complex field $\Psi = \boldsymbol{\psi} \cdot \boldsymbol{\psi}$ [69, 70]:

$$\Phi_D = \frac{1}{2} \int_C \nabla \mathrm{Arg}\Psi \cdot d\mathbf{r}. \tag{13}$$

This phase can be associated with the dynamical phase in the field, because it is independent of the direction of the field polarization. Alternatively, one can calculate the phase using the local wave vector of the field, determined by the expectation value of the $-i\nabla$ (canonical-momentum) operator [66–68]:

$$\Phi = \int_C \mathbf{k}_{loc} \cdot d\mathbf{r} \equiv \mathrm{Im} \int_C \frac{\boldsymbol{\psi}^* \cdot (\nabla)\boldsymbol{\psi}}{\boldsymbol{\psi}^* \cdot \boldsymbol{\psi}} \cdot d\mathbf{r}. \tag{14}$$

This phase can be called the total phase of the field, because the operator $-i\nabla$ acts on both the scalar and polarization parts of the vector field. Accordingly, the difference between the phases Eq. (14) and Eq. (13) is the geometric phase caused by the inhomogeneous polarization along the contour C:

$$\Phi_g = \Phi - \Phi_D. \tag{15}$$

We analyze this phase in detail elsewhere [71]; in particular, we show that it coincides with the well-known Pancharatnam-Berry phase on the Poincaré sphere [72] in the case of paraxial fields.

To apply this formalism to the electromagnetic field in optical media, we introduce the 6-component electromagnetic "wavefunction" $\boldsymbol{\psi} = \omega^{-1/2}(\mathbf{E}, \mathbf{H})$. Importantly, the scalar product for this Maxwell field in a dispersive inhomogeneous medium should be modified, because the macroscopic Maxwell equations are effectively non-Hermitian. As it was shown recently [57] (see also [73, 74]), the modified inner product in a medium involves the "left vector" $\tilde{\boldsymbol{\psi}} = \omega^{-1/2}(\hat{\varepsilon}\mathbf{E}, \hat{\mu}\mathbf{H})$, i.e., $\boldsymbol{\psi}^* \cdot (...)\boldsymbol{\psi} \to \tilde{\boldsymbol{\psi}}^* \cdot (...)\boldsymbol{\psi}$. With this modified scalar product, the canonical momentum, spin, and orbital AM Eq. (1), as well as helicity Eq. (4) represent the local expectation values of the corresponding quantum operators [45, 46, 57], while the Brillouin energy density is determined by the wavefunction norm: $W = \omega\tilde{\boldsymbol{\psi}}^* \cdot \boldsymbol{\psi}$. Furthermore, substituting the "right" and "left" electromagnetic wavefunctions into Eqs. (13)-(15), we can now calculate the increments of the phases (13)-(15) for the waveguide modes Eq. (5) and (6 along a closed circuit $C = \{r = \mathrm{const}, \phi \in (0, 2\pi)\}$. In doing so, $\nabla \cdot d\mathbf{r} = (\partial/\partial\phi)d\phi = i\hat{L}_z d\phi$, and the total phase increment Eq. (14) becomes naturally proportional to the canonical orbital AM Eq. (10). Moreover, the dynamical phase Eq (13) becomes proportional to the total AM Eq. (11), while the geometric phase Eq. (15) becomes proportional to the minus spin AM:

$$\frac{\omega L_z}{W} = \Phi, \quad \frac{\omega S_z}{W} = -\Phi_G, \quad \frac{\omega J_z}{W} = \Phi_D = \ell, \tag{16}$$

where $\Phi = \Phi/2\pi$. The last equality in Eq. (16) readily follows from the definition (13) and fields (5) if we notice that for the circular-polarized components $\boldsymbol{\psi}\cdot\boldsymbol{\psi} = 2\psi^+\psi^- + \psi_z^2 \propto \exp(2i\ell\phi)$. Thus, the quantization of the total AM is explained by the quantization of the dynamical phase along the circuit C (this characterizes the topological vortex number of the scalar field $\Psi = \boldsymbol{\psi}\cdot\boldsymbol{\psi}$). The proportionality between the spin AM and geometric phase is also easy to explain. Moving along the contour C, we are attached to the cylindrical coordinates (r,ϕ) which experience a 2π rotation with respect to the Cartesian axes. Therefore, the right-hand $(+)$ and left-hand $(-)$ circular field components acquire the opposite geometric phases $\mp 2\pi$ [36, 75], which are averaged in the second Eq. (10) with the weights W^+ and W^-.

These results resemble previous calculations of the spin and orbital AM in nonparaxial Bessel beams in free space [11, 14]. However, there are two differences. First, most importantly, the free-space consideration [11] is based on the *Fourier plane-wave decomposition* of the field and the spin-redirection geometric phase in $\mathbf{k}$ *space*. In the present problem, this approach is inapplicable because plane waves are *not* eigenmodes of an inhomogeneous cylindrical medium. Therefore, our treatment is based on another type of geometric phase (similar to the Pancharatnam-Berry one) in $\mathbf{r}$ *space* [71]. Second, one can notice the difference between Eqs. (16) and analogous equations in Ref. [11]. This is because the free-space Bessel beams in [11] are defined such that ℓ is the *orbital-AM* number (corresponding to m in this work), and the $\ell = 0$ beam tends to a uniform circularly polarized plane wave in the paraxial limit. In contrast, the cylindrical-waveguide modes (5) and (6) are defined with respect to the polar coordinates, so that ℓ is the *total-AM* quantum number, and the $\ell = 0$ modes are singular on axis($r = 0$). The two approaches are connected by the substitution $\ell = m + \sigma$, where $\sigma = \pm 1$ is the spin/helicity quantum number. Making this substitution in Eqs. (10), (11), and (16), we find that the spin, orbital, and total AM could be written as $\omega L_z/W = m + \Phi'_G$, $\omega S_z/W = \sigma - \Phi'_G$, $\omega J_z/W = m + \sigma$, where the modified geometric phase (now defined with respect to the Cartesian rather than polar axes) is $\Phi'_G = \Phi_G + 2\pi\sigma$. These relations have exactly the same form as the ones derived for the free-space Bessel beams [11].

EXPLICIT CALCULATIONS

A. Dielectric fibers

We are now in a position to show explicit results for the AM and helicity values for the cylindrical guided modes. We first consider dielectric fibers, which are assumed to be made of nondispersive materials: $\tilde{\varepsilon} = \varepsilon$ and $\tilde{\mu} = \mu$.

Apart from the general result for the canonical total AM Eq. (11), the fields, dispersion, and dynamical properties of the modes require numerical calculations. These can be performed directly using the equations of Section 5.5 and Appendix A. However, we found that a considerable analytical simplification can be executed. Namely, substituting Eq. (5) into Eqs. (1), (2), and (4), we derive the following expressions for the energy, spin, helicity, and Poynting momentum densities inside the fiber ($r < r_0$):

$$W = \frac{1}{4}[b\xi^- G + (a\xi^+ + \zeta)F], \quad \mathscr{P}_z = \frac{1}{4\sqrt{\varepsilon\mu}c}[b\xi^+ F + a\xi^- G],$$
$$S_z = \frac{1}{4\omega}[a\xi^- F + b\xi^+ G], \quad \mathfrak{S} = \frac{1}{4\omega}[b\xi^- F + (a\xi^+ + \zeta)G]. \tag{17}$$

Here, we introduced the following parameters:

$$\xi^+(\rho) = |J_{\ell-1}(\rho)|^2 \pm |J_{\ell+1}(\rho)|^2, \quad \zeta(\rho) = 2\,|J_\ell(\rho)|^2,$$
$$a = \frac{k^2 + \beta^2}{|\kappa|^2}, \quad b = \frac{2k\beta}{|\kappa|^2}, \quad F = |A|^2 + |B|^2, \quad G = 2\mathrm{Im}(AB^*). \tag{18}$$

Outside of the fiber ($r > r_0$),the energy, helicity, and spin densities are given by Eqs. (17) and (18) with the substitution (6). Note that the canonical momentum and the orbital or total AM do not require additional calculations, because, according to Eqs. (9) and (11), they are determined by the energy and spin densities: $P_z = \beta W/\omega$, $J_z = \ell W/\omega$, and $L_z = J_z - S_z$.

Equations (17) and (18) illuminate some properties of the spin and helicity in the waveguide modes, clearly showing that these are different quantities, which characterize the intrinsic AM [1–14] and chirality of the field [51–57], respectively. First, the helicity coincides with the z-component of the spin AM only in the paraxial limit. Indeed, the paraxial limit $\kappa \ll k$ corresponds to $b \simeq a \gg 1$, and $\mathfrak{S} \simeq S_z$. Second, it is easy to see that $F \geq |G|$, and the helicity magnitude is restricted by the fundamental limit of 1 (in $\hbar$ units per photon): $\omega|\mathfrak{S}|/W \leq 1$. Third, the helicity eigenstates with $\omega|\mathfrak{S}|/W = 1$ correspond to $\mathfrak{S} = \pm W$, $F = \pm G$, which yields $A = \pm iB$ or $C = \pm iD$. This condition means that the fields (5) and (6) satisfy $\mathbf{E} = \pm i\sqrt{\frac{\mu}{\varepsilon}}\mathbf{H}$, which are exactly the eigenstates of the helicity operator in a medium: $\hat{\mathfrak{S}} = \begin{pmatrix} 0 & i\sqrt{\mu/\varepsilon} \\ -i\sqrt{\varepsilon/\mu} & 0 \end{pmatrix}$ acting on the vector $\mathbf{\Psi} \propto \begin{pmatrix} \mathbf{E} \\ \mathbf{H} \end{pmatrix}$ [55–57]. Finally, the helicity and longitudinal spin of the fields (5) and (6) are nonzero in the general case, because these are mixed (i.e., neither TE nor TM) modes. The only exception is the $\ell = 0$ case, where, for the TE ($A = C = 0$) and TM ($B = D = 0$) modes, we have $\xi^{-}(\rho) = G = 0$, and all helicity and AM properties vanish in agreement with Eq. (7).

Figure 3 shows the results of numerical calculations of the integral values of the spin/orbital/total AM and helicity, $\langle S_z \rangle$, $\langle L_z \rangle$, $\langle \mathcal{J}_z \rangle$, and $\langle \mathfrak{S} \rangle$ for several dielectric-fiber modes shown in Fig. 2 (a). One can clearly see the quantization of the canonical total AM, noninteger character of the Poynting-Abraham total AM, and helicity different from the spin. While ℓ is the total AM quantum number, these calculations allow one to identify the spin and orbital quantum numbers, $\sigma = \operatorname{sgn}\langle S_z \rangle$ and $m = \ell - \sigma$, discussed in section 5.55.5. One can also see that the normalized spin/helicity and orbital AM values (but not the Poynting-Abraham AM) tend to:

$$\frac{\omega \langle S_z \rangle}{\langle W \rangle} \simeq \frac{\omega \langle \mathfrak{S} \rangle}{\langle W \rangle} \simeq \sigma, \quad \frac{\omega \langle L_z \rangle}{\langle W \rangle} \simeq m, \quad \text{for} \quad k_0 r_0 \ll 1 \tag{19}$$

The non-integer character of these quantities in the general nonparaxial case signals the spin-orbit interaction of light in the fiber [11, 14, 31–36].

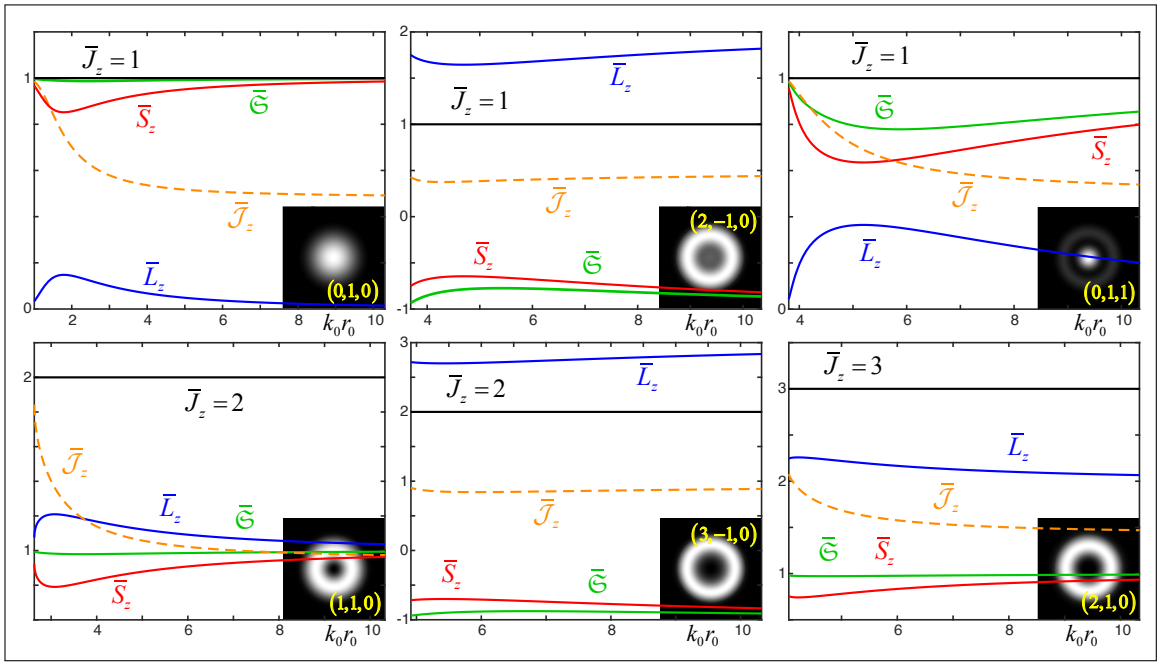

Figure 3: Numerically calculated canonical spin, orbital and total AM [Eqs. (1), (10), (11), and (17)] as well as the helicity [Eqs. (4) and (17)] and the Abraham-Poynting total AM [Eq. (3)] of the modes of a dielectric fiber shown in Fig. 2 (a).Here, plotted are the normalized integral values (in units of $\hbar$ per photon), defined as $\bar{...} = \omega \langle ... \rangle / \langle W \rangle$. One can see the quantization of the canonical total AM $\overline{J}_z = \overline{L}_z + \overline{S}_z = \ell$, the non-integer Poynting-Abraham AM $\overline{\mathcal{J}_z} \neq \ell$, and the differing spin AM and helicity $\overline{S}_z \neq \overline{\mathfrak{S}}$. In the large-radius (paraxial) limit $k_0 r_0 \gg 1$, the canonical spin and orbital AM tend to the quantized values $\overline{L}_z \simeq m$ and $\overline{S}_z \simeq \mathfrak{S} \simeq \sigma$.

B. Metallic wires

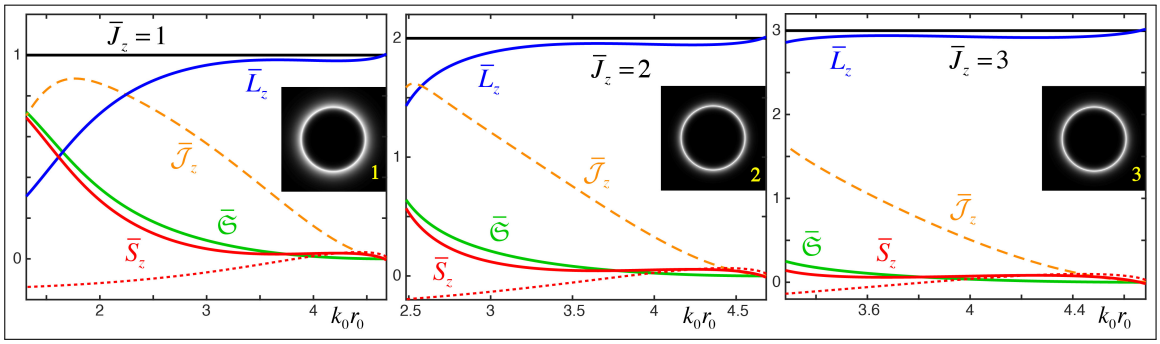

Figure 4: Same as in Fig. 3 but for the metallic-wire modes shown in Fig. 2 (b). The main difference in the behavior of the depicted quantities is that in the large-radius (paraxial) limit $k_0 r_0 \gg 1$, the canonical spin and orbital AM tend to the values $\overline{L}_z \simeq \ell$ and $\overline{S}_z \simeq \overline{\mathfrak{S}} \simeq 0$, whereas, surprisingly, the Poynting-Abraham total AM also vanishes: $\overline{\mathscr{J}_z} \simeq 0$. The red dotted curves correspond to the geometrical-optics model for the spin AM, Eq. (23), based on the transverse spin of surface plasmon-polaritons.

We now consider cylindrical metallic wires characterized by the dispersive permittivity $\varepsilon_1(\omega) < 0$ and the corresponding $\tilde{\varepsilon}_1 > 0$. Figure 4 shows calculations analogous to Fig. 3, using the general equations of Section 2, but now for the eigenmodes of a metallic wire, Fig. 2 (b). There is one important difference in the behavior of the spin and helicity in Figs. 3 and 4. Namely, in the paraxial (large-radius) limit, the metallic-wire modes tend to the TM surface plasmon-polariton waves (the wire surface can be locally approximated by a planar interface) with vanishing longitudinal spin and helicity. Moreover, surprisingly, the Poynting-Abraham total AM also vanishes in this limit:

$$\frac{\omega \langle S_z \rangle}{\langle W \rangle} \simeq \frac{\omega \langle \mathfrak{S} \rangle}{\langle W \rangle} \simeq \frac{\omega \langle \mathscr{J} \rangle}{\langle W \rangle} \simeq 0, \quad \frac{\omega \langle L_z \rangle}{\langle W \rangle} \simeq \ell, \quad \text{for} \quad k_0 r_0 \ll 1 \tag{20}$$

The vanishing Poynting-Abraham AM exhibits a dramatic difference with the quantized canonical AM. This difference can be qualitatively explained as follows. In the large-radius limit, the mode is locally described by the near-planar surface plasmon-polariton wave propagating at an angle with respect to the z-axis, Fig. 1 (b). The Poynting vector of this surface plasmon-polariton has a nonzero azimuthal component $\mathscr{P}_\phi$, which determines the z-component of the Poynting-Abraham total

AM: $\mathscr{J}_z = r\mathscr{P}_\phi$. However, it is known that the group velocity, and hence the integral Poynting-Abraham momentum, of planar surface plasmon-polaritons tends to zero in the large-frequency limit [45, 46, 62, 76]: $\langle\mathscr{P}\rangle \to 0$ for $\omega \to \infty$. At the same time, the canonical AM of the metallic-wire modes does not vanish and is well-defined, because all the field components $H_\phi = (i/\sqrt{2})(H^+e^{i\phi} - H^-e^{-i\phi})$, $E_r = (1/\sqrt{2})(E^+e^{i\phi} + E^-e^{-i\phi})$, and E_z possess the common phase factor $\exp(i\ell\phi)$ [see Eqs. (5) and (6)], subject to the action of the AM operator $-i\partial/\partial\phi$.

Analytical calculations for metallic-wire modes do not produce simple equations similar to Eqs. (17) and (18) because of the dispersion of the metal and the difference between ε and $\tilde{\varepsilon}$. However, the geometrical-optics picture of surface plasmon-polaritons propagating along helical rays on the metal-dielectric interface, Fig. 1(b), allows a simple analytical description of the higher-order mode properties in the paraxial approximation, $k_0 r_0 \gg 1$.

Consider a locally-planar surface plasmon-polarion propagating with the wavevector $\mathbf{k}_p = k_z\overline{\mathbf{z}} + k_\phi\overline{\boldsymbol{\varphi}}$, where the local Cartesian coordinates of the interface are attached to the global cylindrical coordinates (the overbars denote the corresponding unit vectors), and $|\mathbf{k_p}| = k_p$ is the wavenumber of the planar surface plasmon-polariton [45, 46, 62, 76]. Then, the phase-matching (quantization) condition along the cyclical azimuthal coordinate on the cylindrical surface yields $k_\varphi r_0 = \ell$ [64]. In turn, the longitudinal wavevector component determines the propagation constant: $k_z = \beta$. From these relations and known properties of surface plasmon-polaritons [45, 46, 62, 76], we derive the dispersion relation for metallic-wire modes:

$$\beta(\omega) \simeq \sqrt{k_p^2(\omega) - \frac{\ell^2}{r_0^2}}, \quad k_p(\omega) = \sqrt{\frac{\varepsilon_1(\omega)}{1+\varepsilon_1(\omega)}}\frac{\omega}{c}. \tag{21}$$

Remarkably, this is a simple non-transcendental relation without any special functions. The mode group velocity can also be derived either by differentiating from Eq. (21) or by taking the z-projection of the group velocity of planar surface plasmons [45, 46, 62, 76]:

$$v_g \simeq c\frac{(1+\varepsilon_1)^2}{1+\varepsilon_1^2}\sqrt{\frac{\varepsilon_1}{1+\varepsilon_1} - \frac{\ell^2}{k_0^2 r_0^2}}. \tag{22}$$

The comparison of Eqs. (21) and (22) with the results of exact calculations is shown in Fig. 2 (b). These agree well for $k_0 r_0 \gg 1$.
Next, it is known now that planar surface plasmon-polaritons carry *transverse spin AM*, orthogonal to their wavevector $\mathbf{k}_p$ and normal to the interface (r-direction in our case) [6, 36, 45, 46, 49, 50]. Therefore, this transverse spin has both a ϕ-component and a z-component [65]. Using the transverse spin calculated for planar surface plasmons in [45, 46] and projecting it onto the z-axis, we obtain the following longitudinal spin AM of the metallic-wire mode:

$$\frac{\omega \langle S_z \rangle}{\langle W \rangle} \simeq \frac{\sqrt{-1-\varepsilon_1}(2+\varepsilon_1)}{1+\varepsilon_1^2} \frac{\ell}{k_0 r_0}. \tag{23}$$

This equation agrees well with the exact calculations, as shown in Fig. 4, when $k_0 r_0 \gg 1$.
Thus, the geometrical-optics ray picture, supplied with the known properties of planar surface plasmon-polaritons, provides an efficient analytical description for the dispersion and AM properties of the higher-order metallic-wire modes.

CONCLUSION

We have provided the first self-consistent calculations, both analytical and numerical, of the canonical dynamical properties - spin/orbital/total angular momenta (AM), momentum, and helicity - of the eigenmodes of cylindrical waveguides: dielectric fibers and metallic wires. These properties are of major importance for optical communications and information transfer, including AM-based multiplexing [22–24, 29, 30]. Surprisingly, despite the long history of the theoretical and experimental studies of optical waveguides [25–28], there was no proper description of the AM of the cylindrical guided modes. This is because of the lack, until very recently [45, 46], of consistent theoretical definitions of these quantities (well-studied in free space) in inhomogeneous and dispersive media. Our work fills this important gap.

In particular, we have found the fundamental quantization of the total AM of eigenmodes of cylindrical waveguides. Although this result looks very natural from the symmetry viewpoint, it has never been obtained explicitly, apart from numerical

calculations [39] for a single fundamental mode in a nondispersive dielectric fiber. Notably, the traditional approach based on the kinetic Poynting (i.e., Abraham) momentum and AM results in very different non-integer AM values, counterintuitive for cylindrically-symmetric systems. Furthermore, the Poynting-Abraham AM vanishes in the paraxial approximation for metallic-wire modes. This is in strong contrast with the vortex nature of higher-order metallic-wire modes.

We have also calculated the spin and orbital AM of the guided modes. These are noninteger in the general nonparaxial case, because of the spin-orbit interactions induced by the inhomogeneous medium [31-36], but tend to integer values (19) and (20) in the paraxial regime. Remarkably, we have shown that the spin, orbital, and total AM values are intimately related to the generalized *geometric and dynamical phases* in the mode fields. The laconic relations (16) generalize previous free-space results [10, 11, 14] to the case of inhomogeneous and dispersive optical media.

Thus, our approach allows one to quantify the most fundamental dynamical properties of the cylindrical modes in the exact full-vector formalism. In all cases we examined, the results are perfectly consistent with the physical intuition and symmetries of the system, see Eqs. (9), (11), (19), and (20). Therefore, our consideration of cylindrical media can be regarded as a simple *test case* for further application of the general formalism of Eqs. (1) and (4) to optical eigenmodes of complex dielectric and metallic structures. After this work was completed, the relevant recent paper [77] and the preprint [78] came to our attention. The paper [77] examines the spin and orbital AM, as well as the helicity, of the eigenmodes of nondispersive dielectric fibers. However, the Poynting-Abraham-type quantities are analyzed there; they differ considerably from the canonical Minkowski-type quantities considered in our work. In turn, the preprint [78] reports related results on the quantization of the Minkowski-type total AM of optical beams, but only in homogeneous nondispersive media.

APPENDIX A

The electromagnetic boundary conditions for $r = r_0$, i.e. the continuity of the $E_{z,\phi}$ and $H_{z,\phi}$ components of the fields 5 and 6, provide a system of equations for the

coefficients A, B, C, D. It can be written as the matrix equation $\hat{M}\overrightarrow{V} = 0$ [26], with $\overrightarrow{V} = (A, B, C, D)^T$ and

$$\hat{M} \equiv \begin{pmatrix} \sqrt{\varepsilon_2} J_\ell & 0 & -\sqrt{\varepsilon_1} H_\ell^{(1)} & 0 \\ \sqrt{\varepsilon_2} \frac{\ell\beta}{\kappa_1^2 r_0} J_\ell & i\sqrt{\varepsilon_2} \frac{k_1}{\kappa_1} J_\ell' & -\sqrt{\varepsilon_1} \frac{\ell\beta}{\kappa_2^2 r_0} H_\ell^{(1)} & -i\sqrt{\varepsilon_1} \frac{k_2}{\kappa_2} H_\ell^{(1)'} \\ 0 & J_\ell & 0 & -H_\ell^{(1)} \\ -i\frac{k_1}{\kappa_1} J_\ell' & \frac{\ell\beta}{\kappa_1^2 r_0} J_\ell & i\frac{k_2}{\kappa_2} H_\ell^{(1)'} & -\frac{\ell\beta}{\kappa_2^2 r_0} H_l^{(1)} \end{pmatrix}. \tag{A01}$$

Here, $\kappa_{1,2} = \sqrt{k_{1,2}^2 - \beta^2}$, $k_{1,2} = \varepsilon_{1,2}\mu\omega^2/c^2$, $J_\ell \equiv J_\ell(\kappa_1 r_0)$, $H_\ell^{(1)} \equiv H_\ell^{(1)}(\kappa_2 r_0)$, and the prime stands for the derivative with respect to the special-function argument.

The transcendental dispersion equation for the eigenmodes is provided by $\det\hat{M}(\beta\omega) = 0$. After it is solved (numerically), one can find the complex field amplitudes A,B,C, and D, up to a common constant factor. In the special case $\ell = 0$, Eq. (A01) is simplified, and the characteristic equation $\det\hat{M}(\beta\omega) = 0$ can be presented as a product of two factors, one of which must vanish:

$$\frac{J_1}{J_0} - \frac{\varepsilon_2}{\varepsilon_1}\frac{\kappa_1}{\kappa_2}\frac{H_1^{(1)}}{H_0^{(1)}} = 0 \quad \text{TM}, \qquad \frac{J_1}{J_0} - \frac{\kappa_1}{\kappa_2}\frac{H_1^{(1)}}{H_0^{(1)}} = 0 \quad \text{(TE)}, \tag{A02}$$

where we used $J_0' = -J_1$, $H_0^{(1)'} = -H_1^{(1)}$, and $k_2/k_1 = \sqrt{\varepsilon_2/\varepsilon_1}$. One can show that these dispersion relations correspond to pure TM and TE modes with $B = D = 0$ and $A = C = 0$, respectively [26], and only TM modes exist in the metallic-wire case. Spin, orbital, and total AM, as well as the helicity of the modes A02, vanish identically, Eq. (7). In the case of dielectric fibers, none of these modes is the fundamental mode with the lowest frequency. The fundamental mode is the circularly-polarized mode characterized by $(m, \sigma, n) = (0, 1, 0)$, i.e., $\ell = 1$, Fig. 2 (a). All modes with $\ell \neq 0$ are generally *mixed*, i.e., neither TE nor TM, with all nonzero coefficients A, B, C, and D.

Funding

H2020 European Research Council (ERC) (ERC-2016-STG-714151-PSINFONI); H2020 Marie Skłodowska-Curie Actions (MSCA) (748950 BISTRO-LIGHT); Air Force Office of Scientific Research (AFOSR) (FA9550-14-1-0040); Japan Science and Technology Agency (JST) (CREST JPMJCR1676, the ImPACT program); Japan Society for the Promotion of Science (JSPS) (JSPS-RFBR 17-52-50023); John Templeton Foundation (JTF); Australian Research Council (ARC); RIKEN-AIST Challenge Research Fund.

REFERENCES

1. Allen, L., Barnett, S. M. & Padgett, M. J. *Optical Angular Momentum* doi:10.1887/0750309016 (IOP Publishing Ltd, 2003).
2. *Twisted Photons* (eds Torres, J. P. & Torner, L.) doi:10.1002/9783527635368 (Wiley-VCH Verlag GmbH & Co. KGaA, Weinheim, Germany, 2011).
3. *The Angular Momentum of Light* (eds Andrews, D. L. & Babiker, M.) doi:10.1017/CBO9780511795213 (Cambridge University Press, Cambridge, 2012).
4. Allen, L., Padgett, M. J. & Babiker, M. The Orbital Angular Momentum of Light. *Progress in Optics* **39.** doi:10.1016/S0079-6638(08)70391-3 (1999).
5. Yao, A. M. & Padgett, M. J. Orbital angular momentum: origins, behavior and applications. *Advances in Optics and Photonics* **3.** doi:10.1364/AOP.3.000161 (2011).
6. Bliokh, K. Y. & Nori, F. Transverse and longitudinal angular momenta of light. doi:10.1016/j.physrep.2015.06.003 (2015).
7. Berestetskii, V. B., Lifshitz, E. M. & Pitaevski\u{i}, L. P. *Quantum Electrodynamics* (Butterworth-Heinemann, 1982).
8. Soper, D. E. *Classical field theory* doi:10.1007/978-3-030-04738-2_1 (Wiley, 1976).
9. Leader, E. The photon angular momentum controversy: Resolution of a conflict between laser optics and particle physics. *Physics Letters B* **756.** doi:10.1016/j.physletb.2016.03.023 (2016).
10. Van Enk, S. & Nienhuis, G. Commutation Rules and Eigenvalues of Spin and Orbital Angular Momentum of Radiation Fields. *Journal of Modern Optics* **41.** doi:10.1080/09500349414550911 (1994).

11. Bliokh, K. Y., Alonso, M. A., Ostrovskaya, E. A. & Aiello, A. Angular momenta and spin-orbit interaction of nonparaxial light in free space. *Physical Review A* **82.** doi:10.1103/PhysRevA.82.063825 (2010).

12. Barnett, S. M. Rotation of electromagnetic fields and the nature of optical angular momentum. *Journal of Modern Optics* **57.** doi:10.1080/09500341003654427 (2010).

13. Bialynicki-Birula, I. & Bialynicka-Birula, Z. Canonical separation of angular momentum of light into its orbital and spin parts. *Journal of Optics* **13.** doi:10.1088/2040-8978/13/6/064014 (2011).

14. Bliokh, K. Y., Dressel, J. & Nori, F. Conservation of the spin and orbital angular momenta in electromagnetism. *New Journal of Physics* **16.** doi:10.1088/1367-2630/16/9/093037 (2014).

15. He, H., Friese, M. E. J., Heckenberg, N. R. & Rubinsztein-Dunlop, H. Direct Observation of Transfer of Angular Momentum to Absorptive Particles from a Laser Beam with a Phase Singularity. *Physical Review Letters* **75.** doi:10.1103/PhysRevLett.75.826 (1995).

16. Gahagan, K. T. & Swartzlander, G. A. Optical vortex trapping of particles. *Optics Letters* **21.** doi:10.1364/OL.21.000827 (1996).

17. Garcés-Chávez, V. *et al.* Observation of the Transfer of the Local Angular Momentum Density of a Multiringed Light Beam to an Optically Trapped Particle. *Physical Review Letters* **91.** doi:10.1103/PhysRevLett.91.093602 (2003).

18. Grier, D. G. *A revolution in optical manipulation* 2003. doi:10.1038/nature01935.

19. Mair, A., Vaziri, A., Weihs, G. & Zeilinger, A. Entanglement of the orbital angular momentum states of photons. *Nature* **412.** doi:10.1038/35085529 (2001).

20. Leach, J., Padgett, M. J., Barnett, S. M., Franke-Arnold, S. & Courtial, J. Measuring the Orbital Angular Momentum of a Single Photon. *Physical Review Letters* **88.** doi:10.1103/PhysRevLett.88.257901 (2002).

21. Leach, J. *et al.* Quantum correlations in optical angle-orbital angular momentum variables. *Science* **329.** doi:10.1126/science.1190523 (2010).

22. Gibson, G. *et al.* Free-space information transfer using light beams carrying orbital angular momentum. *Optics express* **12.** doi:10.1364/OPEX.12.005448 (2004).

23. Wang, J. *et al.* Terabit free-space data transmission employing orbital angular momentum multiplexing. *Nature Photonics* **6.** doi:10.1038/nphoton.2012.138 (2012).

24. Tamburini, F. *et al.* Encoding many channels on the same frequency through radio vorticity: first experimental test. *New Journal of Physics* **14.** doi:10.1088/1367-2630/14/3/033001 (2012).

25. Snyder, A. W. & Love, J. D. *Optical Waveguide Theory* doi:10.1007/978-1-4613-2813-1 (Springer, Boston, MA, 1983).

26. Marcuse, D. *Light Transmission Optics* doi:10.1080/716099334 (Van Nostrand Reinhold, 1982).

27. Pfeiffer, C. A., Economou, E. N. & Ngai, K. L. Surface polaritons in a circularly cylindrical interface: Surface plasmons. *Physical Review B* **10.** doi:10.1103/PhysRevB.10.3038 (1974).

28. Novotny, L. & Hafner, C. Light propagation in a cylindrical waveguide with a complex, metallic, dielectric function. *Physical Review E* **50.** doi:10.1103/PhysRevE.50.4094 (1994).

29. Bozinovic, N. *et al.* Terabit-scale orbital angular momentum mode division multiplexing in fibers. *Science* **340.** doi:10.1126/science.1237861 (2013).

30. Willner, A. E. *et al.* Optical communications using orbital angular momentum beams. *Advances in Optics and Photonics* **7.** doi:10.1364/AOP.7.000066 (2015).

31. Dooghin, A. V., Kundikova, N. D., Liberman, V. S. & Zeldovich, B. Y. Optical Magnus effect. *Physical Review A* **45.** doi:10.1103/PhysRevA.45.8204 (1992).

32. Liberman, V. S. & Zel'dovich, B. Y. Spin-orbit interaction of a photon in an inhomogeneous medium. *Physical Review A* **46.** doi:10.1103/PhysRevA.46.5199 (1992).

33. Bliokh, K. Y. & Bliokh, Y. P. Modified geometrical optics of a smoothly inhomogeneous isotropic medium: The anisotropy, Berry phase, and the optical Magnus effect. *Physical Review E* **70.** doi:10.1103/PhysRevE.70.026605 (2004).

34. Alexeyev, C. N., Volyar, A. & Yavorsky, M. A. in *Lasers, Optics and Electro-Optics Research Trends* (ed Chen, L. I.) (Nova, 2007).

35. Golowich, S. Asymptotic theory of strong spin-orbit coupling in optical fiber. *Optics Letters* **39.** doi:10.1364/OL.39.000092 (2014).

36. Bliokh, K. Y., Rodríguez-Fortuño, F. J., Nori, F. & Zayats, A. V. Spin-orbit interactions of light. *Nature Photonics* **9.** doi:10.1038/nphoton.2015.201 (2015).

37. Alexeyev, A. & Fadeyeva, T. Optical vortices and the flow of their angular momentum in a multimode fiber. *Semiconductor Physics, Quantum Electronics & Optoelectronics* **1** (1998).

38. Gregg, P., Kristensen, P. & Ramachandran, S. Conservation of orbital angular momentum in air-core optical fibers. *Optica* **2.** doi:10.1364/OPTICA.2.000267 (2015).

39. Kien, F. L., Balykin, V. I. & Hakuta, K. Angular momentum of light in an optical nanofiber. *Physical Review A - Atomic, Molecular, and Optical Physics* **73.** doi:10.1103/PhysRevA.73.053823 (2006).

40. Brevik, I. *Experiments in phenomenological electrodynamics and the electromagnetic energy-momentum tensor* 1979. doi:10.1016/0370-1573(79)90074-7.

41. Pfeifer, R. N. C., Nieminen, T. A., Heckenberg, N. R. & Rubinsztein-Dunlop, H. Colloquium: momentum of an electromagnetic wave in dielectric media. *Reviews of Modern Physics* **79.** doi:10.1103/RevModPhys.79.1197 (2007).

42. Barnett, S. M. & Loudon, R. The enigma of optical momentum in a medium. *Philosophical Transactions of the Royal Society A: Mathematical, Physical and Engineering Sciences* **368.** doi:10.1098/rsta.2009.0207 (2010).

43. Milonni, P. W. & Boyd, R. W. Momentum of Light in a Dielectric Medium. *Advances in Optics and Photonics* **2.** doi:10.1364/AOP.2.000519 (2010).

44. Kemp, B. A. Resolution of the Abraham-Minkowski debate: Implications for the electromagnetic wave theory of light in matter. *Journal of Applied Physics* **109.** doi:10.1063/1.3582151 (2011).

45. Bliokh, K. Y., Bekshaev, A. Y. & Nori, F. Optical Momentum, Spin, and Angular Momentum in Dispersive Media. *Physical Review Letters* **119.** doi:10.1103/PhysRevLett.119.073901 (2017).

46. Bliokh, K. Y., Bekshaev, A. Y. & Nori, F. Optical momentum and angular momentum in complex media: From the Abraham-Minkowski debate to unusual properties of surface plasmon-polaritons. *New Journal of Physics* **19.** doi:10.1088/1367-2630/aa8913 (2017).

47. Jackson, J. D. *Classical Electrodynamics, 3rd Edition* doi:10.1002/3527600434.eap109 (1998).

48. Lifshitz, L. D. L. & M., E. in *Electrodynamics of Continuous Media* (Pergamon, 1984).

49. Bliokh, K. Y. & Nori, F. Transverse spin of a surface polariton. *Physical Review A* **85.** doi:10.1103/PhysRevA.85.061801 (2012).

50. Aiello, A., Banzer, P., Neugebauer, M. & Leuchs, G. From transverse angular momentum to photonic wheels. *Nature Photonics* **9.** doi:10.1038/nphoton.2015.203 (2015).

51. Afanasiev, G. N. & Stepanovsky, Y. P. The helicity of the free electromagnetic field and its physical meaning. *Il Nuovo Cimento A* **109.** doi:10.1007/BF02731014 (1996).

52. Trueba, J. L. & Rañada, A. F. The electromagnetic helicity. *European Journal of Physics* **17.** doi:10.1088/0143-0807/17/3/008 (1996).

53. Cameron, R. P., Barnett, S. M. & Yao, A. M. Optical helicity, optical spin and related quantities in electromagnetic theory. *New Journal of Physics* **14.** doi:10.1088/1367-2630/14/5/053050 (2012).

54. Bliokh, K. Y., Bekshaev, A. Y. & Nori, F. Dual electromagnetism: Helicity, spin, momentum and angular momentum. *New Journal of Physics* **15.** doi:10.1088/1367-2630/15/3/033026 (2013).

55. Fernandez-Corbaton, I. *et al.* Electromagnetic duality symmetry and helicity conservation for the macroscopic maxwell's equations. *Physical Review Letters* **111.** doi:10.1103/PhysRevLett.111.060401 (2013).

56. Van Kruining, K. & Götte, J. B. The conditions for the preservation of duality symmetry in a linear medium. *Journal of Optics* **18.** doi:10.1088/2040-8978/18/8/085601 (2016).

57. Alpeggiani, F., Bliokh, K. Y., Nori, F. & Kuipers, L. Electromagnetic Helicity in Complex Media. *Physical Review Letters* **120.** doi:10.1103/PhysRevLett.120.243605 (2018).

58. Partanen, M., Häyrynen, T., Oksanen, J. & Tulkki, J. Photon mass drag and the momentum of light in a medium. *Physical Review A* **95.** doi:10.1103/PhysRevA.95.063850 (2017).

59. Philbin, T. G. & Allanson, O. Optical angular momentum in dispersive media. *Physical Review A* **86.** doi:10.1103/PhysRevA.86.055802 (2012).

60. Philbin, T. G. Electromagnetic energy momentum in dispersive media. *Physical Review A* **83.** doi:10.1103/PhysRevA.83.013823 (2011).

61. Bliokh, K. Y., Niv, A., Kleiner, V. & Hasman, E. Geometrodynamics of spinning light. *Nature Photonics* **2.** doi:10.1038/nphoton.2008.229 (2008).

62. Maier, S. A. *Plasmonics: Fundamentals and applications* (Springer, 2007).

63. Novotny, L. & Hecht, B. *Principles of Nano-Optics* doi:10.1017/CBO9780511794193 (Cambridge University Press, Cambridge, 2012).

64. Catrysse, P. B. & Fan, S. Understanding the dispersion of coaxial plasmonic structures through a connection with the planar metal-insulator-metal geometry. *Applied Physics Letters* **94.** doi:10.1063/1.3148692 (2009).

65. Garoli, D., Zilio, P., De Angelis, F. & Gorodetski, Y. Helicity locking of chiral light emitted from a plasmonic nanotaper. *Nanoscale* **9.** doi:10.1039/C7NR01674C (2017).

66. Berry, M. V. Optical currents. *Journal of Optics A* **11.** doi:10.1088/1464-4258/11/9/094001 (2009).

67. Bliokh, K. Y., Bekshaev, A. Y., Kofman, A. G. & Nori, F. Photon trajectories, anomalous velocities and weak measurements: A classical interpretation. *New Journal of Physics* **15.** doi:10.1088/1367-2630/15/7/073022 (2013).

68. Barnett, S. M. & Berry, M. V. Superweak momentum transfer near optical vortices. *Journal of Optics* **15.** doi:10.1088/2040-8978/15/12/125701 (2013).

69. Nye, J. in *Sir Charles Frank OBE, FRS: An eightieth birthday tribute.* (eds Chambers, R., Enderby, J., Keller, A., Lang, A. & Steeds, J.) (Adam Hilger, 1991).

70. Berry, M. V. & Dennis, M. R. Polarization singularities in isotropic random vector waves. *Proceedings of the Royal Society A: Mathematical, Physical and Engineering Sciences* **457.** doi:10.1098/rspa.2000.0660 (2001).

71. K. Y. Bliokh, M. A. Alonso, and M. R. Dennis are preparing a manuscript to be called "Space-variant geometric phases and topological indices in 3D polarized fields."

72. Bhandari, R. Polarization of light and topological phases. *Physics Reports* **281.** doi:10.1016/S0370-1573(96)00029-4 (1997).

73. Hassani Gangaraj, S. A., Silveirinha, M. G. & Hanson, G. W. Berry Phase, Berry Connection, and Chern Number for a Continuum Bianisotropic Material From a Classical Electromagnetics Perspective. *IEEE Journal on Multiscale and Multiphysics Computational Techniques* **2.** doi:10.1109/JMMCT.2017.2654962 (2017).

74. De Nittis, G. & Lein, M. The Schrödinger formalism of electromagnetism and other classical waves - how to make quantum-wave analogies rigorous. *Annals of Physics.* doi:10.1016/j.aop.2018.02.019 (2018).

75. Bliokh, K. Y., Gorodetski, Y., Kleiner, V. & Hasman, E. Coriolis effect in optics: Unified geometric phase and spin-hall effect. *Physical Review Letters* **101.** doi:10.1103/PhysRevLett.101.030404 (2008).

76. Nkoma, J., Loudon, R. & Tilley, D. R. Elementary properties of surface polaritons. *Journal of Physics C* **7.** doi:10.1088/0022-3719/7/19/015 (1974).

77. Le Kien, F., Busch, T., Truong, V. G. & Nic Chormaic, S. Higher-order modes of vacuum-clad ultrathin optical fibers. *Physical Review A* **96.** doi:10.1103/PhysRevA.96.023835 (2017).

78. Partanen, M. & Tulkki, J. Angular momentum and field quantization in nondispersive media. *arXiv:1803.10069* (2018).

Discussion of results and conclusions

The work collected in this thesis is the result of more than three years spent trying to answer various questions to the best of our possibilities. I must admit I did not really felt bound to the necessity of the answers to all fit into the same tale, but built more towards each of them being its own story and eventually partake into the same anthology. However, it must be said, most of the questions were alongside the lines of *"But what if there's a magnetic dipole?"*, so the anthology was not particularly complex to put together. With this thesis work I hope to have made a contribution to the field of nanophotonics and hope it can serve as a building block for future stories.
To summarise the main achievements described in this thesis, I believe we obtained the following results:

- We described, using the formalism of the angular spectrum, the fields of dipolar sources. Introducing a simplified notation for the angular spectrum representation of electromagnetic fields, we were able to single out the directional components of the angular spectra of various dipolar sources, such as circular electric and magnetic dipoles and Huygens dipoles.

- We proved the near-field directionality of said Huygens dipole finding it is one of the three fundamental dipolar sources which satisfies the requirement of *not* exciting a guided mode in a given direction.

- We theoretically introduced the Janus dipole, an electromagnetic source similar to the Huygens dipole but with a significant difference in the relative phases between the electric and the magnetic dipole comprising it. This source possesses a dual-face behaviour, either exciting or not exciting a guided mode depending on the phase it is showing to the waveguide. We numerically proved the

feasibility of embedding a Janus dipole between two waveguides and achieving the selective excitation of one of the two. We then experimentally demonstrated the excitation of a linear Janus dipole, inducing it into nanoparticles. Moreover, we predicted and experimentally realised the first spinning Janus dipole. We would like to note that the work on the Janus dipole was selected as Editor's Suggestion and Featured in Physics" in *Physical Review Letters*. It accumulated 38 citations in the first 17 months after its publication, with a field-weighted citation index in the top 1%. Moreover, it was a very conference-appreciated work, as it earned me both a "Best Poster" and a "Best Talk" award at two international conferences (*Nanometa 2019* and *Plasmonica 2019*).

- We extended the optimisation method we had developed, devising a design technique which allows to tailor a dipolar source to the specific excitation of multiple guided modes. This simple approach, based on linear algebra, enables the full control on amplitude, phase and direction of up to six guided modes, and has resulted in a free software which we developed and released for anyone to use.

- We provided analytical and numerical calculations of angular momenta and helicity of the eigenmodes of cylindrical waveguides, both dielectric and metallic, with a description which applies also to inhomogeneous and dispersive materials. We found the quantization of the total angular momentum of said eigenmodes, independently of dispersion. Finally, we showed the relation between the angular momenta of cylindrical modes with geometric and dynamical phases of the fields.

All these results pertain to the field of nanophotonics and possess numerous similarities between each other. Particularly, the totality of our research has been focused on the study of the degrees of freedom of light and how they are exchanged, or shared, with waveguiding structures.

Future works

The works presented here allow for many possible extensions, both from a theoretical and from an experimental point of view.

- From a theoretical point of view, the optimisation of the dipolar sources we presented could fairly easily be extended to higher order multipoles, such as quadrupoles, octupoles and so on. A description of the angular spectrum of higher order multipoles has been very recently developed in our group and their near-field directionality unveiled [240]. Each multipole added to our optimisation technique would mean many more degrees of freedom to utilise to control the excitation of more than six guided modes.

- Also still as a theoretical improvement, it would be interesting to release the assumption of monochromaticity of the dipolar fields and optimise the sources both in space and in time. Being bound to the dispersion relation, the frequency and the wavevector of a given guided mode are not independent parameters so the optimisation of the spatial degrees of freedom would influence that of the temporal ones, and viceversa, which might lead to a significant amount of new physics.

- The introduction of the OAM in our angular spectrum formalism could also represent a way of increasing the number of degrees of freedom which are available in our system. Sources with a non-zero OAM could be studied to controllably excite the guided modes of cylindrical waveguides, whose angular momenta we have thoroughly described.

- From the experimental side, we are currently in the process of measuring the behaviour of the Janus dipole between two waveguides, as depicted in figure [3 (c)] of our paper [Paper C]. We have performed numerical simulations to determine the shape and size of the scatterer to use as a Janus dipole at telecom wavelengths, optimising, at the same time, the distance between it and the waveguides and the angle of incidence of light. Due to the numerical simulations being convincing enough, said samples were fabricated and are now in the process of being tested.

- Experimentally, it would also be interesting to test the multimode control from a single source, either via direct excitation of directional different modes or via observation of the angular spectrum of the source. Work needs to be done, in this direction, to determine an effective method of designing the scatterer or, in general, experimentally realise the dipole.

Bibliography

1. Demming, A. L. Nanophotonics: a stimulus for light discussion. *Nanotechnology* **27.** doi:10.1088/0957-4484/27/15/150201 (2016).
2. Editorial. Not so small. *Nature Photonics* **8.** doi:10.1038/nphoton.2014.282 (2014).
3. Haus, J. W. in *Fundamentals and Applications of Nanophotonics* (Woodhead Publishing, 2016). doi:10.1016/B978-1-78242-464-2.00001-4.
4. Editorial. A wonderful spin. *Nature Photonics* **9.** doi:10.1038/nphoton.2015.245 (2015).
5. Smirnova, D. & Kivshar, Y. S. Multipolar nonlinear nanophotonics. *Optica.* doi:10.1364/optica.3.001241 (2016).
6. Cirací, C. *et al.* Probing the Ultimate Limits of Plasmonic Enhancement. *Science* **337.** doi:10.1126/SCIENCE.1224823 (2012).
7. Editorial. Surface plasmon resurrection. *Nature Photonics* **6.** doi:10.1038/nphoton.2012.296 (2012).
8. Meinzer, N., Barnes, W. L. & Hooper, I. R. Plasmonic meta-atoms and metasurfaces. *Nature Photonics* **8.** doi:10.1038/nphoton.2014.247 (2014).
9. Kivshar, Y. All-dielectric meta-optics and non-linear nanophotonics. *National Science Review* **5.** doi:10.1093/nsr/nwy017 (2018).
10. Maxwell, J. C. On physical lines of force - Part I. *The London, Edinburgh, and Dublin Philosophical Magazine and Journal of Science* **21.** doi:10.1080/14786446108643033 (1861).
11. Maxwell, J. C. On physical lines of force - Part II. *The London, Edinburgh, and Dublin Philosophical Magazine and Journal of Science* **21.** doi:10.1080/14786446108643067 (1861).
12. Maxwell, J. C. On physical lines of force - Part III. *The London, Edinburgh, and Dublin Philosophical Magazine and Journal of Science* **23.** doi:10.1080/14786446208643207 (1862).
13. Maxwell, J. C. On physical lines of force - Part IV. *The London, Edinburgh, and Dublin Philosophical Magazine and Journal of Science* **23.** doi:10.1080/14786446208643219 (1862).
14. Maxwell, J. C. A Dynamical Theory of the Electromagnetic Field. *Philosophical Transactions of the Royal Society of London* **155.** doi:10.1098/rstl.1865.0008 (1865).

15. Jackson, J. D. *Classical Electrodynamics, 3rd Edition* doi:10.1002/3527600434.eap109 (1998).

16. Novotny, L. & Hecht, B. *Principles of Nano-Optics* doi:10.1017/CBO9780511794193 (Cambridge University Press, Cambridge, 2012).

17. Poynting, J. On the transfer of energy in the electromagnetic field. *Philosophical Transactions of the Royal Society of London* **175.** doi:10.1098/rstl.1884.0016 (1884).

18. Felsen, L. B. Evanescent waves*. *Journal of the Optical Society of America* **66.** doi:10.1364/JOSA.66.000751 (1976).

19. Saleh, B. E. A. & Teich, M. C. *Fundamentals of Photonics* doi:10.1002/0471213748 (John Wiley & Sons, Inc., New York, USA, 1991).

20. Möller, K. D. *Optics* doi:10.1007/b97508 (University Science Books, 1988).

21. Risner, F. *Opticae Thesaurus: Alhazeni Arabis Libri Septem Nunc Primum Editi, Eiusdem Liber De Crepusculis Et Nubium Asensionibus. Item Vitellonis Thuringopoloni Libri X* doi:10.3931/e-rara-9817 (1572).

22. Massey, G. A. Microscopy and pattern generation with scanned evanescent waves. *Applied Optics* **23.** doi:10.1364/AO.23.000658 (1984).

23. Cragg, G. E. & So, P. T. C. Lateral resolution enhancement with standing evanescent waves. *Optics Letters* **25.** doi:10.1364/OL.25.000046 (2000).

24. Schneckenburger, H. Total internal reflection fluorescence microscopy: technical innovations and novel applications. *Current Opinion in Biotechnology* **16.** doi:10.1016/J.COPBIO.2004.12.004 (2005).

25. Knoll, W. Optical Characterization of Organic Thin Films and Interfaces with Evanescent Waves. *MRS Bulletin* **16.** doi:10.1557/S0883769400056517 (1991).

26. Knoll, W. Polymer thin films and interfaces characterized with evanescent light. *Die Makromolekulare Chemie* **192.** doi:10.1002/macp.1991.021921201 (1991).

27. Kawata, S. & Sugiura, T. Movement of micrometer-sized particles in the evanescent field of a laser beam. *Optics Letters* **17.** doi:10.1364/OL.17.000772 (1992).

28. Kawata, S. & Tani, T. Optically driven Mie particles in an evanescent field along a channeled waveguide. *Optics Letters* **21.** doi:10.1364/OL.21.001768 (1996).

29. Almaas, E. & Brevik, I. Radiation forces on a micrometer-sized sphere in an evanescent field. *Journal of the Optical Society of America B* **12.** doi:10.1364/JOSAB.12.002429 (1995).

30. Mohammadnezhad, M. & Hassanzadeh, A. Evanescent field interferometric optical tweezers with rotational symmetric patterns. *Journal of the Optical Society of America B* **34.** doi:10.1364/JOSAB.34.000983 (2017).

31. Tai, H., Yoshino, T. & Tanaka, H. Fiber-optic evanescent-wave methane-gas sensor using optical absorption for the 3392-μm line of a He-Ne laser. *Optics Letters* **12.** doi:10.1364/OL.12.000437 (1987).

32. Stewart, G., Muhammad, F. & Culshaw, B. Sensitivity improvement for evanescent-wave gas sensors. *Sensors and Actuators B: Chemical* **11.** doi:10.1016/0925-4005(93)85297-N (1993).

33. Hoo, Y., Jin, W., Ho, H., Wang, D. & Windele, R. *Evanescent wave gas sensing using microstructure fibre* in *Technical Digest. CLEO/Pacific Rim 2001. 4th Pacific Rim Conference on Lasers and Electro-Optics (Cat. No.01TH8557)* (IEEE, 2001). doi:10.1109/CLEOPR.2001.968008.

34. Wei, L., Picardi, M. F., Kingsley-Smith, J. J., Zayats, A. V. & Rodríguez-Fortuño, F. J. Directional scattering from particles under evanescent wave illumination: the role of reactive power. *Optics Letters* **43.** doi:10.1364/OL.43.003393 (2018).

35. Wei, L., Zayats, A. V. & Rodríguez-Fortuño, F. J. Interferometric Evanescent Wave Excitation of a Nanoantenna for Ultrasensitive Displacement and Phase Metrology. *Physical Review Letters* **121.** doi:10.1103/PhysRevLett.121.193901 (2018).

36. Golat, S., Lim, E. A. & Rodríguez-Fortuño, F. J. Evanescent Gravitational Waves (2019).

37. Ashcroft, N. W. & Mermin, N. D. *Solid State Physics* 1976. doi:10.1016/0038-1101(66)90069-4.

38. Grosso, G. & Parravicini, G. P. *Solid State Physics (2nd edition)* ISBN: 9783540938033. doi:10.1016/B978-0-12-385030-0.00011-6 (2014).

39. Raether, H. *Surface Plasmons on Smooth and Rough Surfaces and on Gratings* doi:10.1007/BFb0048317 (Springer Berlin Heidelberg, Berlin, Heidelberg, 1988).

40. Zayats, A. V., Smolyaninov, I. I. & Maradudin, A. A. Nano-optics of surface plasmon polaritons. *Physics Reports* **408.** doi:10.1016/j.physrep.2004.11.001 (2005).

41. Maier, S. A. *Plasmonics: Fundamentals and applications* (Springer, 2007).

42. Fleischmann, M., Hendra, P. & McQuillan, A. Raman spectra of pyridine adsorbed at a silver electrode. *Chemical Physics Letters* **26.** doi:10.1016/0009-2614(74)85388-1 (1974).

43. Jeanmaire, D. L. & Van Duyne, R. P. Surface raman spectroelectrochemistry: Part I. Heterocyclic, aromatic, and aliphatic amines adsorbed on the anodized silver electrode. *Journal of Electroanalytical Chemistry and Interfacial Electrochemistry* **84.** doi:10.1016/S0022-0728(77)80224-6 (1977).

44. Moskovits, M. Surface roughness and the enhanced intensity of Raman scattering by molecules adsorbed on metals. *The Journal of Chemical Physics* **69.** doi:10.1063/1.437095 (1978).

45. Albrecht, M. G. & Creighton, J. A. Anomalously intense Raman spectra of pyridine at a silver electrode. *Journal of the American Chemical Society* **99.** doi:10.1021/ja00457a071 (1977).

46. Campion, A. & Kambhampati, P. Surface-enhanced Raman scattering. *Chemical Society Reviews* **27.** doi:10.1039/a827241z (1998).

47. Kneipp, K. *et al.* Surface-enhanced Raman scattering (SERS): a new tool for single molecule detection and identification. *Bioimaging* **6.** doi:10.1002/1361-6374(199806)6:2<104::AID-BIO6>3.0.CO;2-T (1998).

48. Moskovits, M. Surface-enhanced spectroscopy. *Reviews of Modern Physics* **57.** doi:10.1103/RevModPhys.57.783 (1985).

49. Stuart, D. A. *et al.* Glucose Sensing Using Near-Infrared Surface-Enhanced Raman Spectroscopy: Gold Surfaces, 10-Day Stability, and Improved Accuracy. doi:10.1021/AC0501238 (2005).

50. Braun, G. *et al.* Surface-Enhanced Raman Spectroscopy for DNA Detection by Nanoparticle Assembly onto Smooth Metal Films. doi:10.1021/JA070514Z (2007).

51. Maier, S. A. *et al.* Local detection of electromagnetic energy transport below the diffraction limit in metal nanoparticle plasmon waveguides. *Nature Materials* **2.** doi:10.1038/nmat852 (2003).

52. Quinten, M., Leitner, A., Krenn, J. R. & Aussenegg, F. R. Electromagnetic energy transport via linear chains of silver nanoparticles. *Optics Letters* **23.** doi:10.1364/OL.23.001331 (1998).

53. Willingham, B. & Link, S. Energy transport in metal nanoparticle chains via sub-radiant plasmon modes. *Optics Express* **19.** doi:10.1364/OE.19.006450 (2011).

54. Schmidt, M. A., Prill Sempere, L. N., Tyagi, H. K., Poulton, C. G. & Russell, P. S. J. Waveguiding and plasmon resonances in two-dimensional photonic lattices of gold and silver nanowires. *Physical Review B* **77.** doi:10.1103/PhysRevB.77.033417 (2008).

55. Bozhevolnyi, S. I., Volkov, V. S., Devaux, E., Laluet, J.-Y. & Ebbesen, T. W. Channel plasmon subwavelength waveguide components including interferometers and ring resonators. *Nature* **440.** doi:10.1038/nature04594 (2006).

56. Ditlbacher, H. *et al.* Silver Nanowires as Surface Plasmon Resonators. *Physical Review Letters* **95.** doi:10.1103/PhysRevLett.95.257403 (2005).

57. Moreno, E., Garcia-Vidal, F. J., Rodrigo, S. G., Martin-Moreno, L. & Bozhevolnyi, S. I. Channel plasmon-polaritons: modal shape, dispersion, and losses. *Optics Letters* **31.** doi:10.1364/OL.31.003447 (2006).

58. Fang, Y. & Sun, M. Nanoplasmonic waveguides: towards applications in integrated nanophotonic circuits. *Light: Science & Applications* **4.** doi:10.1038/lsa.2015.67 (2015).

59. Burke, J. J., Stegeman, G. I. & Tamir, T. Surface-polariton-like waves guided by thin, lossy metal films. *Physical Review B* **33.** doi:10.1103/PhysRevB.33.5186 (1986).

60. Ebbesen, T. W., Lezec, H. J., Ghaemi, H. F., Thio, T. & Wolff, P. A. Extraordinary optical transmission through sub-wavelength hole arrays. *Nature* **391.** doi:10.1038/35570 (1998).

61. Gordon, R. Extraordinary optical transmission for surface-plasmon-resonance-based sensing. *Journal of Nanophotonics* **2.** doi:10.1117/1.3013629 (2008).

62. Larson, S., Carlson, D., Ai, B. & Zhao, Y. The extraordinary optical transmission and sensing properties of Ag/Ti composite nanohole arrays. *Physical Chemistry Chemical Physics* **21.** doi:10.1039/C8CP07729K (2019).

63. Ying, Z. *et al.* Extraordinary Optical Transmission in a Hybrid Plasmonic Waveguide. *IEEE Photonics Journal* **8.** doi:10.1109/JPHOT.2016.2613599 (2016).

64. Qin, Y. *et al.* Extraordinary optical transmission properties of a novel Bi-layered plasmonic nanostructure array. *Optik* **174.** doi:10.1016/J.IJLEO.2018.08.073 (2018).

65. Zhang, Q., Hu, P. & Liu, C. Giant-enhancement of extraordinary optical transmission through nanohole arrays blocked by plasmonic gold mushroom caps. *Optics Communications* **335.** doi:10.1016/J.OPTCOM.2014.09.020 (2015).

66. Challener, W. A. *et al.* Heat-assisted magnetic recording by a near-field transducer with efficient optical energy transfer. *Nature Photonics* **3.** doi:10.1038/nphoton.2009.26 (2009).

67. Mansuripur, M. *et al.* Plasmonic nano-structures for optical data storage. *Optics Express* **17.** doi:10.1364/OE.17.014001 (2009).

68. Mao, F. *et al. Direct laser coding of plasmonic nanostructures for data storage applications* in *Nanophotonics VII* (eds Andrews, D. L., Nunzi, J.-M., Ostendorf, A. & Bain, A. J.) **10672** (SPIE, 2018). doi:10.1117/12.2306762.

69. Hirsch, L. R. *et al.* Nanoshell-mediated near-infrared thermal therapy of tumors under magnetic resonance guidance. *Proceedings of the National Academy of Sciences* **100.** doi:10.1073/PNAS.2232479100 (2003).

70. Loo, C., Lowery, A., Halas, N., West, J. & Drezek, R. Immunotargeted Nanoshells for Integrated Cancer Imaging and Therapy. doi:10.1021/NL050127S (2005).

71. O'Neal, D., Hirsch, L. R., Halas, N. J., Payne, J. & West, J. L. Photo-thermal tumor ablation in mice using near infrared-absorbing nanoparticles. *Cancer Letters* **209.** doi:10.1016/J.CANLET.2004.02.004 (2004).

72. Lal, S., Clare, S. E. & Halas, N. J. Nanoshell-Enabled Photothermal Cancer Therapy: Impending Clinical Impact. *Accounts of Chemical Research* **41.** doi:10.1021/ar800150g (2008).

73. Gobin, A. M. *et al.* Near-Infrared Resonant Nanoshells for Combined Optical Imaging and Photothermal Cancer Therapy. doi:10.1021/NL070610Y (2007).

74. Wang, H. Plasmonic refractive index sensing using strongly coupled metal nanoantennas: nonlocal limitations. *Scientific Reports* **8.** doi:10.1038/s41598-018-28011-x (2018).

75. Cheng, Y.-C., Chang, Y.-J., Chuang, Y.-C., Huang, B.-Z. & Chen, C.-C. A plasmonic refractive index sensor with an ultrabroad dynamic sensing range. *Scientific Reports* **9.** doi:10.1038/s41598-019-41353-4 (2019).

76. Xu, Y. *et al.* Optical Refractive Index Sensors with Plasmonic and Photonic Structures: Promising and Inconvenient Truth. *Advanced Optical Materials* **7.** doi:10.1002/adom.201801433 (2019).

77. Zafar, R., Nawaz, S., Singh, G., D'Alessandro, A. & Salim, M. Plasmonics-Based Refractive Index Sensor for Detection of Hemoglobin Concentration. *IEEE Sensors Journal* **18.** doi:10.1109/JSEN.2018.2826040 (2018).

78. Kawata, S., Inouye, Y. & Verma, P. Plasmonics for near-field nano-imaging and superlensing. *Nature Photonics* **3.** doi:10.1038/nphoton.2009.111 (2009).

79. Nordlander, P. Subwavelength imaging in colour. *Nature Photonics* **2.** doi:10.1038/nphoton.2008.110 (2008).

80. Maslovski, S. I. Subwavelength imaging with arrays of plasmonic scatterers. *Optics Communications* **285.** doi:10.1016/J.OPTCOM.2011.12.079 (2012).

81. Keiser, G. in *Wiley Encyclopedia of Telecommunications* (John Wiley & Sons, Inc., Hoboken, NJ, USA, 2003). doi:10.1002/0471219282.eot158.

82. Kaminow, I. P. & Koch, T. L. *Optical fiber telecommunications* doi:10.1016/C2009-0-20815-4 (Academic Press, 1997).

83. Senior, J. M. & Jamro, M. Y. *Optical fiber communications : principles and practice* (Prentice Hall, 2009).

84. *Optical Fiber Sensor Technology* (eds Grattan, K. T. V. & Meggitt, B. T.) doi:10.1007/978-1-4757-6077-4 (Springer US, Boston, MA, 1999).

85. Lee, B. Review of the present status of optical fiber sensors. *Optical Fiber Technology* **9.** doi:10.1016/S1068-5200(02)00527-8 (2003).

86. Giallorenzi, T. *et al.* Optical Fiber Sensor Technology. *IEEE Transactions on Microwave Theory and Techniques* **30.** doi:10.1109/TMTT.1982.1131089 (1982).

87. Tearney, G. J. *et al. Method and Apparatus for Performing Optical Measurements Using a Fiber Optic Imaging Guidewire, Catheter or Endoscope* 1996.

88. Tearney, G. J. *et al.* In vivo endoscopic optical biopsy with optical coherence tomography. *Science.* doi:10.1126/science.276.5321.2037 (1997).

89. Marcuse, D. *Light Transmission Optics* doi:10.1080/716099334 (Van Nostrand Reinhold, 1982).

90. Kepler, J. *De cometis libelli tres* doi:https://doi.org/10.3931/e-rara-1007 (1619).

91. Nichols, E. F. & Hull, G. F. The Pressure Due to Radiation. (Second Paper.) *Physical Review (Series I)* **17.** doi:10.1103/PhysRevSeriesI.17.26 (1903).

92. Poynting, J. The Wave Motion of a Revolving Shaft, and a Suggestion as to the Angular Momentum in a Beam of Circularly Polarised Light. *Proceedings of the Royal Society of London. Series A, Containing Papers of a Mathematical and Physical Character* **82** (1909).

93. Beth, R. A. Mechanical Detection and Measurement of the Angular Momentum of Light. *Physical Review* **50.** doi:10.1103/PhysRev.50.115 (1936).

94. O'Neil, A., MacVicar, I., Allen, L. & Padgett, M. Intrinsic and extrinsic nature of the orbital angular momentum of a light beam. *Physical Review Letters* **88.** doi:10.1103/PhysRevLett.88.053601 (2002).

95. Bliokh, K. Y., Rodríguez-Fortuño, F. J., Nori, F. & Zayats, A. V. Spin-orbit interactions of light. *Nature Photonics* **9.** doi:10.1038/nphoton.2015.201 (2015).

96. Allen, L. Orbital angular momentum of light and the transformation of Laguerre-Gaussian laser modes. *Phsyical Review A* **45.** doi:10.1103/PhysRevA.45.8185 (1992).

97. Molina-Terriza, G., Torres, J. P. & Torner, L. Management of the Angular Momentum of Light: Preparation of Photons in Multidimensional Vector States of Angular Momentum. *Physical Review Letters* **88.** doi:10.1103/PhysRevLett.88.013601 (2001).

98. Gibson, G. *et al.* Free-space information transfer using light beams carrying orbital angular momentum. *Optics express* **12.** doi:10.1364/OPEX.12.005448 (2004).

99. Gibson II, G. *et al. Increasing the data density of free-space optical communications using orbital angular momentum* in *Free-Space Laser Communications IV* **5550** (SPIE, 2004). doi:10.1117/12.557176.

100. Li, Y., Han, Y., Cui, Z. & Hui, Y. Performance analysis of the OAM based optical wireless communication systems with partially coherent elegant Laguerre-Gaussian beams in oceanic turbulence. *Journal of Optics* **21.** doi:10.1088/2040-8986/ab0270 (2019).

101. Wang, J. *et al.* Terabit free-space data transmission employing orbital angular momentum multiplexing. *Nature Photonics* **6.** doi:10.1038/nphoton.2012.138 (2012).

102. Willner, A. E. *et al.* Optical communications using orbital angular momentum beams. *Advances in Optics and Photonics* **7.** doi:10.1364/AOP.7.000066 (2015).

103. Bozinovic, N. *et al.* Terabit-scale orbital angular momentum mode division multiplexing in fibers. *Science* **340.** doi:10.1126/science.1237861 (2013).

104. Huang, H. *et al.* 100 Tbit/s free-space data link enabled by three-dimensional multiplexing of orbital angular momentum, polarization, and wavelength. *Optics Letters* **39.** doi:10.1364/OL.39.000197 (2014).

105. Devlin, R. C., Ambrosio, A., Rubin, N. A., Mueller, J. P. B. & Capasso, F. Arbitrary spin-to-orbital angular momentum conversion of light. *Science* **358.** doi:10.1126/science.aao5392 (2017).

106. Devlin, R. C. *et al.* Spin-to-orbital angular momentum conversion in dielectric metasurfaces. *Optics Express* **25.** doi:10.1364/OE.25.000377 (2017).

107. Marrucci, L., Manzo, C. & Paparo, D. Optical Spin-to-Orbital Angular Momentum Conversion in Inhomogeneous Anisotropic Media. *Physical Review Letters* **96.** doi:10.1103/PhysRevLett.96.163905 (2006).

108. Marrucci, L. *et al.* Spin-to-orbital conversion of the angular momentum of light and its classical and quantum applications. *Journal of Optics* **13.** doi:10.1088/2040-8978/13/6/064001 (2011).

109. Biener, G., Niv, A., Kleiner, V. & Hasman, E. Formation of helical beams by use of Pancharatnam-Berry phase optical elements. *Optics Letters* **27.** doi:10.1364/OL.27.001875 (2002).

110. Lin, D., Fan, P., Hasman, E. & Brongersma, M. L. Dielectric gradient metasurface optical elements. *Science* **345.** doi:10.1126/science.1253213 (2014).

111. Yu, N. & Capasso, F. Flat optics with designer metasurfaces. *Nature Materials* **13.** doi:10.1038/nmat3839 (2014).

112. Karimi, E. *et al.* Generating optical orbital angular momentum at visible wavelengths using a plasmonic metasurface. *Light: Science & Applications* **3.** doi:10.1038/lsa.2014.48 (2014).

113. Bouchard, F., Mand, H., Mirhosseini, M., Karimi, E. & Boyd, R. W. Achromatic orbital angular momentum generator. *New Journal of Physics* **16.** doi:10.1088/1367-2630/16/12/123006 (2014).

114. Bliokh, K. Y., Bekshaev, A. Y. & Nori, F. Extraordinary momentum and spin in evanescent waves. *Nature communications* **5.** doi:10.1038/ncomms4300 (2014).

115. Bliokh, K. Y., Smirnova, D. & Nori, F. Quantum spin Hall effect of light. *Science* **348.** doi:10.1126/science.aaa9519 (2015).

116. Bliokh, K. Y. & Nori, F. Transverse and longitudinal angular momenta of light. doi:10.1016/j.physrep.2015.06.003 (2015).

117. Marrucci, L. Quantum optics: Spin gives direction. *Nature Physics* **11.** doi:10.1038/nphys3198 (2015).

118. Van Mechelen, T. & Jacob, Z. Universal spin-momentum locking of evanescent waves. *Optica* **3.** doi:10.1364/OPTICA.3.000118 (2016).

119. Bohren, C. F. & Huffman, D. R. Absorption and scattering of light by small particles (1983).

120. Van de Hulst, H. C. *Light scattering by small particles* (Dover Publications, 1981).

121. García de Abajo, F. J. Colloquium : Light scattering by particle and hole arrays. *Reviews of Modern Physics* **79.** doi:10.1103/RevModPhys.79.1267 (2007).

122. Hecht, B., Mühlschlegel, P., Farahani, J., Eisler, H.-J. & Pohl, D. in *Tip Enhancement* (eds Kawata, S. & Shalaev, V. M.) chap. 9 (Elsevier, 2007). doi:10.1016/B978-044452058-6/50010-4.

123. Zhou, F., Li, Z.-Y., Liu, Y. & Xia, Y. Quantitative Analysis of Dipole and Quadrupole Excitation in the Surface Plasmon Resonance of Metal Nanoparticles. *The Journal of Physical Chemistry C* **112.** doi:10.1021/jp807075f (2008).

124. Evlyukhin, A. B., Reinhardt, C., Evlyukhin, E. & Chichkov, B. N. Multipole analysis of light scattering by arbitrary-shaped nanoparticles on a plane surface. *Journal of the Optical Society of America B* **30.** doi:10.1364/JOSAB.30.002589 (2013).

125. Zywietz, U., Evlyukhin, A. B., Reinhardt, C. & Chichkov, B. N. Laser printing of silicon nanoparticles with resonant optical electric and magnetic responses. *Nature Communications* **5.** doi:10.1038/ncomms4402 (2014).

126. Evlyukhin, A. B. *et al.* Demonstration of Magnetic Dipole Resonances of Dielectric Nanospheres in the Visible Region. *Nano Letters* **12.** doi:10.1021/nl301594s (2012).

127. Evlyukhin, A. B., Reinhardt, C., Seidel, A., Luk'yanchuk, B. S. & Chichkov, B. N. Optical response features of Si-nanoparticle arrays. *Physical Review B* **82.** doi:10.1103/PhysRevB.82.045404 (2010).

128. Sommerfeld, A. Über die Ausbreitung der Wellen in der drahtlosen Telegraphie. *Annalen der Physik* **333.** doi:10.1002/andp.19093330402 (1909).

129. Ishimaru, A. *Electromagnetic wave propagation, radiation, and scattering* doi:10.1002/9781119079699 (Prentice Hall, 1991).

130. Born, M. & Wolf, E. *Principles of Optics, 7th (expanded) edition, Cambridge University Press, Cambridge, 1999* **5.** doi:10.1016/S0030-3992(00)00061-X (2000).

131. Mandel, L. & Wolf, E. *Optical coherence and quantum optics* (Cambridge university press, 1995).

132. Weyl, H. Ausbreitung elektromagnetischer Wellen über einem ebenen Leiter. *Annalen der Physik* **365.** doi:10.1002/andp.19193652104 (1919).

133. Espinosa-Soria, A. & Martinez, A. Transverse Spin and Spin-Orbit Coupling in Silicon Waveguides. *IEEE Photonics Technology Letters* **28.** doi:10.1109/LPT.2016.2553841 (2016).

134. Petersen, J., Volz, J. & Rauschenbeutel, A. Chiral nanophotonic waveguide interface based on spin-orbit interaction of light. *Science* **346.** doi:10.1126/science.1257671 (2014).

135. Le Feber, B., Rotenberg, N. & Kuipers, L. Nanophotonic control of circular dipole emission. *Nature Communications* **6.** doi:10.1038/ncomms7695 (2015).

136. Rodríguez-Fortuño, F. J. *et al.* Near-field interference for the unidirectional excitation of electromagnetic guided modes. *Science* **340.** doi:10.1126/science.1233739 (2013).

137. Neugebauer, M., Bauer, T., Aiello, A. & Banzer, P. Measuring the Transverse Spin Density of Light. *Physical Review Letters* **114.** doi:10.1103/PhysRevLett.114.063901 (2015).

138. O'Connor, D., Ginzburg, P., Rodríguez-Fortuño, F. J., Wurtz, G. A. & Zayats, A. V. Spin-orbit coupling in surface plasmon scattering by nanostructures. *Nature Communications* **5.** doi:10.1038/ncomms6327 (2014).

139. Bliokh, K. Y. & Nori, F. Transverse spin of a surface polariton. *Physical Review A* **85.** doi:10.1103/PhysRevA.85.061801 (2012).

140. Lin, J. *et al.* Polarization-controlled tunable directional coupling of surface plasmon polaritons. *Science.* doi:10.1126/science.1233746 (2013).

141. Mitsch, R., Sayrin, C., Albrecht, B., Schneeweiss, P. & Rauschenbeutel, A. Quantum state-controlled directional spontaneous emission of photons into a nanophotonic waveguide. *Nature Communications* **5.** doi:10.1038/ncomms6713 (2014).

142. Sayrin, C. *et al.* Nanophotonic Optical Isolator Controlled by the Internal State of Cold Atoms. *Physical Review X* **5.** doi:10.1103/PhysRevX.5.041036 (2015).

143. Young, A. B. *et al.* Polarization Engineering in Photonic Crystal Waveguides for Spin-Photon Entanglers. *Physical Review Letters* **115.** doi:10.1103/PhysRevLett.115.153901 (2015).

144. Burresi, M. *et al.* Observation of polarization singularities at the nanoscale. *Physical Review Letters* **102.** doi:10.1103/PhysRevLett.102.033902 (2009).

145. Shen, Y., Bradford, M. & Shen, J.-T. Single-Photon Diode by Exploiting the Photon Polarization in a Waveguide. *Physical Review Letters* **107.** doi:10.1103/PhysRevLett.107.173902 (2011).

146. Yao, P., Manga Rao, V. & Hughes, S. On-chip single photon sources using planar photonic crystals and single quantum dots. *Laser & Photonics Reviews* **4.** doi:10.1002/lpor.200810081 (2010).

147. Arcari, M. *et al.* Near-unity coupling efficiency of a quantum emitter to a photonic crystal waveguide. *Physical Review Letters* **113.** doi:10.1103/PhysRevLett.113.093603 (2014).

148. Söllner, I. *et al.* Deterministic photon-emitter coupling in chiral photonic circuits. *Nature Nanotechnology.* doi:10.1038/nnano.2015.159 (2015).

149. Lang, B., Beggs, D. M. & Oulton, R. Time-reversal constraint limits unidirectional photon emission in slow-light photonic crystals. *Philosophical Transactions of the Royal Society A: Mathematical, Physical and Engineering Sciences* **374.** doi:10.1098/rsta.2015.0263 (2016).

150. Scarpelli, L. *et al.* 99% beta factor and directional coupling of quantum dots to fast light in photonic crystal waveguides determined by spectral imaging. *Physical Review B* **100.** doi:10.1103/PhysRevB.100.035311 (2019).

151. Mahmoodian, S., Prindal-Nielsen, K., Söllner, I., Stobbe, S. & Lodahl, P. Engineering chiral light–matter interaction in photonic crystal waveguides with slow light. *Optical Materials Express* **7.** doi:10.1364/OME.7.000043 (2017).

152. Gonzalez-Ballestero, C., Gonzalez-Tudela, A., Garcia-Vidal, F. J. & Moreno, E. Chiral route to spontaneous entanglement generation. *Phys. Rev. B* **92.** doi:10.1103/PhysRevB.92.155304 (2015).

153. Luxmoore, I. J. *et al.* Interfacing Spins in an InGaAs Quantum Dot to a Semiconductor Waveguide Circuit Using Emitted Photons. *Physical Review Letters* **110.** doi:10.1103/PhysRevLett.110.037402 (2013).

154. Espinosa-Soria, A., Rodríguez-Fortuño, F. J., Griol, A. & Martínez, A. On-Chip Optimal Stokes Nanopolarimetry Based on Spin-Orbit Interaction of Light. *Nano Letters* **17.** doi:10.1021/acs.nanolett.7b00564 (2017).

155. Rodríguez-Fortuño, F. J., Barber-Sanz, I., Puerto, D., Griol, A. & Martínez, A. Resolving Light Handedness with an on-Chip Silicon Microdisk. *ACS Photonics* **1.** doi:10.1021/ph500084b (2014).

156. Rodríguez-Fortuño, F. J. *et al.* Universal method for the synthesis of arbitrary polarization states radiated by a nanoantenna. *Laser & Photonics Reviews* **8.** doi:10.1002/lpor.201300184 (2014).

157. Rodríguez-Fortuño, F. J. *et al.* Sorting linearly polarized photons with a single scatterer. *Optics Letters* **39.** doi:10.1364/OL.39.001394 (2014).

158. Mueller, J. P. B., Leosson, K. & Capasso, F. Ultracompact metasurface in-line polarimeter. *Optica* **3.** doi:10.1364/OPTICA.3.000042 (2016).

159. Kapitanova, P. V. *et al.* Photonic spin Hall effect in hyperbolic metamaterials for polarization-controlled routing of subwavelength modes. *Nature Communications* **5.** doi:10.1038/ncomms4226 (2014).

160. Antognozzi, M. *et al.* Direct measurements of the extraordinary optical momentum and transverse spin-dependent force using a nano-cantilever. *Nature Physics.* doi:10.1038/nphys3732 (2016).

161. Kalhor, F., Thundat, T. & Jacob, Z. Universal spin-momentum locked optical forces. *Applied Physics Letters* **108.** doi:10.1063/1.4941539 (2016).

162. Canaguier-Durand, A. & Genet, C. Transverse spinning of a sphere in a plasmonic field. *Physical Review A - Atomic, Molecular, and Optical Physics.* doi:10.1103/PhysRevA.89.033841 (2014).

163. Hayat, A., Mueller, J. P. B. & Capasso, F. Lateral chirality-sorting optical forces. *Proceedings of the National Academy of Sciences.* doi:10.1073/pnas.1516704112 (2015).

164. Wang, S. B. & Chan, C. T. Lateral optical force on chiral particles near a surface. *Nature communications* **5.** doi:10.1038/ncomms4307 (2014).

165. Sukhov, S., Kajorndejnukul, V., Naraghi, R. R. & Dogariu, A. Dynamic consequences of optical spin-orbit interaction. *Nature Photonics* **9.** doi:10.1038/nphoton.2015.200 (2015).

166. Scheel, S., Buhmann, S. Y., Clausen, C. & Schneeweiss, P. Directional spontaneous emission and lateral Casimir-Polder force on an atom close to a nanofiber. *Physical Review A* **92.** doi:10.1103/PhysRevA.92.043819 (2015).

167. Rodríguez-Fortuño, F. J., Engheta, N., Martínez, A. & Zayats, A. V. Lateral forces on circularly polarizable particles near a surface. *Nature Communications* **6.** doi:10.1038/ncomms9799 (2015).

168. Philbin, T. G. A note on conserved quantities for electromagnetic waves (2018).

169. Kerker, M., Wang, D.-S. & Giles, C. L. Electromagnetic scattering by magnetic spheres. *Journal of the Optical Society of America* **73.** doi:10.1364/JOSA.73.000765 (1983).

170. Zambrana-Puyalto, X., Fernandez-Corbaton, I., Juan, M. L., Vidal, X. & Molina-Terriza, G. Duality symmetry and Kerker conditions. *Optics Letters* **38.** doi:10.1364/OL.38.001857 (2013).

171. Alaee, R., Filter, R., Lehr, D., Lederer, F. & Rockstuhl, C. A generalized Kerker condition for highly directive nanoantennas. *Optics Letters* **40.** doi:10.1364/OL.40.002645 (2015).

172. Fu, Y. H., Kuznetsov, A. I., Miroshnichenko, A. E., Yu, Y. F. & Luk'yanchuk, B. Directional visible light scattering by silicon nanoparticles. *Nature Communications* **4.** doi:10.1038/ncomms2538 (2013).

173. Geffrin, J. *et al.* Magnetic and electric coherence in forward- and back-scattered electromagnetic waves by a single dielectric subwavelength sphere. *Nature Communications* **3.** doi:10.1038/ncomms2167 (2012).

174. Person, S. *et al.* Demonstration of Zero Optical Backscattering from Single Nanoparticles. *Nano Letters* **13.** doi:10.1021/nl4005018 (2013).

175. Staude, I. *et al.* Tailoring directional scattering through magnetic and electric resonances in subwavelength silicon nanodisks. *ACS Nano* **7.** doi:10.1021/nn402736f (2013).

176. Hurst, D. L. *et al.* Nonreciprocal Transmission and Reflection of a Chirally Coupled Quantum Dot. *Nano Letters.* doi:10.1021/acs.nanolett.8b01869 (2018).

177. Coles, R. J. *et al.* Path-dependent initialization of a single quantum dot exciton spin in a nanophotonic waveguide. *Physical Review B.* doi:10.1103/PhysRevB.95.121401 (2017).

178. Curto, A. G. *et al.* Unidirectional emission of a quantum dot coupled to a nanoantenna. *Science.* doi:10.1126/science.1191922 (2010).

179. Shomroni, I. *et al.* All-optical routing of single photons by a one-atom switch controlled by a single photon. *Science.* doi:10.1126/science.1254699 (2014).

180. Ghimire, A., Shafran, E. & Gerton, J. M. Using a sharp metal tip to control the polarization and direction of emission from a quantum dot. *Scientific Reports.* doi:10.1038/srep06456 (2014).

181. Permyakov, D. *et al.* Probing magnetic and electric optical responses of silicon nanoparticles. *Applied Physics Letters* **106.** doi:10.1063/1.4919536 (2015).

182. García-Cámara, B., Moreno, F., González, F. & Martin, O. J. F. Light scattering by an array of electric and magnetic nanoparticles. *Optics Express* **18.** doi:10.1364/OE.18.010001 (2010).

183. Rolly, B., Stout, B. & Bonod, N. Boosting the directivity of optical antennas with magnetic and electric dipolar resonant particles. *Optics Express* **20.** doi:10.1364/OE.20.020376 (2012).

184. Nieto-Vesperinas, M. *Scattering and Diffraction in Physical Optics* doi:10.1142/5833 (WORLD SCIENTIFIC, 2006).

185. Molesky, S. *et al. Inverse design in nanophotonics* 2018. doi:10.1038/s41566-018-0246-9.

186. Su, L., Piggott, A. Y., Sapra, N. V., Petykiewicz, J. & Vučković, J. Inverse Design and Demonstration of a Compact on-Chip Narrowband Three-Channel Wavelength Demultiplexer. *ACS Photonics.* doi:10.1021/acsphotonics.7b00987 (2018).

187. Piggott, A. Y. *et al.* Inverse design and demonstration of a compact and broadband on-chip wavelength demultiplexer. *Nature Photonics.* doi:10.1038/nphoton.2015.69 (2015).

188. Dory, C. *et al.* Inverse-designed diamond photonics. *Nature Communications* **10.** doi:10.1038/s41467-019-11343-1 (2019).

189. Stratton, J. *Electromagnetic theory* (Wiley-IEEE Press, 1941).

190. Picardi, M. F., Zayats, A. V. & Rodriguez-Fortuno, F. J. *Code available on Zenodo at the link:* https://doi.org/10.5281/zenodo.3239121.

191. Neugebauer, M., Woźniak, P., Bag, A., Leuchs, G. & Banzer, P. Polarization-controlled directional scattering for nanoscopic position sensing. *Nature Communications* **7.** doi:10.1038/ncomms11286 (2016).

192. Neugebauer, M., Bauer, T., Banzer, P. & Leuchs, G. Polarization tailored light driven directional optical nanobeacon. *Nano letters* **14.** doi:10.1021/nl5003526 (2014).

193. Woźniak, P., Banzer, P. & Leuchs, G. Selective switching of individual multipole resonances in single dielectric nanoparticles. *Laser & Photonics Reviews* **9.** doi:10.1002/lpor.201400188 (2015).

194. Wei, L., Xi, Z., Bhattacharya, N. & Urbach, H. P. Excitation of the radiationless anapole mode. *Optica.* doi:10.1364/optica.3.000799 (2016).

195. Snyder, A. W. & Love, J. D. *Optical Waveguide Theory* doi:10.1007/978-1-4613-2813-1 (Springer, Boston, MA, 1983).

196. Balanis, C. A. *Antenna theory : analysis and design* (Wiley Interscience, 2005).

197. Yablonovitch, E. Inhibited Spontaneous Emission in Solid-State Physics and Electronics. *Physical Review Letters* **58.** doi:10.1103/PhysRevLett.58.2059 (1987).

198. Yablonovitch, E., Gmitter, T. & Leung, K. Photonic band structure: The face-centered-cubic case employing nonspherical atoms. *Physical Review Letters* **67.** doi:10.1103/PhysRevLett.67.2295 (1991).

199. Foresi, J. S. *et al.* Photonic-bandgap microcavities in optical waveguides. *Nature* **390.** doi:10.1038/36514 (1997).

200. Joannopoulos, J. D., Villeneuve, P. R. & Fan, S. Photonic crystals: putting a new twist on light. *Nature* **386.** doi:10.1038/386143a0 (1997).

201. Lin, S. Y. *et al.* A three-dimensional photonic crystal operating at infrared wavelengths. *Nature* **394.** doi:10.1038/28343 (1998).

202. Wang, Z., Chong, Y., Joannopoulos, J. D. & Soljačić, M. Observation of unidirectional backscattering-immune topological electromagnetic states. *Nature* **461.** doi:10.1038/nature08293 (2009).

203. Rechtsman, M. C. *et al.* Photonic Floquet topological insulators. *Nature* **496.** doi:10.1038/nature12066 (2013).

204. Khanikaev, A. B. *et al.* Photonic topological insulators. *Nature Materials* **12.** doi:10.1038/nmat3520 (2013).

205. Bozhevolnyi, S. I. *Plasmonic nanoguides and circuits* (Jenny Stanford Publishing, 2009).

206. Krasavin, A. V. & Zayats, A. V. Guiding light at the nanoscale: numerical optimization of ultrasubwavelength metallic wire plasmonic waveguides. *Optics Letters* **36.** doi:10.1364/OL.36.003127 (2011).

207. Lee, J.-M. *et al.* Low bending loss metal waveguide embedded in a free-standing multilayered polymer film. *Optics Express* **17.** doi:10.1364/OE.17.000228 (2009).

208. Lipkin, D. M. Existence of a New Conservation Law in Electromagnetic Theory. *Journal of Mathematical Physics* **5.** doi:10.1063/1.1704165 (1964).

209. Tang, Y. & Cohen, A. E. Optical Chirality and Its Interaction with Matter. *Physical Review Letters* **104.** doi:10.1103/PhysRevLett.104.163901 (2010).

210. Tang, Y. & Cohen, A. E. Enhanced enantioselectivity in excitation of chiral molecules by superchiral light. *Science.* doi:10.1126/science.1202817 (2011).

211. Vázquez-Lozano, J. E. & Martínez, A. Optical Chirality in Dispersive and Lossy Media. *Physical Review Letters* **121.** doi:10.1103/PhysRevLett.121.043901 (2018).

212. Crimin, F., Mackinnon, N., Götte, J. & Barnett, S. Optical Helicity and Chirality: Conservation and Sources. *Applied Sciences* **9.** doi:10.3390/app9050828 (2019).

213. Alpeggiani, F., Bliokh, K. Y., Nori, F. & Kuipers, L. Electromagnetic Helicity in Complex Media. *Physical Review Letters* **120.** doi:10.1103/PhysRevLett.120.243605 (2018).

214. Humblet, J. Sur le moment d'impulsion d'une onde électromagnétique. *Physica* **10.** doi:10.1016/S0031-8914(43)90626-3 (1943).

215. Barnett, S. M. & Allen, L. Orbital angular momentum and nonparaxial light beams. *Optics Communications* **110.** doi:10.1016/0030-4018(94)90269-0 (1994).

216. Trueba, J. L. & Rañada, A. F. The electromagnetic helicity. *European Journal of Physics* **17.** doi:10.1088/0143-0807/17/3/008 (1996).

217. Bliokh, K. Y., Bekshaev, A. Y. & Nori, F. Optical Momentum, Spin, and Angular Momentum in Dispersive Media. *Physical Review Letters* **119.** doi:10.1103/PhysRevLett.119.073901 (2017).

218. Bliokh, K. Y., Bekshaev, A. Y. & Nori, F. Optical momentum and angular momentum in complex media: From the Abraham-Minkowski debate to unusual properties of surface plasmon-polaritons. *New Journal of Physics* **19.** doi:10.1088/1367-2630/aa8913 (2017).

219. Goldstein, H. (1980).

220. Landau, L. & Lifshitz, E. *Course of theoretical physics. vol. 1: Mechanics* (Oxford, 1960).

221. Noether, E. Invariante Variationsprobleme. Nachrichten der Königlichen Gesellschaft der Wissenschaften zu Göttingen, Mathematisch-Physikalische Klasse pp. 235–257 (1918). Translated as "Invariant Variation Problems" by MA Tavel. *Transp. Theor. Stat. Phys* **1,** 183–207 (1918).

222. Eisberg, R. & Resnick, R. *Quantum physics of atoms, molecules, solids, nuclei and particles* (1983).

223. Brevik, I. *Experiments in phenomenological electrodynamics and the electromagnetic energy-momentum tensor* 1979. doi:10.1016/0370-1573(79)90074-7.

224. Barnett, S. M. & Loudon, R. The enigma of optical momentum in a medium. *Philosophical Transactions of the Royal Society A: Mathematical, Physical and Engineering Sciences* **368.** doi:10.1098/rsta.2009.0207 (2010).

225. Jones, R. V. & Richards, J. C. S. The pressure of radiation in a refracting medium. *Proceedings of the Royal Society of London. Series A. Mathematical and Physical Sciences* **221.** doi:10.1098/rspa.1954.0043 (1954).

226. Ashkin, A. & Dziedzic, J. M. Radiation Pressure on a Free Liquid Surface. *Physical Review Letters* **30.** doi:10.1103/PhysRevLett.30.139 (1973).

227. Jones, R. V. & Leslie, B. The Measurement of Optical Radiation Pressure in Dispersive Media. *Proceedings of the Royal Society A: Mathematical, Physical and Engineering Sciences* **360.** doi:10.1098/rspa.1978.0072 (1978).

228. Gibson, A. F., Kimmitt, M. F., Koohian, A. O., Evans, D. E. & Levy, G. F. D. A Study of Radiation Pressure in a Refractive Medium by the Photon Drag Effect. *Proceedings of the Royal Society A: Mathematical, Physical and Engineering Sciences* **370.** doi:10.1098/rspa.1980.0035 (1980).

229. Walker, G. B., Lahoz, D. G. & Walker, G. Measurement of the Abraham Force in a Barium Titanate Specimen. *Canadian Journal of Physics* **53.** doi:10.1139/p75-313 (1975).

230. Campbell, G. K. *et al.* Photon Recoil Momentum in Dispersive Media. *Physical Review Letters* **94.** doi:10.1103/PhysRevLett.94.170403 (2005).

231. James, R. P. *A "Simplest Case" Experiment Resolving the Abraham-Minkoski Controversy on Electromagnetic Momentum in Matter* in *Proceedings of the National Academy of Sciences of the United States of America - National Academy of Sciences Autumn Meeting* (1968).

232. Hinds, E. A. & Barnett, S. M. Momentum Exchange between Light and a Single Atom: Abraham or Minkowski? *Physical Review Letters* **102.** doi:10.1103/PhysRevLett.102.050403 (2009).

233. Barnett, S. M. Resolution of the Abraham-Minkowski Dilemma. *Physical Review Letters* **104.** doi:10.1103/PhysRevLett.104.070401 (2010).

234. Kemp, B. A. Resolution of the Abraham-Minkowski debate: Implications for the electromagnetic wave theory of light in matter. *Journal of Applied Physics* **109.** doi:10.1063/1.3582151 (2011).

235. Pfeifer, R. N. C., Nieminen, T. A., Heckenberg, N. R. & Rubinsztein-Dunlop, H. Colloquium: momentum of an electromagnetic wave in dielectric media. *Reviews of Modern Physics* **79.** doi:10.1103/RevModPhys.79.1197 (2007).

236. Milonni, P. W. & Boyd, R. W. Momentum of Light in a Dielectric Medium. *Advances in Optics and Photonics* **2.** doi:10.1364/AOP.2.000519 (2010).

237. Pfeiffer, C. A., Economou, E. N. & Ngai, K. L. Surface polaritons in a circularly cylindrical interface: Surface plasmons. *Physical Review B* **10.** doi:10.1103/PhysRevB.10.3038 (1974).

238. Novotny, L. & Hafner, C. Light propagation in a cylindrical waveguide with a complex, metallic, dielectric function. *Physical Review E* **50.** doi:10.1103/PhysRevE.50.4094 (1994).

239. A. Balanis, C. *Advanced Engineering Electromagnetics* (John Wiley & Sons, 1989).

240. Vázquez-Lozano, J. E., Martinez, A. & Rodríguez-Fortuño, F. J. Near-field directionality beyond the dipole approximation: Electric quadrupole and higher-order multipole angular spectra. *Physical Review Applied* **12.** doi:10.1103/PhysRevApplied.12.024065 (2019).

List of figures

List of tables

Author's merits

List of publications

Published papers

[Paper A] M. F. Picardi, A. Manjavacas, A. V. Zayats and F. J. Rodríguez-Fortuño, "Unidirectional evanescent-wave coupling from circularly polarized electric and magnetic dipoles: An angular spectrum approach", Physical Review B 95, 245416, (2017)

[Paper B] M. F. Picardi, A. V. Zayats and F. J. Rodríguez-Fortuño, "Janus and Huygens Dipoles: Near-Field Directionality Beyond Spin-Momentum Locking", Physical Review Letters 120, 117402, (2018)

[Paper C] M. F. Picardi, A. V. Zayats and F. J. Rodríguez-Fortuño, "Not every dipole is the same: the hidden patterns of dipolar near fields", Europhysics News 49, 14-18, (2018)

[Paper D] M. F. Picardi, M. Neugebauer, J. S. Eismann, G. Leuchs, P. Banzer, F. J. Rodríguez-Fortuño and A. V. Zayats, "Experimental demonstration of linear and spinning Janus dipoles for polarisation- and wavelength-selective near-field coupling", Light: Science & Applications 8, 52, (2019)

[Paper E] M. F. Picardi, K. Y. Bliokh, F. J. Rodríguez-Fortuño, F. Alpeggiani, F. Nori, "Angular momenta, helicity, and other properties of dielectric-fiber and metallic-wire modes", Optica 5, 1016-1026, (2018)

[Paper 6] B. Piccirillo, M. F. Picardi, L. Marrucci and E. Santamato, "Flat polarization-controlled cylindrical lens based on the Pancharatnam-Berry geometric phase", European Journal of Physics 38, 034007, (2017)

[Paper 7] F. J. Rodríguez-Fortuño, M. F. Picardi and A. V. Zayats, "Repulsion of polarized particles from two-dimensional materials", Physical Review B 97, 205401, (2018)

[Paper 8] L. Wei, M. F. Picardi, J. J. Kingsley-Smith, A. V. Zayats and F. J. Rodríguez-Fortuño, "Directional scattering from particles under evanescent wave illumination: the role of reactive power", Optics letters 43, 3393-3396, (2018)

[Paper 9] J. J. Kingsley-Smith, M. F. Picardi, L. Wei, A. V. Zayats and F. J. Rodríguez-Fortuño, "Optical forces from near-field directionalities in planar structures", Physical Review B 99, 235410, (2019)

Pre-print submissions

[Paper 10] M. F. Picardi, A. V. Zayats and F. J. Rodríguez-Fortuño, "Amplitude and phase control of guided modes excitation from a single dipole source: engineering far- and near-field directionality", ArXiv preprint arXiv:1907.06573, (2019)

Conferences

[Conf 1] F. J. Rodríguez-Fortuño, M. F. Picardi and A. V. Zayats "Repulsion of dipoles from two-dimensional materials", in *Nanometa 2017*, (Seefeld), 2017

[Conf 2] M. F. Picardi, A. V. Zayats and F. J. Rodríguez-Fortuño, "Generalized directional evanescent coupling", in *ICOAM 2017- 4th International Conference on Optical Angular Momentum*, (Anacapri), 2017

[Conf 3] M. F. Picardi, L. Wei, J. J. Kingsley-Smith, A. V. Zayats and F. J. Rodríguez-Fortuño, "Full control of near-field dipolar coupling beyond spin-momentum locking", in *META 2018*, (Marseille), 2018

[Conf 4] K. Y. Bliokh, A. Y. Bekshaev, M. F. Picardi, F. Alpeggiani, F. J. Rodríguez-Fortuño, L. Kuipers, and F. Nori, "Optical momentum, angular momentum, and helicity in plasmonics and dielectric structures", in *META 2018*, (Marseille), 2018

[Conf 5] M. F. Picardi, A. V. Zayats and F. J. Rodríguez-Fortuño, "Janus and Huygens dipoles: near field directionality beyond spin-momentum locking", in *Nanolight 2018*, (Benasque), 2018

[Conf 6] M. F. Picardi, L. Wei, J. J. Kingsley-Smith, A. V. Zayats and F. J. Rodríguez-Fortuño, "Directional emission from dipolar sources: the Janus source", in *URSI AT-RASC 2018*, (Gran Canaria), 2018

[Conf 7] M. F. Picardi, L. Wei, J. J. Kingsley-Smith, A. V. Zayats and F. J. Rodríguez-Fortuño, "Near-field directionality beyond circularly polarized dipoles: the Janus source", in *Metamaterials 2018*, (Espoo), 2018

[Conf 8] M. F. Picardi, A. V. Zayats and F. J. Rodríguez-Fortuño, "The hidden patterns of dipolar near fields", in *London Plasmonic Forum 2018*, (London), 2018

[Conf 9] M. F. Picardi, M. Neugebauer, J. S. Eismann, P. Banzer, A. V. Zayats and F. J. Rodríguez-Fortuño, "Selective excitation of guided modes via analytically designed dipolar sources: from the Janus dipole to multimode control", in *Nanometa 2019*, (Seefeld), 2019

[Conf 10] M. F. Picardi, A. V. Zayats and F. J. Rodríguez-Fortuño, "From the Janus dipole to multimode control: dipolar sources for guided modes excitation", in *London Plasmonic Forum 2019*, (London), 2019

[Conf 11] M. F. Picardi, M. Neugebauer, J. S. Eismann, P. Banzer, A. V. Zayats and F. J. Rodríguez-Fortuño, "Dipolar sources for directional and selective excitation of guided modes", in *Plasmonica 2019*, (Naples), 2019

[Conf 12] L. Wei, J. J. Kingsley-Smith, M. F. Picardi, A. V. Zayats and F. J. Rodríguez-Fortuño, "Exploiting the polarization of nanoparticles near surfaces: position sensing, recoil optical forces, and full angular spectrum engineering", in *META 2019*, (Lisbon), 2019

Visual representation of my gratitude

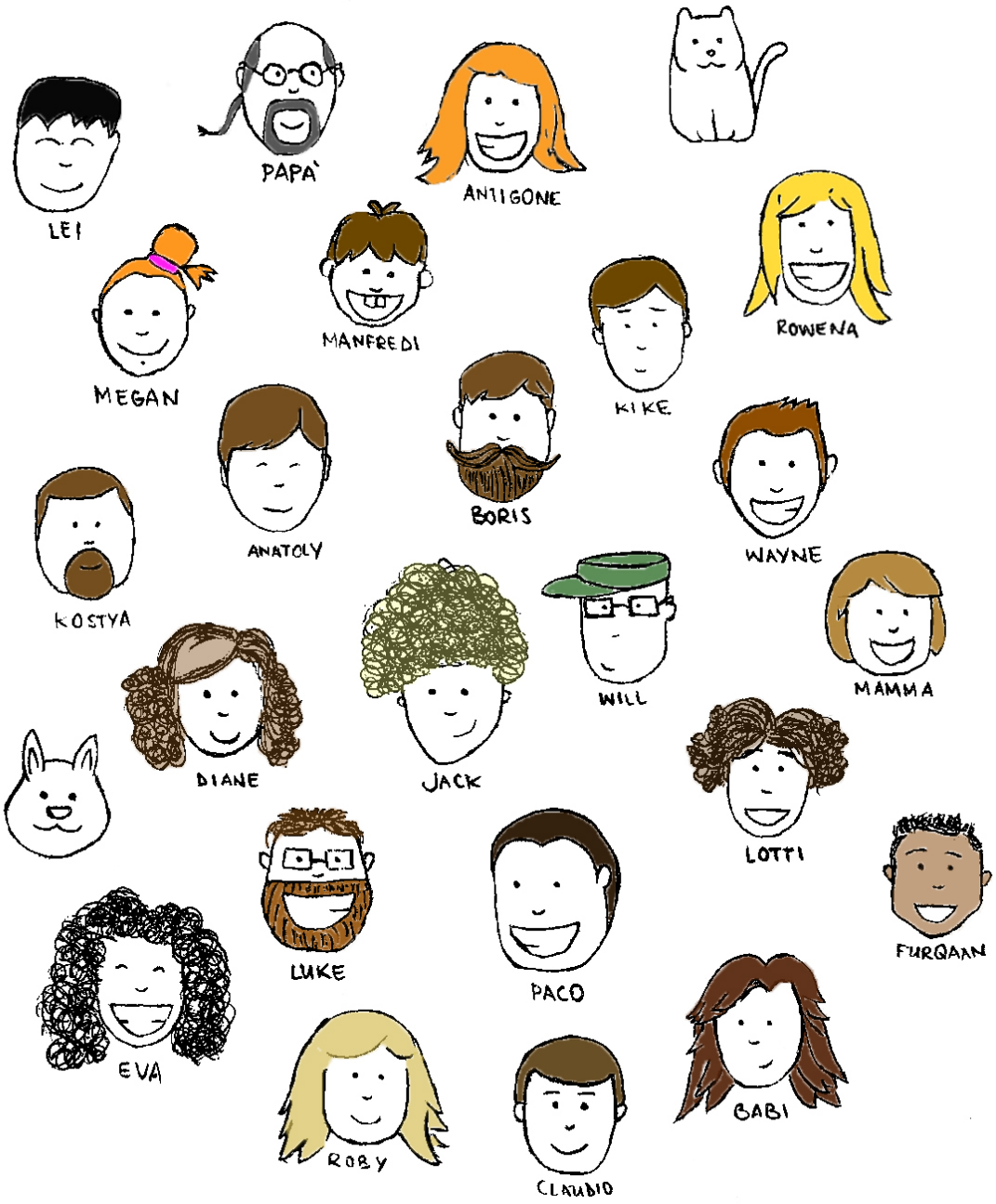

Schematic representation of the many I am thankful to. You are all much more beautiful than this and, to be fair, you all have ears and eyebrows in real life.